

Non-linear modelling of saturated internal and external MHD instabilities in tokamaks

Thèse N° 9155

Présentée le 8 février 2019
à la Faculté des sciences de base
SPC - Théorie
Programme doctoral en physique

pour l'obtention du grade de Docteur ès Sciences

par

ANDREAS KLEINER

Acceptée sur proposition du jury
Prof. F. Courbin, président du jury
Dr J. Graves, directeur de thèse
Dr H. Lütjens, rapporteur
Dr S. Medvedev, rapporteur
Dr H. Reimerdes, rapporteur

2019

Abstract

Macroscopic instabilities and their unfavourable effects on plasma confinement pose a central challenge for the development of reactor relevant tokamak scenarios. Some promising operation scenarios feature extended regions of low magnetic shear. These are in the core region for hybrid scenarios, and in the pedestal-edge region for e.g. the ELM-free quiescent H-mode (QH-mode). This thesis presents a non-linear study of macroscopic magnetohydrodynamic (MHD) instabilities with a focus on plasmas with regions of low magnetic shear. In the first part, we investigate the triggering of fast growing resistive modes in hybrid tokamak plasmas, where infernal modes can couple to neoclassical tearing modes (NTMs). Numerical simulations with the non-linear resistive initial value code XTOR-2F with and without inclusion of bootstrap current effects allow us to determine the evolution of MHD modes from the linear to the late non-linear phase. An analytical model is developed to describe the vanishing of mode coupling in the early non-linear regime. In this context, we extend the tearing stability parameter Δ' from the linear to the non-linear phase and calculate the individual contributions to the growth of the resistive mode. This allows for an identification of the triggering mechanism in the initial phase and the dominant terms in the non-linear phase. A comparison with the numerical results shows that infernal mode coupling can destabilise otherwise stable NTMs and thus seed 2/1 magnetic islands. The helically perturbed bootstrap current is found to further destabilise the magnetic islands in the non-linear phase. In the second part of the thesis, 3D free-boundary equilibrium computations are employed to describe saturated external kink-type modes. The approach is first demonstrated to capture the salient features of non-linearly saturated external kink modes in standard baseline tokamak scenarios and is then applied to QH-mode plasmas. A method to conveniently extract the saturated displacement amplitude from edge-corrugated VMEC equilibria in terms of straight field line Fourier modes is presented. For standard current-driven modes the amplitude is compared with a non-linear analytical model, for which a numerical solver is implemented. In QH-mode plasmas, dangerous edge localised modes (ELMs) are replaced by benign edge harmonic oscillations (EHOs). The latter are commonly assumed to be connected to saturated external kink states. In our study of QH-mode plasmas, we consider two different driving mechanisms for external kink type-modes separately. We find that standard current-driven external kinks are linearly unstable, and non-linearly stable in a wide parameter range, especially where $q_{\text{edge}} \lesssim m/n$. But, where standard current-driven kinks are linearly stable we find that coupling of pressure-driven infernal modes can cause instability, and their upper sideband drives edge corrugations that appear to have external kink features. Both types of modes are identified with the VMEC equilibrium code, and the spectra are compared favourably with those of linear numerical approaches and analytic methods. EHOs could be connected to both type of modes.

Keywords: tokamak, magnetohydrodynamics, MHD, nonlinear, neoclassical, tearing, infernal, external kink, quiescent H-mode, edge harmonic oscillations

Zusammenfassung

Makroskopische Plasmaintabilitäten und deren Auswirkungen auf den magnetischen Einschluss von Fusionsplasmen sind eine zentrale Herausforderung bei der Entwicklung von reaktorrelevanten Tokamakszenarien. Einige vielversprechende Operationsszenarien weisen räumliche Regionen mit geringer magnetischer Scherung der Feldlinien auf. Solche Regionen befinden sich im Zentrum des Plasmas in Hybridszenarios, und in der Randregion (pedestal), z. B. in der ELM-freien QH-Mode. In dieser Dissertation präsentieren wir eine nichtlineare Untersuchung von makroskopischen magneto-hydrodynamischen Instabilitäten mit Fokus auf Plasmen mit geringer magnetischer Scherung der Feldlinien. Im ersten Teil beschäftigen wir uns mit dem Auslösen von schnell wachsenden resistiven Moden in hybriden Tokamakszenarien, wo sogenannte 'Infernal Modes' mit neoklassischen Tearingmoden (NTMs) koppeln können. In numerischen Berechnungen mit dem resistiven Anfangswertcode XTOR-2F mit und ohne Berücksichtigung des Bootstrapstroms, ist es möglich die Entwicklung von MHD-Moden von der linearen bis zur nichtlinearen Phase zu bestimmen. Ein analytisches Modell wird entwickelt um den Verlust der Modenkopplung in der frühen nichtlinearen Phase zu beschreiben. Dabei erweitern wir den Tearingstabilitätsparameter Δ' vom linearen in das frühe nichtlineare Stadium und berechnen die individuellen Beiträge zum Wachstum der resistiven Mode. Dies erlaubt sowohl eine Identifikation des Auslösemechanismus in der Anfangsphase, sowie der dominanten physikalischen Effekte in der nichtlinearen Phase. Ein Vergleich mit den numerischen Ergebnissen zeigt, dass eine Kopplung mit Infernal Modes ansonsten stabile neoklassische Tearingmoden destabilisieren, und damit magnetische Inseln generieren kann. In der nichtlinearen Phase destabilisiert die spiralförmige Störung des Bootstrapstroms die magnetischen Inseln weiter. Im zweiten Teil dieser Dissertation werden 3D Gleichgewichtsberechnungen mit frei beweglichem Plasmarand dazu verwendet gesättigte externe Kinkmoden zu beschreiben. Zuerst wird anhand von Standardtokamakszenarien demonstriert, dass dieser Ansatz die herausragenden Eigenschaften solcher Moden erfasst. Anschließend wird die Methode auf QH-Modeplasmen angewandt. Eine Berechnungsmethode zur Bestimmung der Sättigungsamplitude der Randmoden in den 3D VMEC Gleichgewichtszuständen in Form von Fouriermoden wird vorgestellt. Dazu wird ein Koordinatensystem eingeführt, in welchem die Magnetfeldlinien gerade sind. Für stromgetriebene externe Kinkmoden wird die Amplitude mit der eines nichtlinearen analytischen Modells verglichen, wozu eine numerische Lösungsmethode implementiert wird. In QH-Modeplasmen werden ELMs durch gutartige harmonische Oszillationen am Rand (EHOs) ersetzt. Letztere werden in der Literatur mit gesättigten externen Kinkmoden assoziiert. In unserer Untersuchung von QH-Modeplasmen berücksichtigen wir separat zwei unterschiedliche Destabilisierungsmechanismen (Strom und Druck). Die Ergebnisse zeigen, dass externe Kinkmoden über einen breiten Parameterbereich linear instabil und nichtlinear stabil sind, insbesondere wenn $q_{\text{Rand}} \lesssim m/n$. Wenn aber stromgetriebene externe Kinkmoden linear stabil sind, beobachten wir druckgetriebene Infernal Modes mit einem oberen Seitenband, das durch die Kopplung benachbarter poloidaler Moden destabilisiert wird. Diese Seitenbänder haben die Eigenschaften von externen Kinkmo-

den. Beide Modentypen werden mit dem Gleichgewichtscode VMEC identifiziert und die Spektren erfolgreich mit denen von linearen numerischen und analytischen Methoden verglichen.

Stichwörter: Tokamak, Magnetohydrodynamik, MHD, nichtlinear, Plasmainstabilitäten, NTM, infernal, Kinkmoden, quiescent H-mode, edge harmonic oscillations

Résumé

Les instabilités macroscopiques et leurs effets néfastes sur le confinement du plasma comptent parmi les défis majeurs du développement de scénarios pour un réacteur tokamak. Certains scénarios prometteurs présentent des régions étendues de bas cisaillement magnétique. Ces régions sont situées dans le coeur dans le cas des scénarios hybrides et dans la région du bord/piédestal dans le cas, par exemple, des modes QH sans ELM. Cette thèse traite d'études non-linéaires des instabilités macroscopiques magnétohydrodynamiques en se concentrant sur des plasmas comportant des régions de bas cisaillement. La première partie porte sur l'amorçage des modes résistifs à croissance rapide dans les plasmas de scénarios hybrides pour lesquels les modes infernaux peuvent se coupler aux "Neoclassical Tearing Modes" (NTMs). Les simulations numériques du code non-linéaire résistif et à valeur initial XTOR-2F, avec et sans prise en compte de l'effet du courant de bootstrap, permettent de déterminer l'évolution des modes MHD de la phase linéaire jusqu'à des phases non-linéaires avancées. Un modèle analytique a été développé afin de décrire la disparition du couplage de mode dans la première phase non-linéaire. De cette manière, le "tearing stability parameter" Δ' est étendu de la phase linéaire à la phase non-linéaire et les contributions individuelles à la croissance du mode résistif sont calculées, permettant l'identification du mécanisme d'amorçage dans la phase initiale, et des termes dominants dans la phase non-linéaire. Des comparaisons avec les résultats numériques montrent que le couplage avec les modes infernaux peuvent déstabiliser des modes NTMs normalement stables et ainsi déclencher des îles magnétiques 2/1. Additionnellement, la perturbation hélicoïdale du courant de bootstrap déstabilise les îles magnétiques dans la phase non-linéaire. Dans la deuxième partie de cette thèse, des modes kink externes saturés sont décrits par le truchement de calculs 3D d'équilibres au bord libre. Tout d'abord, la démonstration que l'approche est capable de saisir les éléments essentiels des modes externes kink non-linéaires dans les scénarios de base standard des tokamaks a été démontrée. Cette approche a ensuite été appliquée à des configurations de plasmas de mode H calme (quiescent H-mode ou QH-mode). Une méthode pratique pour extraire l'amplitude de déplacement saturée d'un équilibre VMEC corrugé au bord, en terme de modes de Fourier de ligne de champ droit, est présentée. Pour des modes standards entraînés par le courant, l'amplitude est comparée à un modèle analytique non-linéaire, pour lequel un code a été implémenté. Pour les plasmas de mode QH, les modes dangereux localisés dans le bord (ELMs) sont remplacés par des oscillations harmoniques bénignes (EHOs). Ces dernières sont communément liées aux états kink externes saturés. Dans nos études des plasmas de mode QH, nous considérons séparément deux mécanismes de stimulation pour les modes de types kink externes. Les modes standards kink externes entraînés par le courant sont linéairement instables, et non-linéairement stables pour une large échelle de paramètres, en particuliers quand $q_{\text{bord}} \lesssim m/n$, comme attendu. Néanmoins, là où les modes kink entraînés par le courant sont linéairement stables, on trouve que le couplage des modes infernaux entraînés par la pression peuvent être la cause d'instabilité. Leur bande latérale supérieure entraîne des corrugations dans le bord du plasma et semble posséder des caractéristiques kink externes. Les deux types de modes sont identifiés avec

le code d'équilibre VMEC et le spectre est comparé avec succès avec celui provenant d'approches numériques linéaires et de méthodes analytiques. Les oscillations harmoniques bénignes (EHOs) pourraient être liées aux deux types de modes.

Mots clefs : tokamak, magnétohydrodynamique, MHD, non-linéaire, instabilités, plasma, NTM, mode infernaux, kink externe, quiescent H-mode, edge harmonic oscillations

Contents

Abstract (English / Deutsch / Français)	i
1 Introduction	1
1.1 Nuclear fusion as energy source	1
1.2 Magnetic confinement of plasmas	2
1.2.1 The basics	2
1.2.2 Toroidal confinement devices	3
1.2.3 Current fusion challenges & future development	6
1.3 Thesis focus and contribution	7
1.4 Outline of this thesis	9
2 Fluid description of a plasma	11
2.1 Basic and extended MHD models for tokamak plasmas	11
2.1.1 Ideal and resistive single-fluid MHD model	11
2.1.2 Bootstrap current	13
2.2 The safety factor profile	15
2.3 Toroidal plasma equilibrium	16
2.3.1 Axisymmetric equilibrium: the Grad-Shafranov equation	17
2.3.2 The CHEASE 2D equilibrium code	18
2.3.3 Non-axisymmetric equilibrium and the VMEC code	19
2.3.4 Stellarator symmetry	23
2.4 Macroscopic plasma stability	23
2.4.1 Linearisation and initial value formulation	24
2.4.2 Normal modes & Energy principle	25
2.4.3 The KINX code	26
2.4.4 Non-linear stability	27
2.5 Summary and thesis outlook	28
3 NTM seeding by coupling with infernal modes	31
3.1 Introduction	31
3.2 Fast growing resistive modes in experiments	33
3.3 Resistive instabilities and tearing modes	35
3.3.1 Classical tearing modes	35
3.3.2 Non-linear neoclassical tearing modes	37
3.4 Extension of the Rutherford equation to include seeding by infernal modes	39
3.4.1 Linear model of resistive infernal modes	39
3.4.2 Infernal mode saturation and modelling of Δ' in the early non-linear phase	42
3.4.3 Ad-hoc calculation of coupled non-linear infernal modes and their eigenfunctions	45

Contents

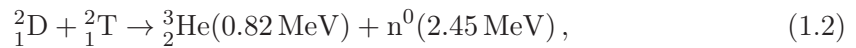
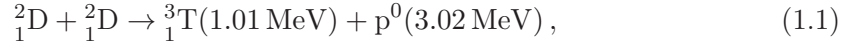
3.5	Resistive non-linear stability simulations	48
3.5.1	The non-linear initial value code XTOR-2F	48
3.5.2	Physical model & Equilibrium	52
3.5.3	Evolution of coupled modes in a MAST-like plasma	54
3.6	Comparison of the Model with the XTOR-2F Simulations	58
3.7	Conclusions	61
4	Non-linear saturated current-driven external kink modes modelled with 3D free-boundary equilibria	63
4.1	Introduction	63
4.2	Linear and non-linear external kink modes	64
4.2.1	Linear theory of external kink modes	64
4.2.2	Non-linear external kink stability	67
4.3	3D equilibrium simulations	70
4.3.1	Fourier analysis of VMEC saturated external kink modes	74
4.4	Linear stability analysis	77
4.5	Analytical predictions and comparison with VMEC results	79
4.6	Conclusions	83
5	Saturated current-driven and pressure-driven external kink modes in extended low-shear QH-mode plasmas	85
5.1	Introduction	85
5.2	Experimental observation of quiescent H-mode regimes	88
5.3	Current-driven external kinks in QH-mode plasmas	90
5.4	Pressure-driven external kink modes in QH-mode plasmas	96
5.4.1	Prediction of edge infernal modes with external kink sidebands	96
5.4.2	Non-linear numerical simulations & linear stability analysis	96
5.5	Higher n modes and non-linear damping	105
5.6	Conclusions	106
5.7	Outlook: Non-linear stability simulations with XTOR-2F	108
6	Summary & conclusions	109
A	Curvilinear coordinates & vector formalism	113
A.1	Definition of general curvilinear coordinates	113
A.2	Cylindrical coordinates	115
A.3	Straight field line coordinates	115
B	Reconstruction of the magnetic field perturbation from the radial displacement	117
C	Development of numerical codes & tools	119
C.1	Calculation of the magnetic island width based on Poincaré plots	119
C.2	Solver for non-linearly saturated external kink amplitudes	120
C.2.1	Numerical scheme & Implementation	120

C.2.2 Benchmark of the solver	124
Bibliography	127
Acknowledgements	135
Curriculum Vitae	137

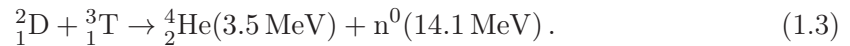
Introduction

1.1 Nuclear fusion as energy source

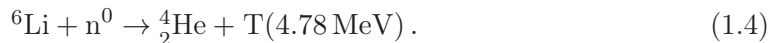
The global rise in energy demands and the limitations of fossil fuels in terms of availability and pollution requires a search for new energy sources. Renewable energy sources such as wind and solar power are more sustainable than fossil fuels, but the power output depends strongly on the location and is not constant in time. This brings the need for energy storage, which itself relies on lithium batteries (not good for the environment) or hydro storage. The risks and political whims associated with nuclear fission have resulted in the shutdown of multiple nuclear power plants in the western world. Another possible energy source is nuclear fusion. Two light elements fuse to a heavier element while releasing binding energy. This energy can be used to operate a generator. Fusion reactions with a net energy gain are possible among a multitude of light isotopes, with varying cross sections and some reactions require large energies. For laboratory fusion devices the fusion reactions involving deuterium and tritium as fuel are favourable:



and



The cross sections of the reactions of Eqs. (1.1)-(1.3) are shown in Fig. 1.1a and their reactivity in Fig. 1.1b [1]. Deuterium is available on earth in large scales and can mainly be found in the oceans. Tritium is radioactive with a half life of 12.32 years. For this reason there are no practical natural sources on earth. However, tritium can be bred from lithium reacting with neutrons resulting from the fusion reactions inside the plasma:



Such fusion reactions (and many others) occur naturally in the sun's core, where gravity ensures the confinement of a vast number of reacting particles under high pressure and temperature. This is necessary since it provides the energy required for two particles to overcome the barrier due to electrostatic forces and fuse. In the centre of the sun, a pressure of $p \approx 26.5 \times 10^{15} \text{ Pa}$ acts on the matter at a temperature of $1.57 \times 10^7 \text{ K}$. Recreating such conditions (without the luxury of strongly localised gravitational fields) on earth is challenging. Matter at such a temperature requires thermal isolation from any surrounding material since thermal transport would cool down the fuel, but also because no known material can withstand such temperatures. The approaches on earth are thus focused on inertial confinement fusion (high density) and magnetic confinement (low density, high temperature).

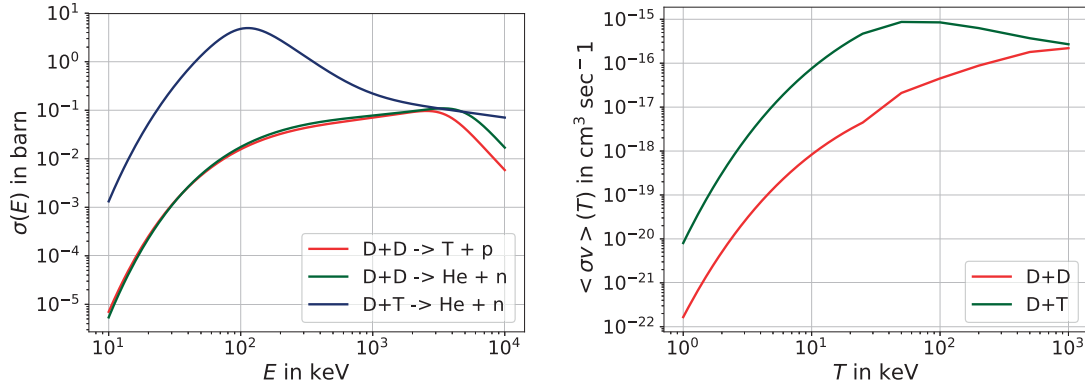


Figure 1.1(a): Cross sections of commonly used fusion reactions as a function of energy.

Figure 1.1(b): Reactivity of commonly used fusion reactions as a function of temperature.

1.2 Magnetic confinement of plasmas

The confinement of the fuel for nuclear fusion reactions within an isolated space requires a force to act on the matter. Electromagnetic forces are appropriate, since gravity is too weak on earth, and the weak and strong nuclear forces are of very short range. Due to the high temperatures required to enable nuclear fusion reactions, the matter is in the plasma state. In the following, we define this fourth state of matter and introduce toroidal magnetic fusion devices.

1.2.1 The basics

A plasma is characterised by a separation of electrons from initially neutral atoms, creating a gas of freely moving electrons and ions interacting with electromagnetic forces. This charge separation is only visible at microscopic scales. At scales larger than the Debye length $\lambda_D = \sqrt{\varepsilon_0 k_B T_i / n_e e^2}$, where ε_0 is the vacuum permittivity, k_B the Boltzmann constant, T_i the ion temperature, n_e the electron density and e the electron charge, the plasma appears electrically neutral [2]. This principle is called quasi-neutrality. A plasma can be fully or partially ionised and is an electrical conductor. In fact most matter in the visible universe is in the plasma state. It is found in stars and the intergalactic medium, but also on earth e.g. in the form of lightnings or fluorescent lamps. Thus, plasmas exist in a wide range of temperature and density. Now, any charged particle with non-zero velocity \mathbf{v} experiences the force

$$\mathbf{F} = q(\mathbf{E} + \mathbf{v} \times \mathbf{B}), \quad (1.5)$$

in the presence of an electric \mathbf{E} and magnetic field \mathbf{B} . This results in a helical trajectory with finite radius around a magnetic field line, enabling the confinement of a plasma inside a magnetic field (surrounded by a vacuum). In particular, to leading order the particle streams along a magnetic field. Salient features of plasma confinement can be assessed by the trajectories of magnetic field lines.

The development of magnetic confinement devices began in the 1950s, starting with simple magnetic field geometries, e.g. mirror machines, z-pinch. The confinement time

1.2. Magnetic confinement of plasmas

for these machines turned out to be very low. One disadvantage of these concepts is the existence of at least one point where the magnetic field line exits the vessel or the machine, allowing free streaming of particles. Or the magnetic field strength would vanish locally, which introduces poor confinement for other reasons. According to the hairy ball theorem [3] only a torus has the property that a vector field with $\nabla \cdot \mathbf{B} = 0$ does not vanish in any point. Such toroidal confinement systems are discussed in the next section.

1.2.2 Toroidal confinement devices

There are currently two competing toroidal designs considered for future power plants: the stellarator and the tokamak. Since this thesis focuses on tokamak studies, we introduce its principles in the following and briefly explain the differences to the stellarator.

The word tokamak as well as the design originates from Russia, meaning *toroidal chamber with axial magnetic field*. Plasma confinement is achieved by the creation of toroidal and poloidal magnetic fields. The magnetic field lines lie on toroidal surfaces. An example of such a surface is shown in Fig. 1.2 together with essential parts of a tokamak. Ideally, the radial component of the magnetic field, which is perpendicular to the toroidal flux surfaces should vanish for the particles to remain confined. The toroidal magnetic field \mathbf{B}_ϕ , which is the dominant component of \mathbf{B} in a tokamak, is created by current-carrying external magnetic field coils surrounding the plasma. At the inboard side of the plasma the distance in between the toroidal field coils is much lower than on the outboard side, as depicted in Fig. 1.2. This results in a strong magnetic field closer to the central axis that decreases radially outwards, leading to the terminology high-field and low-field side. Due to their finite Larmor radius, the plasma particles would experience a variation in magnetic field strength during their gyro motions (c.f. Lorentz force), causing a drift of particles. This drift is in the opposite direction for unlike charges, so that electric fields build up and this in turn causes catastrophic loss of confinement (due to so-called $\mathbf{E} \times \mathbf{B}$ drifts). This is counteracted by applying a poloidal magnetic field that results in helical magnetic field lines, forcing particles to execute periodic orbits over the poloidal cross section, averaging out drifts due to magnetic inhomogeneity, and preventing charge accumulation. A solenoid in the centre of the tokamak (c.f. Fig. 1.2) acts as a primary transformer coil and induces a current in the plasma, which acts as a secondary transformer coil. The plasma current then enhances the poloidal magnetic field. The superposition of toroidal and poloidal fields results in helical field lines which are aligned on closed surfaces, where the magnetic flux is constant (flux surfaces). As will be discussed later in this thesis, the exact topology of the magnetic field - particularly the field line helicity - is crucial for plasma stability. The toroidal shape has another side effect: the plasma tries to expand in radial direction. This is due to two reasons. First, because the pressure is distributed equally on a flux surface, but the plasma surface is smaller on the inboard side than on the outboard side, thus a net force arises in radial direction. Second, the currents on two opposing sides of the torus repel each other causing the torus to increase in diameter. This can be compensated by enclosing the plasma in a (perfectly) conducting wall, which increases the magnetic pressure on the outboard

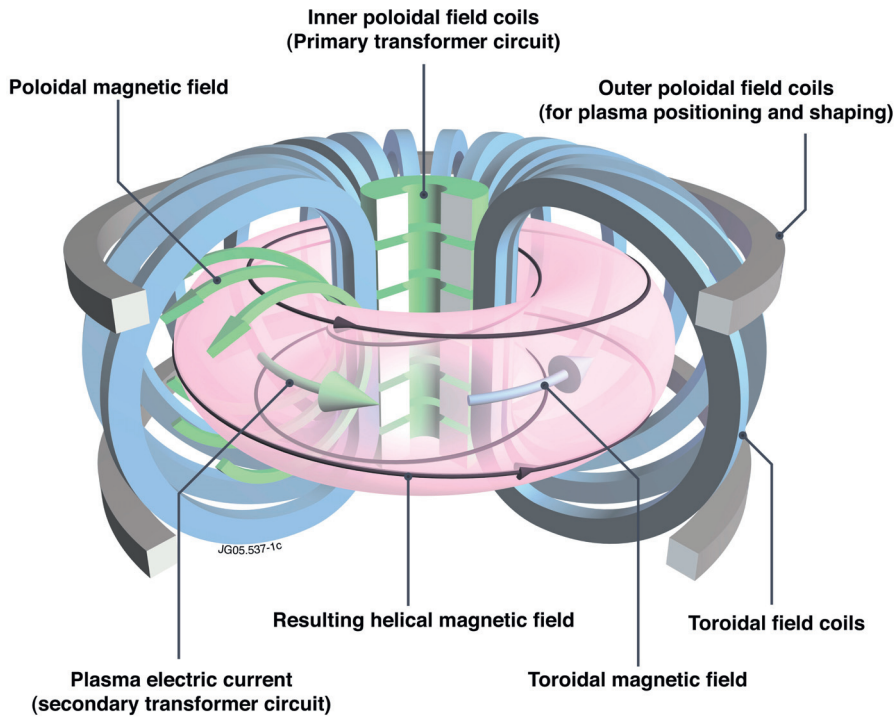


Figure 1.2 – Schematic of a typical tokamak. Toroidal and poloidal field coils are arranged such that the resulting magnetic field has the topology of a torus and the plasma particles follow helical field lines. Courtesy of EUROfusion.

side and enables the existence of another equilibrium state in which the magnetic axis is shifted with respect to the geometrical centre (Shafranov shift). Furthermore, a vertical magnetic field can be applied to provide a Lorentz force that counteracts the expansion [4].

The temperatures of 100 Mio. K to 150 Mio. K required to achieve nuclear fusion are achieved by several heating mechanisms. The primary heat source is Ohmic heating as a result of the internal plasma resistivity and the solenoid (and plasma) induced plasma current. Additional heating mechanisms are neutral beam injection (NBI) and radio-frequency heating via electromagnetic waves. The latter can be applied to electrons (electron cyclotron resonance heating (ECRH)) or to ions (ion cyclotron resonance heating (ICRH)). The optimisation and effects of these auxiliary heating mechanisms are subject of current research.

An important measure for the performance of the plasma is the ratio of thermal and magnetic pressure called plasma beta $\beta = \frac{p}{B^2/(2\mu_0)}$, where p is the pressure, $B = |\mathbf{B}|$ and μ_0 the vacuum permeability. For a confined plasma $\beta < 1$. However, in real fusion devices $\beta \ll 1$ with typical values of a few percent. The maximum possible value of β is limited by plasma instabilities. Some of these instabilities are investigated in the frame of this thesis. A well known gross prediction for the operational limits of tokamaks is the Troyon limit [5].

As alternative concept to the tokamak, the stellarator [6] is characterised by having

1.2. Magnetic confinement of plasmas

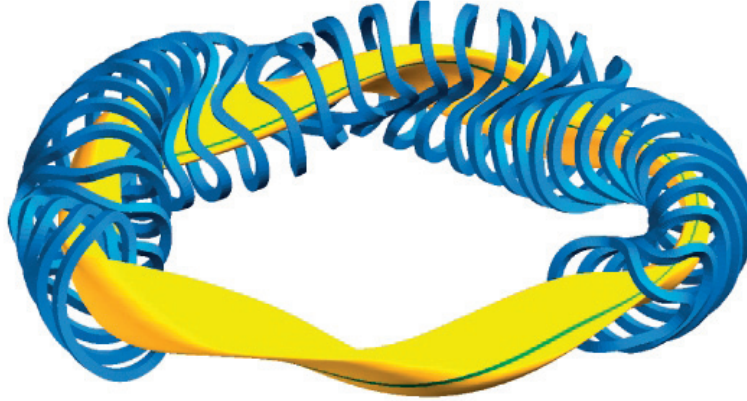


Figure 1.3 – Magnetic field coils (blue) and resulting flux surface (yellow) in Wendelstein 7-X, a stellarator. Courtesy of Max-Planck Institut für Plasmaphysik.

a magnetic field that is entirely generated by external coils and no current is induced in the plasma (small self-generated currents such as the bootstrap current exist though). This has the advantage of avoiding current-driven instabilities and being able to operate the machine in a continuous manner. However, the coil design is much more complicated for the stellarator, where the plasma is always non-axisymmetric as shown in Fig. 1.3. Another challenge in the development of stellarators is the confinement of fast particles such as alpha particles (necessary to reach fusion burn conditions). In stellarators, fast particles can form an energetic particle beam that can leave the plasma and damage the machine.

The high electrical energy costs for creating the magnetic field and heating the plasma together with further energy losses during operation, require that conditions for nuclear fusion are maintained sufficiently long to obtain an energy gain. The neutrons created in the fusion reaction with an energy of 14.1 MeV are available for electricity generation, while the α particles can collide with other particles in the plasma and provide an additional heat source. Power losses occur in the form of Bremsstrahlung and particle transport. In order to maintain fusion reactions, the power gain must be larger or equal to the power losses. Then the fusion reaction becomes self-sustaining. Based on Lawson criterion [7] ignition is achieved when

$$n_e \tau_E T \geq \frac{12 k_B T^2}{\langle \sigma v \rangle E_{dt}}, \quad (1.6)$$

where the electron density n_e , the energy confinement time τ_E and the temperature T define the so-called triple product. Here, $E_{dt} = 3.5$ MeV and $\langle \sigma v \rangle$ is the product of the fusion reaction cross section σ and velocity v averaged over a Maxwellian distribution. As we can see from Eq. (1.6), a requirement for energy gain in a fusion reactor is a long energy confinement time. Hence, the plasma state needs to be retained sufficiently long, i.e. instabilities of the plasma are to be avoided. Generally, an instability occurs when

the plasma response to a perturbation is such that the perturbation grows further in time, away from an equilibrium state. This can lead to a loss of plasma particles, energy and eventually the plasma itself. The investigation of such instabilities in experimental conditions is thus an important topic and the main focus of this thesis.

1.2.3 Current fusion challenges & future development

In tokamaks, macroscopic plasma instabilities are often associated with the sudden loss of confinement. Such an event is called a disruption. While disruptions are undesired (but no real threat to small existing tokamaks), they are intolerable in ITER (International Thermonuclear Experimental Reactor)¹. With a plasma volume of 840 m³ and a major radius of $R_0 = 6.2$ m [8] it will be the largest tokamak built to date. The occurrence of a disruption can be deleterious in ITER, since the energy deposited in the surrounding vessel is proportional to the plasma volume. Disruption avoidance is an important topic for the development of the next generation of tokamaks.

The definitive goal of fusion research is to reach steady state conditions, where the current is driven fully non-inductively. ITER is expected to demonstrate the feasibility of long plasma discharges and high fusion power gain. Requirements for steady state include a high bootstrap current fraction (explained in chapter 2) and high beta limits together with good confinement properties. In the past decades a lot of research has been conducted with the aim of finding parameter and operating spaces to achieve these goals. A very important parameter that determines the performance of a tokamak plasma is the current profile. The current profile is directly related to the helicity of the magnetic field lines, described by the safety factor or q profile (defined in chapter 2). The derivative of this profile determines the magnetic shear, a measure for the variation of the field line helicity and an important quantity for the magnetohydrodynamic (MHD) stability of a plasma. A variety of current profiles from monotonic to deeply reversed shapes have been studied in experimental reactors and on this basis three operational scenarios were proposed for ITER. In the **standard scenario** the current is driven inductively, but is expected to have the best fusion performance ($Q = P_{\text{fusion}}/P_{\text{heat}} = 10$). The q profile is monotonic with a rational value of $q = 1$ contained inside the plasma, and hence the plasma is susceptible to sawtooth oscillations. Further MHD instabilities can cause possible disruptions and damage to the machine, and some of these instabilities are triggered by sawtooth oscillations. A larger fraction of non-inductive current is achieved in **hybrid scenarios** aimed to achieve long burn times (> 1000 s) and $Q = 5$. The total current is lower in this scenario than in the standard scenario and has a higher beta limit. A main characteristic of the hybrid scenario is an extended region in the core where the q profile is flat and the magnetic shear very low with $q > 1$ everywhere (sawteeth are avoided). Disruption threatening instabilities can be triggered by ideal modes in these hybrid regimes and we study this phenomena in this thesis. In the **advanced scenario** the current is driven predominantly non-inductively or fully inductively to reach true steady state. The q profile is reversed in the core and gives rise to an internal transport barrier (ITB) with strongly reduced transport. However, the fusion power in

¹Under construction in Cadarache, France and expected to start operation by 2025.

1.3. Thesis focus and contribution

such discharges is low and alpha-driven instabilities, and impurity confinement can be problematic [9].

A major step towards achieving good plasma confinement in tokamaks, was the discovery of the high confinement mode (H-mode) [10], which occurs when enough plasma heating is applied to exceed a certain threshold. In the H-mode, the pressure, temperature and density profiles steepen close to edge forming the so-called edge pedestal [11]. This causes a strong bootstrap current, which again is desirable to achieve steady state. However, the improved confinement is accompanied by periodic oscillations at the plasma edge called edge localised modes (ELMs) [12]. The control and avoidance of ELMs is one of the biggest challenges of current fusion research, since ELMs cause large heat loads from the plasma towards the surrounding machine components. For large machines like ITER ELMs can be deleterious and have to be mitigated if not fully suppressed. Current research is thus focused on mitigating ELMs for example by application of resonant magnetic perturbations (RMPs) [13] and exploring experimentally observed high confinement regimes without ELMs. The latter is investigated in the frame of this thesis.

1.3 Thesis focus and contribution

The aim of this thesis is an investigation of macroscopic plasma instabilities in tokamak plasmas with a focus on non-linear phenomena. In this context, we review the theoretical background of macroscopic instabilities including analytical and numerical methods. These are applied to compute stability of current-driven and pressure-driven instabilities in a variety of tokamak configurations with high and low magnetic shear. The latter is found in the plasma core in hybrid scenarios and after sawtooth crashes, but also in plasmas with edge pedestal. The common element connecting most of the instabilities in this thesis is an extended region of low magnetic shear, where infernal modes are driven, either at the core or the edge.

Macroscopic instabilities are usually investigated using the magnetohydrodynamics (MHD) model, which forms a set of partial non-linear differential equations. Finding analytical solutions to this model is challenging. One way to simplify the model is to linearise it. Numerous studies have been carried out treating the linear stability of tokamak plasmas. The resulting linear MHD equations are easier to solve, but analytical solutions are found only for specific simple configurations such as cylindrical limits, large aspect ratio or circular poloidal cross sections. In the linear model a plasma is perturbed about an equilibrium state. This approach is valid only in the limit of small perturbations and is sufficient to determine whether a perturbed plasma goes back to its equilibrium state (stability), or whether it exhibits further growth (instability). However, there are two limitations associated with the linear model. First, linear stability analysis does not apply for modes with large perturbations that occur in experiments, such as neoclassical tearing modes (NTMs) and (to some extent) edge harmonic oscillations. Hence, linear models cannot provide a full explanation of these phenomena. Second, dominant linearly unstable modes are not always dominant in the non-linear phase. In order to predict the impact of unstable modes in tokamak scenarios a pure linear treatment is usually insufficient. Non-linear models describe effects such as saturation, non-linear growth

or damping of certain linearly unstable modes and non-linear coupling. As a result, certain modes can be dominant in the non-linear phase that were not dominant during the initial linear phase [14]. For neoclassical tearing modes, non-linearity is particularly important. These meta-stable modes are driven unstable by a seed (a sufficiently strong initial perturbation is required to cause the mode to be unstable). The development of non-linear analytic models is even more challenging. However, a few models exist for some ideal MHD modes, resistive NTMs usually require the adoption of simple geometries. Plasmas in modern and future tokamaks with finite aspect ratio are quite highly shaped, i.e. the poloidal cross section is elongated and triangular to a certain degree. Ignoring these geometrical effects can lead to inaccurate results and some experimental phenomena cannot be explained without neoclassical effects. To take these effects into account, non-linear studies necessitate the application of numerical techniques.

Part of the thesis addresses the triggering of NTMs in hybrid scenario low-shear plasmas by coupling to infernal modes. Motivated by the experimental observation of fast-growing resistive modes in various tokamaks, this study is important for the development of hybrid scenarios but also for the prediction of fast-growing modes after sawtooth crashes. Non-linear stability of the classical tearing mode is well described by Rutherford's model [15], originally developed for cylindrical plasmas. It predicts that the growth in the early non-linear phase is linear in time and proportional to $\Delta' = \psi'/\psi|_{r_s}$, the tearing stability parameter, which measures the jump of the eigenfunction ψ on the rational surface r_s . Several extensions to Rutherford's model have been investigated to include neoclassical effects and therefore to describe NTMs [16, 17]. In developing the Rutherford equation for plasmas that have a region of extended low magnetic shear, we define a new driving contribution to Δ' that originates from toroidal coupling to an infernal mode. By including effects due to the bootstrap current an additional destabilising mechanism is considered, that could still be maintained even if the driving effect of infernal modes on the island growth were to disappear, e.g. due to the q profile in the low-shear region moving away from a rational surface where $q = m_0/n$. In such a situation, a NTM would be envisaged as developing from the infernal mode 'seed', and would be maintained by the bootstrap effect. This allows us to see whether the bootstrap current is able to maintain NTMs that have been triggered with the help of infernal modes after the contribution from the triggering mechanism vanished. To do this, an analytic estimate for $\Delta'_0(\gamma)$ is made, in order to calculate the strength of the coupling contribution to stability. This is compared with numerical simulations performed by using the initial value code XTOR-2F. The numerical simulations can calculate the size of magnetic islands, but it does not permit certain individual contributions to stability (such as the infernal mode drive) to be identified in isolation. Hence, comparison with the analytic approach is highly valuable. Nevertheless, by carrying out simulations with and without bootstrap current, the magnitude of the bootstrap contribution is estimated and compared with the analytical prediction.

The discovery of ELM-free high confinement regimes in tokamak experiments motivates the study of non-linearly saturated external kink modes. Experiments observe harmonic oscillations localised at the plasma edge in the quiescent high confinement regime (QH-mode). These edge harmonic oscillations (EHOs) are desirable, since they

1.4. Outline of this thesis

are associated to particle and impurity exhaust with tolerable heat and energy loads. It is still unclear if the QH-mode can be accessed under reactor conditions, but the parameter range in which the QH-mode is obtained is increasing [18]. The QH-mode can thus be a promising alternative to the ELMy H-mode in future tokamaks like ITER. In this context, it is important to understand the nature of EHOs. A link to kink-peeling modes (saturated external kink modes localised at the plasma edge) is assumed based on numerical analyses, but the character of these low- n modes is not fully understood. In a novel approach, we describe non-linearly saturated external kink modes as free-boundary 3D equilibrium states and present a method to calculate the saturated amplitude of the radial displacements. For a reliable analysis of the dominant Fourier modes, the equilibria are transformed to straight field line coordinates. The validity of this approach is justified by a study of typical tokamak baseline scenario plasmas. For standard current-driven external kink modes, the non-linear saturated external kink mode amplitude is calculated from an analytical model using a numerical scheme to solve the corresponding system of equations. In QH-mode plasmas, we investigate two driving mechanisms: On the one hand standard external kink modes are driven by the large current gradient in the pedestal. On the other hand, pressure drives infernal modes that are coupled to external kink sidebands, the bootstrap current having caused low magnetic shear at the edge. We determine the relevance of both driving mechanisms in situations where EHOs are seen in experiments.

1.4 Outline of this thesis

Having introduced the concept of magnetic confinement in this chapter, the main thesis is organised as follows:

First, the concepts for investigating macroscopic plasma instabilities are explained in chapter 2. This includes analytical models and numerical tools used for the studies presented in the next chapters. The basic model governing the dynamics of plasmas that have long timescales and long wavelengths are introduced together with extended MHD effects such as the bootstrap current. The behaviour of resistive plasmas are discussed briefly. We describe methods to compute axisymmetric and non-axisymmetric toroidal plasma equilibria and introduce the CHEASE and VMEC codes. Finally, the concepts of linear and non-linear stability are discussed. Of particular relevance is non-linear stability, i.e. saturation of instabilities. The approach for obtaining saturated states is briefly introduced.

Chapter 3 presents an investigation of neoclassical tearing mode (NTM) triggering by coupling to infernal modes in plasmas with extended regions of low magnetic shear in the core. Classical and neoclassical tearing modes are described together with the Rutherford equation. Initial value simulations of hybrid tokamak configurations are performed using the non-linear resistive code XTOR-2F with and without consideration of bootstrap current effects. An analytical linear model is extended to the early non-linear phase to reflect the vanishing of the coupling.

In chapter 4 we explore a novel approach to describe non-linearly saturated external kink modes by using free-boundary 3D equilibrium simulations. This proof-of-principle study, focused on tokamak baseline scenarios shows that the equilibrium code VMEC well describes features of saturated external modes. We discuss the importance of choosing a straight field line coordinate system for the mode analysis and provide a method to calculate the displacement amplitude from VMEC. A numerical solver is developed to calculate the saturated non-linear amplitude of external kink modes from an analytical model, and it is compared to the results obtained from VMEC computations. Details about the numerical scheme are described in appendix C.2. A numerical linear analysis demonstrates that external kink modes are unstable in the range where 3D equilibrium states are found.

Following the approach and philosophy of chapter 4, chapter 5 addresses non-linear stability of external kink type-modes in quiescent H-mode configurations. Linearly unstable, but non-linearly stable standard current-driven external kink modes are identified in a wide parameter range. In addition, it is shown that VMEC can also capture pressure-driven infernal modes coupled to external kink sidebands. We present free-boundary non-axisymmetric equilibrium computations that describe saturated coupled infernal and external kink modes. Linear analytical and numerical calculations show the existence of such coupled modes, which have recently been named external modes [19, 20].

A summary of the thesis, a discussion of the main results and an outlook for future investigations is provided in chapter 6.

Fluid description of a plasma

In this chapter we introduce the theoretical models to describe macroscopic phenomena in fusion plasmas. Analytical and numerical tools suited for the investigation of resistive and ideal modes in low-shear plasmas are explained. This chapter introduces magnetohydrodynamics (MHD) theory with various extensions, and the physical concepts that are later used for the investigations carried out in this thesis. We first give an overview of the ideal and resistive single-fluid model and then define the safety factor, an important quantity for stability considerations. Non-MHD effects that can however be combined with the MHD model and determine the evolution of macroscopic instabilities are described. This is followed by the calculation of axisymmetric (2D) and non-axisymmetric (3D) toroidal equilibria. The concepts of linear and non-linear stability are discussed in the end.

2.1 Basic and extended MHD models for tokamak plasmas

Due to the complexity of magnetised plasmas together with the non-trivial toroidal geometry of fusion devices it has not yet been possible to develop a practical unified model that explains all relevant effects. For example, kinetic models - based on distribution functions for the plasma particles $f(\mathbf{x}, \mathbf{v})$ - are successful in describing microscopic phenomena and turbulence, but it is not generally suitable for fully electromagnetic, non-linear, large scale fluctuations of MHD instabilities. The MHD fluid model is valid on larger length and time scales and is naturally fully electromagnetic and non-linear. It quite accurately describes dynamics perpendicular to the magnetic field.

2.1.1 Ideal and resistive single-fluid MHD model

The basic equations of the magnetohydrodynamics (MHD) model combine the continuity equation and equation of motion for a given fluid element and Maxwell's equations describing the behaviour of the magnetic and electric field. It is also possible to derive the MHD equations by taking moments of the Boltzmann equation [21]. The MHD model is suitable for slow dynamics on a macroscopic length scale $L \gg \lambda_D$ and time scales of $\tau \gg \Omega_{ci}^{-1}$, where $\Omega_{ci} = q_i B / m_i$ (with ion charge q_i and ion mass m_i) is the ion cyclotron frequency. High collisionality is assumed such that the ion and electron distribution functions are close to a Maxwellian, and relatively slow time scales. The

MHD model is given by the following equations [21]:

$$\frac{\partial \rho}{\partial t} = -\nabla \cdot (\rho \mathbf{v}), \quad (2.1a)$$

$$\rho \left(\frac{\partial \mathbf{v}}{\partial t} + \mathbf{v} \cdot \nabla \mathbf{v} \right) = -\nabla p + \mathbf{J} \times \mathbf{B}, \quad (2.1b)$$

$$\frac{\partial p}{\partial t} = -\mathbf{v} \cdot \nabla p - \Gamma p \nabla \cdot \mathbf{v}, \quad (2.1c)$$

$$\frac{\partial \mathbf{B}}{\partial t} = -\nabla \times (\mathbf{v} \times \mathbf{B}), \quad (2.1d)$$

$$\nabla \times \mathbf{B} = \mu_0 \mathbf{J}, \quad (2.1e)$$

$$\nabla \cdot \mathbf{B} = 0, \quad (2.1f)$$

$$\mathbf{E} + \mathbf{v} \times \mathbf{B} = \eta \mathbf{J}, \quad (2.1g)$$

where ρ is the ion mass density, \mathbf{B} is the magnetic field, \mathbf{J} is the current density, \mathbf{v} the fluid velocity, p the pressure, \mathbf{E} the electric field, η the plasma resistivity, μ_0 the vacuum permeability and $\Gamma = 5/3$ the adiabatic index. We first focus on the ideal MHD case $\eta = 0$ in Eq. (2.1g). With assumptions of pre-Maxwell Ampère's law (no displacement current in Eq. (2.1e)), the MHD model is appropriate to describe slow electromagnetic waves ($v \ll c$) with frequencies well below the plasma frequency $\omega_{pe} = (n_e e^2 / m_e \epsilon_0)^{1/2}$, where e is the elementary charge, n_e the electron density, m_e the electron mass and ϵ_0 is the vacuum permittivity. Neglecting space charges ($\epsilon_0 \nabla \cdot \mathbf{E}$) implies quasi-neutrality of the plasma, i.e. the charge density of ions is equal to that of electrons $q_i n_i = e n_e$. Should a charge imbalance on macroscopic scale develop in the plasma, the fast response of electrons due to their small masses creates an electric field opposite to the imbalance, keeping the plasma in quasi-neutrality. Thus, the MHD model can only describe waves with wavelengths of a characteristic scale a (with wavenumber $k \sim 1/a$) much above the Debye length λ_D . Since the electron mass $m_e/m_i \ll 1$ is small, a further approximation is made to neglect electron inertia $m_e \rightarrow 0$, such that the mass density is only due to the ions $\rho = m_i n$.

It is interesting to look at the conservation of magnetic flux in ideal MHD [22]. Given an open surface \mathbf{S} with normal vector \mathbf{n} , the magnetic flux through this surface is

$$\psi = \int_{\mathbf{S}} \mathbf{B} \cdot \mathbf{n} \, d\mathbf{S}. \quad (2.2)$$

A change of ψ can be either due to a change of \mathbf{B} but also due to the surface moving with the plasma velocity \mathbf{v} , and thus it is given by

$$\frac{d\psi}{dt} = \int_{\mathbf{S}} \frac{\partial \mathbf{B}}{\partial t} \cdot \mathbf{n} \, d\mathbf{S} - \oint \mathbf{v} \times \mathbf{B} \cdot d\mathbf{l} = - \oint (\mathbf{E} + \mathbf{v} \times \mathbf{B}) \cdot d\mathbf{l}, \quad (2.3)$$

where $d\mathbf{l}$ is the length element along the surface. For the second equality Stokes' theorem and Faraday's law were applied. Resistive Ohms law (2.1g) gives therefore

$$\frac{d\psi}{dt} = - \oint \eta \mathbf{J} \, d\mathbf{l}. \quad (2.4)$$

2.1. Basic and extended MHD models for tokamak plasmas

Hence, in the ideal MHD limit $\eta = 0$, where we have conservation of magnetic flux, $d\psi/dt = 0$. Since this applies to any surface it implies that the magnetic field lines move with the fluid and are said to be frozen into the plasma. The conservation of magnetic flux furthermore restricts the allowed motions of the fluid such that the magnetic topology is preserved.

The assumption of ideal MHD that a plasma is perfectly conducting is not exactly satisfied for a real plasma with finite resistivity (Eq. (2.4)). Even though the magnetic Reynolds number is very low for fusion plasmas with values of $R_m \sim 10^9$, the finite resistivity gives rise to more complex effects. Even very small resistivity allows the magnetic field to dissipate through the fluid and allows magnetic field lines to tear and reconnect. This can form isolated structures, known as magnetic islands. Resistivity enters via Ohm's law

$$\mathbf{E} + \mathbf{v} \times \mathbf{B} = \eta \mathbf{J}, \quad (2.5)$$

where η is the resistivity and \mathbf{J} the current density. Various models exist for the plasma resistivity η . A simple and widely used model is the Spitzer resistivity [23]

$$\eta = \frac{\pi Z e^2 m^{1/2} \ln \Lambda}{(4\pi\epsilon_0)^2 (k_B T)^{3/2}}, \quad (2.6)$$

where Z is the ionisation of nuclei and $\Lambda \approx 10 - 20$ is the Coulomb logarithm. The degree of resistivity in a plasma is often expressed by the dimensionless Lundquist number defined by $S = \mu_0 l_0 v_A / \eta$, where l_0 is the characteristic length of the system and $v_A = B / \sqrt{\mu_0 \rho}$ is the Alfvén speed. Finite resistivity gives rise to another class of instabilities, which typically grow on a slower time scale, but nevertheless affect the plasma performance. A more detailed description of resistive instabilities can be found in section 3.3.

In the derivation of the MHD model, high collisionality is assumed such that the electron and ion distributions take the form of a Maxwellian, as particles have short mean free path. In reality, tokamak plasmas are almost collisionless, but nevertheless the model has been proven to describe the salient macroscopic properties of fusion plasmas. This is underlined by experimental evidence, which are broadly instabilities of long wavelengths, consistent with MHD predictions. The ideal MHD model will later be used to study the stability of external kink modes and non-resistive infernal modes. The resistive fluid model will become important for the study of neoclassical tearing modes.

2.1.2 Bootstrap current

Even though it is not derived from the MHD model, the bootstrap current has a crucial influence on the features of MHD perturbations close to so-called 'rational' surfaces. Resistivity plays a major role for the non-linear stability of neoclassical tearing modes and to a lesser extent for the stability of edge modes in H-mode and QH-mode plasma configurations. In chapter 3 we investigate the direct effect of the bootstrap current on the non-linear evolution of neoclassical tearing modes, while in chapter 5 we focus on plasma configurations where the bootstrap current has an indirect effect on the stability of external kink modes and infernal modes by flattening the q profile. The bootstrap

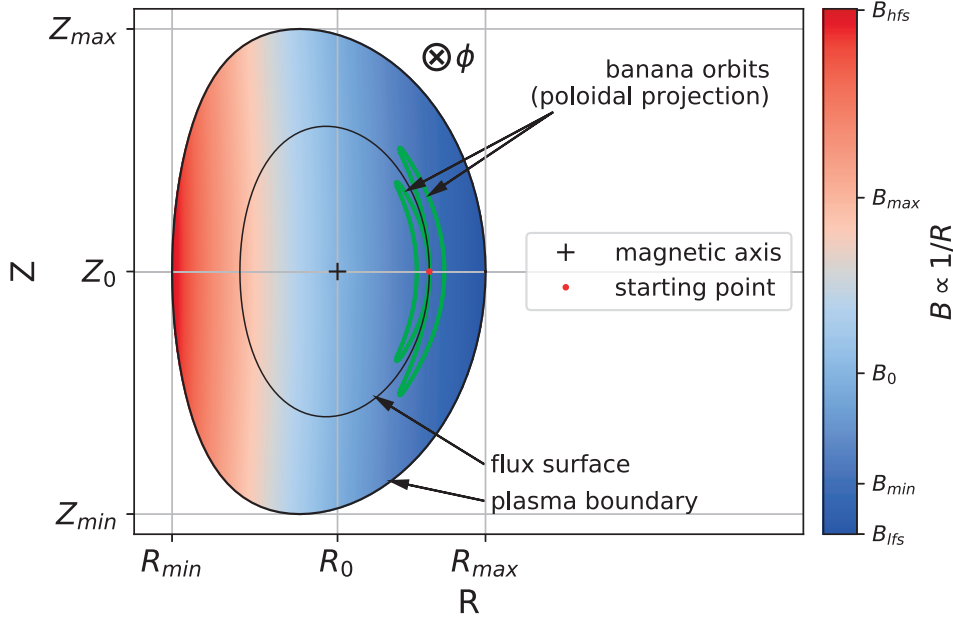


Figure 2.1 – Poloidal projection of the banana orbits of trapped particles originating from $\theta = 0$ (red dot) with opposite velocities on a chosen flux surface in realistic toroidal geometry. In the presence of a density gradient, more particles populate the inner orbit than the outer.

current is parallel to the magnetic field and arises in toroidal configurations in the presence of a pressure gradient in the low collisionality regime. As such it is in the same direction as the main toroidal current and can provide steady state current in addition to the Ohmic current without external current drive [24]. In a tokamak the magnetic field strength scales with the major radius R as $B \sim 1/R$, where R is the horizontal coordinate in Fig. 2.1 (and also depicted in Fig. 2.2). During their motion along a field line, particles hence experience a maximum and a minimum of the magnetic field strength. Consequently, particles with the property

$$v_{\parallel}^2 < \frac{B_{max} - B_{min}}{B_{min}} v_{\perp}^2 \approx 2\epsilon v_{\perp}^2, \quad (2.7)$$

cannot complete full poloidal orbits and are trapped on the outboard side of the torus, where they follow banana orbits of finite width w_b . For the generation of the bootstrap current the existence of a fraction of trapped particles together with passing particles is necessary. The banana orbits of trapped particles that start at the same point, but with opposite parallel velocities have a different averaged radius, as depicted in Fig. 2.1 for the case of particles starting at $\theta = 0$. In the presence of a density (or pressure) gradient, the inner banana orbit is more populated than the outer orbit, leading to an asymmetry in the parallel velocity distribution, where the maximum is shifted towards negative values of v_{\parallel} (negative toroidal direction) for ions and opposite for electrons. In the presence of a density gradient a diamagnetic current is generated within the trapped particle species. Similarly, passing particles with opposite velocities follow different orbits and generate

2.2. The safety factor profile

another small diamagnetic current. These two currents however provide only a small contribution to the bootstrap current.

The largest part of the bootstrap current arises due to collisions between trapped and passing particles. For passing particles to lose their momentum they need to scatter in an angle of $\pi/2$, whereas trapped particles lose momentum at low scattering angles. In this process ion-ion and electron-ion collisions dominate and net momentum is transferred from trapped to passing particles. This would create a momentum imbalance between passing and trapped particles if only the two diamagnetic currents were considered. The collisions cause an asymmetry in the parallel velocity distributions of both passing particle species (ions and electrons), such that the total distribution function (of passing and trapped particles) is a shifted Maxwellian. The resulting current is the bootstrap current and ensures that momentum balance between trapped and passing particles is satisfied.

In the simple explanation provided above, only a density gradient was assumed. In reality the situation is more complex. A good representation of the bootstrap current is provided by the Sauter model [25, 26] and reads

$$\langle \mathbf{J}_{\text{bs}} \cdot \mathbf{B} \rangle = -F(\psi)p_e \left[L_{31} \frac{p}{p_e} \frac{\partial \ln p}{\partial \psi} + L_{32} \frac{\partial \ln T_e}{\partial \psi} + L_{34} \alpha \frac{1 - R_{pe}}{R_{pe}} \frac{\partial \ln T_i}{\partial \psi} \right], \quad (2.8)$$

where ψ is the poloidal flux, $F(\psi) = RB_\phi$, R is the major radius, $B_\phi = \mathbf{B} \cdot \hat{\mathbf{e}}_\phi$, $R_{pe} = p_e/p$ and the coefficients L_{31} , L_{32} , L_{34} and α determine the relative contributions of the pressure and temperature gradients to the bootstrap current. They are defined as

$$L_{31} = -1 + \frac{1}{Fp_e} \left\langle \int \chi_e Z_i \nu_{e0} \gamma_1 \frac{v_{Te}^3}{v^3} \mathbf{d}\mathbf{v} \right\rangle, \quad (2.9)$$

$$L_{32} = \frac{1}{Fp_e} \left\langle \int \chi_e \nu_{e0} \gamma_1 \left[-h \left(\frac{v}{v_{Te}} \right) + Z_i \frac{v_{Te}^3}{v^3} \left(\frac{v^2}{v_{Te}^2} - \frac{5}{2} \right) \right] \mathbf{d}\mathbf{v} \right\rangle, \quad (2.10)$$

$$L_{34} = -1 + \frac{1}{Fp_e} \left\langle \frac{B^2}{\langle B^2 \rangle} \int \chi_e Z_i \nu_{e0} \gamma_1 \frac{v_{Te}^3}{v^3} \mathbf{d}\mathbf{v} \right\rangle, \quad (2.11)$$

$$\alpha = -\frac{q_e}{\nu_i T_e} \left\langle \int \chi_i \nu_{i0} h \left(\frac{v}{v_{Ti}} \right) \frac{v_{\parallel}}{\Omega_i} \mathbf{d}\mathbf{v} \right\rangle, \quad (2.12)$$

where Z_s is the charge of species $s = i, e$, $\gamma_1 = F(\psi)v_{\parallel}/\Omega_e$, $\nu_{e0} = 3\sqrt{\pi}/(4Z_i\tau_e)$, $\nu_{i0} = 3\sqrt{\pi/2}/(2\tau_i)$ and $h(x) = x^{-3} [10 \operatorname{erf}(x) - 10x \operatorname{erf}'(x) - 4x^2 \operatorname{erf}(x)]$. Contributions to the bootstrap current arise due to the pressure gradient, but also ion and electron temperature gradients.

2.2 The safety factor profile

In a general tokamak the magnetic field lines follow helical paths around the torus. The helicity of the field lines is an important quantity in stability analysis. As magnetic field lines lie on flux surfaces (i.e. at a constant value of the radial variable ψ), the local pitch

of a magnetic field line is given by the change in toroidal direction ϕ in relation to the change in poloidal direction θ :

$$q_l = \frac{d\phi}{d\theta} = \frac{\mathbf{B} \cdot \nabla \phi}{\mathbf{B} \cdot \nabla \theta}. \quad (2.13)$$

In a general flux coordinate system q_l varies along the field line. The safety factor q is defined as the average of q_l along the poloidal angle

$$q(\psi) = \frac{1}{2\pi} \int_0^{2\pi} q_l(\theta, \psi) d\theta. \quad (2.14)$$

This quantity describes the number of toroidal turns of a magnetic field line during one poloidal turn on a flux surface at radial position ψ . Calculating the integral in Eq. (2.14) and writing the magnetic field in the form $\mathbf{B} = F(\psi)\nabla\phi + \nabla\phi \times \nabla\psi$, we obtain for the q profile

$$q(\psi) = \frac{F(\psi)}{2\pi} \oint \frac{dl}{R|\nabla\psi|}, \quad (2.15)$$

where $F(\psi) = RB_\phi$, R is the major radius, B_ϕ the toroidal magnetic field strength and $|\nabla\psi| = R|B_\theta|$. Integration is performed along the poloidal arc length l (direction parallel to the poloidal magnetic field) with $dl = \sqrt{dR^2 + dZ^2}$, where the coordinates R and Z are depicted in Fig. 2.1. This expression is convenient, when the R and Z coordinates of a flux surface are known, and a more basic definition is provided in appendix A.3. The q profile determines the magnetic shear, which is defined as

$$s(\psi) = \frac{\psi}{q} \frac{dq}{d\psi}, \quad (2.16)$$

where ψ denotes the radial variable.

We can distinguish two cases for the value of q . First, the value of q on a flux surface can be irrational. In this case a magnetic field line does not close on itself and covers the whole flux surface. In the second case, the field line closes on itself after a finite amount of toroidal N and poloidal M turns and the flux surface with such a value is called rational. The safety factor here is $q = m/n$, where m and n are the poloidal and toroidal mode number respectively. It is on (or near) these surfaces that the plasma is prone to instabilities, and in addition it is only on these surfaces that resistivity is important. This thesis will explore the effect of the q profile deeply, especially were $q(\psi)$ depends only weakly on ψ close to a $q = m/n$ surface (so-called extended weak magnetic shear).

The value of q at the plasma-vacuum interface is important for plasma stability. This quantity is well defined for plasmas with nested flux surfaces or limited plasmas. In diverted plasmas however, q goes to infinity at the separatrix. Hence, the value of q at the flux surface enclosing 95% of the toroidal flux is taken as the edge value.

2.3 Toroidal plasma equilibrium

The concept of plasma equilibrium is very important in nuclear fusion studies. In equilibrium the net force on the plasma is zero and theoretically the plasma would remain

2.3. Toroidal plasma equilibrium

confined. Achieving such a state exactly over the long term is difficult and often perturbations exist that break the equilibrium state. When the plasma is in equilibrium the force from the pressure gradient ∇p balances $\mathbf{J} \times \mathbf{B}$,

$$\nabla p = \mathbf{J} \times \mathbf{B}. \quad (2.17)$$

Hence, it is assumed that at equilibrium plasma flows are quite weak (i.e. $\rho \mathbf{v} \cdot \nabla \mathbf{v} \ll \mathbf{J} \times \mathbf{B} - \nabla p$). By separately forming the dot product of this relation with \mathbf{J} and \mathbf{B} , it can be seen that ∇p is perpendicular to the current density and also the magnetic field. Furthermore, the pressure is constant along the magnetic field lines. In addition, from Eq. (2.17) it can be seen that $\mathbf{J}_\perp = \mathbf{B} \times \nabla p / B^2$, where \perp is perpendicular to \mathbf{B} . There is of course a component of \mathbf{J} parallel to \mathbf{B} (the induced current mentioned earlier in section 1.2.2).

This thesis is dedicated to 3D equilibria, but axisymmetric (2D) equilibrium states are also important, since they form the initial conditions for initial value computations that can potentially lead to a saturated 3D state. Both concepts are discussed in the following.

2.3.1 Axisymmetric equilibrium: the Grad-Shafranov equation

In axisymmetry the magnetic field can be written

$$\mathbf{B} = F(\psi)\nabla\phi + \nabla\phi \times \nabla\psi. \quad (2.18)$$

We can apply the force balance equation to tokamak geometry (assuming perfect axisymmetry - meaning that all MHD scalars are independent of the toroidal coordinate ϕ). The resulting equilibrium equation, known as the Grad-Shafranov equation, was first derived by Grad [27] and Shafranov [28]. For this derivation we use cylindrical coordinates (R, Z, ϕ) (c.f. appendix A), suited for the description of an axisymmetric tokamak equilibrium. In these coordinates the components of the force balance equation read

$$\begin{aligned} \frac{\partial p}{\partial R} &= j_Z B_\phi - j_\phi B_Z, \\ \frac{\partial p}{\partial Z} &= j_\phi B_R - j_R B_\phi, \\ \frac{\partial p}{\partial \phi} &= j_R B_Z - j_Z B_R. \end{aligned} \quad (2.19)$$

From Maxwell's equations and in cylindrical coordinates we further know that

$$\nabla \cdot \mathbf{B} = 0 = \frac{1}{R} \frac{\partial(RB_R)}{\partial R} + \frac{\partial B_Z}{\partial Z}, \quad (2.20)$$

and

$$\nabla \cdot \mathbf{j} = 0 = \frac{1}{R} \frac{\partial(Rj_R)}{\partial R} + \frac{\partial j_Z}{\partial Z}. \quad (2.21)$$

The axisymmetric nature of the equilibrium enables us to introduce stream functions ψ and F , determined from Eqs. (2.20,2.21) and given by

$$B_R = -\frac{1}{R} \frac{\partial \psi}{\partial Z}, \quad B_Z = \frac{1}{R} \frac{\partial \psi}{\partial R}, \quad (2.22)$$

$$j_R = \frac{1}{\mu_0} \frac{1}{R} \frac{\partial F}{\partial Z} \quad , \quad j_Z = -\frac{1}{\mu_0} \frac{1}{R} \frac{\partial F}{\partial R} \quad , \quad (2.23)$$

where $\psi = \psi_{SI}/(2\pi)$ is the normalised poloidal flux. Writing Ampère's law in cylindrical coordinates and exploiting axisymmetry ($\partial x/\partial\phi = 0$ for any quantity x) and with Eq. (2.22) we obtain from the ϕ -component

$$-\mu_0 R j_\phi = R \frac{\partial}{\partial R} \left(\frac{1}{R} \frac{\partial \psi}{\partial R} \right) + \frac{\partial^2 \psi}{\partial Z^2} =: \Delta^* \psi \quad , \quad (2.24)$$

where we defined the Grad-Shafranov operator Δ^* . From the R and Z components we can identify the second stream function $F \equiv RB_\phi$. Expressing the quantities in Eq. (2.19) in terms of the stream functions it can be seen that $F = F(\psi)$ and $p = p(\psi)$. Now, $p' = dp/d\psi$ can be written as

$$p' = \frac{j_\phi}{R} - \frac{FF'}{\mu_0 R^2} \quad . \quad (2.25)$$

Using this result in Eq. (2.24) provides the Grad-Shafranov equation

$$\Delta^* \psi = -\mu_0 R^2 \frac{dp}{d\psi} - F \frac{dF}{d\psi} \quad , \quad (2.26)$$

where the two stream functions ψ and F can be chosen freely. The boundary condition for the Grad-Shafranov equation is the poloidal flux at the plasma-vacuum interface $\psi = \text{const.}$. In analytical calculations the solution is of the form $R(\psi), Z(\psi)$, with $R(\psi)$ and $Z(\psi)$ at the edge (where $p \rightarrow 0$) forming the boundary conditions of a fixed boundary problem. Free-boundary problems can also be defined, where the currents in coils must be prescribed. Note that free-boundary problems will be deployed in much of this thesis (Chapters 4 and 5). A class of analytical solutions to the Grad-Shafranov equation exists. These are called Solov'ev equilibria [29]. For most choices of the pressure profile and magnetic field configurations however the equation needs to be solved numerically. Note also that the Grad-Shafranov operator Δ^* can be defined in flux Coordinates

$$\Delta^* \psi = \frac{R^2}{\mathcal{J}} \left[\frac{\partial}{\partial r} \left(\frac{\psi' g_{\theta\theta}}{\mathcal{J}} \right) - \frac{\partial}{\partial \theta} \left(\frac{\psi' g_{r\theta}}{\mathcal{J}} \right) \right] \quad , \quad (2.27)$$

where \mathcal{J} is the Jacobian and together with the metric elements $g_{\theta\theta}$ and $g_{r\theta}$ it is defined in appendix A.

2.3.2 The CHEASE 2D equilibrium code

The CHEASE code [30] is a convenient tool to compute toroidal, axisymmetric equilibria by solving the Grad-Shafranov equation (2.26). It is a widely used code with very good convergence properties. The various possibilities to specify equilibrium quantities make it a flexible tool, and hence it is interfaced with several stability codes. As such, CHEASE equilibria form the initial conditions for linear and non-linear stability simulations in this thesis.

2.3. Toroidal plasma equilibrium

CHEASE uses flux coordinates (s, θ, ϕ) where θ is a generalised poloidal angle, the toroidal angle ϕ can be ignored and the radial variable s is chosen to be the normalised poloidal flux

$$s = s(\psi) = \sqrt{\left| \frac{\psi - \psi_{\text{edge}}}{\psi_0 - \psi_{\text{edge}}} \right|}. \quad (2.28)$$

A specific normalisation for the coordinates can be chosen from the set of COCOS tokamak coordinate conventions [31]. For more detail about curvilinear coordinates, please refer to appendix A.

CHEASE allows only fixed-boundary equilibrium computations, i.e. the plasma boundary is provided as boundary conditions. The plasma cross-section is thus known and for the numerical computations it is discretised and transformed into a rectangular grid of the two variables σ, χ . This grid is then used in a bicubic Hermite finite element method to solve the variational form of the Grad-Shafranov equation.

In the Grad-Shafranov equation, the two functions p' and FF' are to be chosen freely and specified as input to CHEASE, which can be done in multiple manners. For the first function, either $p' = \partial p / \partial \psi$ is provided directly or computed from the pressure $p(\psi)$. Specifying the function FF' directly is possible, but often not very practical, since the current (density) profile allows for a more straightforward plasma configuration. Another convenient option is to prescribe the q profile, and the code computes the function F according to Eq. (2.15).

2.3.3 Non-axisymmetric equilibrium and the VMEC code

Non-axisymmetric equilibria are often associated with stellarators, which are three-dimensional by design. Even though tokamaks are designed to be axisymmetric, in reality this condition is impossible to achieve due to unavoidable imperfections (e.g. small deviations in the production of field coils) and perturbations. An example of such perturbations that is present in all devices is the toroidal field ripple, caused by a finite distance between the toroidal field coils resulting in a variation of the magnetic field strength in the toroidal direction (strong $|\mathbf{B}|$ close to coils, lower $|\mathbf{B}|$ further away). In addition, non-axisymmetry of tokamak plasmas can also be desired, for example by application of resonant magnetic perturbations (RMPs) for ELM mitigation and control [13]. Non-linearly saturated states that would result from a linearly unstable axisymmetric system can also be described as 3D equilibria. This was already shown for internal kink modes [32] where the saturated state is characterised by a helical core and later in this thesis we demonstrate that saturated external modes can also be described as non-axisymmetric equilibrium states.

Unlike in the 2D case, the existence of closed flux surfaces cannot be shown mathematically rigorously for general 3D equilibria. However, a variational principle derived by Kruskal and Kulsrud [33] enables force balance and the existence of nested flux surfaces, when certain constraints are satisfied. To calculate axisymmetric and non-axisymmetric equilibria in this thesis we employ the VMEC code [34], an ideal MHD equilibrium code that uses energy minimisation according to the mentioned variational principle to solve the force balance equation. Due to its capability to obtain three-dimensional equilibria

it is a very useful tool not only in stellarator but also tokamak research. The possibility to provide the code with the currents in the magnetic field coils allows for free-boundary simulations. This is vital for the study of effects that affect the plasma edge and it will be used in the frame of this thesis to investigate external kink modes and edge harmonic oscillations in chapters 4 and 5.

2.3.3.1 Coordinate system

VMEC incorporates two coordinate systems, cylindrical coordinates (R, ϕ, Z) and flux coordinates (ρ, θ, ζ) ¹ as shown in Fig. 2.2. In the (R, ϕ, Z) system, R measures the horizontal distance from the central axis of the solenoid, Z the vertical distance from the plasma midplane and $\phi \in [0, 2\pi]$ is the geometrical toroidal angle. These cylindrical coordinates are orthogonal. In the set of VMEC flux coordinates, $\rho = \Phi/\Phi_a$ is a radial variable corresponding to the normalised toroidal magnetic flux (Φ_a is the toroidal flux at the last closed flux surface) and labels the flux surfaces. The two angular variables θ and $\zeta = \phi$ are the poloidal and toroidal angles respectively. The so-defined coordinate system is non-orthogonal with Jacobian

$$\sqrt{g} = R(R_\theta Z_\rho - R_\rho Z_\theta), \quad (2.29)$$

where the subscripts indicate a derivative with respect to the corresponding variable. For a definition of the Jacobian and an explanation of general non-orthogonal coordinate systems, see appendix A. The poloidal angle θ in VMEC is chosen such that good convergence of the Fourier moment expansion is achieved. This is not the case for a straight field line angle, but the VMEC flux coordinates can be transformed to straight field line coordinates whenever necessary.

Quantities that are periodic in poloidal and toroidal angles can be expressed as a Fourier series in the two angular variables. The choice of the exact Fourier series depends on the symmetry that is assumed for the desired equilibrium. In general equilibria without stellarator symmetry, the full Fourier series for any quantity f reads

$$f(\rho, \theta, \phi) = \left\{ \sum_{m,n} f_{mn}^c(\rho) \cos(m\theta - n\phi) + f_{mn}^s(\rho) \sin(m\theta - n\phi) \right\}, \quad (2.30)$$

but if stellarator symmetry is assumed, R is written as a cosine series, and Z as a sine series.

2.3.3.2 MHD equilibrium by energy minimisation

A solution to the force balance equation (2.17) can be found by applying a variational principle to minimise the energy. Since equilibrium states have $dv/dt = 0$ there is no kinetic energy and only the potential energy W needs to be considered. Inside the plasma W is the sum of magnetic energy W_m and fluid energy W_f :

$$W_p = W_m + W_f = \int \left(\frac{|\mathbf{B}|^2}{2\mu_o} + \frac{p}{\gamma - 1} \right) d^3x, \quad (2.31)$$

¹ ζ is a generalised toroidal angle. In the remainder we will use $\zeta = \phi$, where ϕ is the geometric toroidal angle.

2.3. Toroidal plasma equilibrium

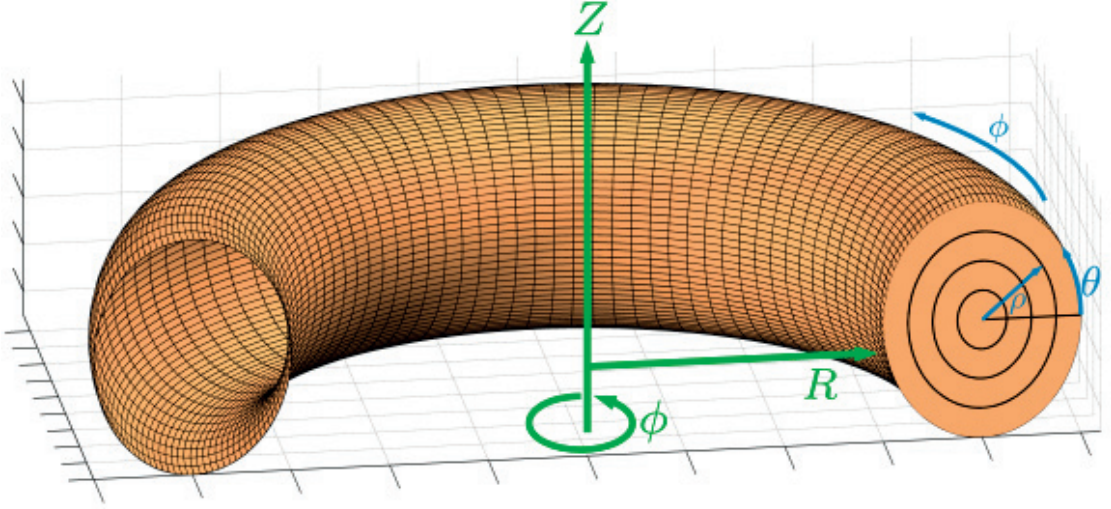


Figure 2.2 – Coordinate systems in VMEC: Cylindrical coordinates (R, ϕ, Z) (green) and VMEC flux coordinates $(\rho, \theta, \zeta = \phi)$ (blue).

where μ_0 is the permeability of the vacuum, p the plasma pressure, γ the adiabatic index and integration is performed over the plasma volume. In free-boundary computations the vacuum energy W_v composed by the magnetic energy of the vacuum magnetic field \mathbf{B}_v needs to be considered as well, such that the total energy functional becomes

$$W = W_p - W_v = \iiint_{plasma} \left[\frac{|\mathbf{B}|^2}{2\mu_0} + \frac{p(\rho)}{\Gamma - 1} \right] d^3x - \iiint_{vacuum} \frac{|\mathbf{B}_v|^2}{2\mu_0} d^3x. \quad (2.32)$$

The minus sign is due to the reciprocal variation in energy caused by a change of the plasma boundary [34]. The vacuum magnetic field $\mathbf{B}_v = -\nabla\nu$ can be written in terms of the vacuum potential ν with descent equation $d\nu/dt = \nabla^2\nu$. Conservation of mass is achieved via

$$p(\rho) = M(\rho)(V')^{-\gamma}, \quad (2.33)$$

with mass function $M(\rho)$ and differential volume element $V' = \iint |\sqrt{g}| d\theta d\phi$. It should be noted that $M(\rho)$ is kept fixed during the variational computations, while V' changes according to the geometry of the flux surfaces. A variation of W is performed with respect to an artificial time parameter t . In this calculation also the cylindrical coordinates (R, ϕ, Z) are functions of t . The variation of W including the vacuum terms is then

$$\begin{aligned} \frac{dW}{dt} = & - \iiint_{plasma} \left(F_R \frac{\partial R}{\partial t} + F_\phi \frac{\partial \phi}{\partial t} + F_Z \frac{\partial Z}{\partial t} \right) d\rho d\theta d\phi + \frac{1}{\mu_0} \iiint_{vacuum} \frac{\partial \nu}{\partial t} \nabla^2 \nu d^3x \\ & - \int_{\rho=1} \left[|\sqrt{g}| \frac{\partial \rho}{\partial x_i} \left(\frac{|\mathbf{B}|^2}{2\mu_0} + p - \frac{|\mathbf{B}_v|^2}{2\mu_0} \right) \right]_{\rho=1} \frac{\partial x_i}{\partial t} d\theta d\phi \\ & - \frac{1}{\mu_0} \left(\int_{\rho=1} \frac{\partial \nu}{\partial t} \mathbf{B}_v \cdot d\mathbf{S}_\rho - \int_{wall} \frac{\partial \nu}{\partial t} \mathbf{B}_v \cdot d\mathbf{S} \right), \end{aligned} \quad (2.34)$$

with $d\mathbf{S}_\rho = \nabla\rho|\sqrt{g}|d\theta d\phi$. The boundary conditions for this energy minimisation require that at the plasma-vacuum interface ($\rho = 1$) the pressure jump is zero and $\mathbf{B}_v \cdot d\mathbf{S}_\rho = 0$, and at the conducting wall $\mathbf{B}_v \cdot d\mathbf{S} = 0$. The force components in the direction of the cylindrical coordinates read

$$\begin{aligned}
 F_R &= -\frac{\partial}{\partial\rho} \left[|\sqrt{g}| \frac{\partial\rho}{\partial R} \left(\frac{|\mathbf{B}|^2}{2\mu_o} + p \right) \right] - \frac{\partial}{\partial\theta} \left[|\sqrt{g}| \frac{\partial\theta}{\partial R} \left(\frac{|\mathbf{B}|^2}{2\mu_o} + p \right) \right] \\
 &\quad - \frac{\partial}{\partial\phi} \left[|\sqrt{g}| \frac{\partial\phi}{\partial R} \left(\frac{|\mathbf{B}|^2}{2\mu_o} + p \right) \right] + \mu_o^{-1} |\sqrt{g}| \nabla \cdot [(\mathbf{B} \cdot \nabla R) \mathbf{B}] \\
 &\quad + \frac{\sqrt{g}}{R} \left[\frac{|\mathbf{B}|^2}{2\mu_o} + p - \frac{R^2 (\mathbf{B} \cdot \nabla \phi)^2}{\mu_o} \right], \\
 F_\phi &= -\frac{\partial}{\partial\rho} \left[|\sqrt{g}| \frac{\partial\rho}{\partial\phi} \left(\frac{|\mathbf{B}|^2}{2\mu_o} + p \right) \right] - \frac{\partial}{\partial\theta} \left[|\sqrt{g}| \frac{\partial\theta}{\partial\phi} \left(\frac{|\mathbf{B}|^2}{2\mu_o} + p \right) \right] \\
 &\quad - \frac{\partial}{\partial\phi} \left[|\sqrt{g}| \frac{\partial\phi}{\partial\phi} \left(\frac{|\mathbf{B}|^2}{2\mu_o} + p \right) \right] + \mu_o^{-1} |\sqrt{g}| \nabla \cdot [(R^2 \mathbf{B} \cdot \nabla \phi) \mathbf{B}], \\
 F_Z &= -\frac{\partial}{\partial\rho} \left[|\sqrt{g}| \frac{\partial\rho}{\partial Z} \left(\frac{|\mathbf{B}|^2}{2\mu_o} + p \right) \right] - \frac{\partial}{\partial\theta} \left[|\sqrt{g}| \frac{\partial\theta}{\partial Z} \left(\frac{|\mathbf{B}|^2}{2\mu_o} + p \right) \right] \\
 &\quad - \frac{\partial}{\partial\phi} \left[|\sqrt{g}| \frac{\partial\phi}{\partial Z} \left(\frac{|\mathbf{B}|^2}{2\mu_o} + p \right) \right] + \mu_o^{-1} |\sqrt{g}| \nabla \cdot [(\mathbf{B} \cdot \nabla Z) \mathbf{B}].
 \end{aligned}$$

It can be shown that these force components correspond to the components of the MHD force balance equation. In equilibrium, each component of the sum of forces vanishes. Due to flux and mass conservation and with $\gamma > 1$, W is positive definite and finding an equilibrium state is equivalent to finding a minimum of W . This is achieved by starting with an initial plasma configuration and following a path of monotonical decrease until a minimum is found.

VMEC quantities are provided in terms of a Fourier series in the two angular variables θ, ϕ . In order to avoid aliasing, the number grid points and poloidal modes should be chosen such that the condition $n\theta_{\text{eta}} \leq 2 * \text{mpol} + 6$ is satisfied. For most equilibrium configurations computed in this thesis, the input profiles $a(\rho) = p(\rho), j(\rho), \iota(\rho) = 1/q(\rho)$ are provided in terms of a polynomial of order 20

$$a(\rho) = \sum_{i=0}^{20} \rho^i a_i, \quad (2.35)$$

with coefficients a_i . This approximation is sufficient for most plasma configurations. However, when toroidal plasmas with advanced profiles, e.g. flat regions far from the magnetic axis are computed, a cubic spline representation is favoured. This is another standard option to provide VMEC input.

2.3.3.3 Fixed and free plasma boundary

A simple approach to obtain an equilibrium is to impose the position of the plasma-vacuum interface (last closed flux surface) as an initial condition and find the magnetic field configuration that corresponds to this equilibrium state. This is called a fixed-boundary run and is for example appropriate for the study of internal modes.

In free-boundary simulations the vacuum magnetic field is calculated from the currents in the magnetic field coils [35] by using the Biot-Savart law

$$\mathbf{B}(\mathbf{x}) = \frac{\mu_0}{4\pi} \int_V \mathbf{J}(\mathbf{x}') \times \frac{\mathbf{x} - \mathbf{x}'}{|\mathbf{x} - \mathbf{x}'|^3} dV'. \quad (2.36)$$

2.4. Macroscopic plasma stability

This numerical calculation is carried out with the MAKEGRID code, which evaluates the magnetic field on a $R - Z$ grid at specific values of the toroidal angle. In VMEC, an initial guess is provided for the position of the magnetic axis and for the plasma boundary from which both evolve during the energy minimisation iterations.

2.3.4 Stellarator symmetry

The existence of symmetries often provides simplifications to a given problem. Most toroidal fusion devices are based on a coil design that inherits stellarator symmetry [36]. In this thesis we simulate plasmas of MAST and JET. Both devices have up-down symmetric field coils, which is a special case of stellarator symmetry (we do not model RMPs). It can be shown that stellarator symmetric current distributions always generate a stellarator symmetric magnetic field [36]. This is important for the study of possible perturbations in toroidal fusion devices, since this symmetry reduces the number of possible states.

Defining a coordinate transformation I_0 such that

$$I_0 [f(R, \phi, Z)] = f(R, -\phi, -Z), \quad (2.37)$$

where f is an arbitrary function, a given vector field \mathbf{F} is called stellarator symmetric if it satisfies

$$I_0 [F_R, F_\phi, F_Z] = [-F_R, F_\phi, F_Z], \quad (2.38)$$

where (R, ϕ, Z) are the coordinates of an orthonormal cylindrical coordinate system. Stellarator symmetry can also be expressed through the coordinate system itself and reads in cylindrical coordinates

$$\begin{aligned} R(\rho, -\theta, -\phi) &= R(\rho, \theta, \phi) \\ Z(\rho, -\theta, -\phi) &= -Z(\rho, \theta, \phi). \end{aligned} \quad (2.39)$$

When R and Z are expressed in terms of a Fourier series, this allows a representation in terms of a pure cosine (for R) or sine (for Z) series. In particular, for the coordinates R and Z describing the position of the flux surfaces Eq. (2.30) reduces to

$$\begin{aligned} R(\rho, \theta, \phi) &= \sum_{m,n} R_{mn}^c(\rho) \cos(m\theta - n\phi), \\ Z(\rho, \theta, \phi) &= \sum_{m,n} Z_{mn}^s(\rho) \sin(m\theta - n\phi). \end{aligned} \quad (2.40)$$

It can be shown that $B = |\mathbf{B}|$ is also a cosine series under stellarator symmetry.

2.4 Macroscopic plasma stability

A confined plasma is never in a perfect equilibrium state. It is thus important to determine how the plasma responds to perturbations. If the plasma response is such that an instantaneous perturbation grows further, it is called unstable, otherwise stable. The

concept is illustrated in Fig. 2.3. Macroscopic instabilities are characterised by long wavelengths and low frequencies. They can be classified in terms of their driving mechanism (current or pressure) and the model they arise from. For the description of macroscopic modes the MHD model and related theories such as the two-fluid model or extended MHD equations are successfully applied and capable of explaining various experimentally observed phenomena such as ELMs. The stability of the plasma with respect to macroscopic modes is crucial since they not only degrade the performance of the plasma, but can also enhance transport and lead to sudden loss of confinement. In the following we discuss general fundamental methods to determine macroscopic plasma stability. A detailed discussion of specific tokamak instabilities can be found in the following chapters, where these instabilities are investigated based on the method presented here.

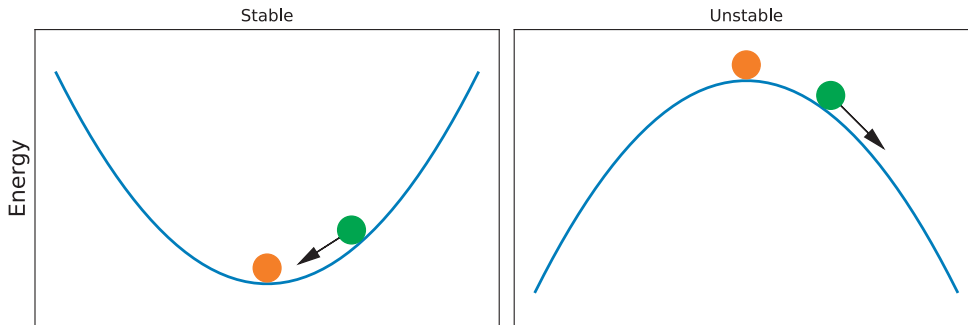


Figure 2.3 – Consider the orange ball at equilibrium, and the green ball representing an instantaneous perturbation. In a linearly stable system the force is such that equilibrium is restored (left). When the system is linearly unstable, the perturbation grows, i.e. moves away from the equilibrium state (right).

2.4.1 Linearisation and initial value formulation

The general MHD equations (2.1) are a set of non-linear differential equations and as such difficult to solve. The problem is simplified by linearising the equations around an equilibrium state and assume small perturbations [22]. For any quantity f this is written as

$$f(\mathbf{r}, t) = f_0(\mathbf{r}) + f_1(\mathbf{r}, t), \quad (2.41)$$

where $|f_1/f_0| \ll 1$. Equilibrium quantities are denoted by the subscript 0 and perturbed quantities by the subscript 1. The initial 2D equilibrium can be specified by a solution of the Grad-Shafranov equation or by the variational problem outlined earlier for a 3D equilibrium. We can model a deviation from the equilibrium by perturbing the velocity

$$\mathbf{v}_1(\mathbf{r}, 0) = \frac{\partial \boldsymbol{\xi}_1(\mathbf{r}, 0)}{\partial t}, \quad (2.42)$$

where the plasma displacement is given by the vector

$$\boldsymbol{\xi}_1(\mathbf{x}, t) = \int \mathbf{v}_1(\mathbf{x}, t) dt. \quad (2.43)$$

2.4. Macroscopic plasma stability

In terms of $\boldsymbol{\xi} \equiv \boldsymbol{\xi}_1$, other MHD perturbations are

$$\begin{aligned}\rho_1 &= -\nabla \cdot (\rho_0 \boldsymbol{\xi}), \\ p_1 &= -\boldsymbol{\xi} \cdot \nabla p_0 - \gamma p_0 \nabla \cdot \boldsymbol{\xi}, \\ \mathbf{B}_1 &= \nabla \times (\boldsymbol{\xi} \times \mathbf{B}_0), \\ \mathbf{J}_1 &= \frac{1}{\mu_0} \nabla \times [\nabla \times (\boldsymbol{\xi} \times \mathbf{B}_0)].\end{aligned}\tag{2.44}$$

With this result we obtain a single equation for the displacement

$$\rho \frac{\partial^2 \boldsymbol{\xi}}{\partial t^2} = \mathbf{F}(\boldsymbol{\xi}),\tag{2.45}$$

with the MHD force operator $\mathbf{F}(\boldsymbol{\xi}) = \mathbf{J}_0 \times \mathbf{B}_1 + \mathbf{J}_1 \times \mathbf{B}_0 - \nabla p_1$, and it has been assumed that $\mathbf{v}_0 = 0$. As we will see later, also the full non-linear problem can be expressed in terms of an initial value formulation.

2.4.2 Normal modes & Energy principle

Equation (2.45) governs the temporal evolution of the displacement $\boldsymbol{\xi}$. Since this equation is linear and the equilibrium is stationary, solutions for $\boldsymbol{\xi}$ can be taken to be of the form $\boldsymbol{\xi} \sim \exp(-i\omega t)$. We therefore obtain,

$$-\omega^2 \rho \boldsymbol{\xi} = \mathbf{F}(\boldsymbol{\xi}) = \frac{1}{\mu_0} (\nabla \times \mathbf{B}_0) \times \mathbf{B}_1 + \frac{1}{\mu_0} (\nabla \times \mathbf{B}_1) \times \mathbf{B}_0 - \nabla p_1,\tag{2.46}$$

which has the form of an eigenvalue problem and is valid for three-dimensional plasma equilibria. From the self-adjointness of the ideal MHD force operator² it can be shown that the normal modes are orthogonal and that the eigenvalue ω^2 is purely real. Now three cases can be distinguished: (1) If $\omega^2 > 0$, the solution is a pure oscillation with frequency ω and the mode does not grow, hence it is stable. (2) On the contrary, if $\omega^2 < 0$, the mode grows exponentially and is unstable. (3) If $\omega^2 = 0$, the mode is called marginally stable. This marks the transition from stability to instability.

The initial value formulation is not always practical when determining linear stability. The variational principle allows an equivalent formulation of the stability problem and is used in section 4.2 to calculate linear external kink growth rates and in chapter 3 for the solution in the ideal region of the plasma. For this formulation we calculate the potential and kinetic energy of the plasma. A minimisation of the energy allows us to reformulate the eigenvalue problem in a more convenient form, as it is solved by the KINX code as described in section 2.4.3. The KINX code assumes perturbations about an initially axisymmetric equilibrium. It performs variation of the sum of the potential energy

$$\delta W = -\frac{1}{2} \int \boldsymbol{\xi} \cdot \mathbf{F}(\boldsymbol{\xi}) \, d\mathbf{x},\tag{2.47}$$

and the kinetic energy

$$-\omega^2 K = -\omega^2 \frac{1}{2} \int \rho |\boldsymbol{\xi}|^2 \, d\mathbf{r},\tag{2.48}$$

² $\int \boldsymbol{\eta} \cdot \mathbf{F}(\boldsymbol{\xi}) \, d^3x = \int \boldsymbol{\xi} \cdot \mathbf{F}(\boldsymbol{\eta}) \, d^3x$

where it can be shown that

$$\omega^2 K - \delta W = 0. \quad (2.49)$$

An estimate about whether a system is linearly stable or unstable can be made from the potential energy given by Eq. (2.47). An equilibrium is stable if and only if $\delta W(\boldsymbol{\xi}^*, \boldsymbol{\xi}) \geq 0$ for each possible displacement $\boldsymbol{\xi}$. This is called the energy principle and proofs can be found in the literature [22, 37]. Finally, an axisymmetric equilibrium can be approximated by a straight cylinder, and perturbations expanded about an inverse aspect ratio $\varepsilon = r/R_0$. Expanding to second order, and retaining vacuum contributions, the following potential energy can be identified:

$$\begin{aligned} \delta W_2 = \frac{2\pi^2 B_0^2}{\mu_0 R_0} & \left\{ \int_0^a \left(\frac{n}{m} - \frac{1}{q} \right)^2 [r^2 \xi_r'^2 + (m^2 - 1) \xi_r^2] r dr \right. \\ & \left. + \left[\frac{2}{q_a} \left(\frac{n}{m} - \frac{1}{q_a} \right) + \left(\frac{n}{m} - \frac{1}{q_a} \right)^2 \right] a^2 \xi_r^2(a) \right\}. \end{aligned} \quad (2.50)$$

This energy, which is of relevance for external and internal kink modes is minimised revealing the following Euler-Lagrange equation for the displacement

$$\frac{d}{dr} \left[\left(\frac{n}{m} - \frac{1}{q} \right)^2 r^3 \frac{d\xi_r}{dr} \right] - (m^2 - 1) \left(\frac{n}{m} - \frac{1}{q} \right)^2 r \xi_r = 0. \quad (2.51)$$

2.4.3 The KINX code

The KINX code [38] computes linear MHD stability (linear growth rates and eigenfunctions) for a given axisymmetric equilibrium. It does this via variation of the total energy, including the effects of a vacuum region and perfectly conducting wall. In the frame of this thesis, KINX is primarily employed to determine a parameter space of linearly unstable external kink modes and their spectrum. The initial equilibrium for the stability analysis is a solution to the Grad-Shafranov equation (2.26) calculated with the CHEASE code. Both codes are interfaced with another equilibrium solver CAXE [38], which adapts the equilibrium to the numerical grids adopted by KINX. The code solves the eigenvalue equation

$$\delta \{ W(\boldsymbol{\xi}, \boldsymbol{\xi}) - \omega^2 K(\boldsymbol{\xi}, \boldsymbol{\xi}) \} = 0, \quad (2.52)$$

with potential energy functional

$$\begin{aligned} W &= W_p + W_v \\ &= \int_{V_p} \left\{ |\nabla \times (\boldsymbol{\xi} \times \mathbf{B})|^2 + 2\xi^\psi (\mathbf{j} \cdot \nabla \xi^D) + \frac{dp}{d\psi} \nabla \cdot \left(\frac{\partial \mathbf{r}}{\partial \psi} |\xi^\psi|^2 \right) \right. \\ & \quad \left. + \frac{\nabla \psi \times \mathbf{j}}{|\nabla \psi|^2} \cdot \nabla \times \mathbf{D} |\xi^\psi|^2 + \Gamma p |\nabla \cdot \boldsymbol{\xi}|^2 \right\} dV + \frac{1}{2} \int_{V_v} |\nabla \times \mathbf{A}|^2, \end{aligned} \quad (2.53)$$

and kinetic energy functional

$$K = \int_{V_p} \rho_p \left\{ |\xi^\psi|^2 \frac{\mathbf{D}^2}{\mathbf{B}^2} - 2\xi^\psi \xi^D \frac{\mathbf{D} \cdot \nabla \psi}{\mathbf{B}^2} + |\xi^D|^2 \frac{|\nabla \psi|^2}{\mathbf{B}^2} + |\xi^B|^2 \frac{1}{\mathbf{B}^2} \right\} dV, \quad (2.54)$$

2.4. Macroscopic plasma stability

due to a plasma displacement $\boldsymbol{\xi}e^{i\omega t}$. The potential energy includes a term for the energy change inside the volume V_p occupied by the plasma W_p and a term W_v for the change of energy in the vacuum region V_v , thus allowing for the description of external modes. For the displacement vector the following projection is used

$$\boldsymbol{\xi} = \xi^\psi \frac{\mathbf{D} \times \mathbf{B}}{\|\mathbf{B}\|^2} + \xi^D \frac{\mathbf{B} \times \nabla\psi}{\|\mathbf{B}\|^2} + \xi^B \frac{\mathbf{B}}{\|\mathbf{B}\|^2}, \quad (2.55)$$

with $\mathbf{B} = F(\psi)\nabla\phi + \nabla\psi \times \nabla\phi = \nabla\psi \times \mathbf{D}$ and $\xi^\psi = \boldsymbol{\xi} \cdot \nabla\psi$. The quantity \mathbf{A} is the vector potential that determines the magnetic field perturbation in the vacuum $\nabla \times \mathbf{A} = \delta\mathbf{B}_v$.

2.4.4 Non-linear stability

Often a pure linear stability analysis is not sufficient to assess the actual consequences of an instability. For strong perturbations the linear model breaks down and the stability properties might be altered. This is illustrated in Fig. 2.4. If a sufficiently strong initial perturbation is given to a system that is linearly stable, it might be destabilised non-linearly. This situation is also called metastable and is found for example in the case of neoclassical tearing modes (NTMs). In contrast to this, the initial exponential growth of a linearly unstable mode might saturate (or even decay) due to stabilising effects from the non-linear terms. The system then approaches a neighbouring equilibrium state and is thus non-linearly stable. A combination of these two cases is found for NTMs, which require an initial seed and can later enter a non-linearly stable state. These modes are investigated in chapter 3. If a mode saturates at low amplitudes, a system that is linearly unstable, might still be feasible for tokamak operation. On the other hand, even if a linear model predicts very small linear growth rates but non-linear terms are further destabilising, a mode can still grow to dangerous levels at a later stage. This is particularly relevant when comparing individual modes in the spectrum. There is experimental [14] and theoretical [39] evidence that the linear spectrum of modes does not necessarily reflect the non-linear spectrum. This means that the most unstable modes in the linear phase, might not be dominant in the non-linear phase. Experimentally relevant instabilities often correspond to non-linear modes. Thus, non-linear analyses are required to explain experimental phenomena but also to make predictions about favourable plasma configurations.

Solutions to the non-linear equations are generally difficult to obtain analytically, though a few non-linear models exist, typically assuming simple geometries. An example is the quasi-linear approximation, where a dynamical system, described by the function f is taken to follow the form $\partial_t f + Lf = Nf^2$, with differential operators L and N [37]. A more sophisticated approach determines non-linear stability for magnetohydrodynamic modes close to marginal stability [40]. It was shown that the non-linear amplitude $A(t)$ is governed by

$$\frac{\partial^2 A(t)}{\partial t^2} + \omega^2 A(t) + \alpha A(t)^3 = 0, \quad (2.56)$$

where ω is the linear growth rate and α governs non-linear effects. The parameters ω and α are calculated from the MHD equations with appropriate boundary conditions, specific to the problem investigated. It is more common to perform non-linear stability

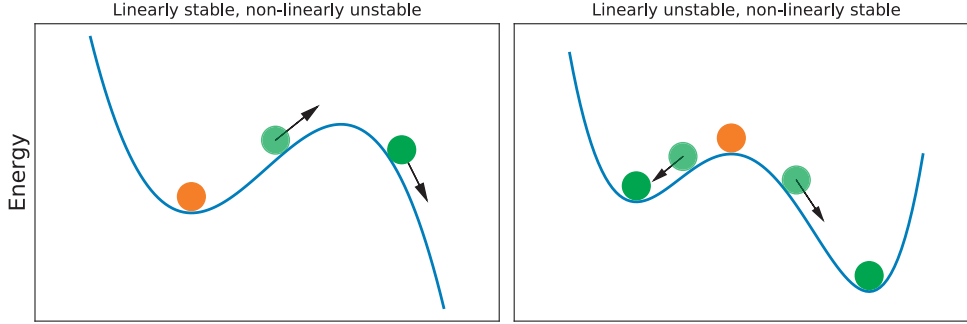


Figure 2.4 – A strong perturbation drives a linearly stable system non-linearly unstable (left). A linearly unstable system can reach neighbouring equilibrium states if non-linear effects are stabilising (such modes are non-linearly stable).

studies with numerical codes, usually using initial value codes such as XTOR [41, 42] and JOREK [43, 44], with and without resistive effects. These codes are initialised from a 2D equilibrium. Finally, if non-linear ideal stability of an initially axisymmetric equilibrium is achieved, it is in principle possible to recover these 3D neighbouring states with a 3D equilibrium code such as VMEC. This has been shown for internal kink modes [32]. In Refs. [45, 46, 47], non-axisymmetric edge corrugations with similarities to kink/peeling modes were observed in equilibrium simulations. These were predominantly driven by the pressure gradient, but a detailed study of the corresponding modes was not carried out. Prior to this thesis it has not been verified whether free-boundary 3D equilibria would verify non-linear stability of external modes, affecting the plasma-vacuum interface.

2.5 Summary and thesis outlook

In this chapter we addressed the theoretical description of macroscopic plasma phenomena. The MHD model is valid on scales much larger than the Debye length and time scales much larger than the ion cyclotron frequency and thus appropriate for this purpose. After reviewing the ideal and resistive single-fluid model, the theoretical description was refined by introducing the bootstrap current. The safety factor q as a measure of the magnetic field helicity was defined. Together with its derivative, q is a central quantity associated with the ideal and resistive instabilities investigated in the remainder of this thesis. The bootstrap current is crucial for the non-linear evolution of NTMs in low-shear plasmas as investigated in chapter 3. But the bootstrap current will also be taken into account in chapter 5, where it flattens the q profile and thus causes regions of low magnetic shear. We then turned to the calculation of axisymmetric (2D) and non-axisymmetric (3D) plasma equilibria. These states, satisfying force balance will be important for the studies presented in the following chapters, where axisymmetric equilibria form the initial values for linear and non-linear stability calculations. Free-boundary 3D equilibrium simulations with the VMEC code, introduced earlier in this chapter, will be used in a novel approach to model ideal non-linearly saturated external MHD modes in chapters 4

2.5. Summary and thesis outlook

and 5. Approaches that will be used later in this thesis were discussed to determine linear and non-linear instability. For non-linear stability studies of resistive plasmas we will employ the initial value method in chapter 3. In this context, we extend an analytical linear model to the early non-linear phase. Non-linear analytical calculations based on Eq. (2.56) and linear eigenvalue computations with KINX complete the study of ideal external kink and infernal modes in chapters 4 and 5.

NTM seeding by coupling with infernal modes

This chapter is dedicated to the numerical and analytical investigation of coupled ideal and resistive MHD modes in hybrid tokamak scenarios. In the hybrid scenario - one of the possible operation scenarios for ITER - a flat q profile in the core associated with low magnetic shear gives rise to (non-resonant) infernal modes. These fast-growing ideal modes can couple to resistive sideband modes with a resonant surface inside the plasma. The growth of resistive modes is much slower compared to that of ideal modes. Nevertheless, fast-growing resistive modes have been observed in experiments. In the following section, we aim to describe this phenomenon theoretically in terms of coupled infernal and neoclassical tearing modes (NTMs) but also considering effects due to the bootstrap current. Numerical simulations of such instabilities in a MAST¹-like configuration are performed with the initial value stability code XTOR-2F including the effect of resistivity. The evolution of magnetic islands is computed from XTOR-2F simulations, and an analytical model [48] is developed based on Rutherford's theory in combination with a model for infernal mode driving. In this framework, the parameter Δ' is extended from the linear phase to the non-linear phase. Additionally, the destabilising contribution due to a helically perturbed bootstrap current is considered. Comparing the numerical XTOR-2F simulations to the analytical model, we find that coupling has a strong destabilising effect on (neoclassical) tearing modes and is able to seed 2/1 magnetic islands in situations when the standard NTM theory predicts stability. The results of this chapter have been published in the journal article [A. Kleiner et al., *Neoclassical tearing mode seeding by coupling with infernal modes in low-shear tokamaks*, Nuclear Fusion **56**, 092007 (2016)]. It is possible to extend the study to $n = 2$ modes. Here, one would expect to find a non-linearly unstable 3/2 mode, driven by coupling with a 2/2 infernal mode. This will be presented in future work.

3.1 Introduction

Future operation scenarios for tokamaks like ITER are the standard, advanced and hybrid scenario [49]. The latter being a scenario of particular interest also in present day tokamaks, since it allows longer sawteeth-free plasma discharges at high beta and reasonably large current [9]. The hybrid scenario is characterised by low magnetic shear in the core with a flat or weakly reversed q profile, slightly above unity, where $q > 1$ across

¹Mega-Ampere Spherical Tokamak (MAST)

the whole plasma. Hybrid plasmas achieve high values of

$$\beta_N = \langle \beta[\%] \rangle \frac{a[m]B_T[\text{T}]}{I_p[\text{MA}]}, \quad (3.1)$$

with $\langle \beta \rangle$ being the volume averaged normalised plasma pressure, $\beta = 2\mu_0 \langle p \rangle / B^2$, a the minor radius, B_T the toroidal magnetic field and I_p the plasma current. Plasmas with low-shear core are also met after sawtooth crashes when the field lines are fully reconnected [50, 51].

Such toroidal, low-shear core plasmas, or plasmas with shear-free core, are susceptible to a class of pressure-driven MHD modes called infernal modes [52, 53], which are related to the quasi-interchange modes described by Wesson for the special case $m = n = 1$ [54]. Infernal modes are characterised by the coupling due to toroidicity, between a fundamental harmonic, which does not need to be resonant, in the core with mode numbers (m_0, n) and its $(m_0 \pm 1, n)$ sidebands due to toroidicity. When resistivity is included, the sidebands show a tearing character on their rational surfaces where $q = (m_0 \pm 1)/n$. Usually the q profile is selected (by physical processes or by design) such that there is no exact rational surface associated with m/n , nor can an island develop. Hence, in an extended region of the core, $0 < q - m_0/n \ll 1$. The perturbation due to the sidebands of the infernal mode contributes to the development of fast growing modes (neoclassical tearing modes (NTMs)) [55], which decrease plasma the performance or can lead to disruptions. The linear theory of infernal modes [56] predicts islands growing up to ideal timescales. Furthermore, it has also been observed experimentally that such resistive modes are able to grow much faster than classical tearing modes [15], especially following sawtooth crashes [55, 57] where the safety factor profile is (in some theoretical models, and according to some experiments) completely above unity. This might be interpreted as $m > 1$ modes coupling to the strong $m = 1$ internal kink perturbation. Other examples of non-resonant infernal modes have recently been considered in Refs. [58, 59, 60].

Previous analyses of resistive infernal modes were investigated without the inclusion of the bootstrap current [53, 61]. The bootstrap current plays a crucial role in the stability of toroidal plasmas, since it has a destabilising effect which allows for unstable NTMs in situations in which classical tearing modes would be stable. In the present work we investigate the (seed island) triggering of NTMs in low-shear plasmas focusing on the coupling to infernal modes. By including effects due to the bootstrap current we consider a destabilising mechanism that is still maintained even if the driving effect of infernal modes on the island growth were to disappear, e.g. due to the q profile in the low-shear region moving away from a rational surface ρ_s where $q(\rho_s) = m_0/n$. This allows us to see, whether the bootstrap current is able to maintain NTMs that have been triggered with the help of infernal modes after the contribution from the triggering mechanism becomes weak. To do this, numerical simulations of MAST-like equilibria using the initial value code XTOR-2F [42] are performed. By carrying out simulations with and without bootstrap current, the effect of the bootstrap contribution on these infernal mode triggered NTMs can be estimated. An analytical model is developed to calculate the infernal modes' contribution to the non-linear evolution of the island width.

3.2. Fast growing resistive modes in experiments

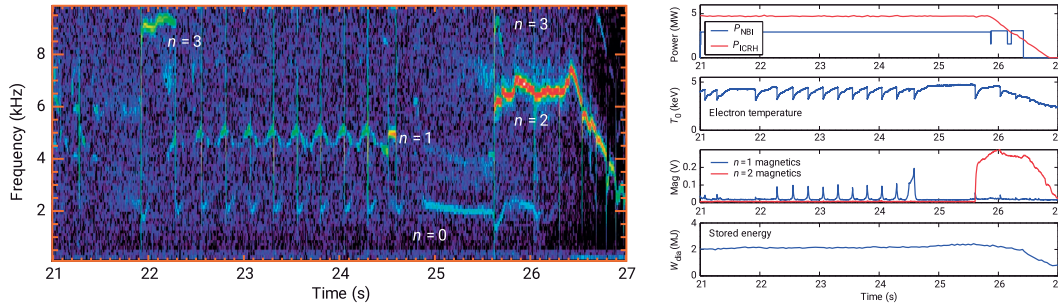


Figure 3.1 – JET pulse 78772 showing a 3/2 NTM starting from $t = 25.6$ s following a sawtooth crash. Courtesy of J. P. Graves et al. [57]. (left): Mode spectrogram. (right): The 3/2 mode is detected by the magnetics signal and is followed by a reduction of the electron temperature.

The model extends the linear coupling of tearing modes and infernal modes mentioned earlier. The predictions of combined linear and non-linear models are compared to the numerical simulations.

This chapter is organised as follows: First, section 3.2 presents experimental observations of fast-growing resistive modes. This is followed by a review of resistive plasma instabilities in section 3.3 where stability of non-linear classical and neoclassical tearing modes is introduced. In section 3.4 the effect of infernal mode coupling on the drive of NTMs is explained and an analytical model is developed to reflect the behaviour in the early non-linear phase. Numerical simulations of MAST-like equilibria using XTOR-2F are then performed in section 3.5, and the resulting magnetic island evolution with and without consideration of bootstrap current effects is presented. By carrying out a variation of the pressure, the dependency of the saturated island width on β_N is investigated. Finally, the analytical predictions are compared with the numerical XTOR-2F simulations in section 3.6.

3.2 Fast growing resistive modes in experiments

As mentioned previously, the time scales of ideal MHD differ from the time scales of resistive MHD. Nevertheless, experiments at JET [62, 57] and TCV [55, 63] found resistive modes that grow much faster than what would be expected for a resistive mode. These modes with helical mode numbers 2/1 and 3/2 are often found during and after sawtooth crashes, but also in hybrid scenario discharges e.g. in JET. For example, Figure 3.1 shows the occurrence of a 3/2 NTM following a sawtooth crash in JET pulse 78772 at $t = 25.6$ s. Quickly after a sawtooth crash, the magnetics signal detects a 3/2 mode that grows within milliseconds and eventually saturates. As a result of this mode, the electron temperature and stored energy decreases with negative effects on plasma performance and confinement. The spectrogram indicates also the existence of $n = 0, 1, 3$ modes.

In TCV fast NTM seeding was observed following sawtooth crashes too. Magnetic islands are formed within microseconds after a sawtooth crash, as can be seen in Fig. 3.2. An $n = 2$ mode appears within microseconds. This mode is associated with a magnetic

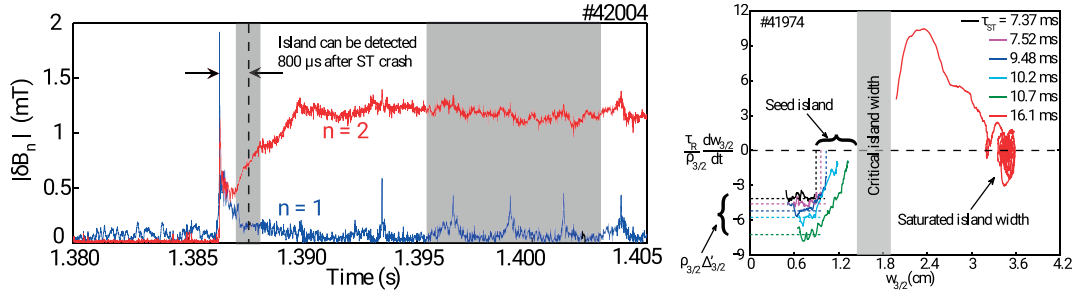


Figure 3.2 – Sawtooth crash and subsequent magnetic island formation in TCV. Courtesy of G. Canal et al. [55]. (left): Magnetics signal showing the sawtooth crash and fast growth of a $n = 2$ mode. (right): Phase space diagram showing magnetic island growth dw/dt as a function of its width w .

island that can be detected $\approx 800 \mu$ s after the sawtooth crash but a seed island is already present before. These experimental results shown in Fig. 3.2b indicate that classical tearing modes are stable, but an initial seed drives neoclassical tearing modes non-linearly unstable. After the initial seed the mode is found to saturate, which again is a non-linear effect.

It is important to know the origin of this fast-seeding of NTMs but also the behaviour in the non-linear phase. The situation during a sawtooth crash [54, 51] modelled with XTOR-2F, when fast-growing resistive modes are triggered is shown in Fig. 3.3. The low magnetic-shear in the core associated with the flat q profile can potentially destabilise infernal modes that couple to a resistive mode due to toroidicity.

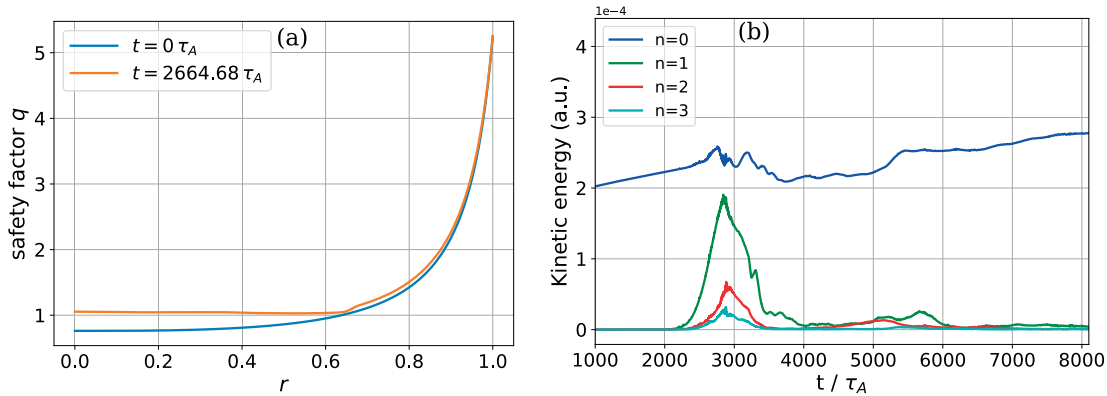


Figure 3.3 – Sawtooth crash in a plasma with circular cross section and $\varepsilon = a/R_0 = 0.37$. (a) Typical safety factor profile before a sawtooth crash at $t = 0 \tau_A$ and during a sawtooth crash ($t = 2664.68 \tau_A$), where it is flattened in the core and completely above 1. The profile at $t = 2664.68 \tau_A$ was obtained from a CHEASE equilibrium reconstruction based on the fields during a XTOR-2F stability simulation. (b) Time trace of the kinetic energy of the lowest n modes.

3.3 Resistive instabilities and tearing modes

In order to develop a model for infernal mode driving of NTMs, it is useful to review linear and non-linear theory of tearing modes. First without toroidal effects included, i.e. without the infernal mode drive. In all cases it is assumed that the q profile is not flat in the region where the tearing mode grows. In the theoretical work ρ is used as an appropriate radial variable. Later, in the numerical work ρ will be defined to be proportional to the square root of the toroidal magnetic flux. However, for the analytical models presented in this section and section 3.4, this definition is not strictly necessary.

3.3.1 Classical tearing modes

The Euler-Lagrange equation (2.51) governing the ideal MHD displacement is singular at rational flux surfaces where $q = m/n$. To describe unstable internal modes, an extension to the model that resolves the physical structure of the eigenfunction near the rational surface is necessary. Such an extension is added in terms of inertia and resistivity [64]. With the assumption that the growth of the mode is relatively slow, it is sufficient to consider inertial and resistive effects only in a narrow region around the singularity, called the resistive layer. The rest of the plasma (outer region) can be described by ideal MHD. To obtain the tearing mode dispersion relation, one set of equations is solved in the resistive layer and one in the outer region with boundary conditions at $\rho = 0$ and $\rho = a$. These solutions are matched at the boundary of the resistive layer.

The derivation usually assumes a plasma with circular cross section and large aspect ratio, i.e. $\varepsilon = a/R \ll 1$. The following ordering for the equilibrium (subscript '0') and perturbed (subscript '1') quantities is assumed:

$$\begin{aligned} B_{\theta 0} \sim \frac{1}{\rho} \frac{dB_{\phi 0}}{d\rho} \sim \varepsilon B_{\phi 0} \quad , \quad B_{\phi 1} \sim \varepsilon B_{\rho 1} \sim \varepsilon B_{\theta 1} \\ j_{\theta 0} \sim \varepsilon j_{\phi 0} \quad , \quad j_{\rho 1} \sim j_{\theta 1} \sim \varepsilon j_{\phi 1} . \end{aligned} \quad (3.2)$$

Outside of the resistive layer the perturbed plasma is in force balance [65] and the dynamics are described by Eq. (2.17). The curl of this equation is $\nabla \times (\mathbf{j} \times \mathbf{B}) = \nabla \times \nabla p = 0$, eliminating the pressure from the problem at lowest relevant order in ε . Applying the large aspect ratio ordering one can identify the toroidal component of the force balance equation as dominant. Perturbed quantities are chosen to be of the form $e^{i(m\theta - n\phi)}$. With that and using Ampère's law as well as $\nabla \cdot \mathbf{B} = 0$, the outer region is governed by

$$\frac{1}{\rho} \frac{d}{d\rho} \left(\rho \frac{d\psi}{d\rho} \right) = \frac{m^2}{\rho^2} \psi - \frac{1}{\frac{B_{\theta}}{\mu_0} \left(1 - \frac{nq}{m} \right)} \frac{dj_{\phi}}{d\rho} \psi = 0 . \quad (3.3)$$

Here, ψ is a magnetic flux function (perturbed flux) and defined in terms of the perturbed magnetic field:

$$B_{\rho 1} = -\frac{1}{\rho} \frac{\partial \psi}{\partial \theta} \quad , \quad B_{\theta \rho} = \frac{\partial \psi}{\partial \rho} , \quad (3.4)$$

and it is seen from Eq. (3.3) that the destabilising drive comes from the radial current density gradient. The parameter that will be used to match the resistive region and the

outer region is:

$$\Delta' = \lim_{\varepsilon \rightarrow 0} \left(\frac{\psi'_{\rho_s + \varepsilon}}{\psi_{\rho_s + \varepsilon}} - \frac{\psi'_{\rho_s - \varepsilon}}{\psi_{\rho_s - \varepsilon}} \right), \quad (3.5)$$

where ρ_s is the position of the resonant surface (where $m - nq$ is singular). We now identify Δ' in the outer and inner regions. For the outer region calculation of Δ' , we simply solve Eq. (3.3) using boundary conditions $\psi(0) = 0$ and $\psi(\rho = a) = 0$, and $\psi(\rho_s - \varepsilon) = \psi(\rho_s + \varepsilon)$. An arbitrary value for $\psi(\rho_s - \varepsilon) = \psi(\rho_s + \varepsilon) = 1$ can be assumed. A shooting method can then be used to solve for ψ separately in the regions $0 < \psi < \rho_s - \varepsilon$ and $\rho_s + \varepsilon < \psi < a$ in order to evaluate Δ' . Note that analytic solutions of Eq. (3.3) are also obtainable, and will be used in chapter 4.

The dynamics in the resistive layer are governed by resistive Ohm's law Eq. (2.5) and the equation of motion. The perturbation in the resistive layer is assumed to have the form $e^{\gamma t + im\theta - in\phi}$. After making use of the expansion

$$\left(1 - \frac{nq}{m}\right) \approx - \left(\frac{q'}{q}\right)_{\rho_s} (\rho - \rho_s), \quad (3.6)$$

at the resonant surface ρ_s , from Ohm's law in combination with Faraday's law and Ampère's law one obtains for the discontinuity

$$\Delta'_{in} = \frac{\mu_0 \gamma}{\eta} \int \left(1 - \frac{B_\theta q'}{q} s \frac{v_\rho}{\psi}\right) ds, \quad (3.7)$$

with $s = \rho - \rho_s$. The equation of motion can be written in the form

$$\frac{d^2 v_\rho}{ds^2} - \left(\frac{B_\theta^2 m^2 q'^2}{\rho \eta \gamma \rho^2 q^2}\right) s^2 v_\rho + \frac{B_\theta m^2 q'}{\rho \eta \rho^2 q} s \psi + \frac{m^2}{\rho \gamma \rho^2} \frac{dj_\phi}{d\rho} \psi = 0, \quad (3.8)$$

and is solved for v_ρ . $\psi(\rho)$ is considered constant over the (narrow) resistive layer [64] (so-called constant ψ approximation), but ψ' is not constant (thus defining Δ'). This approximation is valid as long as $w\Delta' \ll 1$, where w is the magnetic island width. This is satisfied for classical tearing modes, where the initial island is very small. The solution in the inner resistive region is:

$$\gamma = \frac{0.55}{\tau_A^{2/5} \tau_R^{3/5}} \left(n \frac{a^2 q'}{Rq}\right)^{2/5} (a\Delta')^{4/5}, \quad (3.9)$$

where τ_R is the resistive time and $\tau_A = 1/\omega_A = R_0/v_A$ is the Alfvén time with $v_A = I/R_0 \sqrt{(\mu_0 \varrho_0)}$ being the Alfvén speed. The Δ' in Eq. (3.9) is the value of $(\psi'(\rho_s + \varepsilon) - \psi'(\rho_s - \varepsilon))/\psi(\rho_s)$ in the resistive region. We do not know this, but fortunately we may match it to the Δ' evaluated in the outer regions (i.e. the solution of Eq. (3.3)) via the shooting method mentioned earlier. Henceforth, when Δ' is referred to, it is the Δ' evaluated in the outer region.

From Eq. (3.9) it is seen that the tearing mode is marginally stable for $\Delta' = 0$ and unstable when $\Delta' < 0$. This result, derived from a linear analysis is sufficient to determine whether a certain plasma configuration is stable or unstable with respect to tearing modes. It does however not take into account the change of j in the island region

3.3. Resistive instabilities and tearing modes

due to the growing magnetic island. Such finite island width corrections are important to determine the evolution of tearing modes into the non-linear regime, where mode growth is slower due to resistive diffusion. Non-linear stability of the tearing mode was first described by Rutherford [15], originally developed for cylindrical plasmas, predicting that the magnetic island growth in the early non-linear phase is linear in time and related to the tearing stability parameter defined by Eq. (3.5):

$$\Delta'(w) = \lim_{\varepsilon \rightarrow 0} \left(\frac{\psi'(\rho_s + w/2) - \psi(\rho_s - w/2)}{\psi(\rho_s \pm \varepsilon)} \right), \quad (3.10)$$

where $\psi'(\rho_s \pm w/2)$ is obtained again from solution of Eq. (3.3) using the shooting method described earlier. The constant ψ approximation is retained in this non-linear model. As will be seen in more detail in the next section, the non-linear growth of a magnetic island is given by the Rutherford equation [15]

$$\frac{\tau_R}{\rho_s} \frac{dw}{dt} = \rho_s \Delta'(w). \quad (3.11)$$

Writing the flux function as $\psi = \psi_0(r) + \psi_1(r) \cos(m\theta - n\phi)$, the width of the magnetic island associated with a tearing mode can be calculated from $w = 4\sqrt{-\psi_1/\psi_0''}$.

3.3.2 Non-linear neoclassical tearing modes

The classical non-linear tearing mode model described in section 3.3.1 does not include neoclassical effects, which are important for realistic tokamak plasmas. These additional effects are considered now and enable a more sophisticated non-linear treatment of magnetic islands in tokamaks. Neoclassical tearing modes (NTMs) are considered to be metastable, i.e. even if the classical tearing mode is linearly stable, a sufficiently strong 'seed' can destabilise the mode and lead to a non-linear evolution of the mode [16]. Such a seed is often provided by sawteeth, but also by linear and non-linear mode coupling [66]. Rutherford's model, originally describing the non-linear evolution of the classical tearing mode, has been extended to include neoclassical effects and thus to describe neoclassical tearing modes [16, 17]. Denoting the magnetic island width by w , the modified Rutherford equation (modification relative to Eq. (3.11)) describes the growth of magnetic islands by:

$$\frac{\tau_R}{\rho_s} \frac{dw}{dt} = f_n \sum_i \rho_s \Delta'_i(w), \quad (3.12)$$

where τ_R is related to the Alfvén time τ_A by the Lundquist number $S = \tau_R/\tau_A$. The factor f_n comes from a change in radial transport across the island and is typically set to 1.22 or 1.66 [65, 37]. The value of this coefficient cannot be calculated exactly due to the imprecise definition of Rutherford's integrals. In our study we set $f_n = 1.22$ in consent with most of the current literature. Δ'_i are the stabilising or destabilising contributions to the total tearing stability parameter Δ'_{total} . These include the linear cylindrical tearing stability parameter

$$\rho_s \Delta'_0 = -2m\Lambda\pi \cot(\Lambda\pi), \quad (3.13)$$

with $\Lambda \approx -\frac{\mu_0 q^2 R_0^2}{mq'} \frac{R_0^2}{I} j'_{\parallel} |_{\rho_s}$ [67]. Eq. (3.13) is obtained in a simple cylinder and is the solution to Eq. (3.3) (solved analytically, instead of numerically using the shooting method) described earlier in the limit $w = 0$ in Eq. (3.10). Large island corrections for $\Delta'_0(w)$ of Eq. (3.10) are also known in the literature [65], where such a correction was first given by White et al. [68]. However, more recent work [69, 70, 71] reviewed the asymptotic matching required for a non-linear treatment, and the result for the scenarios considered in this thesis are that finite width corrections given by e.g. Eq. (29) of Ref. [69] have the opposite sign to those of Ref. [68]. Taking into consideration these discrepancies, and noting that the finite width correction of Ref. [69] has a small amplitude, we choose to define the cylindrical Δ'_0 as Eq. (3.13) for all widths in the rest of the thesis. The contribution from the bootstrap current

$$\rho_s \Delta'_{bs}(w) = \frac{64}{3\pi} \frac{\mu_0 R_0^3 q_s^2}{F^2 q_s'} \langle \mathbf{J}_{bs} \cdot \mathbf{B} \rangle \frac{w}{w^2 + w_d^2}, \quad (3.14)$$

provides a well known non-linear contribution to Eq. (3.12), arising from the current perturbation associated with pressure flattening in the region of the island [17, 72, 73]. The bootstrap term includes corrections for small island sizes due to transport which are given by $w_d \approx (\chi_{\perp}/\chi_{\parallel})^{(1/4)} \sqrt{2\hat{L}_s/\hat{k}_{\theta}}$ with $\hat{L}_s = q^2/(q'\varepsilon)$, $\varepsilon = qB_p R/F$ and $\hat{k}_{\theta} = m/\rho$, and χ_{\perp} and χ_{\parallel} are the perpendicular and parallel heat transport coefficients respectively.

Other terms usually included in non-linear NTM analysis comprise Δ'_{GGJ} [72, 74, 75], arising from toroidal geometry effects and a polarization current term Δ'_{pol} [76]. We will include the GGJ contribution given by [72]

$$\rho_s \Delta'_{GGJ}(w) = 6\rho_s \frac{D_R}{\beta_p} \frac{w}{w^2 + w_{dGGJ}^2}, \quad (3.15)$$

where $w_{dGGJ}^2 = 0.2w_d^2$ is due to a small island width correction, $\beta_p = 2\mu_0 p/B_p^2$ and the quantity D_R is defined in Refs. [74, 75, 72] and is calculated by the CHEASE code [30, 72]. This contribution represents the stabilising effect of magnetic field line bending on NTMs. In a more recent model [77, 78], where linear and non-linear results are matched, for the GGJ contribution the following expression is found:

$$\rho_s \Delta'_{GGJ}(w) = 6.35\rho_s \frac{D_R}{\sqrt{w^2 + 0.65w_c^2}}, \quad (3.16)$$

with $w_c = 2\sqrt{2}(\chi_{\perp}/\chi_{\parallel})^{(1/4)} \sqrt{\rho_s R/(ns)}$. Eq. (3.16) predicts a more stabilising effect in the limit $w \rightarrow 0$ (initial phase) than Eq. (3.15). Due to the lack of knowledge on how to parameterise Δ'_{pol} , and due to the fact that the polarization effect is missing in XTOR-2F, we will drop Δ'_{pol} from the analysis here.

Finally, in the next section we analyse the toroidal coupling of tearing modes with infernal modes. We choose to look for a coupling contribution $\sum_i \Delta'_i$ that can be inserted into the Rutherford equation, a method analogous to Ref. [79] which looked at the effect of magnetic perturbations.

3.4 Extension of the Rutherford equation to include seeding by infernal modes

The following provides an explanation of the theoretical origin of infernal modes and reviews linear analytical treatment that forms the basis for the study of NTM triggering by infernal modes. A contribution to the modified Rutherford equation is then modelled to reflect the diminishing of coupling in the early non-linear phase when the infernal mode saturates. This is followed by a calculation of the eigenfunctions.

3.4.1 Linear model of resistive infernal modes

The model described here constitutes the basis for the derivation of tearing stability when infernal modes are present. We now focus on the destabilising effect of ∇p , which - according to Eq. (2.47) - constitutes a potential source of free energy. The most important pressure-driven instabilities in tokamaks are ballooning modes and infernal modes. For ballooning modes it is found that largest n modes are linearly the most unstable, whereas unstable infernal modes are of low n . Magnetic shear plays an important role for the destabilisation of both types of instability and the ballooning model assumes finite magnetic shear. On the contrary, infernal modes are a class of pressure-driven MHD modes that occur in toroidal plasmas with extended regions of low or vanishingly low magnetic shear $s = (\rho/q)q'$. They can be both ideal or resistive in character. The stability threshold in resistive plasmas lies below the threshold for ideal infernal modes [53]. These modes occur already at very low β_p when infinite n ballooning theory predicts stable modes.

Infernal modes are characterised by an ideal mode with mode number (m_0, n) located in the low-shear region, coupled to its poloidal sidebands with mode numbers $(m_0 \pm 1, n)$. The existence of such coupled modes was predicted by Zakharov in Ref. [80]. The destabilisation of pressure-driven modes, far below the ballooning stability threshold is due to the effect of the q profile with extended low-shear when it is close to a rational value. Coupling allows for an energy transfer between the ideal mode in the low-shear region and the sideband mode. It can thus result in a much larger growth of the sideband or destabilise a sideband mode that would be stable without the coupling drive. When resistivity is included, the sideband modes develop a tearing character on their magnetic surfaces, which contributes to the formation of magnetic islands and enhances the growth of the m_0 main mode. Classical tearing modes grow on resistive timescales like $\gamma \sim S^{-3/5}$, whereas the scaling for infernal modes is dramatically faster with $\gamma \sim S^{-3/13}$ at the ideal stability boundary. The growth rate of infernal modes is larger for higher pressure and small absolute $\delta q = q - m_0/n$, representing the distance of q in the low-shear region to the rational value. The typical shape of a q profile that gives rise to infernal modes and the parameter δq are shown in Fig. 3.4.

The analysis of tearing modes driven by infernal mode coupling differs from that of classical tearing modes in section 3.3.1 in so far as a region of low magnetic shear is assumed in the core extending from $0 \leq \rho \leq \rho_*$ (region (i) in Fig. 3.4). In this region,

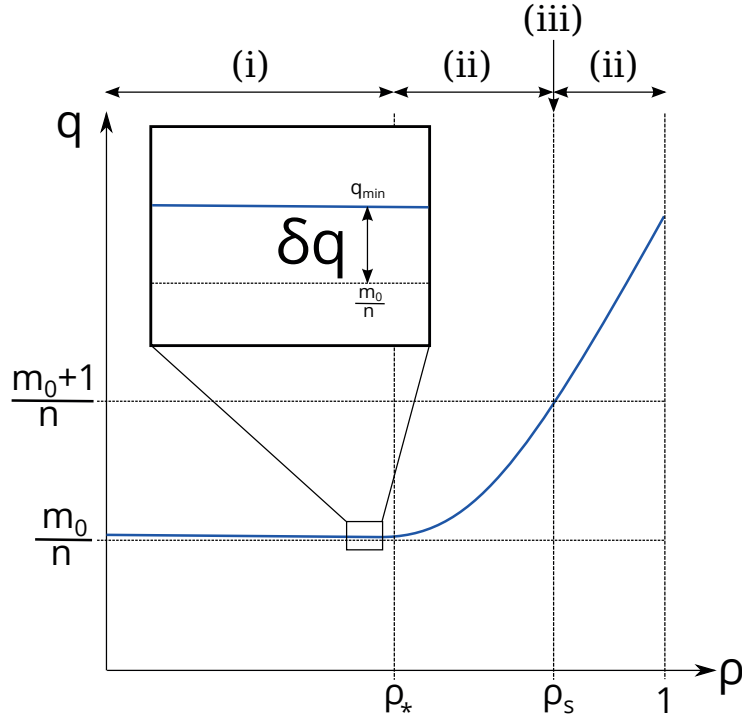


Figure 3.4 – Typical q profile considered in the analytical theory of infernal modes. The radial variable ρ is normalised with respect to the minor radius ($\rho = 1$ at the boundary). Region (i) is characterised by a flat q and low to vanishing shear. Region (ii) constitutes the external region in which the shear is high. The resistive layer (iii) or internal region is located at the resonant $(m_0 + 1)/n$ surface.

the displacement is modelled in the form

$$\xi = \xi_{m_0} e^{im_0\theta - in\phi} + \varepsilon \xi_{m_0 \pm 1} e^{i(m_0 \pm 1)\theta - in\phi} + \mathcal{O}(\varepsilon^2), \quad (3.17)$$

where the main harmonic (infernal mode) has poloidal mode number m_0 and the sidebands with $m = m_0 \pm 1$ are one order in ε smaller than the main mode. In the sheared region extending from $\rho_* < \rho < \rho_s$ and $\rho_s < \rho \leq a$ (region (ii) in Fig. 3.4), the modes are decoupled at leading order [56, 81]. Resistivity is only important in a narrow region around the rational surface at ρ_s (region (iii) in Fig. 3.4) and a solution for the sideband eigenfunction is calculated separately. The equations governing the sideband (tearing) $m_0 + 1$ eigenfunction in the regions $\rho_* < \rho < \rho_s$ and $\rho_s < \rho < 1$ are similar to those describing classical tearing modes, explained in section 3.3.1. However, the boundary conditions are different. For the classical tearing mode the sheared region extends to the magnetic axis, where the eigenfunction ψ reduces to zero, whereas in the infernal mode problem, the eigenfunction in the sheared region is matched to the sideband solution obtained in the low-shear region, where the modes are coupled. The dispersion relation for linear resistive infernal modes for the case $m_0 = n$ (appropriate for our study of non-resonant modes close to $q = m_0/n = 1$) has been derived by Brunetti et al. [56] and

3.4. Extension of the Rutherford equation to include seeding by infernal modes

reads

$$\frac{-\gamma^2}{\omega_A^2} = \frac{n^2}{1 + 2q_*^2} \left[\left(\frac{\delta q}{q_*} \right)^2 + \left[\tilde{\beta}_p(\rho_0) \right]^2 G_0 \frac{B_0 - \rho_s \Delta'_0(\gamma)}{A_0 - \rho_s \Delta'_0(\gamma)} \right], \quad (3.18)$$

where in the region of the resistive layer $\Delta'_0(\gamma)$ is defined as [56]

$$\rho_s \Delta'_0(\gamma) = \bar{S}^{3/4} \hat{\gamma}^{5/4}. \quad (3.19)$$

Here, $\bar{S} = 2.73 [(1 + 2q_s^2)/s_s^2]^{1/3} S$, where $s = q'r/q$ is the magnetic shear and subscript 's' indicates that a quantity is evaluated at the resonant surface ρ_s . Solving the eigenvalue equation requires matching of Eq. (3.19) with Δ'_0 in the outer region, which is identified with Eq. (3.3) and Eq. (3.5), but with different boundary conditions (as compared with those discussed under Eq. (3.5)), taking into account the effect of coupling with the fundamental harmonic (n, m_0) of the infernal mode. This is discussed in detail in Refs. [53, 56], and is included in the calculations for the sideband eigenfunctions in section 3.4. In addition, ω_A is the Alfvén frequency and the subscript * indicates that a quantity is evaluated at position ρ_* , the transition of low-shear and sheared region. The poloidal β in this analytic calculation is given by $\tilde{\beta}_p = \frac{\mu_0 p_0}{B_p^2} \left(\frac{R_0}{R} \right)^2$, where R_0 is the plasma major radius, B_p is the poloidal magnetic field strength and p_0 is the pressure on the magnetic axis (where $R = R_0$) for a pressure profile $p = p_0 (1 - (\rho/\rho_0)^2)$ for $\rho < \rho_0 \leq 1$. Here, $\Delta'_0(\gamma)$ is the tearing stability parameter of the internal resistive layer for the $(m+1)/n$ surface, which is related to the growth rate by Eq. (3.9). The ι profile near this surface, i.e. in the sheared region, is given by:

$$1/q = \iota \approx \frac{1}{m_0 + 1} \left\{ \frac{n}{m_0} \left[1 - \left(\frac{\rho}{\rho_s} \right)^\lambda \right] + n \right\}. \quad (3.20)$$

The closeness of the q profile to the rational value is expressed through $\delta q = q_{min} - m_0/n$. ρ_s is the position of the rational surface of the sideband, where $q = (m_0 \pm 1)/n$. Note that this internal resistive Δ' can be matched to the outer Δ' assuming very small island width. It should therefore be matched with Eq. (3.13). With this, and setting $m = m_0 + 1$, the coefficients $A_0 = -\frac{\pi \cot(\pi \tilde{a})}{\lambda} (m^2 - \bar{m}^2)$ and $B_0 = \pi \cot(\pi b) (m^2 - \bar{m}^2)/\lambda$ carry information locally on the shape of q . Here, \bar{m} is defined as $\bar{m} = \sqrt{m^2 + 2\lambda + \lambda^2}$, $\tilde{a} = (m - \bar{m})/\lambda$ and $b = (m + \bar{m})/\lambda$. The quantity

$$G_0 = \frac{\varepsilon_*^2 (\rho_*/\rho_s)^{2m}}{m(m+1)} \frac{\Gamma(\tilde{a})\Gamma(b)\Gamma(1 - \tilde{a} - b)}{\Gamma(-\tilde{a})\Gamma(-b)\Gamma(1 + \tilde{a} + b)}, \quad (3.21)$$

with $\varepsilon_* = qB_p R/I|_{\rho_*}$, carries information about the shape of eigenfunction in terms of the q profile in the region $\rho < \rho_s$ and is written in terms of the Γ function. In general the model [56] also includes plasma diamagnetism, subsonic equilibrium toroidal flow shear and viscosity, but these effects are not considered in our study of MAST-like plasmas.

With infernal mode coupling effects taken into account in the calculation of $\Delta'_0(\gamma)$ according to Eq. (3.18) and adding other relevant contributions to the non-linear evolution of the NTM, the modified Rutherford equation (3.12) now reads

$$\frac{\tau_R}{\rho_s} \frac{dw}{dt} = 1.22 \rho_s \left[\Delta'_0(\gamma) + \Delta'_{GGJ}(w) + \Delta'_{bs}(w) \right]. \quad (3.22)$$

Note that here $\Delta'_0(\gamma)$ replaces Δ'_0 of Eq. (3.13) and depends on the linear growth rate γ of the infernal mode. For $\gamma = 0$, i.e. when the infernal modes disappears, the classical tearing mode is recovered and $\Delta'_0(\gamma = 0) = \Delta'_0$. In the next section, we will introduce $\Delta'_0(\gamma, w)$, a finite width correction to $\Delta'_0(\gamma)$.

3.4.2 Infernal mode saturation and modelling of Δ' in the early non-linear phase

The destabilising effect of infernal modes coupling to NTMs is described in the linear phase by the solution to the dispersion relation Eq. (3.18). In the later non-linear phase close to saturation of the island, the main infernal mode has already saturated and thus the coupling from the main infernal mode to the NTM would be expected to vanish. We will now develop a model that captures the decrease of the linear growth rate in the early non-linear phase and hence the loss of coupling for the further non-linear evolution of the sideband mode. In this model the tearing contribution in the presence of infernal modes to the modified Rutherford equation (Eq. (3.12)) depends on the magnetic island width, i.e. $\Delta'_0(\gamma) \rightarrow \Delta'_0(\gamma, w)$. Hence, mode coupling can play an important role in the initial phase of mode growth, but vanishes in the deep non-linear phase (so that for large width the RHS of Eq. (3.12) will depend only on the standard contributions Δ'_0 , Δ'_{bs} and Δ'_{GGJ}). The evolution of the early non-linear phase will depend on a parametrisation based on consistency with the XTOR-2F fully numerical simulations.

In order to obtain $\Delta'_0(\gamma)$ explicitly during the linear phase, one has to solve Eq. (3.18) for the growth rate of the resistive infernal mode as discussed earlier and substitute it back into Eq. (3.19). Examples of such solutions for varying $\delta q = q_{min} - m_0/n$ and β_p are shown in Fig. 3.5. For larger β_p and low δq the mode is more unstable as expected for infernal modes. The growth rate is very large for small δq . As δq is increased the

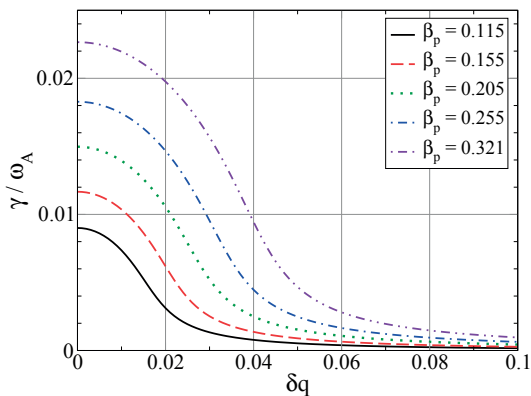


Figure 3.5 – Normalised growth rate $\hat{\gamma} = \gamma/\omega_A$ versus δq for different values of β_p . The Lundquist number is chosen to be $S = 10^6$.

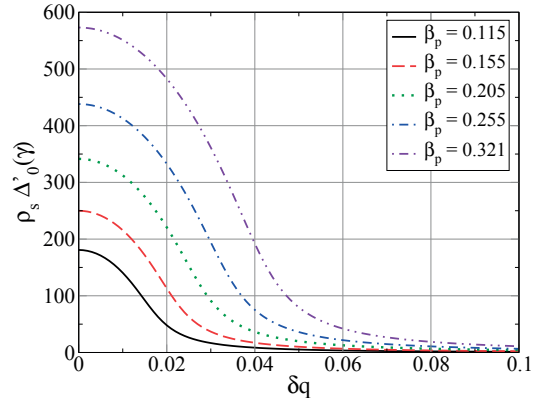


Figure 3.6 – Dependence of the linear tearing stability parameter $\Delta'_0(\gamma)$ of Eq. (3.5) calculated in presence of infernal modes on δq for different values of β_p . The Lundquist number is chosen to be $S = 10^6$.

3.4. Extension of the Rutherford equation to include seeding by infernal modes

growth rate drops drastically and undergoes a transition to tearing-like behaviour. This behaviour is also reflected in Fig. 3.6, where $\Delta'_0(\gamma)$ is shown as a function of δq . The transition point appears at larger δq as β_p is increased.

Solving the general non-linear resistive infernal mode problem analytically is outside the scope of this thesis. In order to provide an analytical estimate of the magnetic island evolution in the non-linear phase, we choose an approach based on extending the linear results, with a transient diminishing of infernal mode coupling as the island grows. In particular, it is assumed that the coupling between the main harmonic and its sidebands vanishes around the time that the main infernal mode saturates in amplitude. The vanishing of the coupling causes a dramatic change of the eigenfunction and thus affects the parameter $\Delta'_0(\gamma)$. For the non-linear extension to the linear model, we choose the growth rate to decrease with the island width as

$$\hat{\gamma}(w) = \hat{\gamma}_{\text{lin}} \exp[-w/w_I], \quad (3.23)$$

where $\hat{\gamma}_{\text{lin}}$ is the linear growth rate obtained from Eq. (3.18) and w_I is the characteristic width of the island at the time when the infernal mode is saturated. We incorporate this change of γ with the growing magnetic island into the calculation of $\Delta'_0(\gamma)$ and thus obtain a finite width correction reflecting the loss of infernal mode coupling:

$$\Delta'_0(\gamma, w) = \Delta'_0(\gamma) \exp\left[-\frac{5}{4}(w/w_I)\right] + \Delta'_0(\gamma = 0) \left(1 - \exp\left[-\frac{5}{4}(w/w_I)\right]\right). \quad (3.24)$$

In the initial phase when $w = 0$, Eq. (3.24) reduces to the expression for $\Delta'_0(\gamma)$ in the linear model. In the late non-linear stage when the infernal mode is saturated ($\gamma = 0$), Eq. (3.24) recovers the classical tearing mode stability index Δ'_0 of Eq. (3.13) and the boundary conditions of the sideband mode correspond to those of the classical tearing mode described in section 3.3.1. It is argued that the characteristic width w_I should not change significantly when adding or neglecting bootstrap effects or other physics that affect the late non-linear evolution of the island. With this model, the width evolution can be obtained either by solving the modified Rutherford equation or from numerical simulations. However, for the Rutherford approach, w_I is determined from the XTOR-2F simulations.

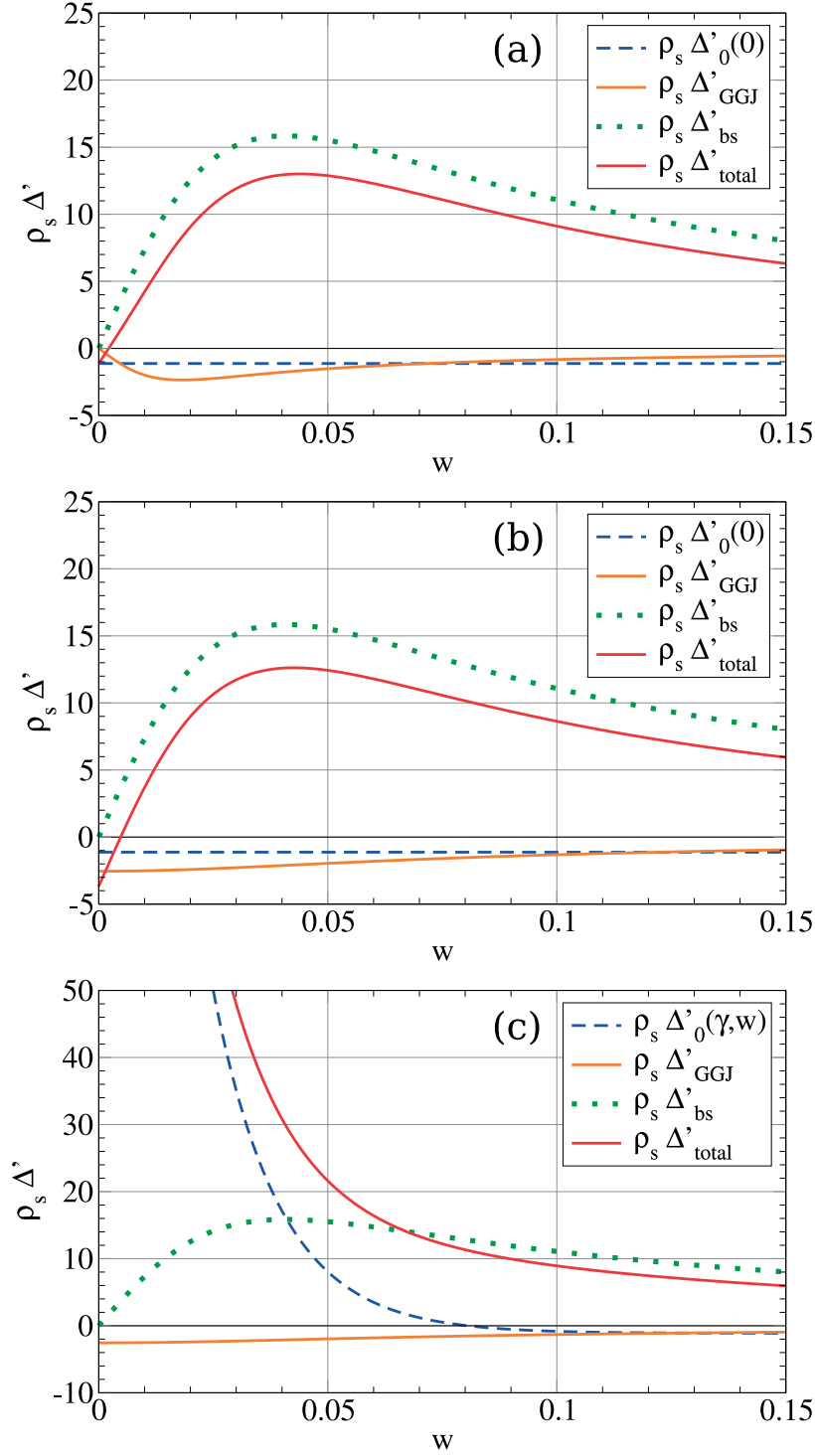


Figure 3.7 – Δ' contributions and their dependency on island width w . (a) without coupling and Δ'_{GGJ} calculated according to Eq. (3.15). (b) without coupling and Δ'_{GGJ} calculated according to Eq. (3.16). (c) with infernal mode coupling. It is seen that the coupling term is dominant for small w , whereas for increasing island width it drops and its value is comparable with the bootstrap current term Δ'_{bs} . For this calculation $\delta q = 0.019$, $\beta_N = 1.17$ and $S = 10^6$ in a MAST-like equilibrium.

3.4. Extension of the Rutherford equation to include seeding by infernal modes

The growth of an NTM with helicity $m = 2/n = 1$ is calculated using Eq. (3.22) for the MAST-like equilibrium chosen for the numerical study and explained in section 3.5. Cases with and without inclusion of bootstrap current are considered. In the latter case the term Δ'_{bs} in Eq. (3.22) is set to zero. Plots of the contributions to the Rutherford equation Δ'_0 (with and without coupling), $\Delta'_{GGJ}(w)$ and $\Delta'_{bs}(w)$ are shown in Fig. 3.7, where w_I has been set to 0.015. First, we do not consider the coupling effect, and in Fig. 3.7a the curvature contribution is calculated according to Eq. (3.15) and vanishes in the limit $w \rightarrow 0$. The cylindrical contribution (classical tearing mode) $\Delta'_0(\gamma = 0)$ is negative and thus stabilising. In addition, at $w = 0$ the bootstrap contribution is zero. As a result a standard 2/1 NTM would be stable, if infernal mode coupling was not considered. Hence, for an unstable 2/1 mode an additional seed is required. If $\Delta'_{GGJ}(w)$ is calculated according to Eq. (3.16) the total stability parameter Δ' is more negative at $w = 0$, and thus an even larger seed is necessary to trigger an NTM, as shown in Fig. 3.7b. Such a seed is provided by coupling, as demonstrated in Fig. 3.7c. For small islands, the infernal mode coupling contribution is dominant and triggers the creation of a 2/1 magnetic island. The coupling drops very strongly as the island width increases and its magnitude becomes comparable to Δ'_{bs} for $w \gtrsim 0.04$. For large islands the coupling term approaches zero and $\Delta'_0(\gamma, w)$ approaches $\Delta'_0(0)$, recovering the standard cylindrical contribution. In the non-linear phase the bootstrap effect is proportional to $1/w$ for $w \gg w_d$ and thus as a result reduces in amplitude more slowly than the infernal mode contribution. So strong is this coupling effect at small w that it is seen that evolution of w is almost independent of the choices of model (Eq. (3.15) or (3.16)) for $\Delta'_{GGJ}(w)$. The neglect of Δ'_{pol} is also not a significant approximation.

This shows that infernal mode coupling provides a necessary seed island for NTM growth. During the early non-linear phase, the growth of the island is very fast. In addition, as seen in the last section, the destabilising effects from the bootstrap current are able to maintain island growth to considerably larger widths than in situations where the bootstrap current is not considered.

3.4.3 Ad-hoc calculation of coupled non-linear infernal modes and their eigenfunctions

It is interesting to examine the eigenfunction evolution that would be expected from Eq. (3.23) and Eq. (3.24) in the linear and non-linear phase. The sideband eigenfunctions obtained from the linear model drop rapidly before the rational surface due to the strong drive from the infernal mode. Together with the rather flat eigenfunctions at $\rho > \rho_s$ this results in a strong discontinuity of the radial derivative of ψ and thus a large $\Delta'_0(\gamma)$. In the non-linear regime, the mode coupling diminishes and this behaviour should also be reflected in a change of the eigenfunctions. The sideband ($m = m_0 + 1, n$) eigenfunctions $\xi_{r\pm}$ are governed by [56]

$$\frac{d}{dz} \left[z^{2/\lambda+1} (1-z)^2 \frac{d\xi_{r\pm}}{dz} \right] - \frac{m^2 - 1}{\lambda^2} z^{2/\lambda-1} (1-z)^2 \xi_{r\pm} = 0, \quad (3.25)$$

where a new radial variable $z = (\rho/\rho_s)^\lambda$ has been introduced. The fluid displacements $\xi_{r\pm}$ are related to the perturbed poloidal flux by

$$\psi_\pm = -(f'_0 \hat{k}_\parallel / m) \xi_{r\pm}, \quad (3.26)$$

where $f'_0 \sim \rho B_0$ is the radial derivative of the equilibrium toroidal flux, $\hat{k}_\parallel = m\iota - n$ is the parallel wave vector. For ι profiles given by Eq. (3.20) this differential equation can be solved analytically. The eigenfunctions $\xi_{r\pm}$ describe the fluid displacement at $\rho < \rho_s$ (ξ_{r-}) respectively at $\rho > \rho_s$ (ξ_{r+}) and are given by

$$\begin{aligned} \xi_{r-}(z, w) = & z^{(m-1)/\lambda} (1-z)^{-1} \left(A_1^*(w) F(\tilde{a}, b; \tilde{a} + b + 1; z) \right. \\ & \left. + B_1^*(w) z^{-\tilde{a}-b} F(-b, -\tilde{a}; 1 - \tilde{a} - b; z) \right), \end{aligned} \quad (3.27)$$

$$\begin{aligned} \xi_{r+}(z, w) = & z^{-(1+\bar{m})/\lambda} (z-1)^{-1} \left(A_2^*(w) F(b, -\tilde{a}; 1 + b - \tilde{a}; 1/z) \right. \\ & \left. + B_2^*(w) z^{b-\tilde{a}} F(-b, \tilde{a}; 1 + \tilde{a} - b; 1/z) \right), \end{aligned} \quad (3.28)$$

where we defined the quantities $\tilde{a} = (m - \bar{m})/\lambda$ and $b = (m + \bar{m})/\lambda$, and $F(a, b; c; d)$ denotes the hypergeometric function of the kind ${}_2F_1$ [82].

The external (sheared region) eigenfunctions, given by Eqs. (3.27) and (3.28) both consist of a regular term, describing the classical tearing behaviour and a term due to mode coupling. The coefficients $A_1^*, B_1^*, A_2^*, B_2^*$ in Eqs. (3.27) and (3.28) are calculated from the boundary conditions and matching of the eigenfunctions in the three regions of Fig. 3.4. Ensuring the asymptotic behaviour of ξ_{r-} for $z \ll 1$ [83, 56]

$$\frac{B_1^*}{A_1^*} = -C^* \frac{A_0 - \frac{D_0}{1+D_0} (A_0 + B_0 + \bar{m}) - \rho_s \Delta'_0(\gamma, w)}{B_0 - \frac{D_0}{1+D_0} (A_0 + B_0 + \bar{m}) - \rho_s \Delta'_0(\gamma, w)}, \quad (3.29)$$

where

$$D_0 = -\rho_s^{2\bar{m}} \frac{F(b, -\tilde{a}; 1 - \tilde{a} + b; \rho_s^\lambda) \Gamma(-\tilde{a}) \Gamma(b) \Gamma(1 + \tilde{a} - b)}{F(-b, \tilde{a}; 1 + \tilde{a} - b; \rho_s^\lambda) \Gamma(\tilde{a}) \Gamma(-b) \Gamma(1 - \tilde{a} + b)}, \quad (3.30)$$

and $C^* = \frac{\Gamma(-\tilde{a}) \Gamma(-b) \Gamma(1 + \tilde{a} + b)}{\Gamma(\tilde{a}) \Gamma(b) \Gamma(1 - \tilde{a} - b)}$ with Γ being the Gamma function. In Eq. (3.29), a finite width generalisation for $\Delta'_0(\gamma)$ is assumed, i.e. Eq. (3.24), so that the effect of time evolving coupling to the infernal mode can be examined. The condition $\xi_{r+}(a) = 0$ provides an equation for the coefficient B_2^* :

$$\frac{B_2^*}{A_2^*} = -\rho_s^{2\bar{m}} \frac{F(b, -\tilde{a}; 1 - \tilde{a} + b; \rho_s^\lambda)}{F(-b, \tilde{a}; 1 + \tilde{a} - b; \rho_s^\lambda)}. \quad (3.31)$$

From the matching of ξ_{r-} with ξ_{r+} on the rational surface ρ_s we obtain

$$\frac{A_1^*}{A_2^*} = \frac{F(b, -\tilde{a}; 1 + b - \tilde{a}; 1) + \frac{B_2^*}{A_2^*} F(-b, \tilde{a}; 1 + \tilde{a} - b; 1)}{F(\tilde{a}, b; \tilde{a} + b + 1; 1) + \frac{B_1^*}{A_1^*} F(-b, -\tilde{a}; 1 - \tilde{a} - b; 1)}, \quad (3.32)$$

3.4. Extension of the Rutherford equation to include seeding by infernal modes

where the ratios $\frac{B_2^*}{A_2^*}$ and $\frac{B_1^*}{A_1^*}$ are already known from Eqs. (3.29) and (3.31).

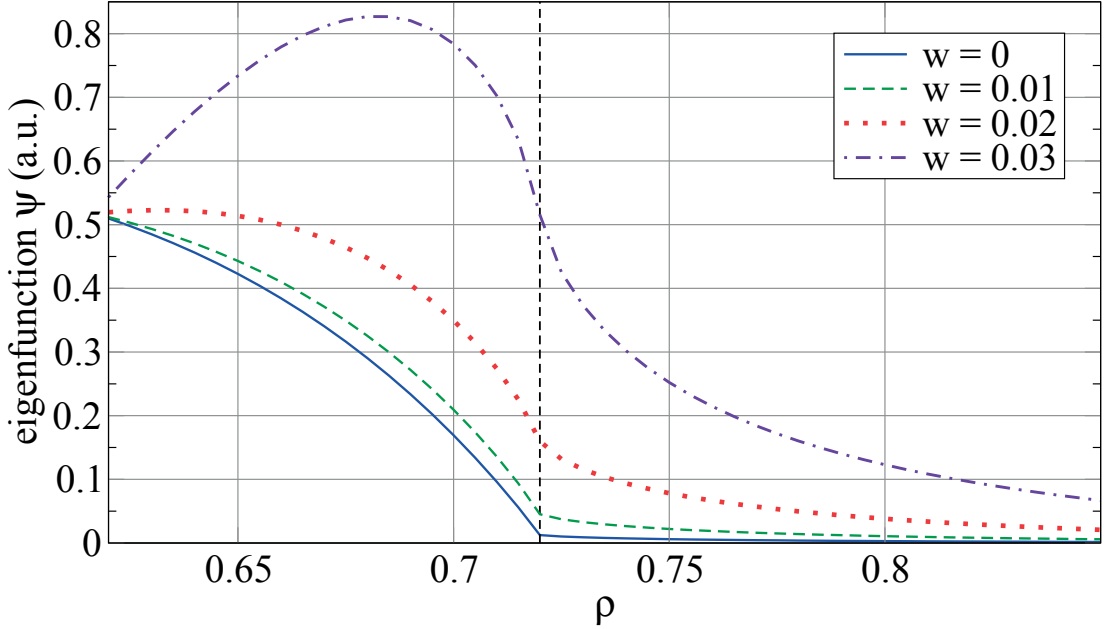


Figure 3.8 – Sideband eigenfunction ψ in the external region (high magnetic shear) for the MAST-like equilibrium, plotted for different widths of the magnetic island. The rational $(m_0 + 1, n)$ surface is indicated by the dashed black line. As the island width increases, the steepening of the eigenfunction due to coupling relaxes.

We are now ready to examine the evolution of the eigenfunction expected during the early non-linear phase when the infernal mode contribution to the Rutherford equation would be dominant, but weakening as the width of the island grows, and coupling diminishes. This is undertaken simply by substituting Eq. (3.24) into Eq. (3.29), taking $\hat{\gamma}^{5/4}$ from the solution to the linear dispersion relation (Eq. (3.18)), and calculating the eigenfunction for various widths. The result is shown in Fig. 3.8 where $\psi(\rho)$ is plotted for different magnetic island widths from the beginning of the linear phase until the later non-linear phase. At $w = 0$, which corresponds to $t = 0$ the eigenfunction drops very strongly close to the rational surface due to the effect of the strong coupling between the 1/1 infernal mode and its 2/1 sideband. As the island grows, the eigenfunction relaxes to a smoother profile. For large width, which corresponds to the situation in the non-linear phase, the infernal mode contribution diminishes and the eigenfunction becomes that of the cylindrical linear tearing mode at marginal stability, i.e. Eq. (3.13). The constant ψ approximation underlying the Rutherford equation is seen to be satisfied better in the non-linear stage than at earlier times when the infernal mode drive is very strong.

3.5 Resistive non-linear stability simulations

In this section, resistive XTOR-2F simulations of a MAST-like equilibrium are presented. The simulations have been performed with and without inclusion of bootstrap current. Because the effect of coupling is stronger for tighter aspect ratio tokamaks, a MAST-like equilibrium is chosen. We first introduce the initial value code XTOR-2F used for the numerical simulations, followed by an explanation of the plasma equilibrium and physical model and a discussion of the numerical results.

3.5.1 The non-linear initial value code XTOR-2F

XTOR-2F is an initial value stability code based on the two-fluid model [42]. As for any initial value calculation, an initial state needs to be provided. For XTOR-2F the initial conditions are provided in form of a solution to the Grad-Shafranov equation (2.26) calculated with the CHEASE code (c.f. section 2.3.2).

3.5.1.1 Extended MHD equations and geometry

The physical model used in XTOR-2F [42] is derived from the full resistive MHD equations that result from the full Braginskii equations [84] and includes non-MHD effects like thermal transport, diamagnetism and some neoclassical effects such as bootstrap current [42]:

$$\begin{aligned}
 \rho \partial_t \mathbf{v} &= -\rho(\mathbf{v} \cdot \nabla) \mathbf{v} - \rho(\mathbf{v}_i^* \cdot \nabla) \mathbf{v}_\perp + \mathbf{j} \times \mathbf{B} - \nabla p + (\nabla \nu \nabla) \mathbf{v}, \\
 \partial_t \mathbf{B} &= \nabla \times (\mathbf{v} \times \mathbf{B}) + \alpha \nabla \times \frac{\nabla_\parallel p_e}{\rho} - \nabla \times \eta(\mathbf{j} - \mathbf{j}_{boot}), \\
 \partial_t p &= -\Gamma p \nabla \cdot \mathbf{v} - \mathbf{v} \cdot \nabla p - \alpha \Gamma \frac{p_i}{\rho} \nabla p \cdot \nabla \times \frac{\mathbf{B}}{B^2} \\
 &\quad + \nabla \cdot \chi_\perp \nabla p + \nabla \cdot \left[\mathbf{B} \left(\frac{\chi_\parallel}{B^2} (\mathbf{B} \cdot \nabla) p \right) \right] + H,
 \end{aligned} \tag{3.33}$$

with

$$\rho = Cp^{-\Gamma}, \tag{3.34}$$

or

$$\partial_t \rho = -\rho \nabla \cdot \mathbf{v} - \mathbf{v} \cdot \nabla \rho - \alpha \nabla p_i \cdot \nabla \times \frac{\mathbf{B}}{B^2} + \nabla \cdot D_\perp \nabla \rho + S. \tag{3.35}$$

In the above equations the density and the pressure are defined as $\rho = m_i n_i = m_i n_e$ and $p = p_e + p_i$ respectively. The subscripts e, i denote the electron and ion species, respectively. The fluid velocity is given by \mathbf{v} . ν is the viscosity, η the resistivity and Γ the ratio of specific heats. $\mathbf{J} = \nabla \times \mathbf{B}$ is the current density field. Diamagnetic effects are written in terms of the quantity $\alpha = (\omega_{ci} \tau_A)$ with ion cyclotron frequency ω_{ci} and $\mathbf{v}_i^* = \alpha \frac{\mathbf{B} \times \nabla p_i}{\rho B^2}$ is the ion diamagnetic velocity. Transport is modelled in terms of the parallel and perpendicular diffusion coefficients χ_\parallel , χ_\perp and D_\perp . Via the quantities H and S heat and density sources can be added, respectively. For the exact normalisations of the physical quantities in the XTOR-2F model we refer to Refs. [42, 41].

3.5. Resistive non-linear stability simulations

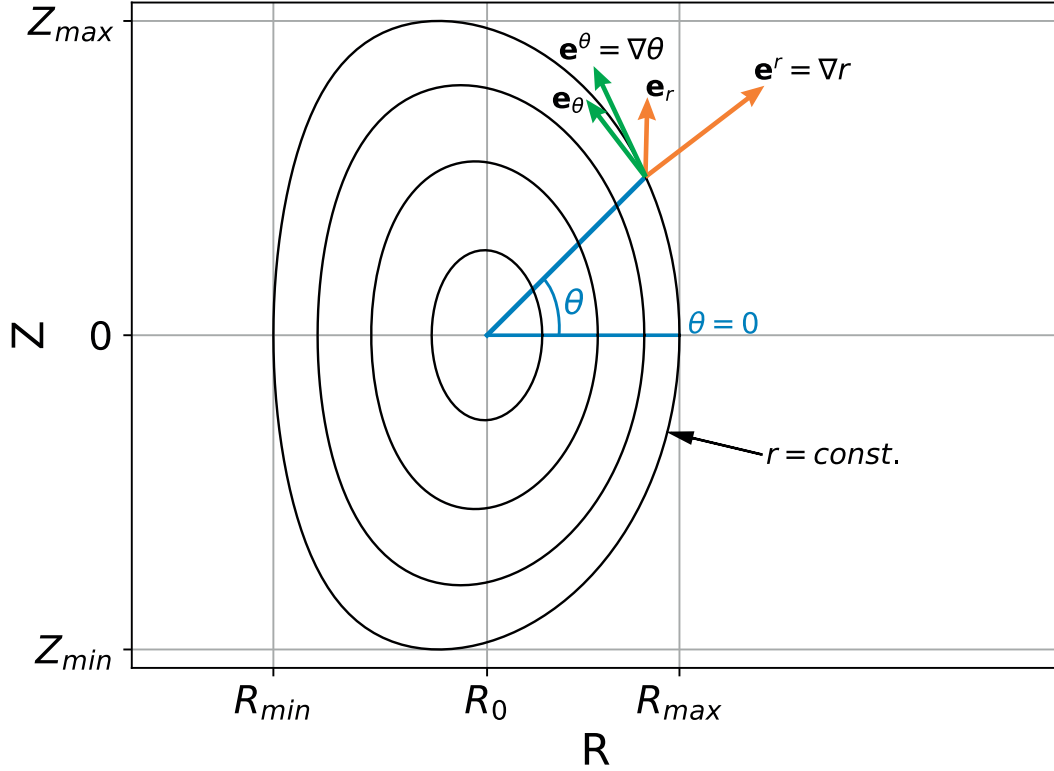


Figure 3.9 – Coordinate system of XTOR-2F in the poloidal plane. For a given point, the covariant and contravariant basis vectors of the coordinates r and θ are shown. Lines of constant r are plotted in black.

XTOR-2F includes the effect of resistivity, which in the model equations enters as a free parameter. This is because the density profile ρ is a free variable that is chosen as input for the simulations. The initial temperature depends on the choice for the density profile like $T_0 = p_0/\rho_0$, where p_0 is the equilibrium pressure provided by CHEASE. The initial resistivity profile in XTOR-2F is set such that $\eta_0(j_{\phi 0} - j_{\phi, bs0}) = E_{\phi 0}$. The toroidal component of the equilibrium electric field $E_{\phi 0}$ is held constant in the plasma and is imposed as a boundary condition. This initial η profile can either be kept constant throughout the temporal evolution of the system, i.e. $\partial_t \eta = 0$, or it can be evolved according to Spitzer's resistivity model Eq. (2.6), where the temperature is a function of time and calculated in each time step. The magnitude of η in XTOR-2F is specified via the Lundquist number $S \propto 1/\eta$ in the core (parameter `snumber`) and a lower limit of S (parameter `slimit`). We note that another recently developed implementation [85] of Ohm's law allows for a splitting of Ohmic and non-inductive current to model plasmas with additional heating more realistically. This model is not used in this thesis and hence not discussed further.

Like its predecessor, the one fluid code XTOR [41], XTOR-2F uses a flux coordinate system (r, θ, ϕ) , with equidistant poloidal θ and toroidal angles ϕ , and the radial variable

$r = \sqrt{\psi/\psi_a}$ is defined in terms of the normalised poloidal flux. The contravariant metric elements are provided by the CHEASE equilibrium and read

$$g^{rr} = \left(\frac{\partial r}{\partial R}\right)^2 + \left(\frac{\partial r}{\partial Z}\right)^2, \quad g^{r\theta} = \frac{\partial r}{\partial R} \frac{\partial \theta}{\partial R} + \frac{\partial r}{\partial Z} \frac{\partial \theta}{\partial Z}, \quad (3.36)$$

$$g^{\theta\theta} = \left(\frac{\partial \theta}{\partial R}\right)^2 + \left(\frac{\partial \theta}{\partial Z}\right)^2, \quad g^{\phi\phi} = \frac{1}{R^2}, \quad (3.37)$$

where R and Z are cylindrical coordinates. More detail about curvilinear coordinates is given in appendix A. An illustration of the XTOR-2F coordinate system is shown in Fig. 3.9. In XTOR-2F, the initial perturbation to the 2D equilibrium can be applied either to the magnetic field or to the velocity field.

3.5.1.2 Numerical method

The set of equations (3.33)-(3.35) can be expressed in the form $\dot{\mathbf{x}} = \mathbf{F}(\mathbf{x})$, where $\mathbf{x} = (v^r, \sqrt{g}v^\theta, v^\phi, B^r, \sqrt{g}B^\theta, B^\phi, p)$ represents all variables of the system. This is then solved by a Newton-Krylov method. In tokamak geometry the MHD equations form a very stiff problem. Furthermore, it is necessary for studies to capture the long time behaviour of the system due to the coexistence of very fast (compressible Alfvén) and very slow (resonant shear Alfvén) modes and the fact that relevant physics are slow compared to the basic time scale (Alfvén time). A fully implicit time advance method is used to tackle this problem. In XTOR-2F, for a finite time step Δt the system evolves according to

$$\mathbf{x}_{n+1} - \mathbf{x}_n = \Delta t F \left[\frac{x_{n+1} + x_n}{2} + \Theta(x_{n+1} - 2x_n + x_{n-1}) \right] \quad (3.38)$$

where n labels the time steps and Θ is a numerical constant. It can be shown that this numerical scheme is linearly unconditionally stable for $\Theta > 0$. At each time step Eq. (3.38) needs to be inverted and solved for \mathbf{x}_{n+1} . It is convenient to rewrite the previous equation in the form

$$G(\Delta_n, \bar{x}) \equiv \Delta_n - \Delta t F \left[\left\{ \frac{1}{2} + \Theta \right\} \Delta_n + \bar{x} \right] = 0, \quad (3.39)$$

where $\Delta_n = x_{n+1} - x_n$ and $\bar{x} = (1 - \Theta)x_n + \Theta x_{n-1}$. The non-linear problem is now solved for Δ_n with a preconditioned Newton-Krylov method:

$$M^{-1}G'(\Delta_n^k, \bar{x}) (\Delta_n^{k+1} - \Delta_n^k) + M^{-1}G(\Delta_n^k, \bar{x}) = 0, \quad (3.40)$$

where M denotes the preconditioner, k labels the Newton iterations and $G'(\Delta_n^k, \bar{x})$ is the MHD operator linearised around \bar{x} . More details about the preconditioner are given in Ref. [42]. It is evident from Eq. (3.40) that in each iteration the Krylov method requires only matrix-vector products. This is exploited to avoid an exact evaluation and inversion of the Jacobian matrix G' by expressing the product $G'(\Delta_n^{k+1} - \Delta_n^k)$ as a finite difference. This so-called 'matrix-free' method [86] replaces the matrix G' in the first term in Eq. (3.40) with an evaluation of G . In the first versions of the XTOR-2F

3.5. Resistive non-linear stability simulations

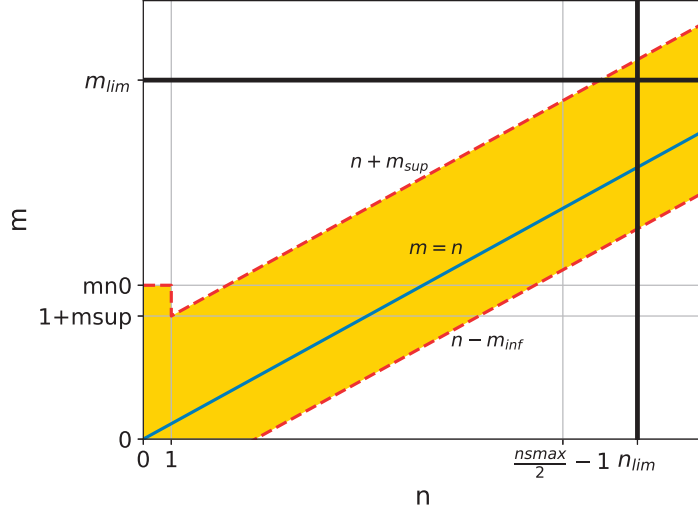


Figure 3.10 – Domain of poloidal and toroidal Fourier modes in XTOR-2F. Physical modes lie inside the yellow shaded band limited by aliasing constraints indicated by the black lines.

code the Newton-Krylov solver is provided by the NITSOL library [87], while the newer, parallelised versions of the code use PETSC [88, 89]. For the calculations of coupled infernal modes and NTMs presented below, the results were obtained with a version based on NITSOL.

The implementation of MPI as well as OpenMP parallelisation [90] reduces the real time required for simulations particularly of complex plasma configurations. Another recent version of the code considers the presence of a vacuum region around the plasma with a conducting or resistive wall [91]. Effects due to the vacuum are not important for the study of internal modes and hence we employ the fixed boundary version of XTOR-2F.

The discretised grid has \mathbf{lmax} radial points - each corresponding to one equilibrium flux surface - and consists of \mathbf{mmax} equally spaced points in the poloidal angle and \mathbf{nmax} points in the toroidal angle. The combinations of toroidal and poloidal modes taken into account in a simulation lie in a band around the $m = n$ line with a width determined by the values \mathbf{minf} and \mathbf{msup} as sketched in Fig. 3.10. An exception is the $n = 0$ mode, which has $\mathbf{mn0}$ poloidal harmonics. Toroidal mode numbers span the range $0 \leq n \leq \mathbf{nsmax}/2 - 1$, where \mathbf{nsmax} is an integer and determines the highest n considered. Aliasing criteria set constraints for the highest possible mode number for a given grid size as indicated by the black lines in Fig. 3.10. Physical modes satisfy the conditions

$$\mathbf{nsmax} < \frac{2}{3}\mathbf{nmax} \quad , \quad \frac{\mathbf{nsmax}}{2} - 1 + \mathbf{msup} < \frac{2}{3} \left(\frac{\mathbf{mmax}}{2} - 1 \right) \quad , \quad (3.41)$$

and for the poloidal $n = 0$ modes

$$\mathbf{mn0} < \frac{2}{3} \left(\frac{\mathbf{mmax}}{2} - 1 \right) \quad . \quad (3.42)$$

At the largest toroidal mode number this allows us to resolve MHD modes up to a rational value of $q = 1 + \text{msup}/(\text{nsmx}/2 - 1)$. In the simulations carried out later, $\text{nsmx} = 4$ in order to include only $n = 0, 1$ modes. The memory required for a simulation scales like $\text{lmax} * \text{nmax} * \text{mmax}^2$.

3.5.2 Physical model & Equilibrium

For convenience in the following we make use of the normalised time $\hat{t} = t/\tau_A$. The radial variable used in the remainder of this chapter is defined as $\rho = \sqrt{\Phi/\Phi_a}$, where Φ is the toroidal flux and the subscript 'a' indicates that the quantity is evaluated at the plasma boundary. x' describes a derivative of x with respect to ρ . The magnetic island width w is a dimensionless relation to coordinate ρ , i.e. $w = 1$ would correspond to the width of an island extending from the magnetic axis to the plasma boundary.

The physical model used in XTOR-2F [42] was introduced in Section 3.5.1. Since the main extended MHD effect of interest is that of the bootstrap current, the general model Eq. (3.33) providing the time evolution of the velocity field \mathbf{v} , magnetic field \mathbf{B} , pressure field p and density field ϱ , used by XTOR-2F is simplified to

$$\begin{aligned}
 \varrho [\partial_t \mathbf{v} + (\mathbf{v} \cdot \nabla) \mathbf{v}] &= \mathbf{J} \times \mathbf{B} - \nabla p + (\nabla \nu \nabla) \mathbf{v}, \\
 \partial_t \mathbf{B} &= \nabla \times (\mathbf{v} \times \mathbf{B}) - \nabla \times \eta (\mathbf{J} - \mathbf{J}_{\text{bs}}), \\
 \partial_t p &= -\Gamma p \nabla \cdot \mathbf{v} - \mathbf{v} \cdot \nabla p + \nabla \cdot \chi_{\perp} \nabla p \\
 &\quad + \nabla \cdot \left[\mathbf{B} \left(\frac{\chi_{\parallel}}{B^2} (\mathbf{B} \cdot \nabla) p \right) \right], \\
 \partial_t \varrho &= -\varrho \nabla \cdot \mathbf{v} - \mathbf{v} \cdot \nabla \varrho + \nabla \cdot D_{\perp} \nabla \varrho.
 \end{aligned} \tag{3.43}$$

We choose for the bootstrap current density \mathbf{J}_{bs} to be calculated according to the Sauter model [25, 26] given by Eq. (2.8). Resistivity is allowed to vary over the radial extension of the plasma, but is kept constant in time. The resistivity profile is chosen in a way that the equilibrium toroidal electric field is kept constant over the radius [42]. χ_{\perp} and χ_{\parallel} are the perpendicular respectively the parallel heat transport coefficients and D_{\perp} the perpendicular diffusion coefficient.

For simulating MAST-like plasmas we set the major radius at the magnetic axis to $R_0 = 0.796$ m and the elongation to $\kappa = 1.60015$. The minor radius of the plasma boundary is defined as $a := (R_{\text{max}} - R_{\text{min}})/2 = 0.466$ m, where R_{max} and R_{min} denote the maximum and minimum radial position of the plasma. The resonant $q = 2/1$ surface is located at the normalised radius $\rho_s = 0.72$. The equilibrium profiles are shown in Fig. 3.11a. The q profile is flat from the magnetic axis up to $\rho \approx 0.45$. We refer to this region as low shear region. For $\rho \geq 0.45$ finite and considerably large shear is present (high shear region). We stress the fact that Eq. (3.20) cannot be used to express the q profile over the whole range. Nevertheless, in the region around ρ_s the q profile can be approximated by $1/\iota$ with ι given by Eq. (3.20). The value of λ lies between 6.3 and 7 and is set to 6.7 for the following calculations. Finally, in the XTOR-2F simulations to come, the island width is defined as the radial extension of the magnetic island, i.e. the difference between the outer and inner radial position of the island separatrix. For the

3.5. Resistive non-linear stability simulations

cases considered in this paper, stochasticity associated with large islands is weak, so the island width is fairly easy to identify.

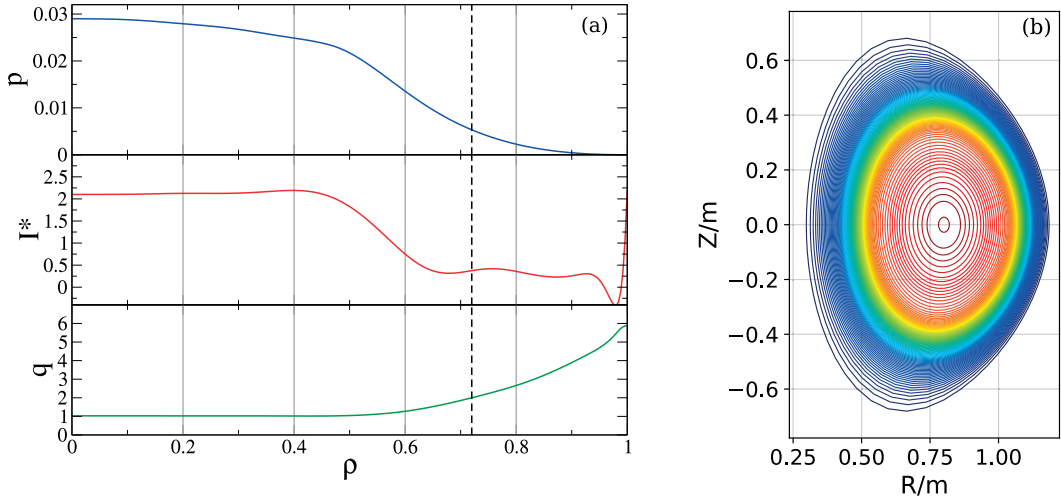


Figure 3.11 – A MAST-like configuration which is susceptible to infernal modes. (a) Equilibrium profiles are plotted over the radial position $\rho = \sqrt{\Phi/\Phi_a}$. The dashed line indicates the position of the resonant $q = 2/1$ surface. p is presented in CHEASE units [30]. I^* is proportional to the surface averaged current density and is also given in CHEASE units [30]. (b) Lines of constant pressure indicating the shape and location of the flux surfaces.

The numerical simulations are carried out with the equilibrium code CHEASE [30] which is interfaced with the initial value code XTOR-2F [42], used for the stability calculation. The CHEASE equilibrium (profiles and magnetic topology) constitutes the initial conditions for the stability computations and is shown in Fig. 3.11. First, simulations are performed with the exact profiles shown in Fig. 3.11a. Further simulations with varied pressure and current profiles enable the investigation of the effect that β_p and δq have on the growth of the sideband magnetic island. In all the XTOR-2F simulations resistivity is included, while ion and electron diamagnetic effects are switched off. We set $n_{\text{smax}} = 4$ in XTOR, such that only $n = 0, 1$ modes are retained. Poloidal modes up to $m = 13$ for $n = 1$ are considered in the simulations. For $n = 0$ the maximum poloidal mode number is chosen for each equilibrium configuration individually such that convergence is achieved. The largest poloidal mode considered m_{sup} , lies in the range $12 \leq m_{\text{sup}} \leq 24$ for each simulation. The discretisation grid consists of 201 points in radial direction, 24 points in toroidal direction and in poloidal direction of 96 points when $m_{\text{sup}} \geq 20$ and 64 points in simulations where $m_{\text{sup}} < 20$. The Lundquist number is set to $S = 10^6$ on the magnetic axis. This value is lower than the typical values for present day tokamaks (ranging from $S = 10^8 - 10^9$), but larger values in the simulation can lead to unnecessary convergence problems. Equilibrium toroidal rotation is neglected in the simulations. The resistivity is allowed to vary over the radial extension of the plasma, unlike in the analytical model, where resistivity matters only in the resonant region, where it can be

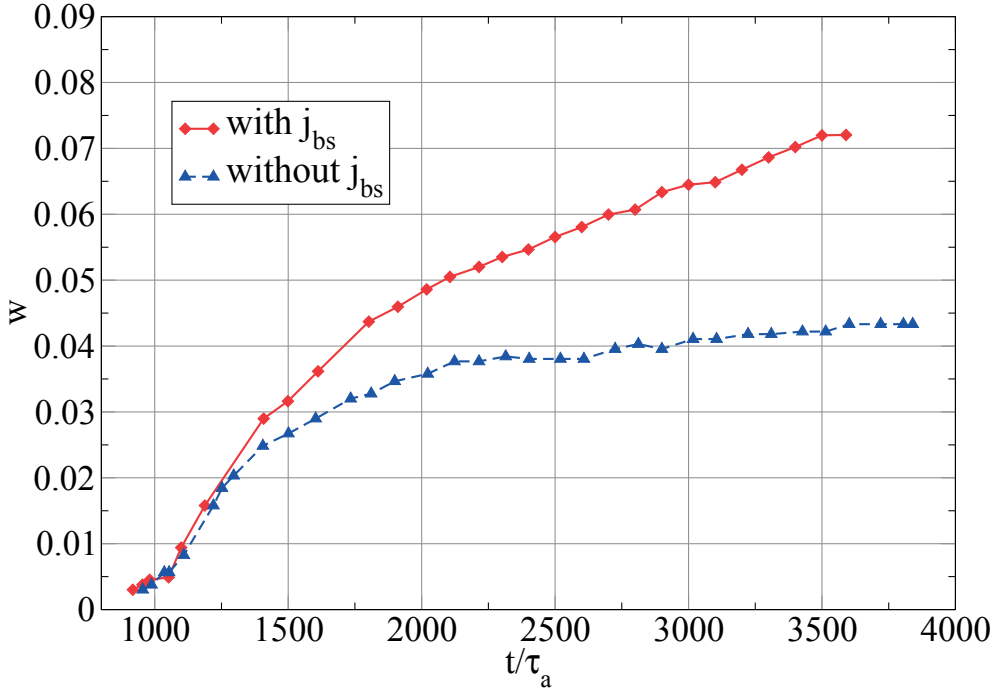


Figure 3.12 – Island width with and without bootstrap current as computed in the XTOR-2F simulations with $\beta_N = 1.17$ and $q_{min} = 1.019$. When bootstrap current is included, the island grows to a larger size.

considered constant. With the resistivity model adopted by XTOR-2F, the value of the Lundquist number on the resonant surface is $S = 1.10711 \times 10^6$. The value for the normalised viscosity is $\nu = 5 \times 10^{-6}$.

3.5.3 Evolution of coupled modes in a MAST-like plasma

First, simulations with the above equilibrium profiles are performed with $q_{min} = 1.019$. The poloidal beta for this equilibrium is $\beta_p = 0.2243$ for which $\beta_N = 1.17$. In XTOR-2F, only $n = 0, 1$ modes are retained to isolate the relevant physics (coupling of $n = 1$ poloidal harmonics) and to avoid $n > 1$ island chains that would overlap with the relevant 2/1 magnetic islands. In the simulations, growing $n = 1, m = 2$ islands are observed, both in the cases with and without bootstrap current. For the evaluation of the size of magnetic islands from Poincaré plots, a tool has been developed as described in appendix C.1. The island evolution can be seen in Fig. 3.12. During the linear phase which ends at $t \approx 1200 \tau_A$ the growth of the magnetic island is exponential and comparable in both cases. The large growth rate occurs due to coupling to the infernal mode as will be explored in more detail in section 3.6. For $t > 1200 \tau_A$, during the early non-linear stage, the mode growth is stronger and maintained for a longer time in the case where the bootstrap current is included. The effect of bootstrap current is seen in the non-linear phase as expected, since Δ'_{bs} becomes important there and has a strong destabilising effect for larger island width. Fig. 3.13 shows Poincaré plots of the poloidal cross section

3.5. Resistive non-linear stability simulations

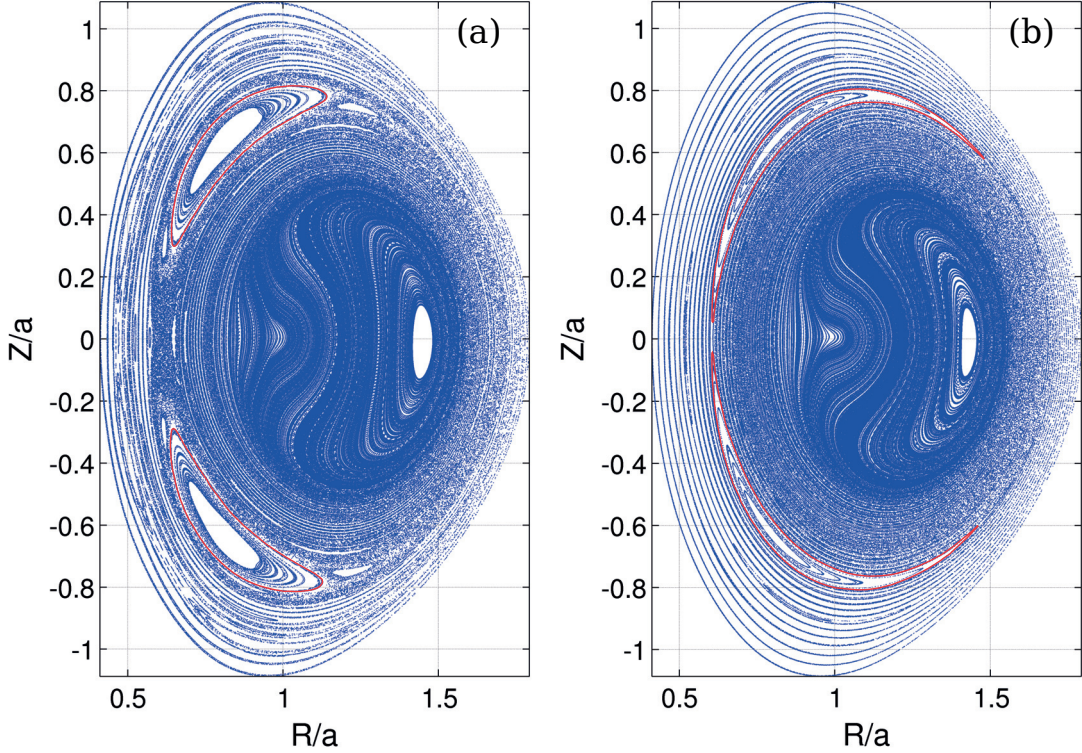


Figure 3.13 – Poincaré plot at $\varphi = 0$ at time $t = 2480 \tau_A$ in simulations with equilibrium profiles as in Fig. 3.11a with $\beta_N = 1.66$ and $q_{min} = 1.022$. The magnetic 2/1 island is clearly visible. (a) with inclusion of bootstrap current. (b) without inclusion of bootstrap current.

at toroidal angle $\phi = 0$ at $t \approx 2480 \tau_A$, when the 2/1 island reaches a significant size in both simulations. The main 1/1 mode can also be seen, shifting the magnetic axis outward and giving the flux surfaces in the core a bean-like shape. We note that in both cases the amplitude of the 1/1 mode appears to be quite similar. In contrast, the difference is the size of the 2/1 islands for the cases with and without bootstrap current is seen to be considerable (Fig. 3.13a and b).

The typical evolution of the kinetic energy of an $n = 1$ infernal mode is shown in Fig. 3.14. The energy grows linearly until $t \approx 1200 \tau_A$ and then enters the non-linear stage, characterised by an oscillating behaviour. The poloidal spectrum is well converged. The kinetic energy is related to the linear growth rate by $\gamma = -i\omega = 1/2 \ln(E_K)/dt$, where E_k is the kinetic energy of the mode and is linked to the fluid displacement ξ by $E_{kin} = 1/2 m (\partial\xi/\partial t)^2$. This therefore allows the estimation of the mode amplitude during the linear phase. In both cases, the amplitude of the oscillations reduces during the non-linear phase. However, the infernal mode saturation is seen more easily via the magnetic energy which is shown in Fig. 3.15. The main 1/1 harmonic saturates at $t \approx 1200 \tau_A$ no matter if bootstrap current effects are considered or not.

The saturated state in the case without bootstrap current effects is illustrated by the Poincaré plot Fig. 3.16. The infernal mode is located at $r \approx 0.4$, and several $n = 1$

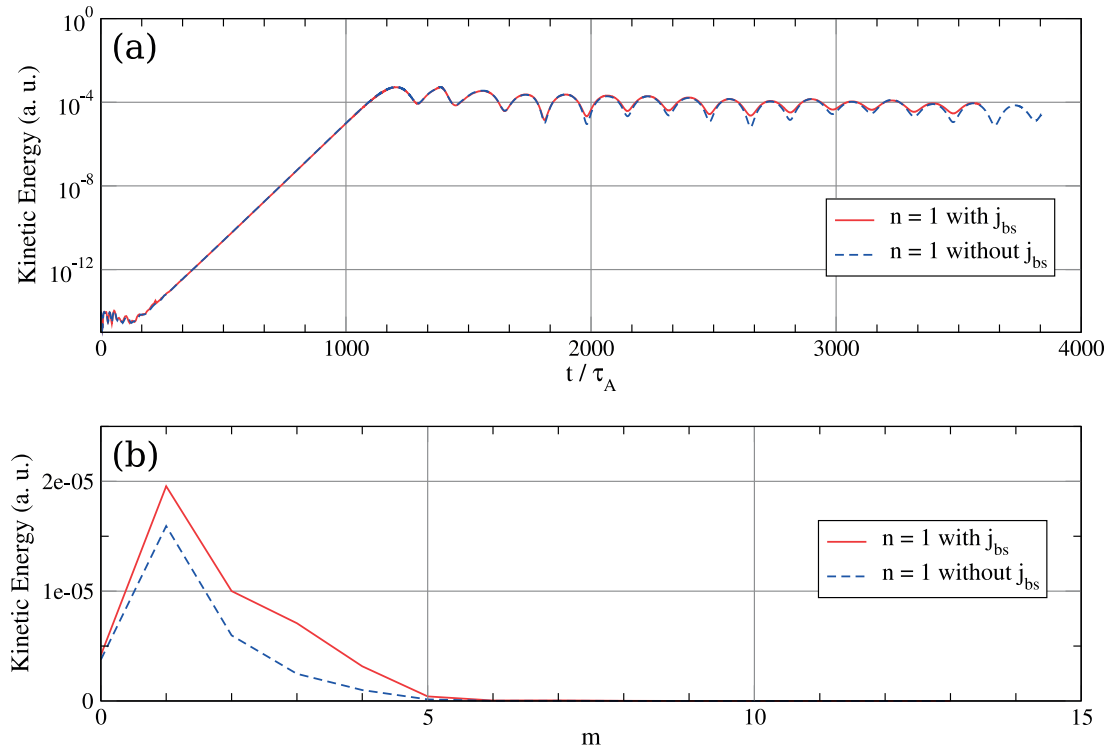


Figure 3.14 – Comparison of the kinetic energy of the $n = 1$ mode in the simulations with and without inclusion of bootstrap current and using the equilibrium profiles seen in Fig. 3.11a with $\beta_N = 1.17$ and $q_{min} = 1.019$. (a) shows the kinetic energy on a logarithmic scale. The m spectrum of the $n = 1$ mode is shown in (b) for $t = 2000 \tau_A$.

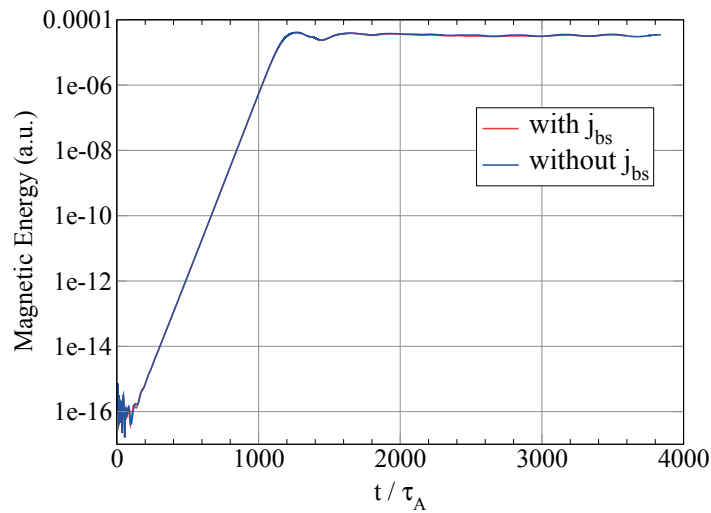


Figure 3.15 – Magnetic energy of the 1/1 mode in the two cases with and without inclusion of bootstrap current effects as result of XTOR-2F simulations. The equilibrium profiles of Fig. 3.11a are used with $\beta_N = 1.17$ and $q_{min} = 1.019$ in a MAST-like configuration.

3.5. Resistive non-linear stability simulations

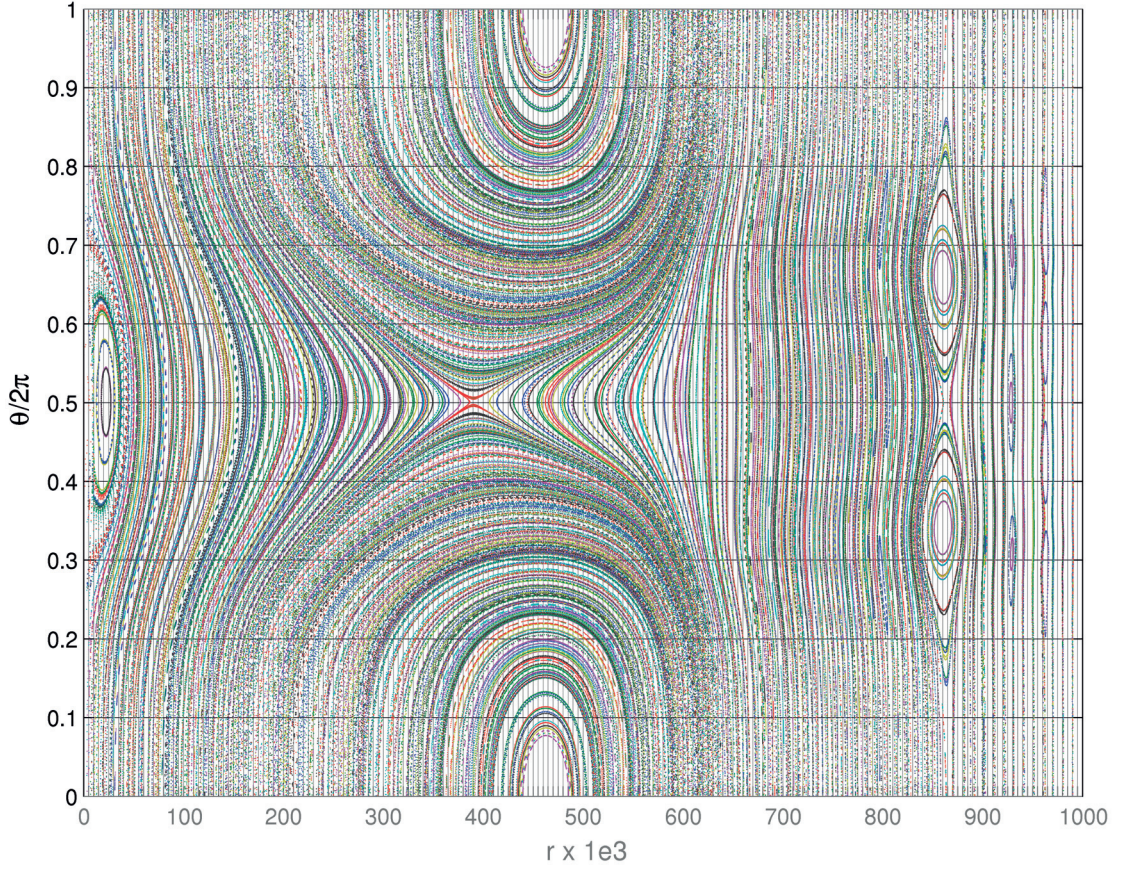


Figure 3.16 – Poincaré plot showing the magnetic topology in the $r - \theta$ plane of the saturated state in the XTOR-2F simulation without bootstrap current effects. The saturated infernal mode in the plasma core and multiple island chains can be identified.

island chains with poloidal mode number $m = 2, 3, 4$ are distributed in the outer part of the plasma, where the q profile takes rational values. For the case with inclusion of bootstrap current effects the picture is similar, but the magnetic island chains have a larger width.

From the dispersion relation Eq. (3.18) it can be seen that the growth rate of infernal modes depends on $\beta_p = 2\mu_0 p / B_p^2$. In order to examine the influence of β_p on the growth of the 2/1 NTM, the pressure profile is scaled by multiplying $p(\rho)$ with a constant parameter c over the range $0.2 \leq c \leq 1$, while the shape of the profile is maintained. The q profile has an extended region of low shear and the value of q on the magnetic axis is set to $q_0 = 1.03$ when varying β_N . This is the same q_0 as in the case considered in Figs. 3.12 - 3.15, and in those figures $\beta_N = 1.17$ was chosen. In each case q_{min} is close to 1.019 but varies very slightly with varying β_N . Including only $n = 0, 1$ modes to isolate the relevant physics, these simulations are done for cases with and without bootstrap current and the result is shown in Fig. 3.17. With the effect of bootstrap current, and its dependence on pressure, the island width is seen to scale non-linearly on the pressure. In Fig. 3.17 the island width w is plotted with respect to $\beta_N = \langle \beta \rangle a B_T / I_p$.

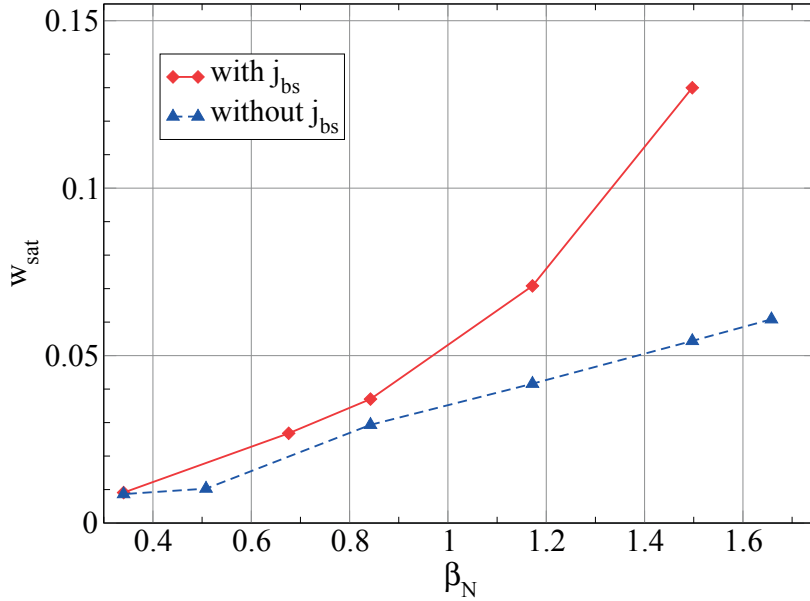


Figure 3.17 – Saturated magnetic island width w_{sat} versus normalised beta β_N as obtained from XTOR-2F simulations with and without inclusion of bootstrap current. The equilibrium profiles of Fig. 3.11a are used. The different values of β_N are obtained by scaling the pressure profile and keeping all other equilibrium quantities unchanged.

3.6 Comparison of the Model with the XTOR-2F Simulations

Saturation in the width of the island can be estimated by parameterising $dw/d\hat{t} = \tau_A dw/dt$ with the width w . The relation between island growth and width is shown in Fig. 3.18 for both the analytical results and XTOR-2F, with and without bootstrap current effects. This case has $\beta_N = 1.17$ and $q_{min} = 1.019$ and corresponds to the case with third largest β_N (bootstrap free) respectively second largest β_N (with bootstrap current) in Fig. 3.17. The value for w_I for both cases is chosen to be 0.015, based on the XTOR-2F simulations which indicate infernal mode saturation at this island width. In the XTOR-2F simulation without inclusion of bootstrap current, magnetic island saturation is achieved at a width around $w_{sat} = 0.045$. In the case with bootstrap current the island grows only very slowly at the end of the simulation at $t = 4590\tau_A$, as indicated by the small value of $dw/d\hat{t}$ in Fig. 3.18. For the analytic modelling of the case with no bootstrap current, the island reaches saturation at a width of $w_{sat} = 0.070$. This is slightly larger than in the numerical simulation. The saturated island widths are evaluated at the point in time where $dw/d\hat{t} = 0$, i.e. where $\Delta'_{total} = 0$.

For small island width the values of $dw/d\hat{t}$ obtained in the numerical simulations for the case of no bootstrap current agree well with the analytical prediction from the Rutherford equation. In the case with bootstrap current effects, the term Δ'_{bs} contains a small width correction (associated with finite w_d), which may not be accurate in the limit

3.6. Comparison of the Model with the XTOR-2F Simulations

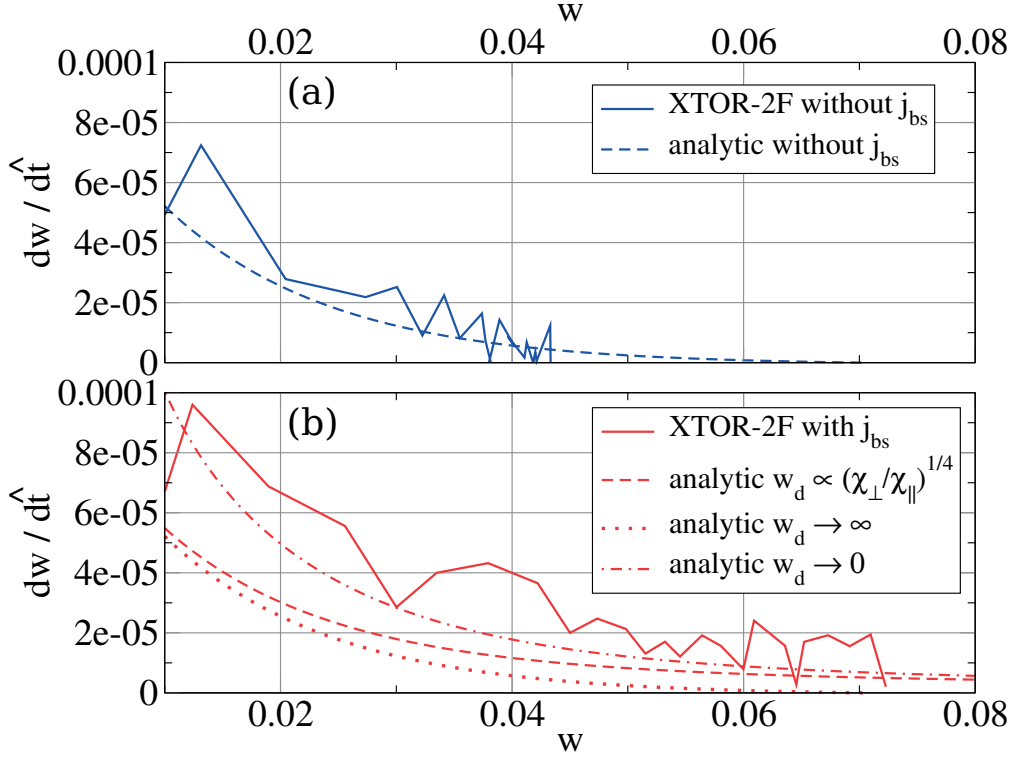


Figure 3.18 – Island growth $dw/d\hat{t} = \tau_A dw/dt$ is shown with respect to island width w for XTOR-2F simulations and the analytical prediction for (a) cases without and (b) with bootstrap current. For this calculation $q_{min} = 1.019$, $\beta_N = 1.17$ and $S = 10^6$ have been chosen in the MAST-like equilibrium described above. For the case with bootstrap current several curves are shown, reflecting various limits of the finite width correction w_d .

of tight aspect ratio. Therefore, Fig. 3.18 shows the analytical island growth calculated with the Rutherford equation for various choices of w_d . When w_d is calculated with the analytic formula $w_d \propto (\chi_{\perp}/\chi_{\parallel})^{1/4}$, and $\chi_{\perp}/\chi_{\parallel}$ employed values used in the XTOR-2F simulations (dashed graph), $dw/d\hat{t}$ is lower than in the numerical simulations. In the limit of infinite parallel conductivity ($\chi_{\perp}/\chi_{\parallel} \rightarrow 0$ or $w_d = 0$), the island growth $dw/d\hat{t}$ is then comparable to the numerical result. In the opposite limit $w_d \rightarrow \infty$ the bootstrap current contribution reduces to zero and the situation is identical to the one shown in Fig. 3.18 (a). It can be seen in Fig. 3.18 that for large (nearly saturated widths), the agreement between the XTOR-2F simulation with bootstrap current and the Rutherford equation becomes better. The strong influence of w_d on island growth at smaller island width is due to the effects of parallel heat conductivity, which plays a negligible role as w increases. As a consequence the value of w_d is of little importance when looking at island growth at large width. Both, the numerical and analytical methods predict that the magnetic island maintains growth longer times and to larger width when compared to the case without inclusion of bootstrap current. It is therefore clear that effects from

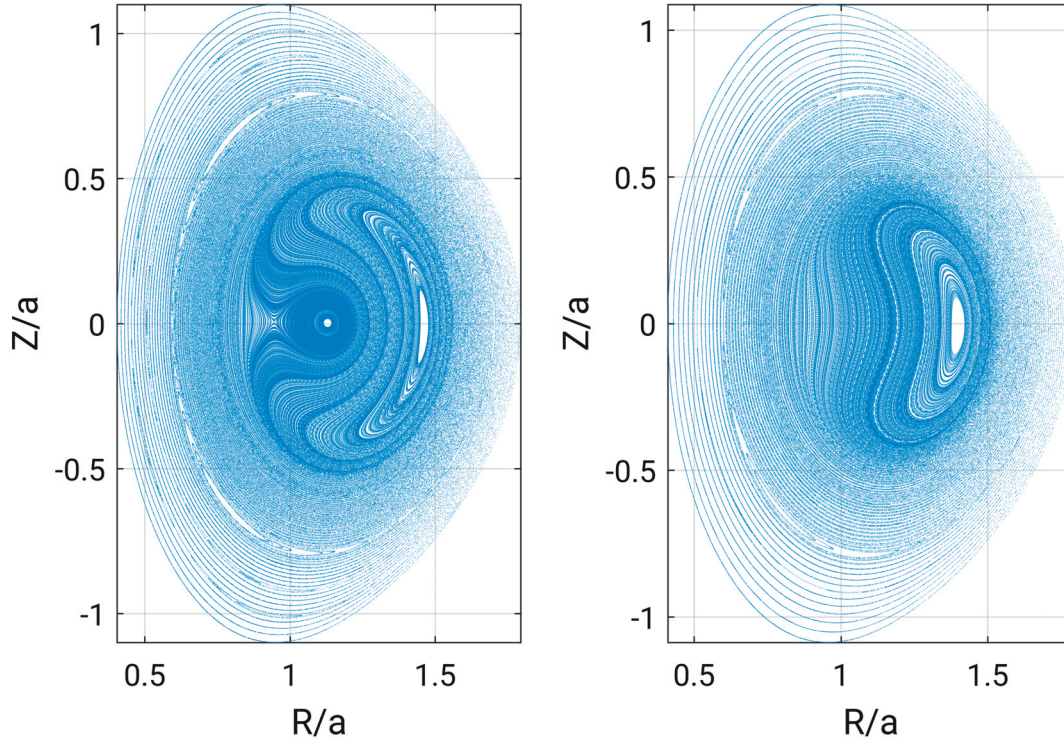


Figure 3.19 – Poincaré plot of the saturated infernal mode and 2/1 magnetic islands at $\phi = 0$ for a case with strong (left) and small (right) seed from the infernal mode.

the bootstrap current can drive a magnetic island to a larger width, compared to a case when its effect is neglected. However, it should be pointed out that, as seen in Fig. 3.18, the XTOR-2F simulation with finite bootstrap current may not have quite saturated for $w > 0.075$. The analytical island growth is calculated using Eq. (3.22). In order to compare bootstrap-free XTOR-2F simulations to the analytical model, the term Δ'_{bs} in Eq. (3.22) is set to zero. For both cases the numerical and analytical results agree reasonably. The apparent large seed island effect, where $dw/d\hat{t}$ is large for small w is observed in both the analytic results and XTOR-2F. As mentioned earlier, differences between saturated values in w are likely to be due to the approximations that have been made for the non-linear corrections in the derivation of Eq. (3.22). In so far as the infernal and classical contributions, these assumptions and approximations are most accurate in the early non-linear phase, which continues the linear analytical model for resistive infernal modes. More refined non-linear modelling is reserved for future publications.

It was argued in section 3.4.2 that infernal mode coupling can provide a seed for an NTM, and that in the non-linear phase the coupling vanishes. The modes are then decoupled and can evolve independently. If this is the case, the strength of the seed should not have a strong effect on the saturated magnetic island width in the XTOR-2F simulations. This means that small infernal modes, which saturate at small amplitudes, should trigger NTMs that saturate at comparable magnetic island widths as those that were seeded by a strong infernal mode. To verify this, we compare the saturated states

3.7. Conclusions

of two plasmas with $\beta_N = 1.17$, but different values of δq . For the case with strong seed we choose $\delta q = 0.019$, and the case with small seed has $\delta q = 0.031$. It can be seen in Fig. 3.19, that the amplitude of the saturated infernal mode differs considerably in the two cases while the width of the 2/1 magnetic islands are comparable in size, thus indicating that the modes are indeed decoupled in the non-linear regime.

3.7 Conclusions

In this chapter analytical and numerical studies in the frame of resistive MHD with inclusion of bootstrap current have been presented. In particular we investigated the triggering of fast growing MHD modes by infernal modes in low-shear plasmas. Analytical and numerical results for cases with and without bootstrap current have been compared and reasonable agreement has been found.

Standard NTM analysis [72] is not applicable when islands are coupled to infernal modes. In this work a derivation of the infernal mode coupling contribution to the modified Rutherford equation has been presented. To obtain the linear contribution to Δ' , which describes the seed that can trigger the creation of an NTM, the external eigenfunctions have been evaluated in the limit of vanishing island width. The resulting destabilising effect is much stronger than that of standard contributions to tearing modes, suggesting that coupling provides the dominant destabilising effect in the early evolution of the island. A non-linear extension which evaluates Δ' at finite width has been provided in order to generalise the equation governing island growth. This non-linear extension includes a model which ensures that coupling to the infernal mode diminishes as the main harmonic of the infernal mode saturates in amplitude. The characteristic width of the island when this occurs is identified from XTOR-2F numerical simulations.

The linear and non-linear analytical model has been applied to a MAST-like equilibrium with low-shear core. In such a plasma, where infernal modes are present, the modified Rutherford equation used in standard (neoclassical) tearing theory predicts stability, even when the destabilising contribution of bootstrap current is included. With the new contribution $\Delta'_0(\gamma, w)$ in the modified Rutherford equation, the island initially grows very fast. This highly destabilising effect of coupling can explain the triggering of magnetic islands in numerical simulations and the experimentally observed fast growing modes.

Numerical simulation results obtained with the XTOR-2F code in the same equilibrium, show the existence of a fast growing 2/1 island. When bootstrap current is considered, the island grows to a larger width than in the case without bootstrap current. By virtue of the bootstrap effect the numerical simulations show how the width of the infernal mode seeded tearing modes increase non-linearly with the plasma pressure. A comparison with the analytical model shows reasonable agreement for the island growth for cases with and without bootstrap current.

An investigation of $n = 2$ modes, focusing on 2/2 infernal modes driving 3/2 NTMs, is reserved for future work. This involves a modification of the q profile such that classical $n = 2$ tearing modes are stable. It is also required that the rational surfaces of the most unstable modes (presumably having poloidal mode numbers $m = 1, 2, 3, 4$) are sufficiently

separated and thus island chains do not overlap.

Non-linear saturated current-driven external kink modes modelled with 3D free-boundary equilibria

In this chapter we present a study of current-driven non-linear saturated external kink modes by means of free-boundary 3D equilibrium simulations. It is shown that free-boundary 3D equilibrium calculations in tokamak geometry are capable of capturing the physics of non-linearly saturated external kink modes for monotonic current and q profiles typical of standard (baseline) plasma scenarios [92]. The VMEC ideal MHD equilibrium model exhibits strong flux surface corrugations of the plasma vacuum boundary, driven by the core current profile. A method is presented which conveniently extracts the amplitude of the corrugation in terms of Fourier components in straight field line coordinates. The Fourier spectrum, and condition for non-linear corrugation agrees well with linear simulations, and the saturated amplitude agrees well with non-linear analytic calculations. This chapter is based on an extension of the work that has been published in the journal article [A. Kleiner et al., *Free boundary 3D ideal MHD equilibrium calculations for non-linearly saturated current driven external kink modes in tokamaks*, Nuclear Fusion **58**, 074001 (2018)].

4.1 Introduction

External kink modes are known [22, 93] to be of concern for the development of plasma scenarios. They set operational limits and define inaccessible windows for the edge safety factor and the peaking of the current profile. External kink modes tend to be linearly unstable for large current gradients, especially when these gradients are close to the plasma edge and where the edge safety factor is just below a rational value (especially assuming external kink has $n = 1$). After an initial linear growth in the non-linear phase, a mode usually saturates (non-linear stability) [94, 95], though in practice, the corrugation can be so large as to touch the vacuum vessel or plasma-facing components, thus causing disruptions [22].

The investigation of non-linear instabilities is typically carried out [32] with initial value codes (e.g. XTOR-2F [42]). Such simulations are computationally expensive due to the resolution and number of time steps necessary and require a certain level of parallelisation [90]. Since a saturated state without equilibrium flows is characterised by being time-independent, an equilibrium code can in theory obtain a saturated state, satisfying the force balance equation $\mathbf{j} \times \mathbf{B} - \nabla p = 0$. Indeed, this was already shown for

non-resonant internal kink modes with $q > 1$, where initial value (XTOR-2F) saturated states and VMEC fixed-boundary calculations showed similar $m = n = 1$ displacement amplitudes [32].

The goal of this chapter is to investigate the degree to which 3D free-boundary equilibrium codes can model conventional external kink modes, driven by current gradients associated with standard tokamak operation (baseline scenario) with monotonic (standard [Wesson-like [93]]) q profiles. The work differs from recent [45, 46, 47] deployment of VMEC for modelling edge harmonic oscillations in plasmas with low magnetic shear at the edge. Those oscillations are driven predominantly by pressure gradients, rather than current gradients. The 3D converged equilibria in this manuscript will be compared with the spectral properties of linear numerical stability analysis, and further verified by analytic non-linear calculations [95]. Lack of a converged equilibrium will be taken to mean that an unstable external kink mode forms, but non-linear saturation has not been achieved. The advantages of the equilibrium approach to external kink mode problems are numerous. First, the computations are fast and accurate, and second they provide convenient Fourier decomposed magnetic geometry for advanced studies such as fast particle [96] and impurity transport [97] in non-axisymmetric plasmas. Such studies require long and highly accurate particle simulations. To obtain the required accuracy, the VENUS-LEVIS guiding centre code [98] for example exploits the Fourier decomposition of the magnetic field for orbit calculations.

After discussing the linear and non-linear treatment of external kink modes in Section 4.2, we present in section 4.3 ideal MHD free-boundary computations of JET-like plasmas carried out with the VMEC code [34]. First, the characteristics of the observed three-dimensional equilibria and the choice of the coordinate system for mode spectrum analysis are discussed. This is followed by the VMEC calculation of the non-linear saturated displacement amplitude for varying edge q value, and two choices of current density profiles. The spectral properties of VMEC are compared with those of the linear code KINX in section 4.4. Then in section 4.5, the VMEC results are compared with the helical external kink amplitude calculated from an analytical model based on a non-linear large aspect ratio expansion.

4.2 Linear and non-linear external kink modes

This section provides an overview of external kink modes and their physical background. External kink modes move the plasma boundary and are driven by current gradients. The linear stability of these modes sets an operational limit on various plasma parameters. However, the non-linear behaviour of a linearly unstable mode is important, since it determines whether the perturbation saturates or grows further.

4.2.1 Linear theory of external kink modes

The NTMs and infernal modes studied in the previous chapter are both internal modes and as such do not necessarily affect the position of the plasma-vacuum boundary. On the contrary, external kink modes have a finite displacement at the edge, i.e. $[\mathbf{n} \cdot \boldsymbol{\xi}_{\perp}]_{r=a}$.

4.2. Linear and non-linear external kink modes

For these modes the resonant surface can be seen to lie in the vacuum region and hence external kinks are unstable when the edge safety factor lies below a rational value. The existence of external kink modes is predicted by the ideal MHD model when including the vacuum region [22, 93]. The linear growth rate ω and displacement ξ can be derived from the energy principle for a standard tokamak (large aspect ratio, circular cross section and $\beta \sim \varepsilon^2$). The total energy change δW is given by the sum of a change of plasma energy due to a displacement ξ given by Eq. (2.50) (including the boundary term) and vacuum energy

$$\delta W_V = \frac{1}{2} \int_V d^3x |\mathbf{B}_1|^2, \quad (4.1)$$

where the integral is performed over the vacuum region extending from the plasma boundary at $r = a$ to a perfectly conducting wall at $r = b$. Due to the absence of plasma in the vacuum region, the displacement vanishes here. Because the parallel component of the perturbed field $\delta B_{\parallel} \approx \delta B_{\phi}$, vanishes in the vacuum, $\delta B^2 \approx \delta B_r^2 + \delta B_{\theta}^2$. These components of the magnetic field can be expressed in terms of a flux function as $\delta B_r = -(1/r)\partial\psi/\partial\theta = -im\psi/r$ and $\delta B_{\theta} = \partial\psi/\partial r$. Inserting this into the condition $\nabla \cdot \delta \mathbf{B} = 0$ leads to a Laplace equation for ψ ($\delta \mathbf{B} = -\nabla\psi$)

$$\frac{1}{r} \frac{d}{dr} \left(r \frac{d\psi}{dr} \right) - \frac{m^2}{r^2} \psi = 0, \quad (4.2)$$

with solutions of the form $\psi = \alpha r^m + \beta r^{-m}$. The two constants α and β can be determined from the boundary conditions. At the conducting wall the radial component of the perturbed magnetic field vanishes $\delta B_r = 0$ i.e. at $r = b$ it follows that $\psi(r = b) = \text{const.}$. The perturbed radial magnetic field is continuous across the plasma-vacuum interface and thus for the boundary condition at $r = a$ we get $\psi(r = a) = B_{\theta a} \left(\frac{nq_a}{m} - 1 \right) \xi_a$. One then obtains

$$\psi = B_{\theta a} \left(\frac{nq_a}{m} - 1 \right) \frac{\left(\frac{r}{b} \right)^m - \left(\frac{b}{r} \right)^m}{\left(\frac{a}{b} \right)^m - \left(\frac{b}{a} \right)^m} \xi_a. \quad (4.3)$$

Expressing δB in terms of ψ and inserting Eq. (4.3) into Eq. (4.1) the total potential energy reads

$$\begin{aligned} \delta W = \frac{\pi^2 B_{\phi}^2}{\mu_0 R} \left\{ \int_0^a \left[\left(r \frac{d\xi}{dr} \right)^2 + (m^2 - 1)\xi^2 \right] \left(\frac{n}{m} - \frac{1}{q} \right)^2 r dr \right. \\ \left. + \left[\frac{2}{q_a} \left(\frac{n}{m} - \frac{1}{q_a} \right) + (1 + m\lambda) \left(\frac{n}{m} - \frac{1}{q_a} \right)^2 \right] a^2 \xi_a^2 \right\}, \end{aligned} \quad (4.4)$$

with $\lambda = \frac{1+(a/b)^{2m}}{1-(a/b)^{2m}}$. The first term is always positive and describes the stabilising effect of magnetic field line bending inside the plasma. The second term is strongly destabilising when $q_a < m/n$. However, a plasma below such a rational value can still be stable if the contribution of field line bending is strong enough. The displacement ξ can be obtained from a solution of the Euler-Lagrange equation (2.51) and substituted back into Eq. (4.4). The sign of the potential energy in Eq. (4.4) determines whether the system is linearly stable or unstable according to the energy principle (c.f. section 2.4.2). Note that the

Chapter 4. Non-linear saturated current-driven external kink modes modelled with 3D free-boundary equilibria

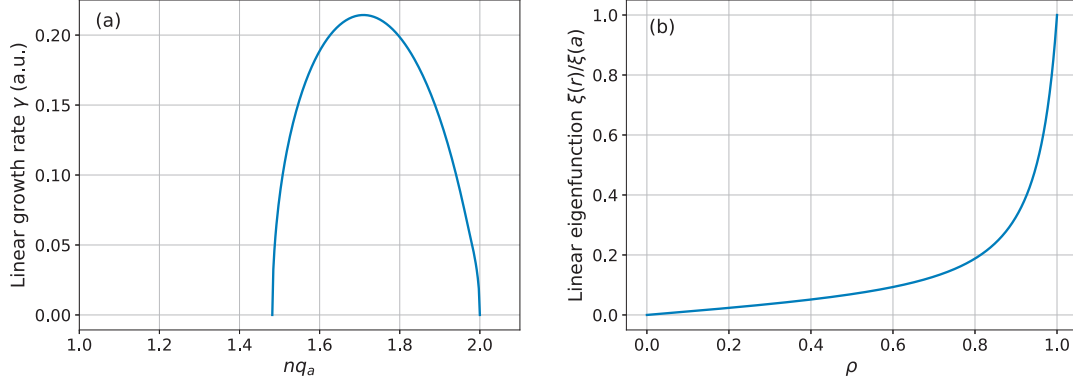


Figure 4.1 – (a) Linear growth rate of a $m = 2/n = 1$ external kink mode with parabolic j profile ($\nu = 1$) and conducting wall at infinity. (b) Typical external kink eigenfunction (here $m = 2$, $\nu = 3$, $b \rightarrow \infty$, $nq_a = 1.8$).

growth rate of an external kink mode can be calculated from a minimisation of the total energy, i.e. inertia contributions and potential energy (which includes the vacuum and boundary terms in δW in Eq. (4.4)). This provides the following Euler-Lagrange equation for external kink modes in the plasma region of a cylinder [81]:

$$\begin{aligned} & \frac{1}{r} \frac{\partial}{\partial r} \left\{ r^3 \left(\frac{B^2 m^2}{\mu_0 R^2} \left(\frac{1}{q} - \frac{n}{m} \right)^2 + \varrho \gamma^2 \right) \xi'_{rm} \right\} \\ & - \left\{ (m^2 - 1) \frac{B^2 m^2}{\mu_0 R^2} \left(\frac{1}{q} - \frac{n}{m} \right)^2 + \gamma^2 [\varrho(m^2 - 1) - r \varrho'] \right\} \xi_{rm} = 0, \end{aligned} \quad (4.5)$$

where ξ_{rm} is the radial displacement of the harmonic with poloidal mode number m , ϱ the mass density and γ the growth rate. In the vacuum region $a < r < b$, the perturbation can be described in terms of the radial projection of the perturbed magnetic field

$$[r(r\delta B_r)]' - m^2 \delta B_r = 0. \quad (4.6)$$

By solving Eqs. (4.5) and (4.6) with the boundary conditions

$$\begin{aligned} \delta B_r(r = a) &= \frac{iB_\phi m}{R} \left(\frac{1}{q} - \frac{n}{m} \right) \xi_{rm}, & (\text{plasma-vacuum interface}), \\ \delta B_r(r = b) &= 0, & (\text{conducting wall}), \end{aligned} \quad (4.7)$$

one obtains the dispersion relation

$$\begin{aligned} \gamma^2 \left(\frac{\varrho \mu_0}{B^2} [\ln(r\xi_{rm})]' \right)_{a-\varepsilon} &= \frac{m^2}{R^2 a} \left(\frac{1}{q_a} - \frac{n}{m} \right)^2 \left(\frac{2}{q_a} \frac{1}{\frac{1}{q_a} - \frac{n}{m}} \right. \\ & \left. - \frac{m+1 + (m-1) \left(\frac{a}{b} \right)^{2m}}{1 - \left(\frac{a}{b} \right)^{2m}} - a (\ln \xi_{rm})'_{a-\varepsilon} \right). \end{aligned} \quad (4.8)$$

Linear external kink growth rates are illustrated in Fig. 4.1 for the Wesson-like current density profiles of the form $j(r) = (\nu + 1)(1 - \rho^2)^\nu$ as a function of q_a . For these profiles,

4.2. Linear and non-linear external kink modes

as ν is increased the plasma becomes more stable (lower growth rate and lower marginal point moves to a larger value of q_a). The window of q_a values, where the mode is linearly unstable will be important in the next section. If the conducting wall is placed on the plasma boundary ($\rho = 1$), external kink modes are linearly stable and the destabilising effect increases as the wall is moved away from the plasma.

4.2.2 Non-linear external kink stability

Due to the general complexity of non-linear problems, analytical non-linear models of the external kink mode [99, 100, 94, 95] make use of multiple approximations and simplifications to make the problem tractable. In the following we provide a concise and self-contained summary of an analytical model [95] for the non-linear saturated external kink amplitude. In this context, we correct Eq. (34) of [95], where one term in the typed equations (not in the calculations / numerical results in the Figures) is missing. The model assumes cylindrical geometry, circular cross section and no pressure effects. The variables used to describe the system are the helical angle $\zeta = \phi - kz/m$ and a radial coordinate ρ describing the position of the flux surfaces in equilibrium. In this straight tokamak model, k replaces the toroidal mode number n , and z represents the variable in the direction of the cylindrical axis. By adding a perturbation, the position of the flux surfaces in the perturbed helical state is written as

$$r_s(\rho, \zeta) = \rho + \eta(\rho, \zeta), \quad (4.9)$$

where close to marginal stability a third order expansion provides a reasonable approximation for the helical displacement

$$\eta(\rho, \zeta) = \eta_m^{(1)}(\rho) \cos m\zeta + \eta_{2m}^{(2)}(\rho) \cos 2m\zeta + \eta_m^{(3)}(\rho) \cos m\zeta - \frac{[\eta_m^{(1)}(\rho)]^2}{4\rho}. \quad (4.10)$$

The last term in Eq. (4.10) ensures that the volume of flux tubes stays constant up to third order. For non-resonant modes the non-linear evolution [40, 101, 102] of the helical displacement η is given by the solution of

$$\frac{\partial^2 \eta}{\partial t^2} + D_1 \eta + D_3 \eta^3 = 0, \quad (4.11)$$

where the parameters D_1 and D_3 are defined below. For the saturated and hence time-independent state the solution to the amplitude η is

$$\eta = \sqrt{-\frac{D_1}{D_3}}. \quad (4.12)$$

For linear instability D_1 is negative. It is proportional to the square of the linear growth rate ω^2 and thus $D_1 = 0$ defines the marginal points. Non-linear stability is determined by the coefficient D_3 . The system is non-linearly stable, i.e. the mode can saturate if $D_3 > 0$. We do not explicitly explore conditions of non-linear instability where $D_3 < 0$. The non-linear stability problem can be seen as a bifurcation, which is subcritical in the case of non-linear growth or supercritical in the case of non-linear saturation. The

**Chapter 4. Non-linear saturated current-driven external kink modes
modelled with 3D free-boundary equilibria**

bifurcation is called subcritical for $D_3 < 0$ and supercritical for $D_3 > 0$. The coefficients D_1 and D_3 are obtained from physical constraints on the plasma surface [95]. The requirement of having a tangential magnetic field at the plasma boundary, together with the boundary condition at the conducting wall $\mathbf{B} \cdot \mathbf{n} = 0$ and pressure balance across flux surfaces results in an equation consisting of terms proportional to $\cos(m\zeta)$ and $\cos(2m\zeta)$ and of the same form as Eq. (4.11). Thus, from this equation D_1 and D_3 can be identified and read

$$D_1 = [F(f_{1\rho} - m^2\beta_1 + 1) - 2] F, \quad (4.13)$$

and

$$\begin{aligned} D_3 = & \frac{F^2 f_{1\rho}}{4} [6f_{1\rho}(f_{1\rho} + 1) + m^2 - 3] - F^2 \left(\frac{3}{2} n_{2\rho} f_{1\rho} - n_{3\rho} + \frac{1}{4} \right) \\ & + m^2 F^2 \left[\frac{\beta_1}{4} (6m^2 + 1) + m^2 \beta_1 \beta_2 (1 - 2m^2 \beta_1) - \frac{11}{8} m^2 \beta_1^2 + \frac{3}{8} \right] \\ & - F \left[m^2 \left(\frac{7}{2} \beta_1 - \beta_2 + 4m^2 \beta_1 \beta_2 - 2 \right) - \frac{1}{2} \right] \\ & + \frac{n_2 F^2}{2} [m^2 (\beta_1 (m^2 \beta_1 - 1) + 8m^2 \beta_1 \beta_2 - 5) + 1] \\ & + n_2 F [2m^2 (\beta_1 + 2\beta_2) - 1] - 2m^2 \beta_2 - \frac{5}{2} + 2n_2 + \frac{1}{\ln b} (Fm^2 \beta_1 + 1)^2, \end{aligned} \quad (4.14)$$

where $x_\rho = \partial x / \partial \rho$. The coefficients D_1 and D_3 in Eqs. (4.13) and (4.14) differ from D_1 and D_3 in Eq. (4.11) by a constant but common factor that cancels out [103] in the calculation of η in Eq. (4.12). The wall distance b is normalised by the minor radius, i.e. for $b = 1$ the wall is located at the plasma boundary and we define $\beta_1 := -\frac{1}{m} \frac{b^{2m+1}}{b^{2m}-1}$ and $\beta_2 := -\frac{1}{2m} \frac{b^{4m+1}}{b^{4m}-1}$. The function F is defined as

$$F(\rho) := \frac{I(\rho)}{\rho^2} - \frac{nq_a}{m}, \quad (4.15)$$

where $I(\rho) = \int_0^\rho 2\rho' j(\rho') d\rho'$ is the total current enclosed by a flux surface with radius ρ and normalised such that $I(1) = 1$. To obtain the functions f_1 , n_2 and n_3 , with the expansion of Eq. (4.10) a coupled system of differential equations arising from the ideal MHD model is solved numerically providing a solution for η to each order. These solutions can be written as sums of homogeneous $f_i(\rho)$ and particular $g_i(\rho)$ solutions and are denoted $\eta_m^{(1)}(\rho) \equiv f_1(\rho)\eta_m^{(1)}(1)$ to first, $\eta_{2m}^{(2)}(\rho) \equiv f_2(\rho)\eta_{2m}^{(2)}(1) + g_2(\rho)$ to second and $\eta_m^{(3)}(\rho) \equiv g_3(\rho)$ to third order. They satisfy the boundary conditions

$$\begin{aligned} \lim_{\rho \rightarrow 0} f_1(\rho) &\propto \rho^{m-1} \quad , \quad f_1(1) = 1, \\ \lim_{\rho \rightarrow 0} f_2(\rho) &\propto \rho^{2m-1} \quad , \quad f_2(1) = 1, \\ g_2(0) = g_2(1) &= 0 \quad , \quad g_3(0) = g_3(1) = 0. \end{aligned} \quad (4.16)$$

Using a normalisation constant $\hat{\eta} := \eta_m^{(1)}(1)$, we further define the normalised solutions to second and third order $n_2 := \eta_{2m}^{(2)}(\rho) / \hat{\eta}^2$ and $n_3 := g_3(\rho) / \hat{\eta}^3$ respectively. In Eqs. (4.13)

4.2. Linear and non-linear external kink modes

and (4.14), $F, f_{1\rho}, n_2, n_{2\rho}$ and $n_{3\rho}$ are evaluated at $\rho = 1$. Defining the operator

$$\mathcal{L}_k = \frac{d^2}{d\rho^2} + \left[\frac{3}{\rho} + 2 \frac{d}{d\rho} \ln F(\rho) \right] \frac{d}{d\rho} + \frac{1 - k^2 m^2}{\rho^2}, \quad (4.17)$$

with $k = 1, 2$ we obtain the solutions for η to each order from the following system of ODEs: [95]

$$\mathcal{L}_1 \eta_m^{(1)} = 0, \quad (4.18)$$

$$\begin{aligned} \mathcal{L}_2 \eta_{2m}^{(2)} = & -\frac{F_\rho}{2F\rho^2} \left(3\rho^2 (\eta_{m\rho}^{(1)})^2 + m^2 (\eta_m^{(1)})^2 \right) \\ & - \frac{1}{2\rho^3} \left[(3m^2 - 1) (\eta_m^{(1)})^2 + 2\rho \eta_m^{(1)} \eta_{m\rho}^{(1)} + 5\rho^2 (\eta_{m\rho}^{(1)})^2 \right], \end{aligned} \quad (4.19)$$

$$\begin{aligned} \mathcal{L}_1 \eta_m^{(3)} = & (\eta_m^{(1)})^3 \frac{1}{4\rho^4 F} [F(12m^2 - m^4 - 7) - 2\rho m^2 F_\rho] \\ & + \eta_{m\rho}^{(1)} (\eta_m^{(1)})^2 \frac{1}{4\rho^3 F} [F(2 - 16m^2) - 3\rho m^2 F_\rho] \\ & + (\eta_{m\rho}^{(1)})^2 \eta_m^{(1)} \frac{1}{4\rho^2 F} [F(41 - 19m^2) + 12\rho F_\rho] \\ & + \eta_m^{(1)} \eta_{2m}^{(2)} \frac{1}{\rho^3 F} [F(1 - 3m^2) + 2\rho m^2 F_\rho] - \eta_m^{(1)} \eta_{2m\rho}^{(2)} \frac{1}{\rho^2} (1 - 3m^2) \\ & + (\eta_{m\rho}^{(1)})^3 \frac{1}{4\rho F} [18F + 15\rho F_\rho] - \eta_{m\rho}^{(1)} \eta_{2m\rho}^{(2)} \frac{1}{\rho F} [5F + 3\rho F_\rho] \\ & - \eta_{m\rho}^{(1)} \eta_{2m}^{(2)} \frac{1}{\rho^2} (1 - 6m^2). \end{aligned} \quad (4.20)$$

The normalisation constant $\hat{\eta}$ can be eliminated by exploiting pressure balance across the plasma-vacuum interface [95], resulting in the expression

$$\begin{aligned} D_2 n_2(1) = & -\frac{1}{4} \left(m^2 (m^2 \beta_1^2 + 8m^2 \beta_1 \beta_2 - 4\beta_2 - 2) - 3(f_{1\rho})^2 + 4 \frac{g_{2\rho}}{\hat{\eta}^2} + 1 \right) F^2 \\ & - \left(m^2 (\beta_1 + 2\beta_2) - \frac{1}{2} \right) F - 1, \end{aligned} \quad (4.21)$$

with

$$D_2 = (F(f_{2\rho} - 4m^2 \beta_2 + 1) - 2) F. \quad (4.22)$$

Note that Eq. (4.21) corrects Eq. (34) of [95], where one term was found to be missing. We stress the fact that in this model, η depends only on single helical mode numbers m and n (as expected for cylindrical geometry), current density profile $j(\rho)$, wall distance b and edge safety factor q_a . This completes the equations and identities required for solving for saturated states of Eq. (4.11), i.e. for η with $\partial\eta/\partial t = 0$.

The window in q_a where external kink modes are linearly unstable is limited by two marginal points. The upper marginal point is the rational value $q_a < m/n$ and the lower marginal point is given by

$$nq_a = m \frac{f'_1 - m^2 \beta_1 - 1}{f'_1 - m^2 \beta_1 + 1}. \quad (4.23)$$

In the numerical solver this point is determined by iteration, starting with an initial guess for f' . Eq. (4.18) is then solved with the corresponding marginal point according to Eq. (4.23). This procedure is repeated until the guess and the resulting value of f' match.

The set of equations (4.18)-(4.20) is numerically solved using a finite difference scheme of second order, where the radial domain is reduced to a grid. In this solver, the current density profile can be specified in multiple ways. Besides Wesson-like profiles it is possible to read the current density profile $j(\rho)$ from VMEC input files. The code is also able to solve the equations for a given q profile instead of current density profile. A fourth order scheme has been implemented, but it does not provide more accurate results despite requiring much more computational resources. The numerical scheme and the implementation is discussed in more detail in Appendix C.2.

4.3 3D equilibrium simulations

The computation of 3D ideal MHD equilibria is performed using the free-boundary VMEC code [34, 104], which, as discussed in section 2.3.3, arrives at an equilibrium state by minimising the energy functional

$$W = \iiint_{plasma} \left[\frac{|\mathbf{B}|^2}{2\mu_0} + \frac{p(\rho)}{\Gamma - 1} \right] d^3x - \iiint_{vacuum} \frac{|\mathbf{B}_v|^2}{2\mu_0} d^3x, \quad (4.24)$$

with respect to an artificial time variable. Here, \mathbf{B} is the magnetic field inside the plasma, \mathbf{B}_v is the vacuum magnetic field, $p(\rho)$ is the pressure as a function of the radial variable $\rho = \sqrt{\Phi/\Phi_a}$. (Note that in this chapter the radial variable is the square root of the normalised toroidal flux, whereas in section 2.3.3 it was defined as Φ/Φ_a .) The toroidal flux is denoted by Φ , and subscript ' a ' indicates that a quantity is evaluated at the plasma boundary. The poloidal and toroidal magnetic field coils are modelled as discretised filaments with specified coil currents. In this proof-of-principle study we employ an accurate model of the up-down symmetric toroidal and poloidal JET coils [47], but we do not include the effects of other coil systems (e.g. divertor coils, error field correction coils), the vacuum vessel conductor nor iron core. The set of coils is visualised in Fig. 4.2. The vacuum magnetic field is calculated from the coil currents according to the Biot-Savart law [35] as explained in section 2.3.3.3. During the iterations that minimise the energy functional Eq. (4.24), the plasma boundary is free to move. We impose stellarator symmetry on the 3D equilibrium and choose 289 flux surfaces and for the mode spectrum to include $0 \leq m \leq 14$ poloidal modes and all toroidal modes in the range $-6 \leq n \leq 6$. In order to converge towards the 3D equilibrium quickly, we provide a small perturbation to the magnetic axis initial guess.

The linear growth rate and the non-linear saturated amplitude of external kink modes depend on the distance to a conducting wall surrounding the plasma. The VMEC model does not include such a wall. Instead, the plasma is enclosed inside a structure of magnetic field coils at a finite distance from the plasma. We hence cannot investigate the influence of the wall distance on the VMEC edge corrugations. For comparison with

4.3. 3D equilibrium simulations

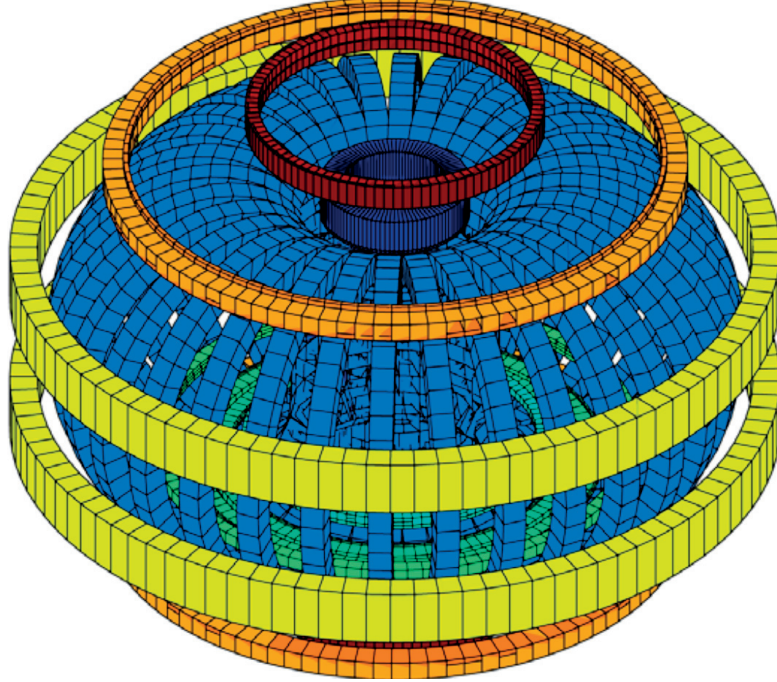


Figure 4.2 – Full set of magnetic field coils of JET (Courtesy of W.A. Cooper [47]). For the numerical simulations presented here, only the (up-down symmetric) toroidal and poloidal field coils - shown in blue, yellow, orange and red - are used. Other coils, e.g. divertor coils (green) are excluded.

VMEC, the conducting wall distance must be set to infinity (very large) for models that have the effect of a conducting wall. These models (linear and non-linear) will investigate the sensitivity of wall distance, and thus the likely correction to VMEC due to the vacuum vessel.

We start by examining dominant $n = 1, m = 4$ external modes with edge safety factor $q_a \lesssim 4$. The mode spectrum includes axisymmetric components ($n = 0$) as well as all non-axisymmetric modes with $|n| \leq 6$. Following the philosophy of previous studies of non-linear external kink modes [95] we choose a current density profile $j(\rho) \propto (1 - \rho^8)$, which is similar to those used by Wesson [93], however with a steeper gradient to make the non-linear structure in VMEC simulations larger, and hence easier to resolve numerically. For all simulations the pressure is chosen to be $p(\rho) \propto (1 - \rho^2)$. These input profiles are shown in Fig. 4.3. In order to investigate the effect of finite pressure on the resulting edge corrugations, $p(\rho)$ is multiplied by a scalar to achieve different values of $\beta_N = \beta a B_\phi / I_p$, where a is the minor radius, B_ϕ the toroidal magnetic field and I_p the plasma current. The value of q_a (edge safety factor) is crucial for both linear and non-linear external kink stability. We vary I_p in the VMEC simulations in order to study the dependency of the saturated edge displacement η on q_a with the given forms of $j(\rho)$ and varying pressure. The q profiles resulting from these equilibrium configurations are monotonic where $q(\rho) \approx \frac{B_\phi \rho^2}{\mu_0 R} / \int_0^\rho j(\rho') \rho' d\rho'$.

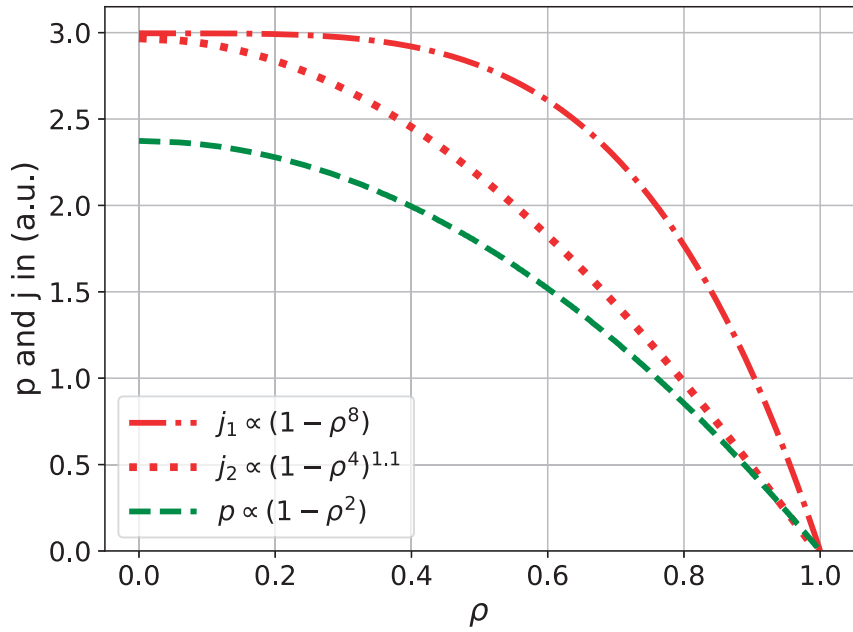


Figure 4.3 – Equilibrium profiles for pressure p and current density j are provided as input to VMEC.

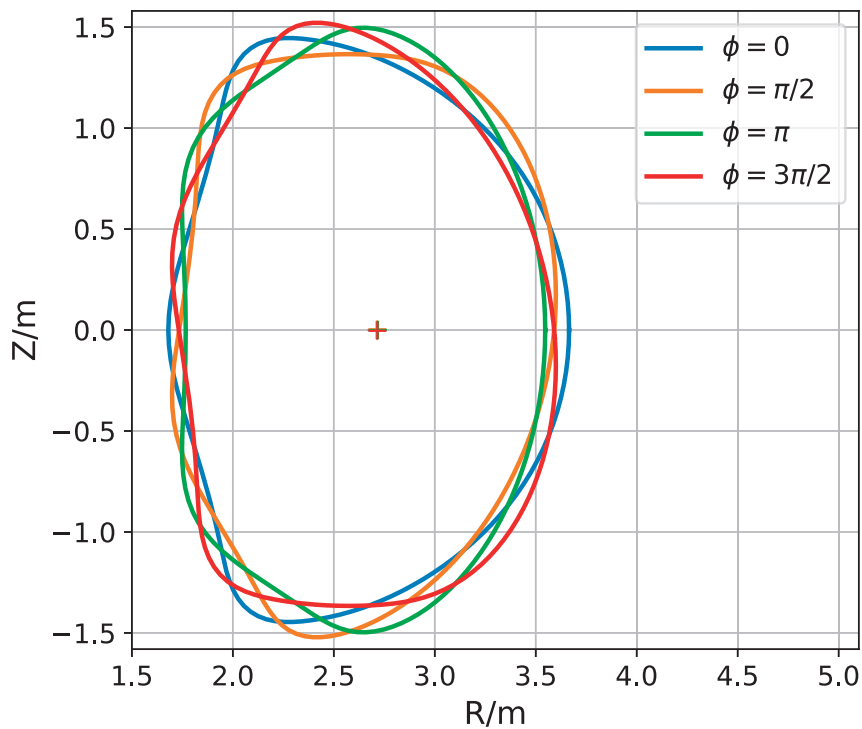


Figure 4.4 – Plasma boundary and magnetic axis (indicated by a cross) of a free-boundary VMEC equilibrium with $q_a = 3.752$ and $\beta_N = 0.552$ are shown at different toroidal angles ϕ . The non-axisymmetric edge corrugation is clearly visible.

4.3. 3D equilibrium simulations

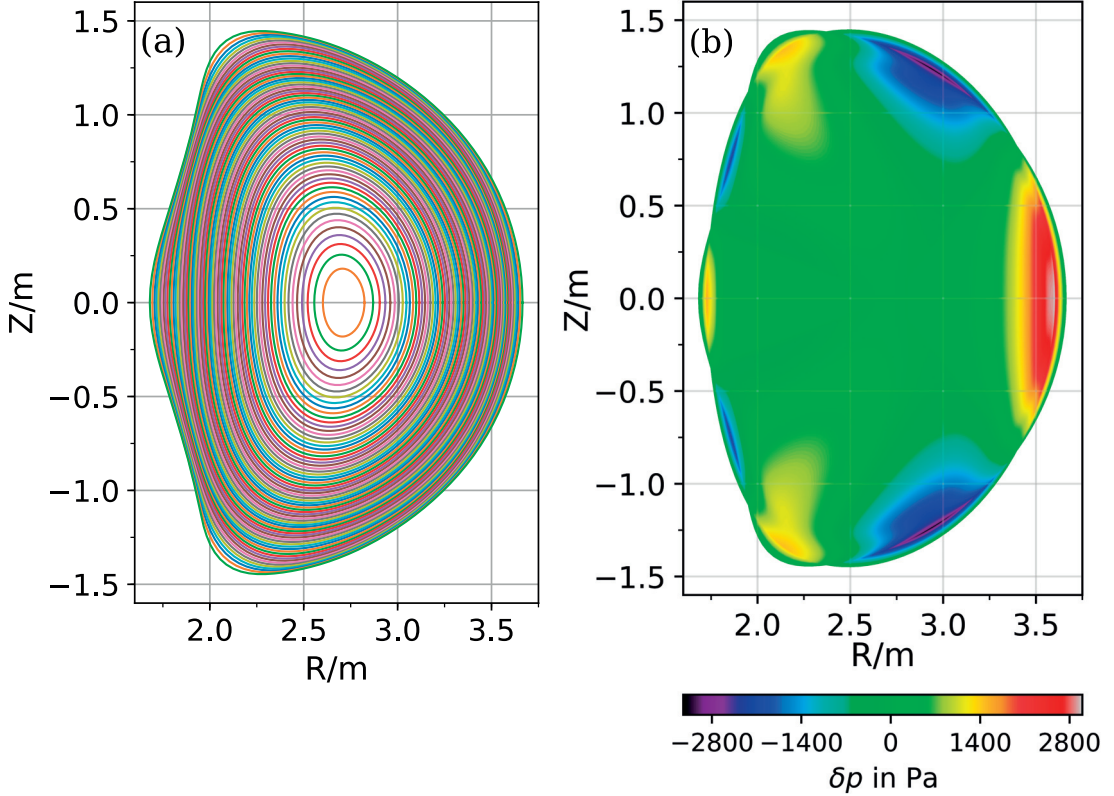


Figure 4.5 – Visualisation of the resulting 3D equilibrium with $q_a = 3.752$ shown for the $\phi = 0$ case of Fig. 4.4. (a) Shape and position of the magnetic flux surfaces. The perturbation is strongest at the plasma edge and vanishes towards the magnetic axis. (b) Perturbation $\delta p = p_{3D} - p_{2D}$ arising from the comparison of the pressure in the 3D equilibrium with the neighbouring state.

First, we simulate a plasma with a total toroidal current of $I_t = 2.6$ MA such that the resulting edge safety factor of $q_a = 3.752$ is below the rational value $m/n = 4/1$. On allowing $n \neq 0$ modes, the resulting VMEC equilibrium is non-axisymmetric with a strong edge corrugation in the toroidal and poloidal directions. This is illustrated in Fig. 4.4, where the plasma boundary and the magnetic axis are shown at different toroidal angles ϕ . From Fig. 4.5a, which shows a poloidal cross section of the flux surfaces for the $\phi = 0$ case of Fig. 4.4, it is evident that the perturbation is strongest at the plasma boundary and decreases towards the magnetic axis where it vanishes (hence only one cross observed in Fig. 4.4). This behaviour is characteristic of external kink modes. By retaining only $n = 0$ modes, we can find a neighbouring axisymmetric state to the obtained 3D equilibrium. This equilibrium is used for the basis of linear external kink calculations, non-linear analytic calculations, and could in principle be used for the initial state of XTOR initial value calculations. A comparison of 3D VMEC states with their neighbouring axisymmetric equilibria was previously used to determine toroidal field ripple [105]. We now employ a similar method for the external kink application. Defining $\delta p = p_{3D} - p_{2D}$ as being the difference of p in the 3D state compared to the axisymmetric

state, we can identify the periodicity and the location of the perturbation. It is noted in passing that the 3D displacement ξ of the magnetic surfaces can be approximately determined via $\xi = -\delta p (\partial p_{2D}/\partial \rho)^{-1}$. Fig. 4.5b shows δp for the $\phi = 0$ case of Fig. 4.4. It can be seen that the perturbation is located at the plasma edge and the $m = 4$ character is evident.

4.3.1 Fourier analysis of VMEC saturated external kink modes

To characterise the non-linear external kink amplitude, emphasis has to be placed on the coordinate system underlying the spectral analysis of the displacement. It will be seen that converting VMEC coordinates to straight field line (sfl) coordinates permits physical insight into the main poloidal mode of the external kink instability and comparison with linear KINX calculations and non-linear analytic calculations.

The VMEC code employs the following poloidal and toroidal angle decomposition (assuming stellarator symmetry):

$$\begin{aligned} R(\rho, \theta, \phi) &= \sum_{m,n}^{M_{\max}, N_{\max}} R_{mn}(\rho) \cos(m\theta - n\phi), \\ Z(\rho, \theta, \phi) &= \sum_{m,n}^{M_{\max}, N_{\max}} Z_{mn}(\rho) \sin(m\theta - n\phi), \end{aligned} \quad (4.25)$$

where R_{mn} and Z_{mn} are Fourier coefficients in VMEC coordinates. From VMEC, at a given radial position $\rho = \hat{\rho}$ the 3D flux surface

$$\mathbf{S}_{3D}(\theta, \phi) = \begin{pmatrix} R(\hat{\rho}, \theta, \phi) \cos \phi \\ R(\hat{\rho}, \theta, \phi) \sin \phi \\ Z(\hat{\rho}, \theta, \phi) \end{pmatrix}, \quad (4.26)$$

as well as the neighbouring, axisymmetric flux surface

$$\mathbf{S}_{2D}(\theta, \phi) = \begin{pmatrix} R(\hat{\rho}, \theta, \phi = 0) \cos \phi \\ R(\hat{\rho}, \theta, \phi = 0) \sin \phi \\ Z(\hat{\rho}, \theta, \phi = 0) \end{pmatrix}, \quad (4.27)$$

are known in VMEC flux coordinates ($s = \rho^2, \theta, \phi$) [34]. Note that the coordinates differ in the 3D and neighbouring 2D states, since they are aligned with the flux surfaces. In the following, the angular variables θ and ϕ are those of the axisymmetric equilibrium. For a given point \mathbf{P}_0 lying on \mathbf{S}_{2D} with normal vector

$$\mathbf{N}(\theta, \phi) = \frac{\frac{\partial \mathbf{S}_{2D}}{\partial \theta} \times \frac{\partial \mathbf{S}_{2D}}{\partial \phi}}{\left| \frac{\partial \mathbf{S}_{2D}}{\partial \theta} \times \frac{\partial \mathbf{S}_{2D}}{\partial \phi} \right|}, \quad (4.28)$$

a convenient definition of the corrugation displacement is

$$\eta(\theta, \phi) \mathbf{N}(\theta, \phi) = \mathbf{S}_{3D} - \mathbf{S}_{2D}(\theta, \phi). \quad (4.29)$$

4.3. 3D equilibrium simulations

The Fourier series representing η is of the same form as that of the magnetic field strength, i.e.,

$$\eta(\theta, \phi) = \sum_{m=0}^{M_{\max}} \sum_{n=0}^{N_{\max}} \eta_{mn} \cos(m\theta - n\phi), \quad (4.30)$$

so that

$$\eta_{mn} = \int_0^{2\pi} \int_0^{2\pi} \cos(m\theta - n\phi) (\mathbf{S}_{3D} - \mathbf{S}_{2D}) \cdot \mathbf{N} \, d\theta \, d\phi. \quad (4.31)$$

We can calculate the mode spectrum separately for $\eta(\theta, \phi)$ using Eq. (4.31), $|\mathbf{B}|(\theta, \phi)$ as well as $R(\theta, \phi)$ and $Z(\theta, \phi)$ at the edge. The spectrum of each of these quantities in VMEC coordinates is rich and exhibits a variety of strong poloidal modes for $n = 1$. For the case shown in Fig. 4.5, the 4/1 VMEC coordinate coefficients of R , Z , $|\mathbf{B}|$ and η are not dominant. This is in contradiction with the visual observations from the magnetic topology, which has a clear 4/1 structure. The mode amplitudes for $\eta(\phi, \theta)$ in VMEC coordinates can be seen in Fig. 4.6a.

Mode spectra are expected to be most narrow (and most peaked) for a straight field line coordinate system. Dominant poloidal modes can thus be identified for comparison with those seen in Figs. 4.4 and 4.5 (simply by inspection), and for suitable comparison with the non-linear analytic treatment described later. For this we introduce the sfl angle

$$\theta_{\text{sfl}}(l) = 2\pi \left[\int_0^L \frac{dl}{R(l) |\nabla\psi|} \right]^{-1} \int_0^l \frac{dl}{R(l) |\nabla\psi|}. \quad (4.32)$$

Integration is performed along a chosen flux surface of the axisymmetric equilibrium at fixed toroidal angle ϕ . L denotes the poloidal circumference and $R(l)$ the major radius which varies along the line of integration. With Eq. (4.31) and the arc length

$$l(\theta, \phi) = \int_0^\theta \sqrt{\left(\frac{\partial R(\theta', \phi)}{\partial \theta'} \right)^2 + \left(\frac{\partial Z(\theta', \phi)}{\partial \theta'} \right)^2} \, d\theta', \quad (4.33)$$

it is possible to relate the poloidal angle in VMEC coordinates θ to the straight field line angle θ_{sfl} . An equivalent, but more straightforward method of calculating the sfl angle is obtained by equating the volume elements in VMEC coordinates and straight field line coordinates

$$\mathcal{J}_{\text{sfl}} \, d\phi \, d\theta_{\text{sfl}} \, d\rho^2 = \mathcal{J}_{\text{VMEC}} \, d\phi \, d\theta \, d\rho^2. \quad (4.34)$$

Since the toroidal angle ϕ and the radial variable ρ are identical in both coordinate systems, the only variables requiring transformation are θ_{sfl} and θ . Integration of Eq. (4.34) yields

$$\theta_{\text{sfl}}(\theta) = 2\pi \left[\int_0^{2\pi} \frac{\mathcal{J}_{\text{VMEC}}(\theta)}{R^2(\theta)} \, d\theta \right]^{-1} \int_0^\theta \frac{\mathcal{J}_{\text{VMEC}}(\theta)}{R^2(\theta)} \, d\theta, \quad (4.35)$$

where $\mathcal{J}_{\text{sfl}} \propto R^2$ was used and $\mathcal{J}_{\text{VMEC}}$ and R are computed by VMEC from the axisymmetric equilibrium. Now with Eq. (4.31) we are able to calculate the coefficients for the Fourier series of $\eta(\theta_{\text{sfl}}, \phi)$. In this sfl coordinate system the mode spectrum cleanly and clearly identifies a standard external kink mode. As shown in Fig. 4.6b the 4/1 mode is dominant as expected from the visual observations of Fig. 4.5 as well as from external

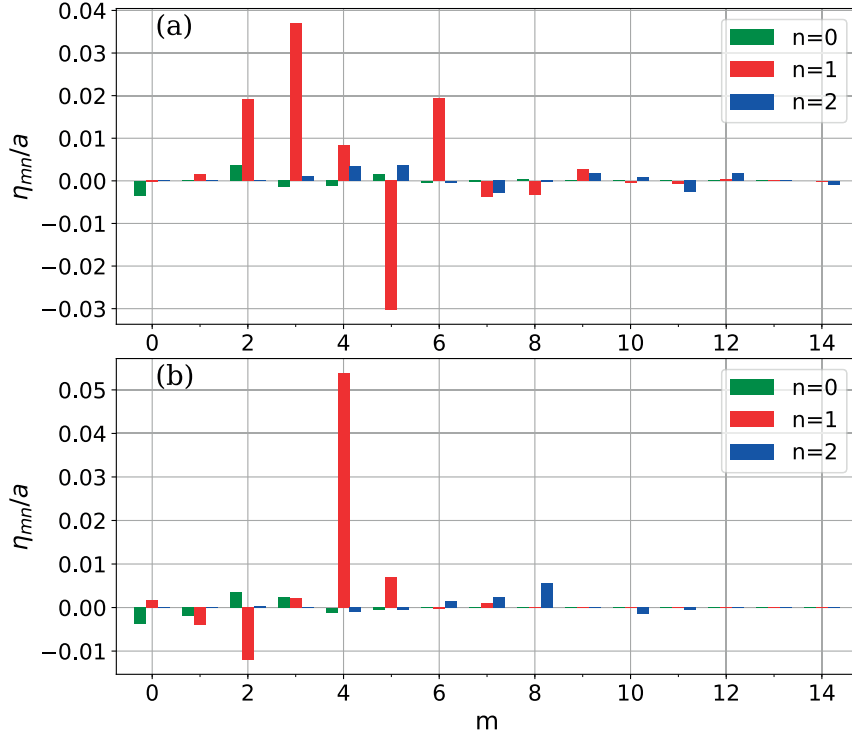


Figure 4.6 – Mode spectrum of the edge displacement obtained in two different coordinate systems. (a) In VMEC coordinates. (b) In straight field line coordinates (dominant $m = 4/n = 1$ mode).

kink mode theory. With all other modes being fairly weak compared to the dominant one, poloidal and toroidal coupling thus appears to have a weak effect. Toroidicity and beta can be expected to have only a mild effect on mode structure, and hence we can compare the mode amplitudes to an analytical model that assumes cylindrical geometry [95] (this is due to the modes being current-driven - in contrast to the modes examined in the second part of chapter 5).

It is also desirable to determine the magnetic field perturbation $\delta\mathbf{B}$ associated with the edge displacements. In analogy to linear approaches $\delta\mathbf{B}$ can be expressed as

$$\delta\mathbf{B}(\rho, \theta_{2D}, \phi_{2D}) = \mathbf{B}_{3D}(\theta_{2D}) - \mathbf{B}_{2D}(\theta_{2D}), \quad (4.36)$$

where quantities with subscript '2D' are evaluated on the axisymmetric flux surfaces. The most relevant component is the radial one

$$\delta\mathbf{B} \cdot \nabla\rho_{2D} = \mathbf{B}_{3D}(\theta_{2D}) \cdot \nabla\rho_{2D}. \quad (4.37)$$

The problem associated with evaluating \mathbf{B}_{3D} along the axisymmetric boundary is illustrated in Fig. 4.7. VMEC explicitly evaluates all physical quantities including \mathbf{B} only inside the space occupied by the plasma in the equilibrium solution. However, the neighbouring axisymmetric flux surfaces on which we want to evaluate \mathbf{B} lie partially outside of the volume occupied by the 3D equilibrium i.e. where the magnetic field is not known explicitly. Another method to calculate the perturbed magnetic field is described in

4.4. Linear stability analysis

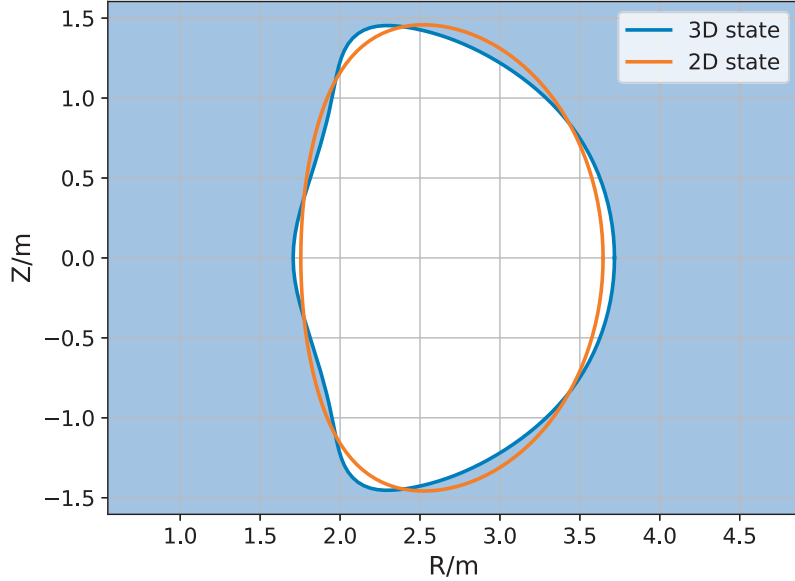


Figure 4.7 – Cross sections of the last closed flux surface of a 3D state and its neighbouring equilibrium. The shaded region corresponds to the vacuum in the 3D state, where no quantities are computed by VMEC.

appendix B. This analytical derivation is strictly valid only in the linear limit. However, since the non-linear structures of the VMEC displacement modes are very similar to the linear eigenmodes, this approach probably provides reasonable estimation of the non-linear $\delta\mathbf{B}$ too.

4.4 Linear stability analysis

To obtain non-linearly saturated external kink modes, the system is initially required to be linearly unstable. This condition is verified from numerical computations with the linear eigenvalue code KINX [38]. The equilibria for the KINX stability computations are the axisymmetric neighbouring states to the 3D VMEC equilibria. The VMEC profiles are expressed as a function of the normalised poloidal flux and together with the position of the unperturbed plasma boundary used as input to CHEASE. The effects of small aspect ratio, shaping and finite beta are retained in these computations and in Figs. 4.8a, 4.8b the distance to the perfectly conducting wall surrounding the plasma is set to $b/a = 10$, i.e. sufficiently large so that the effects due to the wall can be considered negligible. The linear growth rate $\gamma = -i\omega$ of the $n = 1$ mode is calculated as a function of q_a . This is presented in Fig. 4.8a, where γ is normalised by the Alfvén frequency ω_A . $n = 1$ external kink modes (with dominant $m = 4$) are linearly unstable in a wide range of q_a , where saturated non-linear states can possibly arise. The sfl harmonics of the linear radial eigenfunction $\xi \cdot \nabla\rho = \xi \cdot \nabla\psi (d\psi/d\rho)^{-1} = \xi \cdot \nabla\psi q/\rho$ in KINX resemble the mode spectrum calculated in sfl coordinates in Fig. 4.6b (for the non-linear

equilibrium calculations). For an edge safety factor below $q_a < 4$, the eigenfunction (radial displacement) of the $m = 4$ mode is dominant over all the other poloidal modes at the plasma boundary. This is shown in Fig. 4.8b for the case with an edge safety factor of $q_a = 3.752$. The similarity of these linear eigenfunctions and the non-linear saturated VMEC displacement η_{mn} as a function of the radial variable, shown in Fig. 4.8c, is remarkable.

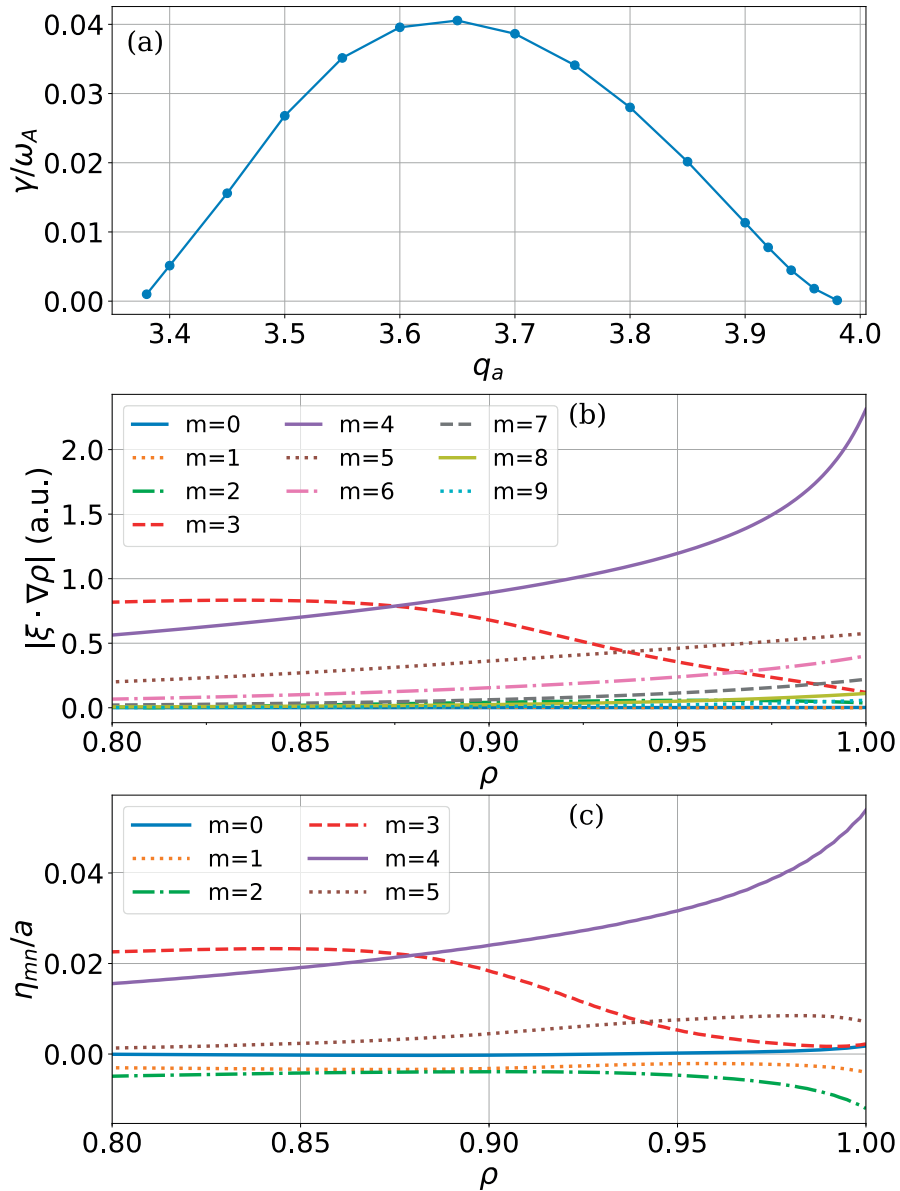


Figure 4.8 – (a) Linear external kink growth rate γ of the $n = 1$ mode calculated with KINX. (b) Linear $n = 1$ (KINX) radial displacement functions for various poloidal mode numbers (sfl coordinates). (c) Non-linear $n = 1$ saturated (VMEC) radial displacement functions η for various poloidal mode numbers (sfl coordinates).

4.5. Analytical predictions and comparison with VMEC results

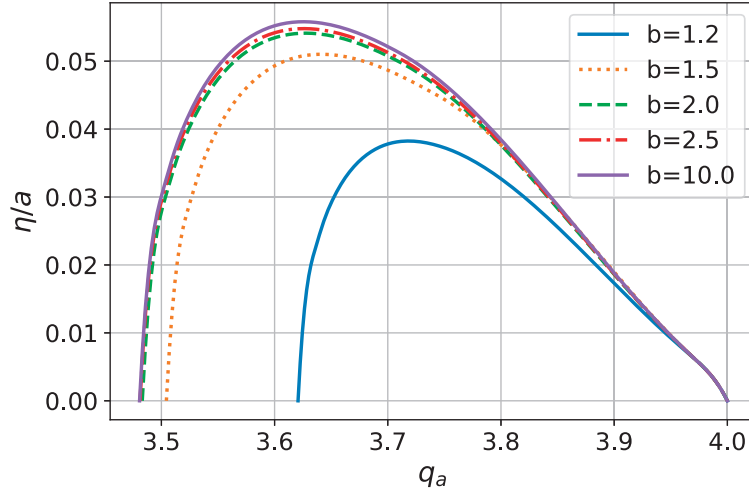


Figure 4.9 – Dependence of the saturated 4/1 external kink amplitude on the wall distance b as calculated from the non-linear analytical model.

4.5 Analytical predictions and comparison with VMEC results

After demonstrating the external kink spectral properties of the VMEC 3D equilibria with the linear KINX code, we now compare the non-linear saturated amplitude of the displacement in VMEC with analytical predictions. In order to study the degree of relevance of the equilibrium free-boundary approach without a conducting wall, it is important to investigate the sensitivity of the effect of the conducting wall distance from the plasma on the non-linear saturated state. This is achieved with the analytical model. Figure 4.9 shows how η depends on q_a for different values of the wall distance b . As the wall distance increases, not only does the mode amplitude grow, but also the unstable domain widens. The variation is strong for $b \leq 1.5$, but weak for $b > 1.5$. Thus we can approximately treat a wall distance of $b \gtrsim 1.5$ as if no wall was present. In the VMEC computations presented here, the field coils have a minimum distance of $b \approx 1.55$ to the plasma surface.

We find that the behaviour of η calculated from VMEC agrees well with the expected characteristics of external kink modes. In particular, the window of q_a over which η is non-zero, and also the shape of η with respect to q_a (plotted in Fig. 4.9) is roughly mirrored by the shape of γ with respect to q_a in Fig. 4.8a. Figure 4.10 shows the amplitude of η for each m (with $n = 1$), with η_{mn} calculated according to Eq. (4.31). For an edge safety factor larger than the upper marginal point – given by the rational value $q_a = m/n$ – the plasma remains (nearly) axisymmetric. Lowering q_a below m/n results in 3D equilibria that have edge corrugations with external kink-like properties as described previously. The amplitude of the saturated non-linear edge displacement is finite and dominated by a 4/1 component throughout the linearly unstable domain, as expected for the spectral properties of Fig. 4.6b. As q_a decreases below the lower marginal

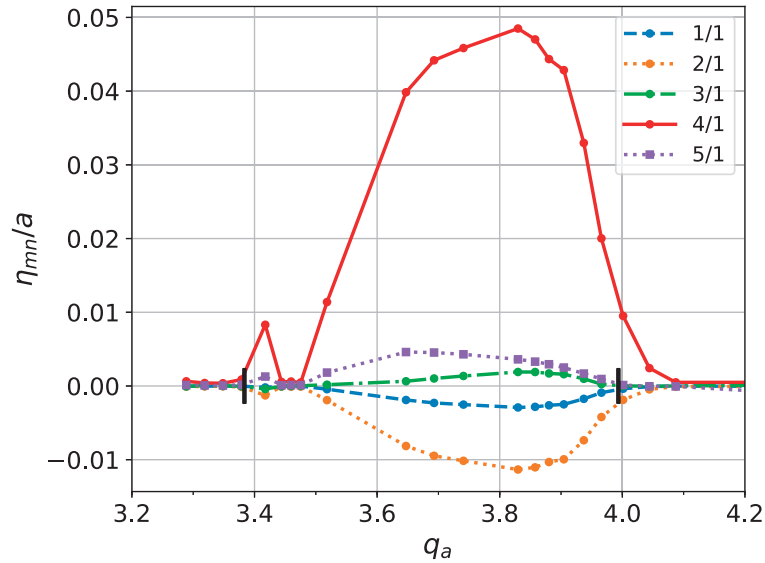


Figure 4.10 – Lowest m components with $n = 1$ of the edge displacement obtained from free-boundary VMEC simulations with current profile $j(\rho) \propto (1 - \rho^8)$ and $\beta_N = 0.08$. $m = 4/n = 1$ is the dominant mode throughout the range of q_a , where the external kink mode is expected to be linearly unstable and non-linearly stable. The two black lines indicate the position of the marginal points computed with KINX.

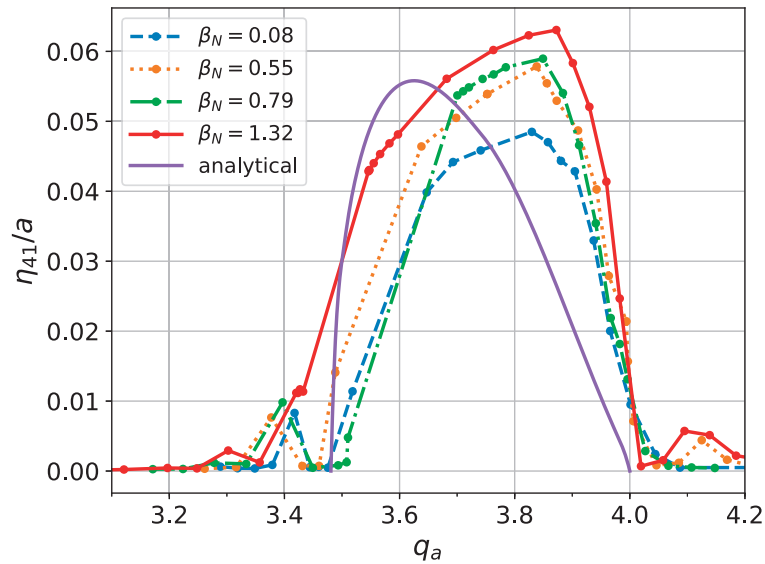


Figure 4.11 – Amplitude of the saturated edge displacement of the 4/1 mode η_{41} computed from VMEC simulations at various values of β_N and comparison to the analytical model for current profile $j(\rho) \propto (1 - \rho^8)$.

4.5. Analytical predictions and comparison with VMEC results

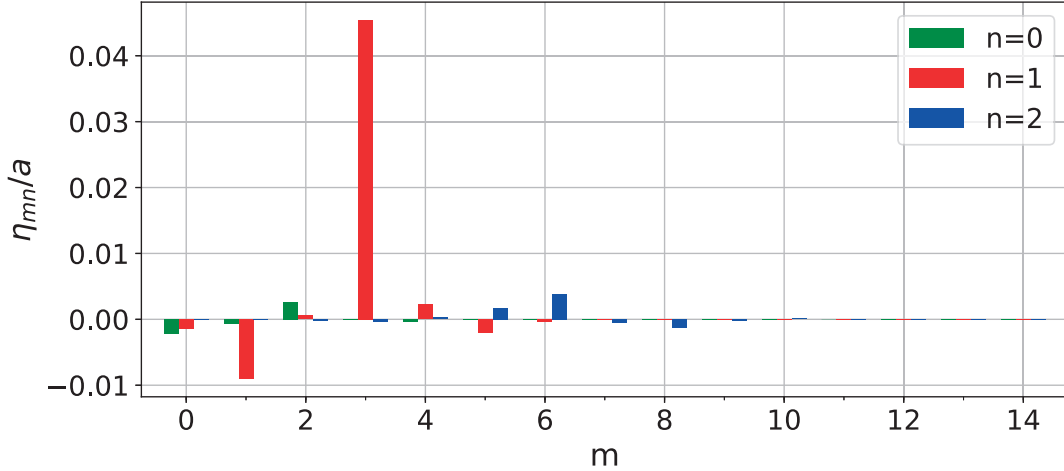


Figure 4.12 – Mode spectrum (straight field line coordinates) of the VMEC edge displacement obtained in a simulation with $j(\rho) \propto (1 - \rho^4)^{1.1}$ and $q_a = 2.913$ at low pressure ($\beta_N = 0.08$). The $m = 3/n = 1$ mode is dominant.

point, i.e. the value at which the linear external kink mode is stable, the displacement vanishes. For a small range of values of q_a slightly higher than the upper marginal point, or slightly lower than the lower marginal point, we see small perturbations to η . We do not yet know the origin of these weak 3D saturated states.

A weak scaling of η with β_N is observed as shown in Fig. 4.11, where η_{41} calculated from VMEC at different values of β_N is compared with the analytically predicted non-linear saturated external kink amplitude η . The mode is present already at very low β_N , strongly indicating that the 3D states are dominantly current-driven, as expected for external kink modes. For the largest value of β_N the lower marginal point is shifted towards lower q_a , whereas it remains approximately constant for lower β_N values. Since finite beta effects are neglected in the analytical model, the most relevant comparison between VMEC and the non-linear analytic model is for small β_N in Fig. 4.11. Considering the shaped plasma and edge aspect ratio of the VMEC JET-like simulations, the comparison with the cylindrical analytic model in Fig. 4.11 is surprisingly good.

Now that agreement between the VMEC displacement amplitude and the non-linear analytical external kink mode amplitude has been demonstrated, we further verify the results for a case with $q_a \lesssim 3$, for which a $n = 1, m = 3$ external mode is dominant. For this, in order to prevent the amplitude of the mode from becoming too large, we choose a less steep current profile $j(\rho) \propto (1 - \rho^4)^{1.1}$. As seen in Fig. 4.12, the 3/1 component (evaluated in sfl coordinates) is dominant in the edge mode spectrum of the resulting VMEC 3D equilibria as expected for a current-driven external kink mode. Figure 4.13 shows the flux surfaces and the 3D pressure perturbation, which are both non-axisymmetric and consistent with the mode spectrum. In Fig. 4.14 the analytically predicted saturated external kink amplitude is compared with the 3/1 component of the VMEC edge displacement at different values of β_N . Again a weak scaling of η with the pressure is observed. The upper marginal point agrees well with the analytical value, whereas the

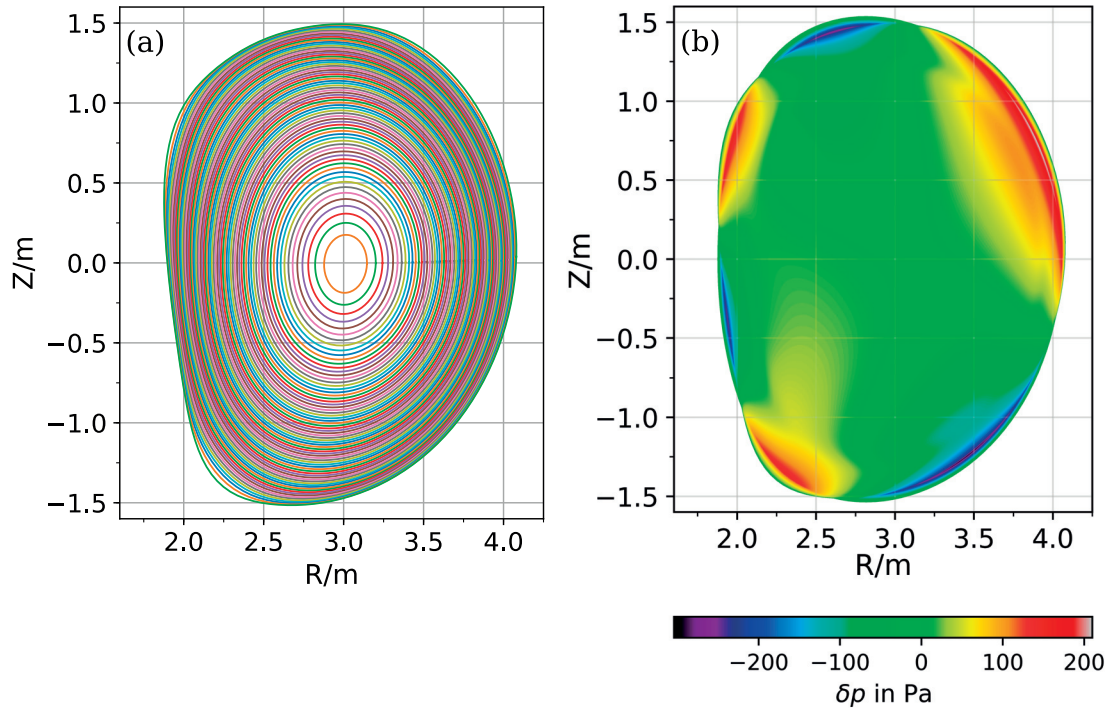


Figure 4.13 – Visualisation of the 3D equilibrium with current profile $j(\rho) \propto (1 - \rho^4)^{1.1}$, $q_a = 2.913$ and $\beta_N = 0.08$ shown at $\phi = \pi/3$. (a) Flux surfaces. (b) Perturbation $\delta p = p_{3D} - p_{2D}$ arising from the comparison of the pressure in the 3D equilibrium with the neighbouring state.

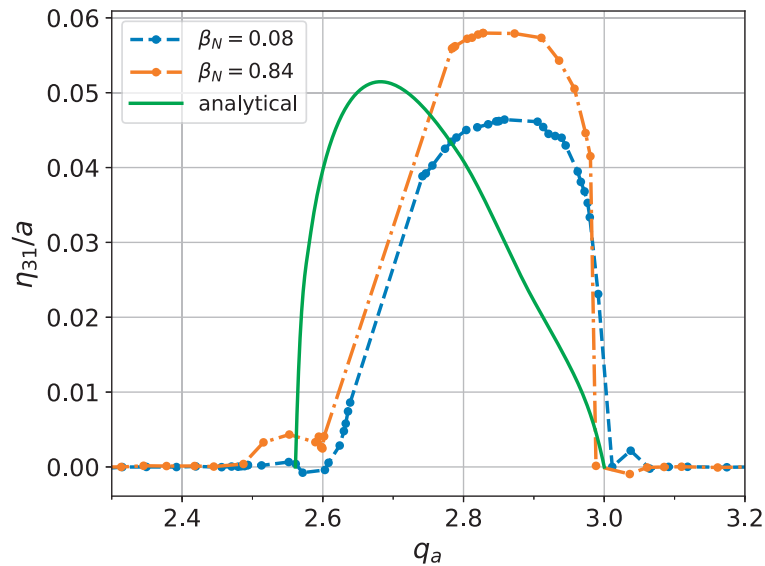


Figure 4.14 – Non-linear amplitude of the 3/1 mode η_{31} obtained from VMEC with current profile $j(\rho) \propto (1 - \rho^4)^{1.1}$ and q_a around 3 at two values of β_N and comparison with the analytical prediction.

4.6. Conclusions

lower one differs slightly. The saturated external kink amplitude peaks at a value of q_a closer to the lower marginal point, whereas the peak in the VMEC computations is somewhat shifted towards larger values. The reason for this is not currently certain, but it could be a result of finite aspect ratio and cross section shaping effects which are not taken into account in the analytic model.

4.6 Conclusions

Employing three-dimensional, free-boundary equilibrium computations, is shown to provide a novel way of obtaining saturated current-driven external kink modes. In principle, such saturated external states are time-independent and thus satisfy the force balance equation solved by an equilibrium code. For the first time, current-driven external kink modes are observed with an equilibrium code in free-boundary plasma configurations with standard monotonic current and q profiles typical of standard (baseline) tokamak plasma scenarios. Windows of the edge safety factor where external kink modes would be linearly unstable have been identified. In VMEC simulations with current profiles that result in an edge q value lying inside these regions, non-axisymmetric edge corrugations are observed. Analytical calculations of non-linear external kink modes reveal linear instability but non-linear stability, i.e. saturated mode amplitudes for the studied plasma configurations. To compare the analytic external kink amplitudes with VMEC, and thus verify that VMEC corrugations are those of standard non-linear saturated external kinks, the spectra of the VMEC fluctuations are converted to spectra of a straight field line coordinate system. The Fourier spectrum calculated in this coordinate system shows one dominant mode, thus indicating consistency between 3D VMEC equilibria and analytical external kink models. Even though the mode amplitude scales weakly with β_N , the external perturbations seen in VMEC are of considerable size already at low β_N , indicating a current-driven mode. Finite pressure is shown to have a weakly destabilising effect. The edge displacement in VMEC is found to be comparable to the analytically calculated saturated external kink mode amplitude. Small differences are observed in the value of q_a where the amplitude reaches a maximum. Due to the lack of the stabilising effect of a conducting wall the 3D equilibrium simulations overestimate the saturated amplitude of a real tokamak by about 25% (for a wall distance $b = 1.2a$), the difference having been quantified via the analytic approach. We conclude that VMEC free-boundary calculations capture the salient features of saturated external kink modes, thus enabling efficient prediction of non-linear instability amplitudes, and e.g. accurate fast ion and impurity transport studies using codes such as VENUS-LEVIS that exploit Fourier decomposition of magnetic equilibria.

Saturated current-driven and pressure-driven external kink modes in extended low-shear QH-mode plasmas

In the previous chapter we demonstrated that the 3D free-boundary code VMEC is capable of describing the characteristics of non-linearly saturated external kink modes in tokamak baseline scenarios. In the current chapter, VMEC is applied to investigate saturated ideal edge modes in quiescent H-mode (QH-mode) plasmas. We consider standard current-driven external kink modes arising due to the strong bootstrap current close to the plasma edge, but also pressure-driven infernal modes with coupled external kink-like sidebands. The goal of this study is to provide a theoretical description of edge harmonic oscillations observed in QH-mode discharges, with special attention given to equilibria with an extended region of low magnetic shear at the edge. A journal article for publication in *Plasma Physics and Controlled Fusion* is currently being prepared [106] covering the main themes of this chapter.

5.1 Introduction

The H-mode [10] is a candidate operating mode in present and future tokamaks because it provides large energy confinement times. By applying auxiliary heating, the plasma undergoes a transition from low to high confinement (L-H transition) when the heating power exceeds a certain threshold. The plasma is then characterised by having an edge transport barrier (ETB) [107], which reduces turbulent transport and hence improves plasma confinement. H-mode operation is however associated with the occurrence of edge-localised modes (ELMs) - periodic relaxations at the plasma edge - which are driven by large gradients in the ETB [12]. ELMs cause large particle and heat loads on the plasma-surrounding structure and thus pose a danger to the plasma vessel. For large tokamaks such as ITER, the energy deposition due to large ELMs is intolerable and thus mitigation or suppression of ELMs is of crucial importance to achieve economic fusion performance in tokamaks.

ELM avoidance can be achieved in two ways: First, conditions can be explored that lead to a weakening and eventually suppression of ELMs (for example by applying resonant magnetic perturbations (RMPs)), which appear to have a stabilising effect on peeling-ballooning modes, commonly associated with ELMs [108, 109]. Another way

is to explore the possibility of fully ELM-free regimes. There are two known ELM-free H-modes, the QH-mode and the I-mode. The I-mode is not considered here. The existence of the ELM-free operating regime known as quiescent H-mode (QH-mode) was first discovered in DIII-D [18] and was subsequently observed in further machines such as ASDEX-U, JET and JT-60U [110, 111, 112, 113] over a large range of parameters. In this so-called QH-mode, ELMs are completely suppressed and benign long wavelength edge harmonic oscillations (EHOs) appear instead [18, 114]. Similar to ELMs, EHOs appear to be capable of providing an energy and impurity exhaust, but without the risk of large heat and particle loads on plasma-facing components. Unlike ELMs, which are generally driven by intermittent high n, m ballooning/peeling modes, EHOs are long wavelength (small n, m) continuous (saturated) perturbations. In JET, the experimentally observed outer mode [115] is assumed to be similar (or identical) to EHOs.

Experimental [18] and numerical [116] studies indicate that QH-mode operation is located below but close to the peeling (external kink) stability limit of the peeling-ballooning stability diagram. In a previous study, saturated modes at the plasma boundary were observed in non-linear numerical simulations with a reduced MHD model. It was shown that edge modes with high toroidal mode number n become suppressed in the non-linear phase and only $n = 1, 2$ modes are dominant [39]. Furthermore, ideal MHD studies with the 3D equilibrium code VMEC have shown edge corrugations in JET and TCV plasmas in which external kink modes are linearly unstable [46, 47]. The numerically observed structures have been argued to correspond to kink/peeling modes [117, 118].

As explained in detail in chapter 4, standard external kink modes affect the plasma boundary and are driven by current gradients. These modes can be linearly unstable in QH-mode plasmas due to the strong bootstrap current localised close to the plasma edge. In chapter 4 it was shown that saturated (non-linearly stable) external kink modes develop in standard (monotonic- q) scenarios when $q_{\text{edge}} \lesssim m/n$, and in the current chapter it is shown that such current-driven modes cause very large edge corrugation when q is flat near the edge and $q_{\text{edge}} \lesssim m/n$. It is shown furthermore that such modes can be avoided by accounting for the effect of a separatrix, which lifts the safety factor sharply above m/n near the edge. With such a mode stabilised, the steep pressure gradient in the edge where q is flat can cause the instability of pressure-driven infernal modes [56]. This has been observed in recent linear numerical computations [119] and analytical modelling [120, 121]. The main mode can couple to sideband modes with $m = m_0 \pm 1$, where, this time, the upper sideband has the character of an external kink mode [120, 121]. The window of instability for coupled pressure-driven external kinks occurs where the low-shear region has q near (either above or below) m/n . When linearly unstable, such external kink modes driven by coupling with pressure-driven edge infernal modes can potentially lead to edge corrugations in a non-linearly saturated state as in the case of standard external kink modes. But, different from current-driven external kinks, the main corrugation is shown here to be connected with the upper sideband ($m = m_0 + 1$) of the infernal mode.

Given the potential of the QH-mode to serve as a viable high confinement regime in future tokamak operation, in the present work we aim to explain the connection between

5.2. Experimental observation of quiescent H-mode regimes

EHOs and saturated non-linear MHD phenomena. This theoretical investigation also helps to determine the parameter space in which QH-mode discharges with EHOs can be expected. Since experimental measurements show that EHOs are saturated modes, a comparison to theoretical predictions can be made in terms of the saturated amplitude of the edge perturbation. The phase of the mode is not important and the fluid velocity \mathbf{v} has no time dependence in the saturated state, i.e. $\partial\mathbf{v}/\partial t = 0$. We do not consider equilibrium flows, such that the convective derivative $d\mathbf{v}/dt = \partial\mathbf{v}/\partial t + \mathbf{v} \cdot \nabla\mathbf{v}$ vanishes and the problem to solve is described by a force balance equation

$$\mathbf{j} \times \mathbf{B} - \nabla p = 0, \quad (5.1)$$

where as usual \mathbf{j} denotes the current density, \mathbf{B} is the magnetic field and p the plasma pressure. This problem can be solved using various approaches. First, non-linear stability simulations based on a perturbed equilibrium can find a saturated state satisfying Eq. (5.1), but must include the vacuum region. Following the approach described in chapter 4 we aim at finding a direct solution to Eq. (5.1) by means of free-boundary 3D equilibrium computations with the VMEC code, which naturally retains non-linear effects. For current-driven external kink modes, we compare the VMEC displacement amplitudes η_{mn} in straight field line coordinates with the analytically predicted non-linear saturated external kink amplitude based on [95] and described in section 4.2. The investigation is completed by a calculation of the linear growth rates and eigenfunctions, verifying that the chosen plasma configurations are indeed linearly unstable to external kink modes. For external modes driven by coupling to edge infernal modes, a model for the saturated amplitude does not exist currently. However, the non-linear results can be compared with a linear analytic model [120, 121] and linear numerical results in terms of the growth rates and structure of the Fourier decomposed eigenfunctions. In this context, we also discuss the damping of modes with higher toroidal mode number in the non-linear phase.

The chapter is organised as follows: In section 5.2 we motivate our investigation by presenting experimental data showing the existence of quiescent tokamak discharges and associated edge harmonic oscillations. Section 5.3 investigates the saturated amplitude of current-driven external kink modes in QH-mode regimes and their linear stability properties. Section 5.3 differs from chapter 4 in that the Wesson-like current profiles are substituted for QH-mode relevant current and pressure profiles, where in particular, the safety factor is very flat near the edge. This is followed by a study of coupled edge infernal and external kink modes in section 5.4. Here, the current profile is chosen so that current-driven external kinks are stabilised and pressure-driven effects can be studied in isolation. The non-linear results are compared with linear results. The non-linear damping of certain toroidal modes is discussed subsequently in section 5.5. Conclusions are presented in section 5.6 and an outlook towards non-linear initial value simulations with XTOR-2F is given in section 5.7.

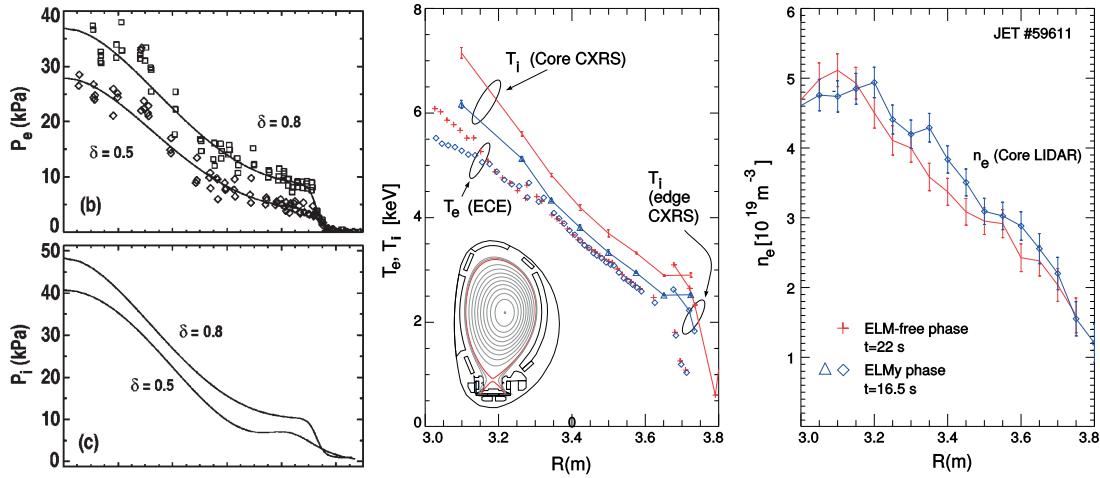


Figure 5.1 – Experimental plasma profiles of quiescent H-mode discharges. (left): Ion and electron pressure profiles for two different values of the triangularity δ of DIII-D shot 115099 [18]. (middle and right): Temperature and density profiles in ELMy and quiescent phases of JET pulse 59611 [110].

5.2 Experimental observation of quiescent H-mode regimes

The good confinement properties of the H-mode are essential for viable operation of a tokamak fusion reactor. Future tokamaks with large plasma volumes such as ITER require methods to at least mitigate ELMs, but completely ELM-free operation is favoured. A widely studied method to mitigate or suppress ELMs in the otherwise ELMing H-mode is the application of resonant magnetic perturbations (RMPs) [122]. However, it is uncertain to which degree this method can fully avoid ELMs in ITER and henceforth such coils could be employed in DEMO. As an alternative, one can aim at finding a quiescent scenario without ELMs. The existence of regimes with good H-mode-like confinement properties and at least partially ELM-free phases has been demonstrated. For example, the Hot ion H-mode [123] and VH-mode [124] both feature improved confinement properties and are initially free of ELMs. However, they are eventually terminated by the onset of large ELMs [115] with the associated deleterious effects. In JET a so-called outer mode (OM) has been observed [125]. This mode - which is localised in the outer 20% of the plasma has a low toroidal mode number, usually dominantly $n = 1$, but $n = 2, 3, 4$ outer modes are also known. Another experimentally described scenario is the I-mode [126] which features a large edge temperature pedestal but a density profile similar to L-mode. The most promising ELM-free high confinement regime is probably the quiescent H-mode (QH-mode), first established in DIII-D [127, 18] and later observed in various other tokamaks including ASDEX-U [128], JT-60U [111] and JET [110]. QH-mode operation is achieved by strong auxiliary plasma heating (neutral beam injection) and a reduction of density via cryopumping [127]. It is typically observed in plasmas with low collisionality ν^* and plasma flows are found to play a role [129, 130] (not considered here). The similarity of the plasma profiles in quiescent and ELMing H-modes is illustrated in Fig. 5.1, where density, temperature and pressure profiles of ion and electron species are

5.2. Experimental observation of quiescent H-mode regimes

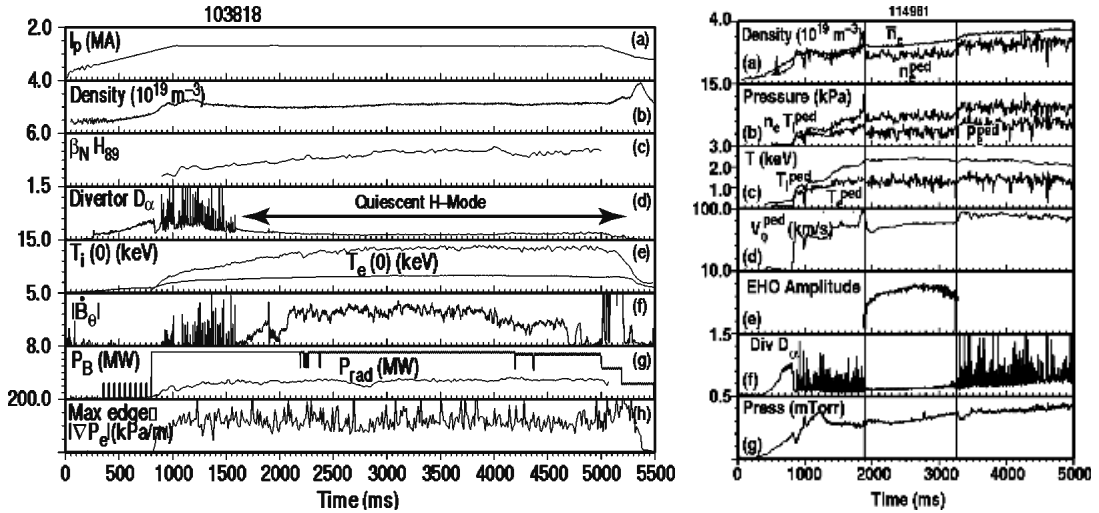


Figure 5.2 – Experimental data from DIII-D indicating a quiescent high-confinement mode with edge harmonic oscillations. (left): Time history of DIII-D shot 103818. The divertor D_α emission signal indicates a long ELM-free period starting around $t = 1500$ ms after the density was slightly reduced [127]. (right): Experimental measurements in DIII-D indicate the absence of ELMs in an H-mode shot. Edge harmonic oscillations are observed in the ELM-free phase [18].

shown in DIII-D and JET discharges. The edge pedestal is clearly visible in the n_s , T_s and p_s profiles ($s = i, e$). Comparing the profiles in an ELMy phase with those of the quiescent phase, reveals only minor differences. This highlights the good confinement properties of the QH-mode, which are attributed to the edge transport barrier. Experiments that achieved QH-mode operation at ITER-relevant values of β_N and density [131] confirm the importance of this regime for ITER and future machines. ELMing and quiescent phases can be easily distinguished in experimental measurements. ELMs drive large particle loads close to the divertor allowing for ELM detection via light emission due to the H_α and D_α Balmer lines with a wavelength of $\lambda = 656$ nm. The left part of Figure 5.2 shows measurements from DIII-D shot 103818 that demonstrate the existence of a long quiescent phase without ELMs. After an initial peak, the density is slightly reduced for most of the remainder of the shot.

QH-mode operation is accompanied by low- n (long wavelength) magnetohydrodynamic oscillations located close to the plasma edge, called edge harmonic oscillations (EHOs). Measurements detecting EHOs are shown in the time history of DIII-D shot 114981 illustrated in Fig. 5.2. During the shot a quiescent phase interrupts an otherwise ELMing plasma as indicated by the divertor D_α emission signal. The amplitude of the EHOs is measured by Mirnov coils, which are commonly used for magnetic measurements. Furthermore it is seen, that the density is lower during the quiescent phase compared with the ELMing part of the discharge. Another type of EHOs with small amplitude is found in NSTX. These oscillations have a higher toroidal mode number of $n = 4 - 6$ and displacement amplitudes of a few mm, and might not be large enough to provide particle exhaust [132]. NSTX however is a spherical tokamak with tight aspect

ratio which could lead to a different behaviour of MHD modes compared to machines with larger aspect ratio.

5.3 Current-driven external kinks in QH-mode plasmas

As in the case of baseline scenarios, QH-mode plasmas can have a q profile with an edge value below a rational value. In these situations current-driven external kink modes are expected to be linearly unstable. In contrast to chapter 4, we now use a q profile with a region of low shear near the edge of the plasma. As described below, we select this q profile so that it causes current-driven external kinks, as opposed to pressure-driven kinks examined in section 5.4. It is the edge pedestal in the QH-mode regime (together with low collisionality) that causes the flattening of the q profile near the plasma boundary via the bootstrap current (the q profile can even become slightly reversed). In this section we do not include the effect of a separatrix, which generally causes the safety factor in the far pedestal to rise quickly. As such, for $q_a \lesssim m/n$ we expect edge corrugations (as seen before in chapter 4). For this analysis we consider a JET-like configuration with up-down symmetric field coils (previously illustrated in Fig. 4.2). We note, that the VMEC model does not include a conducting wall. The mesh of field coils is at a distance of $b/a \approx 1.5$ and a conducting wall at this distance would influence the amplitude only weakly (c.f. Fig. 4.9). Thus the computed saturated displacements correspond to the most unstable situation in the limit $b \rightarrow \infty$. A pressure profile similar to experimental QH-mode profiles [18] with edge pedestal is chosen. Fig. 5.3 shows the current and pressure profiles together with the resulting safety factor q . The latter is flat close to the edge, constituting a region of low magnetic shear $s = (\rho/q)q'$, and the large current gradient has a destabilising effect on external kink modes. The edge safety factor q_a

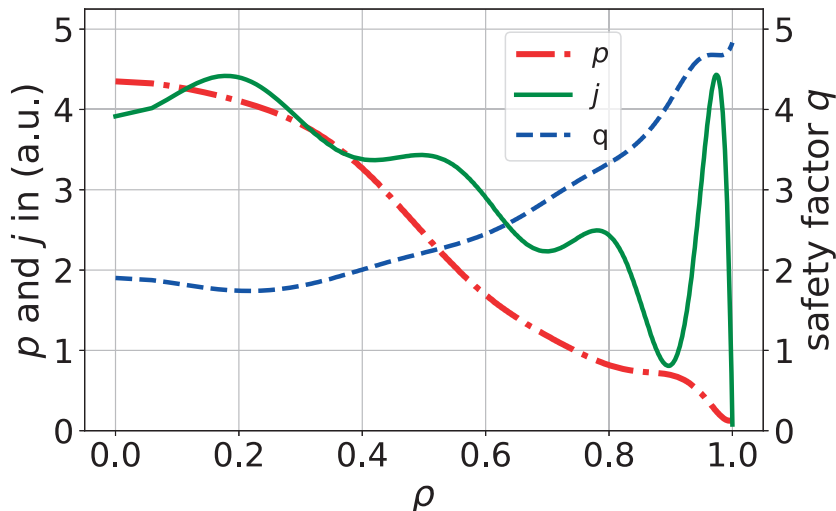


Figure 5.3 – Equilibrium profiles of a JET-like configuration with edge transport barrier and large edge bootstrap current as encountered in QH-mode operation. These profiles give rise to current-driven modes at the plasma edge.

5.3. Current-driven external kinks in QH-mode plasmas

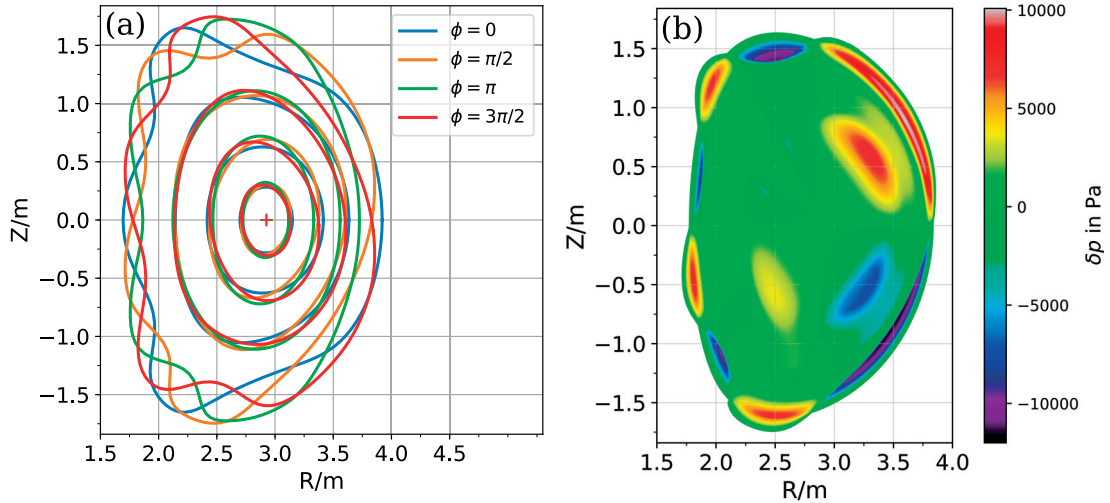


Figure 5.4 – Visualisation of the VMEC 3D equilibrium with $q_a = 3.893$. (a) Shape and position of some magnetic flux surfaces at different toroidal angles. The perturbation is strongest at the plasma edge and vanishes towards the magnetic axis (indicated by a cross). (b) Perturbation $\delta p = p_{3D} - p_{2D}$ arising from the comparison of the pressure in the 3D equilibrium with the neighbouring state.

is below the rational value $m/n = 5$, but is later scaled to study the sensitivity of the saturated non-linear amplitude of the VMEC edge displacement η to q_a . Two scalings are employed, one based on a variation of the total plasma current and another with a fixed shape of the q profile.

With a total toroidal current of $I_t = 2.56$ MA, the edge safety factor $q_a = 3.893$ lies below a rational value. VMEC converges to a 3D equilibrium state with strong edge corrugations as shown in Fig. 5.4. Similar to the 3D states obtained in baseline scenarios (Figs. 4.4 and 4.5 of chapter 4) the perturbation peaks at the last closed flux surface and vanishes towards the magnetic axis. However, the perturbation is very strong as expected from the strong current gradients close to the plasma edge.

We now vary the edge safety factor q_a by modifying the total current I_t in a range of $1.8 \text{ MA} \leq I_t \leq 2.8 \text{ MA}$ while keeping a realistic [131] beta value of $\beta_N = 1.9$ (corresponding to a beta value at the pedestal top of $\hat{\beta} = 0.6\%$). This scaling is easier to access from an experimental point of view, compared to a direct scaling of the q profile, which would modify the current density profile. In the VMEC simulations we obtain 3D states when q_a is below a rational value as seen in Fig. 5.5, where the non-linear displacement η_{mn} is calculated according to Eq. (4.31) in straight field line (sfl) coordinates. Three different windows can be identified where $4/1$, $5/1$ and $6/1$ modes are clearly dominant, while other harmonics are fairly weak. Similar to the case of the current-driven modes in baseline tokamak scenarios, coupling of poloidal modes thus plays a negligible role and therefore we can expect good comparisons with the analytical prediction of the edge displacement η in the straight tokamak limit. We emphasise that the ranges of q_a values, where the plasma remains axisymmetric are very narrow, indicating that saturated external kink modes exist for almost all q_a values. This is consistent with the range of edge

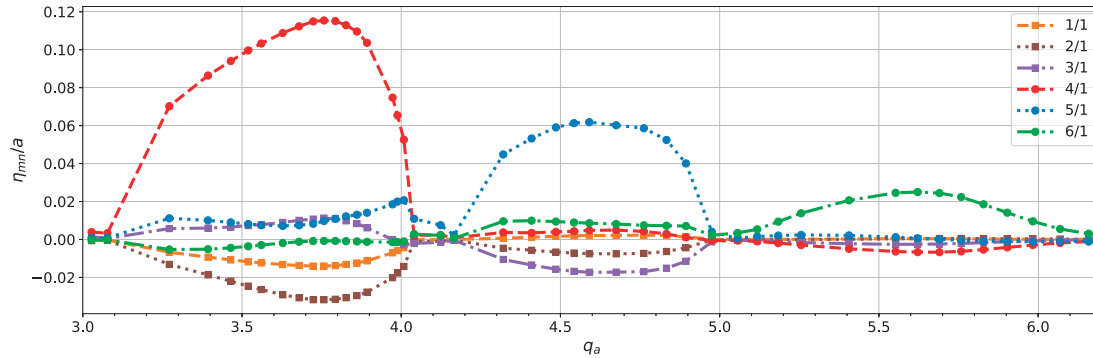


Figure 5.5 – Low- m saturated $n = 1$ edge displacement amplitudes of free-boundary VMEC equilibria with $\beta_N = 1.9$. For the scaling of q_a , the j profile was kept constant and I_t was varied. 3D states with dominant $m = 4, 5, 6$ occur, when q_a is lower than the corresponding rational value m/n .

safety factor values where QH-mode regimes were obtained experimentally in DIII-D [18]. A scaling of the saturated displacement amplitude with the poloidal mode number m is seen, where η decreases with m . This behaviour is expected for non-linear saturated external kink modes and is consistent with analytical non-linear models [99, 95]. The features of these free-boundary 3D equilibria are similar to those obtained in the baseline scenario (c.f. Fig. 4.5), with a perturbation peaking at the last closed flux surface and vanishing towards the magnetic axis.

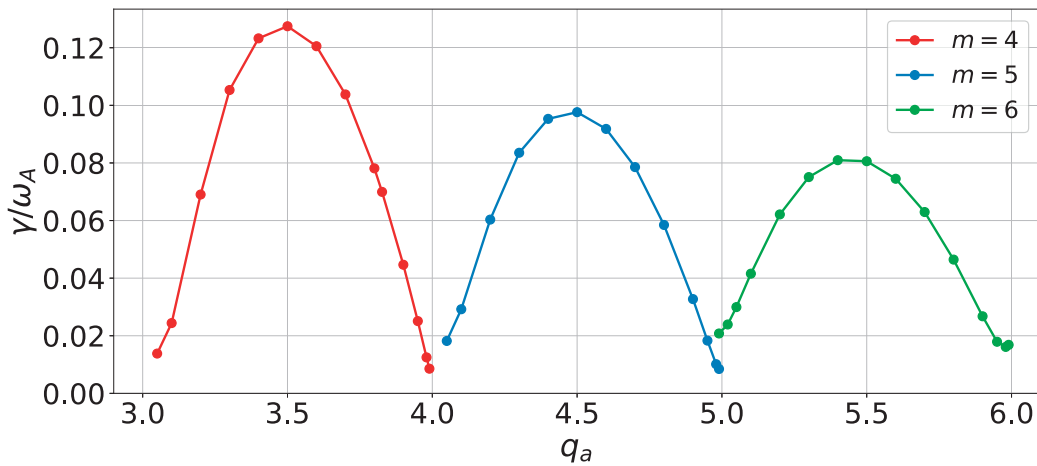


Figure 5.6 – Linear $n = 1$ growth rates γ/ω_A of the dominant $m = 4, 5, 6$ modes as a function of the edge safety factor q_a computed with KINX. A realistic beta value of $\beta_N = 1.9$ is chosen.

Non-linearly saturated external kink states arise from a linearly unstable plasma configuration. We now perform a linear stability analysis with KINX to determine the linear growth rate γ as a function of q_a , to verify that the neighbouring equilibria of the 3D

5.3. Current-driven external kinks in QH-mode plasmas

VMEC states are linearly unstable to external kink modes. For the KINX computations the axisymmetric, neighbouring equilibria of the VMEC 3D states are reconstructed with the CHEASE code. We first calculate γ for $n = 1$ modes, i.e. the same modes that are dominantly seen in the non-linear VMEC states. The normalised growth rates γ/ω_A of the dominant $m = 4, 5, 6$ external kink modes are shown in Fig. 5.6 and the linearly unstable domains agree well with those where VMEC finds corrugated states in Fig. 5.5. For the $m = 4$ and $m = 5$ mode, the growth rate approaches zero very close to $q_a = 4$ and $q_a = 5$ respectively. This corresponds to the expected upper marginal point of these modes. For the lower marginal points and the upper marginal point of the $m = 6$ mode, the situation is not as clear. In the regions of q_a where the lower marginal points would be expected, γ does not vanish. However, the regions where these marginal points are located, are close to a rational value and thus finite pressure (here $\beta_N = 1.9$) and low shear close to the edge gives rise to infernal modes that couple to external kink sidebands. Note that a weaker β case is considered next in order to eliminate the infernal mode coupling effect. A detailed study of infernal mode coupling is treated in section 5.4.

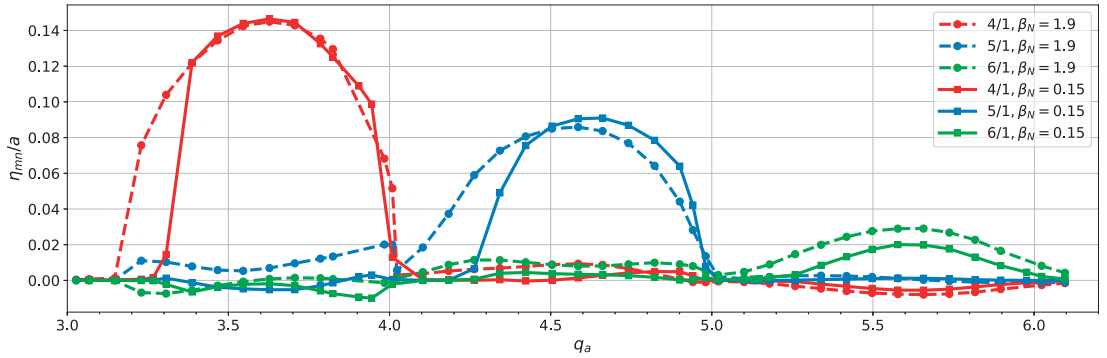


Figure 5.7 – $n = 1$ saturated VMEC edge displacement amplitudes η_{mn} of the $m = 4, 5, 6$ modes obtained at low and realistic values of β_N as a function of q_a using a large aspect ratio scaling for the q profile.

So far we varied q_a indirectly by specifying I_t in the VMEC simulations. With this initial scaling, a reduction of β in the equilibrium computations crucially affects the shape of the q profile close to the edge, making a comparison of η at different values of β_N meaningless. In the large aspect ratio approximation $q(\rho) \propto 1/I(\rho)$ and thus a variation of the total current I corresponds to a multiplication of a scalar with the whole safety factor profile. This does not hold exactly for the shaped, finite aspect ratio equilibria such as those computed with VMEC in the present work. In order to allow for a better comparison with the analytical model, we now use a different scaling of q_a by providing the q profile in VMEC and multiplying it by a scalar. This also permits a reduction of β and thus an investigation of the pressure dependency of the non-linear, saturated displacement η . With this scaling we compute VMEC free-boundary equilibria at very low (e.g. Ohmic plasma beta) pressure with $\beta_N = 0.15$ and with $\beta_N = 1.9$ respectively. For these two cases, Fig. 5.7 shows the $n = 1$ Fourier components of the dominant $m = 4, 5, 6$ modes (according to Eq. (4.31)) versus the edge safety factor q_a .

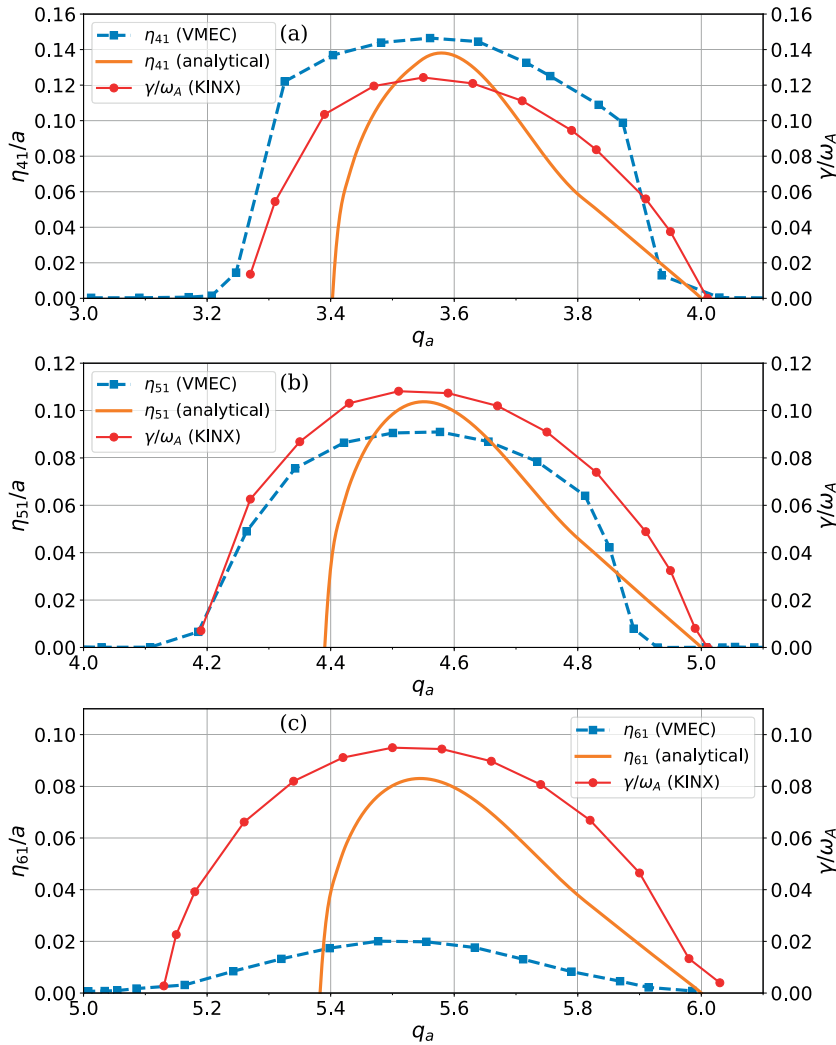


Figure 5.8 – VMEC edge displacements are compared with the analytic saturated external kink amplitude η and the normalised linear growth rate γ/ω_A computed with KINX. (a) 4/1 mode. (b) 5/1 mode. (c) 6/1 mode.

For the $m = 6$ mode a weak scaling with β_N is found, whereas η_{41} and η_{51} remain almost unaffected by the pressure except for a shift of the lower marginal point towards lower values. The displacement amplitudes of all modes are comparable in the low and high pressure case and thus the results clearly identify a current-driven mode. For a few values of q_a the mode is larger for $\beta_N = 0.15$ than for $\beta_N = 1.9$. These minor differences might be the result of changes in plasma shape and aspect ratio as the pressure is increased.

We can now compare the non-linear VMEC displacements in the low β case with the analytical prediction. Figure 5.8 shows the numerical VMEC edge displacement amplitude and analytical saturated external kink mode amplitude η_{mn} together with the normalised linear growth rate γ/ω_A (KINX) for the $m = 4$, $m = 5$ and $m = 6$ dominant modes. Again, the linearly unstable domains are very wide for all considered mode numbers. Even though the linear growth rate can give an idea about the initial growth

5.3. Current-driven external kinks in QH-mode plasmas

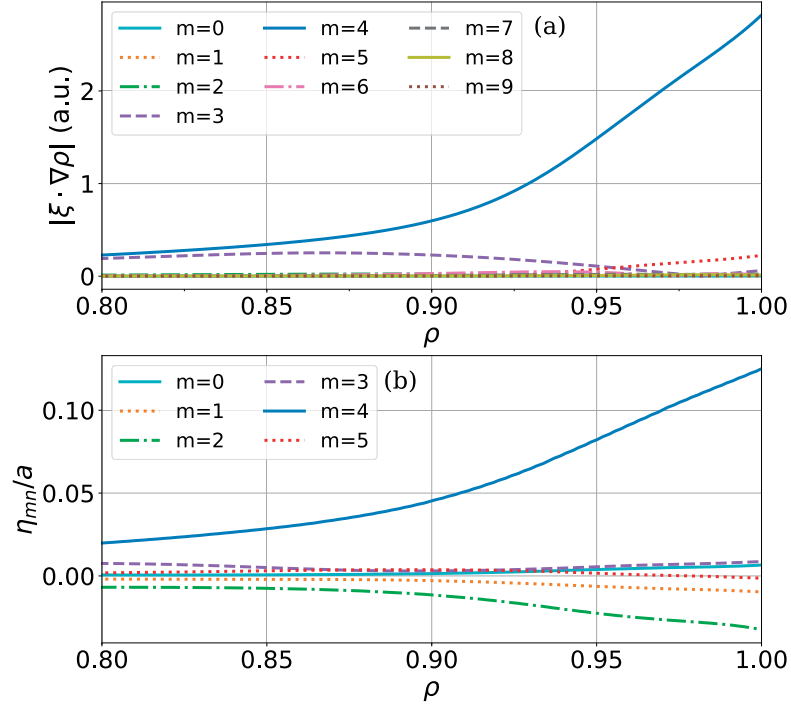


Figure 5.9 – Linear and non-linear radial displacement functions (in straight field line coordinates) in a plasma with $q_a = 3.83$ and $\beta_N = 0.15$. (a) Linear $n = 1$ (KINX) radial displacement functions for various poloidal harmonics. (b) Non-linear $n = 1$ saturated radial displacement functions η_{mn} from VMEC for various poloidal harmonics.

of modes appearing in a system, it does not in general indicate what modes are dominant in the non-linear phase. Nevertheless, it is interesting that the VMEC saturated edge displacement follows the behaviour of the linear growth rate, i.e. larger values of η_{mn} are obtained where γ is large and vice versa. The agreement with the analytical external kink mode amplitude is reasonable for $m = 4$ and $m = 5$. However, the lower marginal point is shifted to a larger value in the analytical calculation. For the $m = 6$ mode, the analytical model predicts considerably larger values for η than those obtained in the equilibrium computations. In other words, the scaling of η with m is weaker in the analytical model compared with VMEC. These differences might be attributed to the large aspect ratio approximation and circular cross section assumption of the analytical model. In KINX, the geometry effects are retained and it is interesting to compare the marginal points in the analytical model with those obtained in the shaped, toroidal equilibrium used in the numerical computations. The marginal points of KINX indeed coincide with the boundary of the domain where VMEC 3D states arise.

The VMEC non-linear radial displacement functions indicate the spatial structure of the non-linearly saturated mode. A comparison with the linear eigenfunctions from KINX is interesting and shown in Fig. 5.9. As in the case of the tokamak baseline scenario, the non-linear results well resemble the linear eigenfunctions.

In the QH-mode plasmas investigated here, external kink modes are more unstable as compared with the baseline scenario, examined in chapter 4. This is seen first from the

linear growth rates in Fig. 5.6, where for the $m = 4$ mode γ/ω_A peaks at a value of 0.124 compared to a peak of $\gamma/\omega_A = 0.04$ in the baseline scenario calculated in Fig. 4.11 of chapter 4. Similarly, comparing the non-linear saturated states of Figs. 4.10 and 4.11 with Fig. 5.7 it is clear that baseline scenario current-driven external kinks modes have smaller helical displacements than in QH-mode plasmas. In real machines the displacements of the QH-mode plasmas would reach the plasma-surrounding vessel. However, in our study the stabilising effect of a conducting wall was not considered and the results correspond to the most unstable situation. In the presence of a conducting wall close to the plasma, the amplitudes are expected to be considerably smaller and presumably small enough to not touch the wall. Even more importantly, in this section we have not modelled the effect of the separatrix on the safety factor. As will be seen in the next section, with more realistic QH-mode q profiles generally stable to the current gradient effect here, the pressure gradient produces smaller corrugations, which would not touch the vessel wall.

5.4 Pressure-driven external kink modes in QH-mode plasmas

External kink modes are mainly driven by the current gradient, but in addition the pressure can have a small destabilising effect as well. In this section we investigate edge instabilities, that are stable at low values of β and unstable as the pressure is increased. Thus, these modes can be seen as not being current-driven, however, the shape of the current profile is important since low magnetic shear close to the edge is required. The main mode seen under these circumstances is of infernal character (having poloidal mode number m_0), but coupled to external kink-like sidebands with a higher poloidal mode number of $m = m_0 + 1$. As a result, external kink modes can arise that are normally stable if only effects due to the current gradient are considered. These modes are important because they can also occur in diverted plasmas with a separatrix. Since $q_a \rightarrow \infty$ at the separatrix, current-driven modes are stabilised under such conditions.

5.4.1 Prediction of edge infernal modes with external kink sidebands

The low collisionality in the QH-mode and the steep pressure gradient in the edge pedestal constitute conditions for a strong edge bootstrap current, which flattens the q profile creating a region of low magnetic shear. As we saw in chapter 3 this can destabilise infernal modes. Linearly unstable low- n infernal modes were observed in numerical studies [133, 119]. While the current peaking close to the plasma edge due to the bootstrap current can directly trigger current-driven modes, it also flattens the q profile creating a region of low magnetic shear. This has a destabilising effect on pressure-driven infernal modes [52, 53], which can couple to sideband modes with external kink character [56, 48].

5.4.2 Non-linear numerical simulations & linear stability analysis

As in the case of current-driven modes we obtain the non-linearly saturated states in terms of free-boundary 3D VMEC equilibria. The non-linear model of external kink

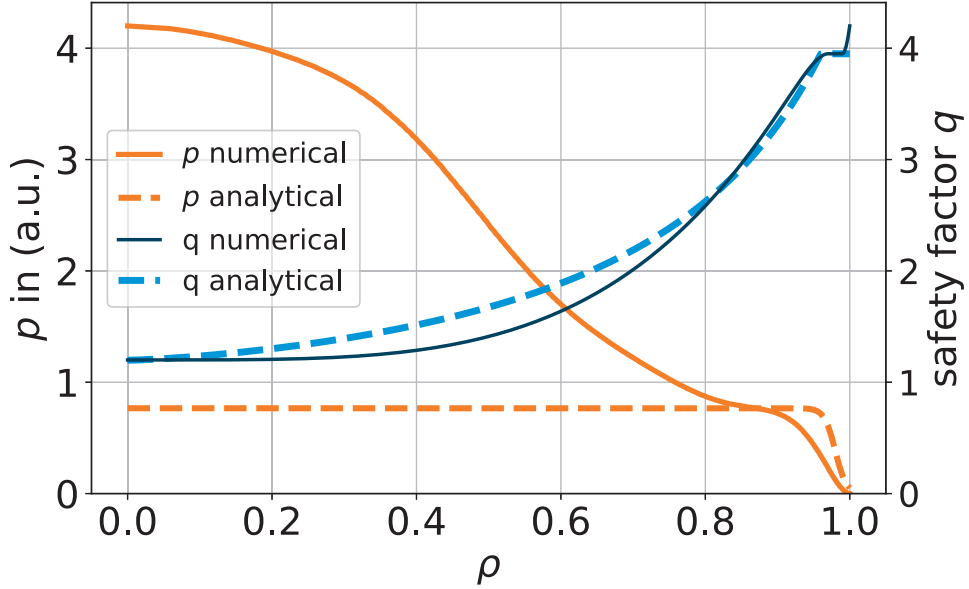


Figure 5.10 – Pressure p and safety factor (q) profiles in the numerical (solid) and analytical (dashed) study.

modes that was used in the previous sections to calculate the saturated amplitude η is not applicable for the coupled pressure-driven modes here. Due to the lack of a non-linear model for this type of modes, the saturated amplitude cannot be directly compared to analytical predictions. However, a comparison with a linear analytical model and linear numerical stability calculations are possible in terms of the growth rate γ , the linearly unstable domain and the eigenfunctions. The latter can be compared to the non-linear radial displacement functions.

The equilibrium setup differs between the analytical model and the numerical simulations. In the simulations we take profiles closer to experiments in shaped JET-like plasmas, whereas in the analytical model the profiles reflect the features of QH-mode configurations, but are chosen such that the calculations are tractable. First, in the analytical linear model [121] the q profile is taken to have the form

$$q(\rho) = \begin{cases} \frac{m_0-1}{\tilde{S} \left[1 - \left(\frac{\rho}{\rho_s} \right)^\lambda \right] + n} & , 0 < \rho < \rho_* \\ q_p & , \rho_* \leq \rho \leq 1 \end{cases}, \quad (5.2)$$

with $\tilde{S} = (n/m_0) / [(\rho_*/\rho_s)^\lambda - 1]$, where q_p is the value of q in the low-shear region, ρ_* denotes the transition from sheared to low-shear region and ρ_s is the position of the resonant surface of the lower sideband. In this model, current-driven modes, relevant when $q_p < m_0/n$, are assumed to be linearly stable. Hence, the analytic calculations do not need the small spike visible in Fig. 5.10. The pressure profile is approximated by a tanh function, which well represents the edge pedestal

$$p(\rho) = p_* \frac{1}{2} [1 - \tanh(\rho - \rho_p)/\delta], \quad (5.3)$$

Chapter 5. Saturated current-driven and pressure-driven external kink modes in extended low-shear QH-mode plasmas

where δ is small and $p_* = p(\rho_*)$ is varied to scale the value of β . In the following, we denote the beta value on top of the pedestal with $\hat{\beta}$. With these profiles - illustrated in Fig. 5.10 - the linear growth rate γ of the coupled infernal mode with mode numbers m_0/n and the external kink sideband with $m = m_0 + 1$ is calculated according to the dispersion relation [121]:

$$\gamma^2 \frac{1 + 2q^2}{2(n\omega_A)^2} + \left(\frac{\delta q}{q}\right)^2 = \left(\frac{\tilde{\beta}}{2\varepsilon}\right)^2 \left[\frac{\hat{L}_+}{1 + m_0} + \frac{\hat{L}_-}{1 - m_0} \right] A_\gamma, \quad (5.4)$$

where $\delta q = q_p - m_0/n$ is the distance of the q profile in the low shear region to the rational value, $\varepsilon = a/R_0$, R_0 is the major radius, $\tilde{\beta} = 2p_*q^2/B_0^2 \equiv \hat{\beta}q^2$, B_0 is the magnetic field strength on the magnetic axis, $A_\gamma = h/c[(ch/\delta - \tanh^{-1}(c \tanh(h/\delta)))/(h/\delta - c \tanh^{-1}(c \tanh(h/\delta)))]$, $h = a(1 - \rho_*)/2$ and the constants \hat{L}_\pm are related to the eigenfunctions and defined in Ref. [121]. In the numerical computations it is imperative that the safety factor profiles be stable to current-driven modes while retaining the features of the QH-mode. We therefore choose a profile with a flat plateau close to the plasma edge. The flattening is caused by the strong edge bootstrap current in the low collisionality regime in QH-mode. Even though the ratio q_a/q_0 is rather large, the profiles would still be linearly unstable to current-driven modes. Such modes are avoided by adding a spike to the plateau at $\rho = 0.99$ as illustrated in Fig. 5.10. This is similar to previous modelling [134, 119] of kink/peeling modes. This spike on the one hand reflects the drop of the bootstrap current in the vicinity of the last closed flux surface, but also provides a more realistic transition to the scrape of layer of a diverted plasma, where $q \rightarrow \infty$ at the separatrix. Small variations of the spike do not affect stability. We emphasise that instead of q_a , the linear growth rate of infernal modes depends on the value of q in the low shear region, denoted by q_p . In the VMEC and KINX computations the q profile is modelled in the form

$$q(\rho) = \begin{cases} q_0 + a_1\rho^{b_1} + a_2\rho^{b_2} & , 0 \leq \rho < \rho_* \\ q_p & , \rho_* \leq \rho < \rho_x \\ a_3\rho^{b_3} + a_4\rho^{b_4} & , \rho_x \leq \rho \leq 1 \end{cases}, \quad (5.5)$$

with $a_1 = b_2(q_p - q_0)\rho_*^{-b_1}/(b_2 - b_1)$, $a_2 = b_1(q_p - q_0)\rho_*^{-b_2}/(b_1 - b_2)$, $a_3 = b_4q_p\rho_x^{-b_3}/(b_4 - b_3)$, $a_4 = b_3q_p\rho_x^{-b_4}/(b_3 - b_4)$. The coefficients b_1, b_2 and b_3 are provided as input to shape the profile. Furthermore, we define

$$b_4 = \frac{-b_3q_a\rho_x^{b_3} \ln(\rho_x) + (q_p - q_a\rho_x^{b_3})W(\hat{S})}{(q_p - q_a\rho_x^{b_3}) \ln(\rho_x)}, \quad (5.6)$$

with

$$\hat{S} = \frac{b_3q_p\rho_x^{(b_3q_p)/(q_p - q_a\rho_x^{b_3})} \ln(\rho_x)}{q_p - q_a\rho_x^{b_3}}, \quad (5.7)$$

where ρ_x is the radial position separating the plateau from a spike and q_a is the value of q at $\rho = 1$, i.e. on top of the spike. To investigate the influence of $\delta q = q_p - m_0/n$ on the non-linear mode amplitude, the value of the safety factor at the plateau q_p is varied.

5.4. Pressure-driven external kink modes in QH-mode plasmas

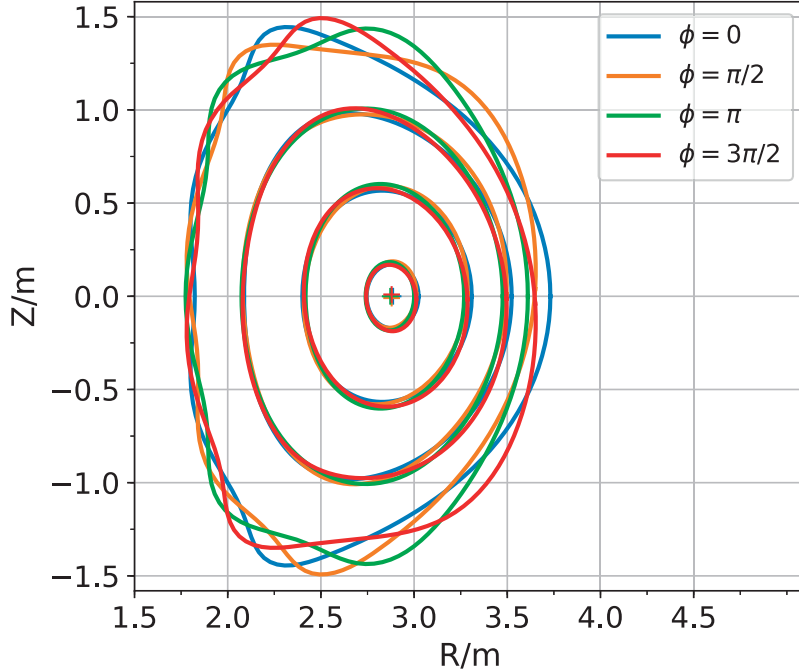


Figure 5.11 – Last closed flux surface and selected inner flux surfaces of the 3D VMEC equilibrium for $\hat{\beta} = 0.87\%$ and $q_p = 3.95$ are shown at different toroidal angles ϕ . The cross indicates the position of the magnetic axis.

However, a change of q_p necessarily affects the shape of the q profile and (with fixed $p(\rho)$) modifies the current profile. The variation of q_p thus needs to be performed such that no qualitative changes of the current density profile arise that would affect infernal mode stability. At the same time, the value of q_a has to remain below the lower marginal point of the current-driven $(m+1)/n$ external kink mode and above the upper marginal point of the current-driven m_0/n mode. This is achieved by keeping the ratio q_p/q_0 constant and fixing the value of q_a , i.e. the scaling is performed by multiplying the q profile from the magnetic axis to the plateau with a scalar α and matching the lower point of the spike $q(\rho_x)$ to αq_p . In order to consistently investigate the influence of pressure on the non-linear amplitude, we directly specify the q profile in the input for the computations. If $j(\rho)$ was provided instead, a variation of β would critically modify the q profile in the low shear region with a strong effect on stability. The pressure profile is modelled in terms of two Gaussians - one representing the core profile and the other one representing the pedestal. The sum of those Gaussians is shown in Fig. 5.10.

In the VMEC computations we now increase the size of the radial grid to 383 flux surfaces to resolve the strong variation of the q profile close to the last closed flux surface and choose coefficients $b_1 = 50$, $b_2 = 4.0$ and $b_3 = 20$ in Eq. (5.5) with $q_a = 4.2$. The VMEC simulations are carried out with edge safety factors below and above the rational value $q_p = 4$ and the features of the resulting 3D equilibrium states are visualised in terms of the perturbed flux surfaces in Fig. 5.11 for a plasma with $\hat{\beta} = 0.87\%$ and $q_p = 3.95$.

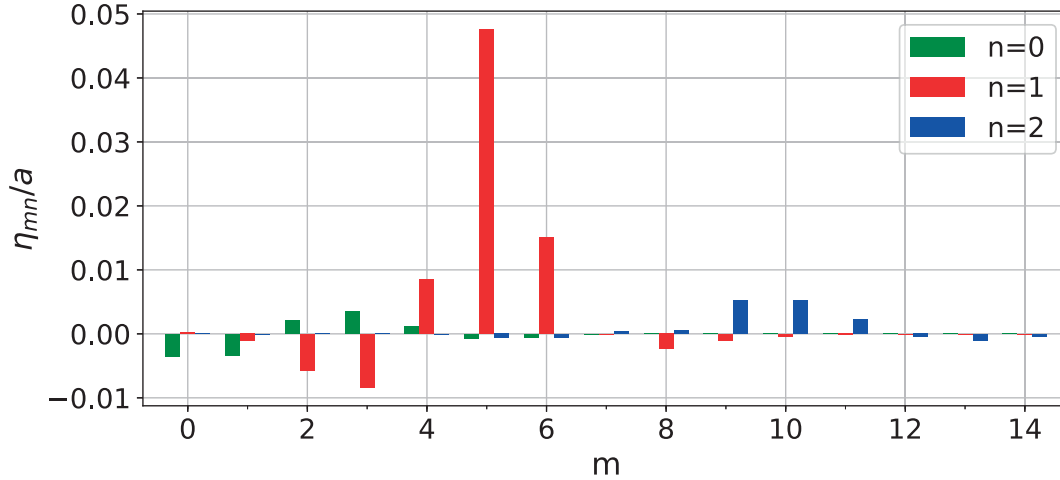


Figure 5.12 – Mode spectrum in straight field line coordinates for the plasma with $q_p = 3.95$ and $\hat{\beta} = 0.89\%$ (and global $\beta_N = 2.28$). $n = 1$ modes are dominant.

It is clear that the equilibrium state is non-axisymmetric with strong corrugations at the plasma boundary (outer flux surface shown in Fig. 5.11). Towards the plasma core the corrugation decreases and eventually vanishes at the magnetic axis, as indicated by the approximately constant position of the cross in Fig. 5.11. These properties characterise the mode as an external mode. The presence of an infernal mode, which is internal and localised in the low shear region, is not seen in this plot of flux surfaces. These connections will later be verified from the harmonics of the radial displacement functions. We now calculate the straight field line (sfl) mode spectrum of the saturated edge displacement at the last closed flux surface according to Eq. (4.31) in combination with the transformation to sfl coordinates Eq. (4.35). The result for the case of Fig. 5.11 with $q_p = 3.95$ and $\hat{\beta} = 0.87\%$ is shown in Fig. 5.12. The $m = 5/n = 1$ mode is dominant, while some other low- m modes with $n = 1$ have a finite but small amplitude. This is clearly different from a current-driven mode that would have a dominant $m = 4/n = 1$ component at the given value of $q_p = 3.95$. The observation is however consistent with the expectation from Eq. (5.4) (and the results of Ref. [121]) predicting a linearly unstable $4/1$ infernal mode with an $m = 5$ external kink-type sideband, and a growth rate of $\gamma/\omega_A = 0.007677$. Even though the $n = 1$ modes dominate, we also find small $n = 2$ modes with $m = 9, 10$ in the sfl spectrum of Fig. 5.12. This could be either due to the finite linear growth rate of the $m = 8, n = 2$ infernal mode (which is larger than that of the $4/1$ infernal mode) or non-linear mode coupling.

If the analytical growth rate and the saturated displacement is assumed to be linked, the amplitude of the VMEC edge displacement should depend on q_p and the pedestal beta $\hat{\beta}$. This dependency is investigated using the scaling for q described above and the resulting edge displacement amplitudes η_{mn} for the $5/1$ and $4/1$ modes are shown in Fig. 5.13 for various values of $\hat{\beta}$. We first focus on the cases where $q_p < 4$. Here, like current-driven external kinks, the modes are non-resonant since the main infernal mode has $m = 4$. At very low pressures, the plasma remains axisymmetric and the saturated

5.4. Pressure-driven external kink modes in QH-mode plasmas

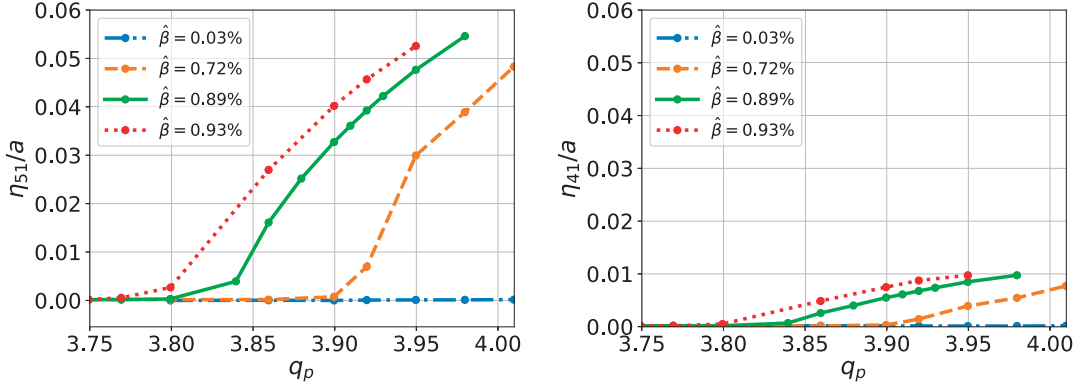


Figure 5.13 – Saturated edge displacement amplitudes of the 5/1 and 4/1 modes obtained from VMEC as a function of q_p around the rational value $q_p = 4$. The 5/1 is clearly dominant, whereas the $m = 4$ mode vanishes even for $q_p < 4$.

displacement amplitude grows with increasing pedestal beta. The domain of q_p , where non-axisymmetric states are found is wider at larger values of $\hat{\beta}$ with dominant $m = 5$ components throughout. The current-driven 4/1 mode is stable as a result of having $q_a = 4.2$ fixed for all cases presented. For $q_p > 4$ the VMEC displacement amplitudes are not as easy to evaluate. Since q_a is fixed at a value of 4.2, the safety factor profile becomes flatter for larger values of q_p . As q_p approaches q_a , a current-driven $m = 5$ external kink mode is triggered. This is shown in Fig. 5.14, where the VMEC edge displacement is nearly independent of the pressure and strong already at vanishing values of beta.

We now verify that the axisymmetric equilibria neighbouring the saturated 3D states are linearly unstable to edge infernal modes by employing the KINX code and also from the dispersion relation Eq. (5.4) with a wall distance of $b/a = 20$. The calculations are performed using the same values of $\hat{\beta}$ as in the VMEC simulations. For the case of $\hat{\beta} = 0.87\%$ the non-linear saturated displacement amplitude of the 5/1 external kink sideband is compared with the linear growth rate in Fig. 5.15. The analytical model

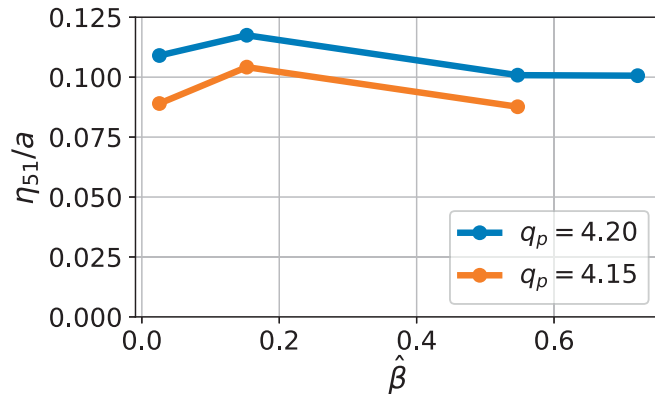


Figure 5.14 – VMEC edge displacement η of the 5/1 mode as a function of the pedestal beta $\hat{\beta}$ identifying a current-driven mode for $q_p > 4$.

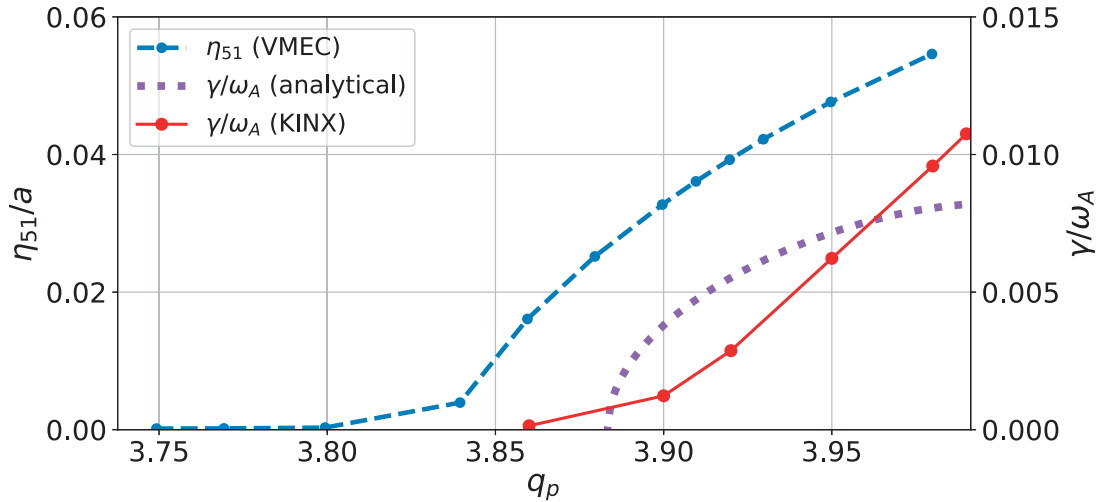


Figure 5.15 – Edge displacement amplitude from VMEC and linear growth rates calculated analytically and with KINX for $\hat{\beta} = 0.89\%$.

predicts a linearly unstable domain that has a lower marginal point of $q_p = 3.877$. When the growth rate is calculated with KINX, the linearly unstable domain agrees reasonably well with the domain where 3D states are found in VMEC. Agreement is less good if the analytic growth rate is compared with VMEC. As seen in Fig. 5.16, for other values of $\hat{\beta}$ the plasma is also linearly unstable in windows of q_p , where VMEC obtains 3D equilibria. However, the lower marginal points are shifted to slightly larger values, which can be attributed to the choice of different profiles in the model and shaping effects.

The VMEC radial displacement functions resemble the linear eigenfunctions as illustrated in Fig. 5.17, and are similar to those of edge-localised infernal modes computed in numerical stability analyses with the MARS code in similar equilibria [135]. Very good agreement between non-linear and linear eigenfunctions was already seen earlier for current-driven modes. In the analytical case the $m = 4$ eigenfunction reduces to zero in the sheared region and at the last closed flux surface due to the imposed boundary conditions, while it peaks in the low-shear region. In the numerical computations the transition from sheared to low-shear region is smoother and thus the $m = 4$ displacements are wider.

Around a rational surface $q = m_0/n$, one would expect a current-driven external kink mode of poloidal mode number m_0 . However, when the mode is driven by coupling to edge infernal modes, the sideband mode that shows external kink character is of poloidal mode number $m_0 + 1$. This observation holds particularly below the rational value, where standard current-driven external kinks of $m_0 + 1$ would be stable. Cases where current-driven m_0 modes with $q_p < m_0/n$ are unstable and at the same time $m_0 + 1$ modes are destabilised by infernal mode coupling were not investigated. For these modes however, one would expect the m_0 eigenfunction to have an infernal mode shape superimposed by an external kink structure, i.e. a bell shape with an additional local maximum at the last closed flux surface.

5.4. Pressure-driven external kink modes in QH-mode plasmas

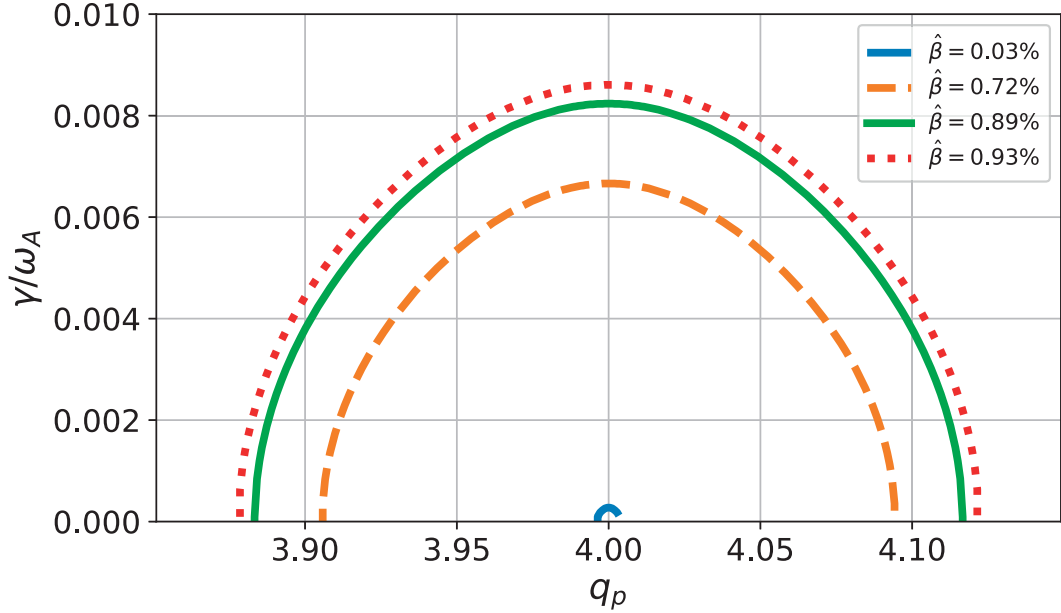


Figure 5.16 – Analytical (Eq. (5.4)) normalised linear growth rate γ/ω_A as a function of q_p for multiple values of $\hat{\beta}$ and a wall distance of $b/a = 20$.

In the non-linear VMEC and linear KINX computations the separatrix was simulated only by its effect on the q profile, but with flux surfaces taking the shape of a non-diverted plasma. External kink modes would probably be stable in a diverted plasma due to $q_a \rightarrow \infty$. Pressure-driven infernal modes and their sidebands however remain unstable, since their stability is determined by δq rather than q_a . This can be verified by computing the linear growth rates and eigenfunctions with KINX but now using a single-null X-point boundary for the equilibrium and with $q \rightarrow \infty$ at the separatrix. For this calculation, the parallel current density j_{\parallel} and pressure gradient p' are kept in the 2D equilibrium reconstruction and the shape of the plasma-vacuum interface is changed to a single-null X-point geometry. Indeed, the mode is also seen under these conditions. Due to the sharp increase of q close to boundary, it is now possible to avoid low- m current-driven instabilities completely and observe an isolated pressure-driven infernal mode with external kink sideband at $q_p > m_0/n = 4$. These results are reserved for future publication in Ref. [106].

Non-axisymmetric equilibrium states are found for values of the pedestal beta $\hat{\beta}$ in between 0.72% and 0.93%. Within this range DIII-D experiments observe QH-mode regimes with EHOs [18]. For larger values of $\hat{\beta}$, convergence in VMEC is more difficult to achieve. This could mean that mode saturation would not be achieved and the plasma would be non-linearly unstable. In experiments this situation would lead to a disruption or could correspond to ELMs.

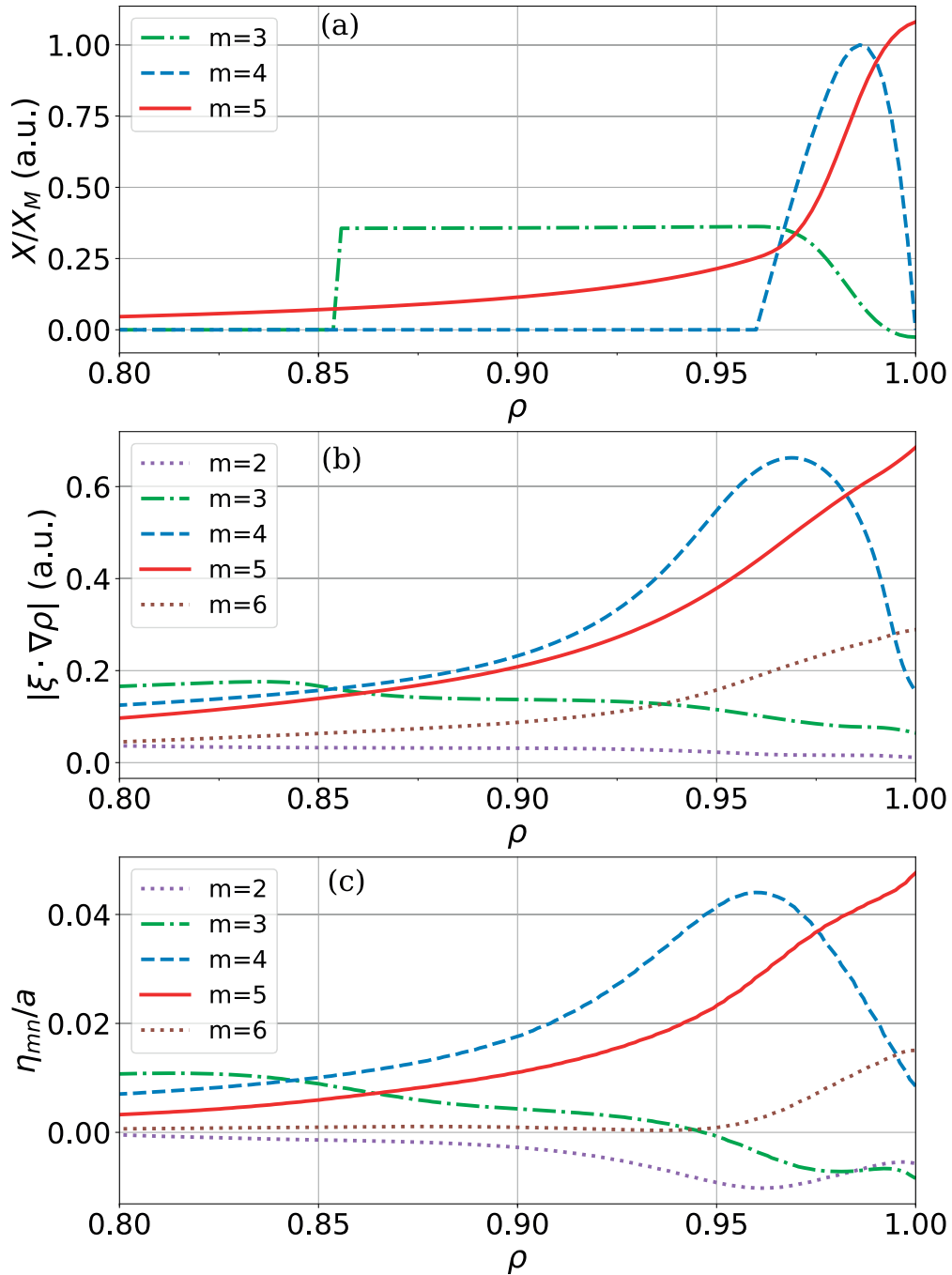


Figure 5.17 – Comparison of linear eigenfunctions and VMEC saturated displacement functions. (a) The analytical model predicts a strong $m = 4$ eigenfunction with smaller sidebands. (b) Linear $n = 1$ (KINX) radial displacement functions for various poloidal harmonics in sfl coordinates. (b) Non-linear $n = 1$ saturated radial displacement functions η from VMEC for various poloidal harmonics in sfl coordinates.

5.5. Higher n modes and non-linear damping

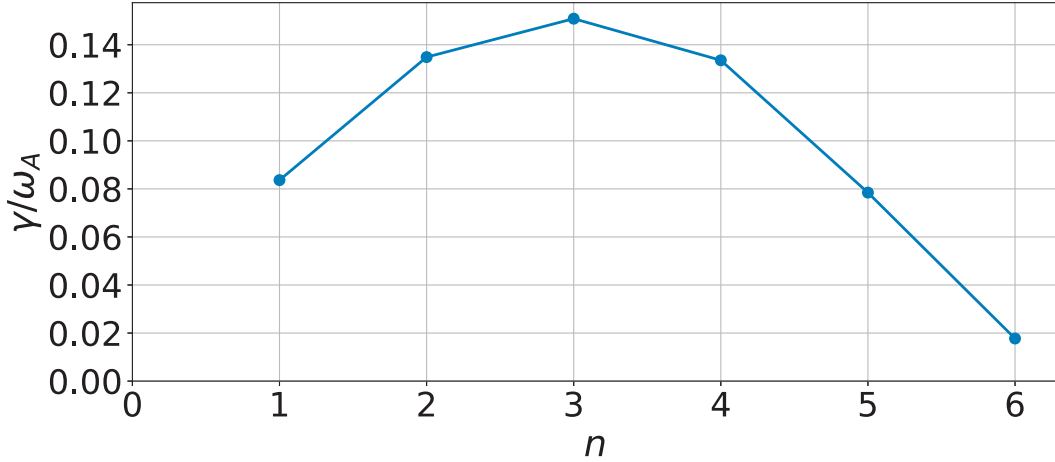


Figure 5.18 – Normalised growth rate γ/ω_A of the most unstable mode versus the toroidal mode number n for current-driven external kinks with $q_a = 3.83$ and $\beta_N = 0.15$.

5.5 Higher n modes and non-linear damping

The results from the VMEC simulations show dominant $n = 1$ modes, while modes with higher toroidal mode number are negligible¹. This is interesting, since it suggests that only $n = 1$ modes dominate the saturated states. We emphasise that in the VMEC computations no flows are considered and the situations might be different when flows are taken into account. The non-linear damping of higher n modes that are the most unstable in the linear phase was already found in reduced MHD stability calculations [39] and in the experiment [14]. We now identify to what extent certain toroidal modes are non-linearly damped in the plasma configurations studied above. For this purpose we first compute the linear growth rates of various toroidal modes with KINX.

For the current-driven external kink mode we choose $q_a = 3.83$ and $\beta_N = 0.15$, and take the same plasma profiles as for the neighbouring 3D state with dominant $n = 1$ structure in VMEC. The growth rate of the most unstable mode for various n is shown in Fig. 5.18. The growth rate of the $n = 1$ mode is rather small while modes with $n = 2 - 4$ have larger linear growth rates and thus appear more unstable linearly. Above these values, γ decreases and modes with $n > 7$ are stable. In all shown cases the most unstable mode corresponds to an external kink mode. Thus the mode spectrum in the non-linear phase is markedly different compared to the linear phase. In particular, $n > 1$ modes are strongly diminished non-linearly. These results are consistent with other observations of non-linear damping [39].

For the pressure-driven modes, we evaluate the linear growth rate γ/ω_A as a function of n for the equilibrium with $q_p = 3.95$ and $\hat{\beta} = 0.89\%$. As in the previous case of the current-driven mode, modes with $n > 1$ grow faster in the linear phase. This is seen

¹VMEC equilibria with dominant external $n = 2$ structures were observed in some plasmas with reversed shear close to the edge and $\beta_N \approx 2$. A detailed investigation of these states might follow in the future.

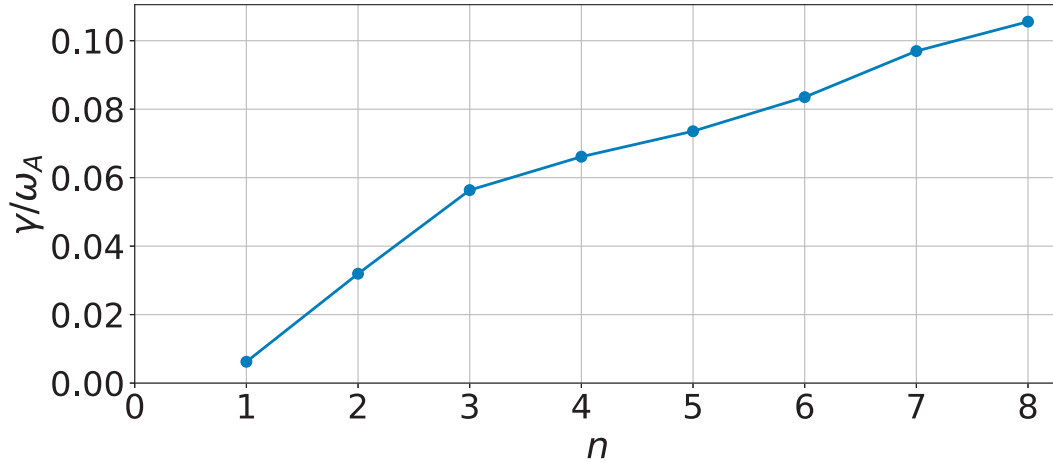


Figure 5.19 – Normalised growth rate γ/ω_A of the most unstable mode versus the toroidal mode number n for an equilibrium with $q_p = 3.95$ and $\hat{\beta} = 0.89\%$.

in Fig. 5.19, where the normalised growth rate of the most unstable mode for each n is plotted. The scaling is almost linear. In addition to the coupled infernal / external kink modes, for $n > 2$, ballooning mode structures can be seen in the spectrum. For $n \leq 4$, the coupled infernal mode/external kink mode is the most unstable. For even larger n , the ballooning modes become unstable as shown in Fig. 5.20. Linearly unstable ballooning modes are found with KINX at high values of β and for small and large values of δq . External infernal modes on the contrary disappear when q_p is far from the rational value. Recent numerical modelling suggests that medium and high n modes are stabilised by non-linear coupling and/or rotation or rotational shear [136, 137], such that only low- n kink/peeling modes remain in the non-linear phase. Even more recently Brunetti [20] has shown that high- n modes can be damped linearly by poloidal flows. In any case, the ideal non-linear damping of high n modes is reflected in the saturated VMEC states.

5.6 Conclusions

A study of non-linearly saturated external MHD modes in JET-like plasmas with edge pedestal and strong edge bootstrap current has been presented. With profiles as encountered in QH-mode operation, where edge harmonic oscillations (EHOs) are observed in experiments, we have investigated current-driven external kink modes and external kink-like sidebands connected to infernal modes by poloidal mode coupling. We have shown experimental data from DIII-D, JET and ASDEX-U that highlight the absence of ELMs in quiescent tokamak discharges accompanied by EHOs. The potential of this regime to serve as a future operation scenario motivated us to study saturated external kink states (kink/peeling modes), since a connection to EHOs is assumed. In the first part of this chapter dedicated to standard external kink modes destabilised by the current, VMEC observes $n = 1$ saturated external 3D states in a wide range of $3 \leq q_a \leq 6$ with

5.6. Conclusions

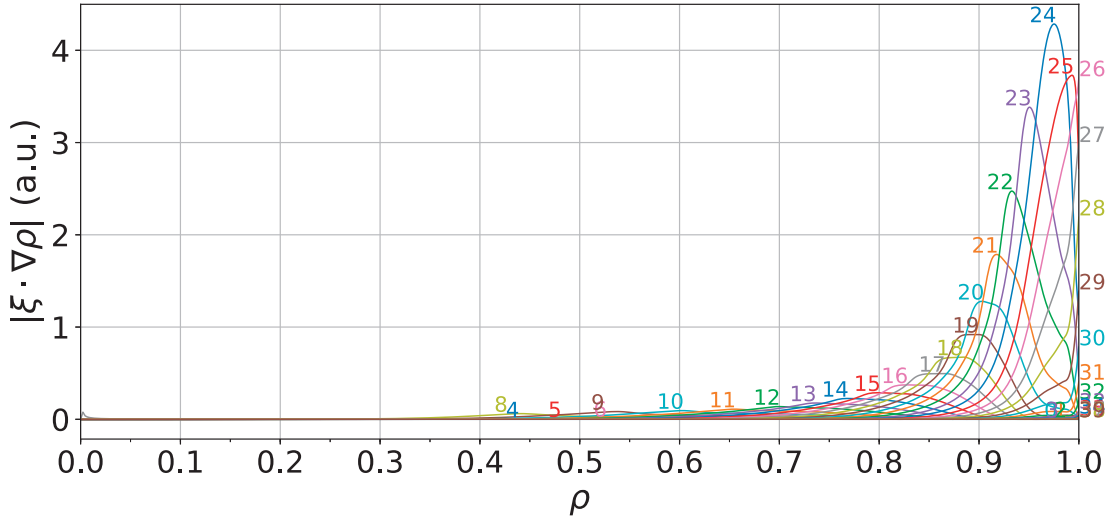


Figure 5.20 – $n = 6$ KINX sfl harmonics of the radial displacement in an equilibrium with $q_p = 3.95$ and $\hat{\beta} = 0.89\%$. The value of m is annotated to each graph.

dominant $m = 4, 5, 6$ Fourier components as expected from linear and non-linear theory. The obtained 3D equilibria clearly show the characteristics of external kink modes, and the obtained mode amplitudes in terms of the radial displacement agree well with the non-linear analytical model, introduced in chapter 4. In the windows of q_a where 3D states are found, the plasma is linearly unstable to external kink modes. The structure of the linear eigenfunctions agrees well with the non-linear radial displacement functions from VMEC.

In addition, it was demonstrated that VMEC also captures the features of external kink modes driven by coupling to pressure-driven edge infernal modes. These modes arise in the low-magnetic-shear region around the edge pedestal. The q profile was chosen such that current-driven modes are stable and the coupled infernal / external kink modes can be investigated in isolation. This was achieved by adding a spike to the q profile before the last closed flux surface, representing the sharp increase of q towards the separatrix of a diverted plasma, where $q_a \rightarrow \infty$. VMEC equilibria remain axisymmetric at low values of β and develop strong edge corrugations as β is increased. A clear scaling with δq is found. Corrugations are strong when the safety factor in the low-shear region is close to the rational value $q_p = 4$, but far away the mode remains linearly and non-linearly stable. The non-linear radial displacement functions clearly show the infernal mode localised in the low-shear region and the associated external kink mode, which peaks at the last closed flux surface. It compares well with the linear eigenfunctions from KINX and an analytical model. The poloidal mode number of external kink modes driven by edge infernal modes $m = m_0 + 1$ is augmented compared to standard current-driven external kinks. Thus, when the q profile is known in an experiment, both modes can be distinguished.

Modes of higher n appear to be damped in the non-linearly saturated states. Even though these modes are linearly more unstable, the non-linear states show dominant

$n = 1$ structures. This is particularly interesting in the pressure-driven cases, where $n \geq 4$ ballooning modes are seen in the linear phase. We conclude that VMEC is capable of capturing the features of non-linearly saturated current-driven external modes as well as external kink modes driven by coupling to pressure-driven edge infernal modes. Current-driven as well as infernal mode-driven external kinks could be connected to EHOs. The obtained VMEC equilibria can be conveniently used for fast particle and impurity transport study under QH-mode conditions.

5.7 Outlook: Non-linear stability simulations with XTOR-2F

The most direct approach to study non-linear instabilities in realistic tokamak geometry and profiles would be in terms of numerical non-linear stability simulations. For such a study the initial value code XTOR-2F could be used. For an investigation of external kink modes the code is required to model the vacuum region around the plasma. A comparison of such non-linear stability simulations with the saturated 3D states from VMEC would be valuable. Furthermore, VMEC is limited to configurations with nested magnetic flux surfaces. In most cases however, the QH-mode is observed in diverted configurations. XTOR-2F simulations including a vacuum region could model the plasma through the X-point of the separatrix and into the vacuum, and allow for a modelling of edge modes closer to experimental situations.

In XTOR-2F this is realised by taking a very high value of the resistivity outside of the plasma volume, such that no current can penetrate into the vacuum [91]. To model external instabilities realistically one needs to focus on the behaviour of the resistivity profile during the time advance in the simulations. In XTOR-2F, the grid is aligned with the initial axisymmetric equilibrium and fixed in time. It does not yet move with the plasma. Since external instabilities are accompanied by a deformation of the plasma-vacuum interface, it is necessary for the resistivity field, to follow the motion of the plasma boundary. Hence, it needs to evolve in time and in the spatial domain. Resolving these difficult technicalities will eventually provide very important results in the future.

Summary & conclusions

In this thesis the non-linear stability of neoclassical tearing modes, infernal modes and external kink modes in tokamaks has been addressed. Various numerical and analytical approaches were applied to describe non-linearly saturated states of macroscopic plasma instabilities. In addition, linear stability of the neighbouring 2D equilibria was evaluated since non-linear states can either be the result of a linearly unstable system or a linearly stable system that requires a strong seed. We now summarise the results of the preceding chapters and in this context discuss open questions that can be addressed in future studies.

The theoretical background required for the study of MHD instabilities was described in chapter 2. The ideal and resistive one-fluid MHD models are valid for long wavelength and long time scale phenomena and are capable of describing most macroscopic plasma dynamics. A central concept in the study of fusion plasmas is the plasma equilibrium, where the plasma is in force balance. We introduced the Grad-Shafranov equation that is solved to find axisymmetric toroidal equilibria. Non-axisymmetric equilibria can be found by energy minimisation, performed e.g. by the VMEC code. The concept of linear and non-linear stability was explained. While the linear approach is valid for infinitesimal perturbations and is easier to handle analytically and numerically, a non-linear treatment is important when the perturbations are of considerable size. This is particularly true for the theoretical explanation of experimentally observed plasma modes.

The occurrence of fast-growing resistive modes in experiments motivated our study of neoclassical tearing mode (NTM) triggering by coupling to infernal modes in chapter 3. Infernal modes are pressure-driven low n modes that arise in regions of low magnetic shear below the stability threshold of ballooning modes and are characterised by coupling to neighbouring poloidal modes with $m = m_0 \pm 1$. We saw that when resistivity is included in the modelling, the upper sideband has a tearing mode character. A linear model describing the dispersion relation of these coupled modes was already known. In the frame of this thesis we extended the linear model to include saturation of the infernal mode in the early non-linear phase and thus a vanishing of the mode coupling. This model requires knowledge about the magnetic island width associated to the NTM at the moment of saturation. Numerical simulations of resistive MAST-like plasmas were performed with the XTOR-2F code. The linear and non-linear evolution of NTMs was investigated with and without inclusion of bootstrap current effects. NTMs are triggered in both cases and the linear evolution is unaffected by the bootstrap current. Calculated from the Rutherford equation, the tearing stability index Δ' indicates that tearing

modes are stable in the considered equilibrium when no coupling effects are taken into account. By including the contribution due to infernal mode coupling the threshold for instability is exceeded and thus coupling is found to seed NTMs. As expected from the standard Rutherford equation, effects due to the bootstrap current are found to provide a destabilising effect in the non-linear phase. The saturated magnetic island width is thus larger when bootstrap current effects are present compared to the case without bootstrap current. The investigation focused only on $m = 1/n = 1$ infernal modes with $m = 2/n = 1$ NTMs.

In a future step, simulations of experimentally important $n = 2$ modes could be carried out. This requires a modification of the equilibrium used for the $n = 1$ study, which is linearly stable to classical $3/2$ tearing modes. A modification of the q profile in the sheared region around the $q = 3/2$ rational surface can stabilise the tearing mode linearly. At the same time, the q profile should be chosen such that this rational surface is sufficiently far from other low m rational surfaces such that the island chains do not overlap. The results could then be compared to the analytical model for the early non-linear phase.

Non-linearly saturated modes are typically calculated with numerical initial value stability codes such as XTOR, or in a few simple cases by analytical calculations. In chapter 4 we explored the possibility to describe current-driven saturated external kink modes by means of free-boundary 3D equilibrium states computed with the VMEC code. Here, the vacuum magnetic field is determined from the currents in the magnetic field coils and the plasma boundary evolves during the energy minimisation iterations. This is essential since external kink modes alter the shape of the last closed flux surface. For this study, monotonic equilibrium profiles were assumed, which is relevant to tokamak baseline scenarios. VMEC obtains 3D states with displacement amplitudes maximum at the last closed flux surface in well defined regions of the edge safety factor q_a , where the system is also linearly unstable. By comparing the 3D states to their neighbouring axisymmetric equilibria, we calculated the radial displacement of the VMEC flux surfaces based on geometric considerations. The radial displacement is taken as the distance of the 3D flux surface to the 2D flux surface (in direction perpendicular to the latter), and as such it is a function of the poloidal and toroidal angles on each flux surface. A transformation from VMEC flux coordinates to straight field line coordinates is performed to describe the Fourier spectrum in the most intuitive way. To compare the saturated VMEC displacement amplitudes to an analytical prediction, a system of three coupled differential equations was solved numerically. The code uses a finite difference scheme of second order, and was implemented in Python and benchmarked with known results. The lack of a conducting wall in VMEC means that the obtained displacement amplitudes correspond to the most unstable situation in the limit of infinite wall distance $b \rightarrow \infty$. The agreement with the analytical model is very good. Differences can be attributed to the simplifications made in the analytical model, especially the neglect of pressure and geometrical effects. Linear growth rates were calculated numerically with KINX, showing that the equilibria are linearly unstable with respect to external kink modes in the parameter space where VMEC captures non-axisymmetric states. The

results show that VMEC is capable of describing the characteristic features of external kink modes.

VMEC was then employed to study the non-linear stability properties of external kink modes in quiescent H-mode (QH-mode) plasmas in chapter 5. In the QH-mode regime, low collisionality and the edge pedestal give rise to a strong bootstrap current close to the edge. Two very different destabilising mechanisms were considered individually. First, standard current-driven external kink modes were investigated at low values of β and with q profiles that have a low ratio q_a/q_0 . Such cases were found to be linearly unstable to external kink modes, but stable to pressure-driven modes. Saturated $n = 1$ states with dominant $m = 4, 5, 6$ components were obtained with VMEC when $q_a < m/n$. Again, the equilibria were shown to be indeed linearly unstable to external kink modes in the parameter space where VMEC converges towards 3D equilibrium states. Good agreement with the analytically predicted saturated external kink mode amplitude η was found for the $m = 4, 5$ modes. However, the scaling of η with m is slightly different.

A different destabilising mechanism is effective when the pressure is kept at realistic QH-mode values of $\beta_N \approx 1 - 2$. Together with the low magnetic shear caused by the bootstrap current, the pressure gradient in the edge pedestal linearly destabilises infernal modes that are coupled to external kink-like sidebands. These instabilities were investigated in the second part of chapter 5. The q profile was modified to have a low value on the magnetic axis above $q = 1$ and a plateau close to the plasma edge where it is flat with a value close to m/n . A spike on top of the plateau lifts the safety factor on the last closed flux surface sufficiently above the rational value to avoid current-driven external kink modes. This also simulates the presence of a separatrix of a diverted plasma. In the spectrum of radial VMEC displacements strong $n = 1$ infernal modes localised in the low-shear region were identified together with an external kink sideband. On the last closed flux surface the external kink mode is dominant. Here, the external kink modes that appear in the form of sidebands differ from current-driven external kinks in the poloidal mode number. The edge corrugation has a poloidal mode number augmented by 1 (compared to current-driven modes), since the rational value corresponds to the main infernal mode. The results suggest that EHOs could correspond to both standard current-driven external kinks or sidebands linked to an infernal mode. Finally, in the saturated VMEC states we find only one dominant toroidal mode number, while in the linear phase multiple modes with higher n are unstable. These modes appear to be damped non-linearly such that only $n = 1$ (and in rare cases also $n = 2$) modes remain. No flows were however considered in the presented analysis, which could alter the mode structure. Dissipative effects could be included in future non-linear initial value simulations, for example with the XTOR-2F code.

This thesis shows that non-linear studies are important to understand the macroscopic processes in toroidal fusion plasmas. On the one hand, a strong initial perturbation can be provided in terms of a seed for neoclassical tearing modes, driving a mode unstable that would be otherwise stable in a purely linear picture. On the

Chapter 6. Summary & conclusions

other hand, this thesis has shown that the spectra of unstable modes differ in the experimentally relevant non-linear stage. Low magnetic shear is experienced in various tokamak operation scenarios and can be central for the development of non-linear pressure-driven instabilities with associated toroidal sidebands.

Curvilinear coordinates & vector formalism

Choosing a coordinate system that reflects the geometry of a given problem does not only simplify its formulation, but can be crucial to finding a solution. Curvilinear coordinates are of crucial importance for the study of toroidal systems and various coordinate choices are used throughout this thesis. We now provide a general description of curvilinear coordinates starting with the definition of the dual basis and an explanation of the related vector formalism. This is followed by the introduction of a few specific curvilinear coordinate systems used in this thesis.

A.1 Definition of general curvilinear coordinates

A system of general, non-orthogonal, curvilinear coordinates u_i in a three-dimensional space can be defined by a set of functions depending on Cartesian coordinates x_i

$$u_1 = u_1(x_1, x_2, x_3) \quad , \quad u_2 = u_2(x_1, x_2, x_3) \quad , \quad u_3 = u_3(x_1, x_2, x_3). \quad (\text{A.1})$$

In the following, Einstein notation is used, i.e. summation is performed over repeated (upper and lower) indices. We have the freedom to choose any set of three linear independent vectors as a basis. After defining appropriate functions u_i and writing the position vector \mathbf{r} in terms of u_i , the basis can either be expressed in terms of covariant basis vectors

$$\mathbf{e}_i = \frac{\partial \mathbf{r}}{\partial u_i}, \quad (\text{A.2})$$

which are tangent to the u_i coordinate curves or in terms of contravariant basis vectors

$$\mathbf{e}^i = \nabla u_i, \quad (\text{A.3})$$

which are perpendicular to the u_i coordinate surfaces [138]. The covariant and contravariant basis vectors are in general a function of the position vector \mathbf{r} . Fig. A.1 sketches the two dual bases in a point P . Any arbitrary vector can be written in terms of both covariant or contravariant basis vectors with contravariant or covariant components respectively:

$$\mathbf{A} = A^i \mathbf{e}_i = A_i \nabla u_i. \quad (\text{A.4})$$

The Jacobian matrix of the coordinate system is defined as

$$\underline{\underline{J}} = \begin{pmatrix} \partial x_1 / \partial u_1 & \partial x_1 / \partial u_2 & \dots & \partial x_1 / \partial u_n \\ \partial x_2 / \partial u_1 & \partial x_2 / \partial u_2 & \dots & \partial x_2 / \partial u_n \\ \vdots & \vdots & & \vdots \\ \partial x_n / \partial u_1 & \partial x_n / \partial u_2 & \dots & \partial x_n / \partial u_n \end{pmatrix}, \quad (\text{A.5})$$

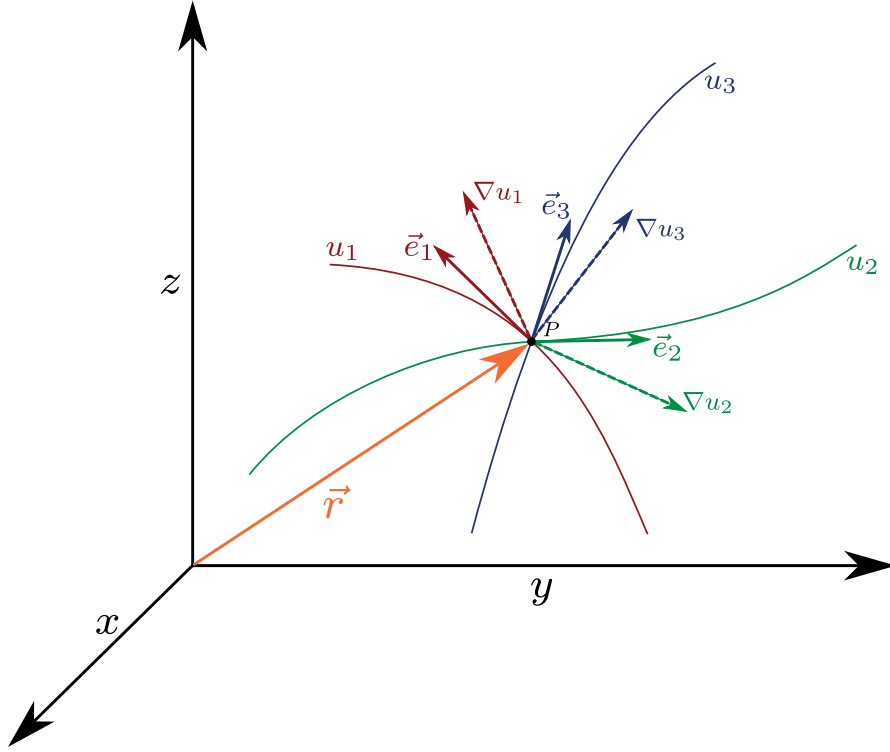


Figure A.1 – Curvilinear coordinates defined by three functions u_1, u_2, u_3 with corresponding covariant \mathbf{e}_i and contravariant ∇u_i basis vectors at the point P .

where a three-dimensional space is assumed in this thesis (i.e. $n = 3$). $\underline{\underline{J}}$ is related to the metric tensor $\underline{\underline{g}} = \underline{\underline{J}}^T \underline{\underline{J}}$. The Jacobian \mathcal{J} is given by [139]

$$\mathcal{J} = \sqrt{g} = \frac{1}{\nabla u_1 \cdot \nabla u_2 \times \nabla u_3} = \mathbf{e}_1 \times \mathbf{e}_2 \cdot \mathbf{e}_3, \quad (\text{A.6})$$

and the volume element of a curvilinear coordinate system reads

$$dV = \mathcal{J} du_1 du_2 du_3. \quad (\text{A.7})$$

This expression is used in chapter 4 to perform a transformation of VMEC flux coordinates to straight field line coordinates. For right-handed coordinate systems the Jacobian is positive, whereas it is negative for left-handed coordinates (e.g. in VMEC). It also allows a transformation of covariant and contravariant basis vectors according to

$$\nabla u_i = \frac{1}{\mathcal{J}} \mathbf{e}_j \times \mathbf{e}_k, \quad \mathbf{e}_i = \mathcal{J} (\nabla u_j \times \nabla u_k). \quad (\text{A.8})$$

Finally, we define the differential operators in curvilinear coordinate systems. First, for a scalar field Φ the gradient is conveniently written in terms of the contravariant basis vectors as

$$\nabla \Phi = \frac{\partial \Phi}{\partial u_i} \nabla u_i. \quad (\text{A.9})$$

A.2. Cylindrical coordinates

For a vector field \mathbf{A} the divergence can be expressed in terms of contravariant vector components

$$\nabla \cdot \mathbf{A} = \frac{1}{\mathcal{J}} \frac{\partial}{\partial u_i} (\mathcal{J} A^i), \quad (\text{A.10})$$

and the curl is

$$\nabla \times \mathbf{A} = \nabla A_j \times \mathbf{e}^j = \frac{\partial A_j}{\partial u_i} \mathbf{e}^i \times \mathbf{e}^j. \quad (\text{A.11})$$

A.2 Cylindrical coordinates

Two types of cylindrical coordinate systems are used in the study of fusion plasmas, both of them are orthogonal. First, standard cylindrical coordinates (r, θ, z) , with position vector

$$\mathbf{r} = r \cos(\phi) \mathbf{e}_x + r \sin(\phi) \mathbf{e}_y + z \mathbf{e}_z, \quad (\text{A.12})$$

are convenient for analytical studies of cylindrical or straight tokamak plasmas. Here, the z coordinate replaces the toroidal angle. A second system of cylindrical coordinates, adapted for toroidal problems, is the one used for example in the VMEC code and shown in Fig. 2.2. The Jacobian of the cylindrical VMEC coordinate system is given by $\mathcal{J} = R \det(G_{ij})$, where $G_{ij} = \partial x_i / \partial \alpha_j$ with $(x_1, x_2, x_3) = (R, \phi, Z)$ and $(\alpha_1, \alpha_2, \alpha_3) = (\rho, \theta, \phi)$ (VMC flux coordinates). In general, the orientation of the angular variable can be chosen. Both systems, (R, Z, ϕ) and (R, ϕ, Z) are right-handed, but with opposite orientation of ϕ .

A.3 Straight field line coordinates

Flux coordinates well reflect the geometry of toroidal systems and consist of a radial variable and two angular variables θ, ϕ in poloidal and toroidal direction respectively. The radial variable is zero on the magnetic axis and increases radially outwards. It is constant on each flux surface and 'labels' the flux surfaces. Common choices for the radial variable are the poloidal magnetic flux ψ or the toroidal magnetic flux Φ . In numerical codes it is also customary to use integers to number the flux surfaces. In general, any flux surface quantity can be used as a radial variable. Straight field line coordinates are a special case of flux coordinates. In general flux coordinates magnetic field lines have a trajectory that is not straight when viewed in the (θ, ϕ) -plane. However, it is possible to modify the angular variables in order to straighten the magnetic field lines. Since such a transformation can be applied either to the poloidal angle, the toroidal angle or a combination of both, there is an infinite number of possible straight field line (sfl) coordinates. In tokamak studies we naturally choose to keep the toroidal angle the same as the orthogonal cylindrical angle described in section A.2. Thus, we modify the poloidal angle, which can be defined in terms of the q profile as given by Eq. (2.15). Similarly, in axisymmetry the poloidal angle is

$$\theta = \frac{F(\psi)}{q(\psi)} \int_0^l \frac{dl}{R|\nabla\psi|}, \quad (\text{A.13})$$

Appendix A. Curvilinear coordinates & vector formalism

where $F(\psi) = RB_\phi$, $|\nabla\psi| = R|\nabla\psi \times \nabla\phi| = R|B_\theta|$ and dl is the poloidal arc length l (arc length in direction of the poloidal magnetic field). A more sophisticated expression for dl is found by equating the volume elements of cylindrical (R, Z) and flux coordinates (ψ, l) [22], i.e. $dRdZ = \mathcal{J}d\psi dl$. In the latter coordinate system the poloidal angle θ is replaced by the arc length in poloidal direction l . The Jacobian of this coordinate transformation is $\mathcal{J} = 1/RB_\theta$ and thus we obtain $dl = RB_\theta dRdZ/d\psi$. The angle given by Eq. (A.13) is equivalent to the sfl angle defined by Eq. (4.35) used to calculate the mode spectrum of the VMEC displacements in chapters 4 and 5.

For 3D systems it is possible to define straight field line angles by a modification of the poloidal and toroidal angles. Examples of such widely used straight field line coordinate systems are Hamada coordinates and Boozer coordinates. The latter are commonly applied in stellarator studies.

One peculiarity of sfl coordinates is the low resolution on the low field side compared to other toroidal coordinates, such as flux coordinates or coordinate systems with geometrical angles. A comparison is shown in Fig. A.2, where equidistant lines of the poloidal variable are plotted among lines of constant magnetic flux.

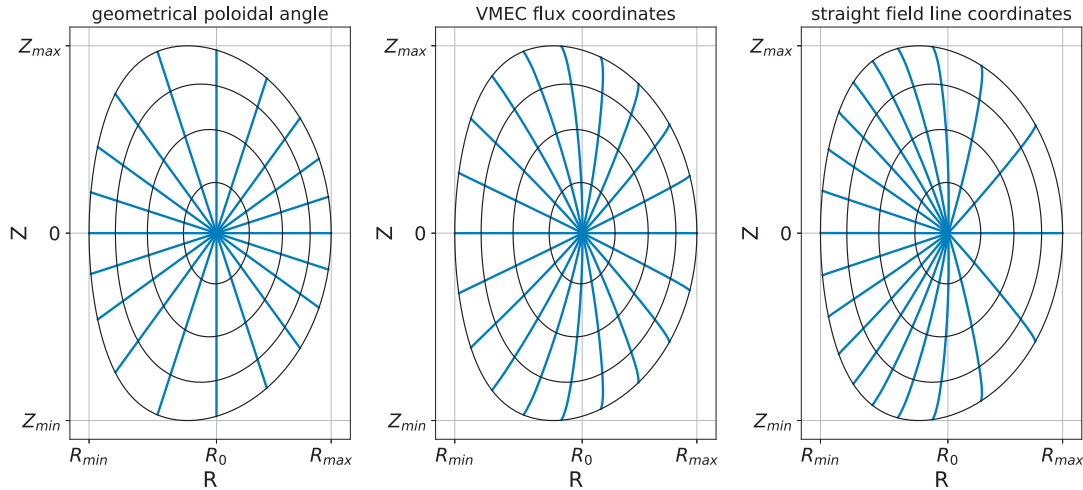


Figure A.2 – Equidistant lines of constant poloidal angle θ with $\Delta\theta = \pi/10$ (blue) are shown in different coordinate systems among lines of constant magnetic flux (black) in the poloidal cross section.

Reconstruction of the magnetic field perturbation from the radial displacement

In the following, we provide equations that allow for a calculation of the magnetic field perturbation based on the radial displacements obtained from the KINX code and eventually the VMEC 3D equilibria.

We start with an axisymmetric magnetic field, written in the form

$$\mathbf{B} = F(\psi)\nabla\phi + \nabla\phi \times \nabla\psi, \quad (\text{B.1})$$

where $F(\psi) = RB_\phi$ is a flux function and ψ is the poloidal flux. The Jacobian is given by $\mathcal{J} = qR^2/F$ and the linear perturbations taken to be of the form $\xi \sim \exp(im\theta + in\phi)$. In linear MHD the perturbed magnetic field is given by $\delta\mathbf{B} = \nabla \times (\xi \times \mathbf{B})$ and the components of $\delta\mathbf{B}$ are determined by [140]

$$\delta\dot{B}^\psi = \frac{1}{\mathcal{J}} \left[inq + \frac{\partial}{\partial\theta} \right] \delta U^\psi, \quad (\text{B.2})$$

$$\delta\dot{B}^\theta = -\frac{1}{\mathcal{J}} \left[\frac{\partial\delta U^\psi}{\partial\psi} + in(\delta U^\phi - q\delta U^\theta) \right], \quad (\text{B.3})$$

$$\delta\dot{B}^\phi = -\frac{1}{\mathcal{J}} \left[\frac{\partial}{\partial\psi}(q\delta U^\psi) + \frac{\partial}{\partial\theta}(q\delta U^\theta - \delta U^\phi) \right], \quad (\text{B.4})$$

where \mathbf{U} is the fluid velocity and related to the displacement by $\mathbf{U} = d\xi/dt$. To obtain the $\delta\mathbf{B}$ components as a function of the displacements, we can straightforwardly integrate Eqs. (B.2)-(B.4) with respect to time. In addition, from the Shear-Alfvén law¹ [141] the parallel perturbed magnetic field is

$$\delta\mathbf{B}_\parallel = \frac{\xi^\psi}{B} \frac{dp}{d\psi}. \quad (\text{B.5})$$

Now, the contravariant component of the perturbed magnetic field is $\delta\mathbf{B}^\phi = \delta\mathbf{B} \cdot \nabla\phi = \delta\mathbf{B} \cdot \mathbf{e}_\phi/R$ and the parallel magnetic field perturbation is approximately given by $\delta\mathbf{B}_\parallel = \delta\mathbf{B} \cdot \mathbf{e}_\phi$. Combining these equations and equating it with the integrated form Eq. (B.4), we obtain

$$\frac{\partial}{\partial\theta} (q\xi^\theta - \xi^\phi) \approx -\frac{\mathcal{J}\xi^\psi}{RB} \frac{dp}{d\psi} - \frac{\partial}{\partial\theta}(q\xi^\psi). \quad (\text{B.6})$$

¹The Shear-Alfvén law is valid for low frequency waves far from the sound frequency and for radial wavelengths much smaller than the size of the system.

Appendix B. Reconstruction of the magnetic field perturbation from the radial displacement

which allows us to eliminate the poloidal and toroidal components of the displacement. Substituting the last term of Eq. (B.4) by Eq. (B.6) we obtain for the contravariant toroidal magnetic field perturbation

$$\delta B^\phi \approx \frac{\xi^\psi}{RB} \frac{dp}{d\psi}. \quad (\text{B.7})$$

Integrating Eq. (B.6) with respect to θ we can substitute $\xi^\phi - q\xi^\theta$ in the last term of the integrated form of Eq. (B.3), yielding

$$\delta B^\theta = -\frac{1}{\mathcal{J}} \left[\frac{\partial \xi^\psi}{\partial \psi} + in \int \left(\frac{\mathcal{J} \xi^\psi}{RB} \frac{dp}{d\psi} + \frac{\partial}{\partial \psi} (q \xi^\psi) \right) d\theta \right]. \quad (\text{B.8})$$

Finally, for the radial component of $\delta \mathbf{B}$, integration of Eq. (B.2) with respect to time directly yields

$$\delta B^\psi = \frac{1}{\mathcal{J}} \left[inq + \frac{\partial}{\partial \theta} \right] \xi^\psi. \quad (\text{B.9})$$

Knowing the radial displacement ξ^ψ from KINX, Eqs. (B.7)-(B.9) provide the perturbed magnetic field. Given the similarity of the linear external kink eigenfunctions and the non-linear radial VMEC displacement functions, Eqs. (B.7)-(B.9) could also provide information about the non-linear perturbed magnetic field.

Development of numerical codes & tools

C.1 Calculation of the magnetic island width based on Poincaré plots

Poincaré plots show the magnetic topology in the poloidal cross section. Remapping the actual poloidal plasma cross section into a plane with θ on the vertical axis and r on the horizontal axis, magnetic islands can be conveniently visualised. Using image processing methods combined with a graphical user interface (GUI) implemented in Matlab, a tool was created to estimate the width of magnetic islands from the location of the island separatrix. This GUI is shown in Fig. C.1.

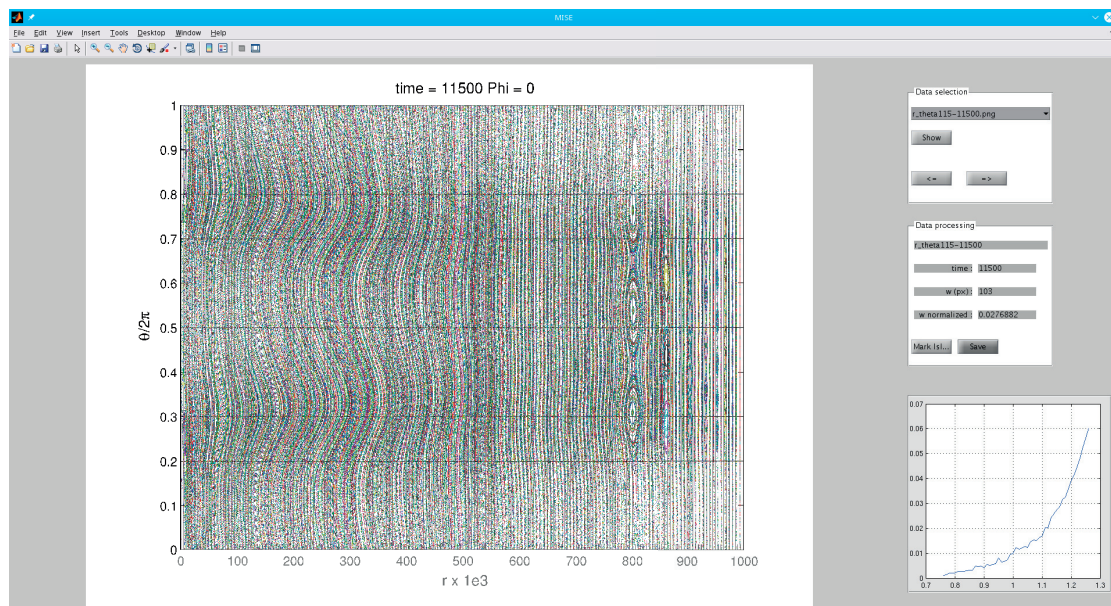


Figure C.1 – Graphical user interface written in MATLAB for the evaluation of the magnetic island width based on Poincaré plots.

The GUI reads a rasterised image file with a fixed position of the plot area inside the image. Each magnetic field line in the Poincaré plot is therefore associated to certain (x, y) coordinates in the image plane. The coordinates of the innermost and outermost points on the island separatrix are determined by selecting these points inside the image. The island width in units of pixel is simply given by $w_{px} = x_{out} - x_{in}$. The width of

the plot area in units of pixel a_{px} corresponds to the normalised plasma minor radius $r(a)$ and is used to express the island width in terms of the normalised poloidal flux $w_\psi = w_{px}/a_{px}$, known from the equilibrium computations. However, since the normalised poloidal flux is not proportional to the minor radius, the actual island width in terms of the normalised toroidal flux can be calculated from further mapping ψ to Φ , since $\Phi(\psi)$ is known from the CHEASE equilibrium computations. Each Poincaré plot is associated to a certain point in time t in the XTOR-2F initial value simulation. The GUI enables the evaluation of multiple plots at different t and associated island width, thus allowing for a quick determination of the temporal evolution of a magnetic island.

C.2 Solver for non-linearly saturated external kink amplitudes

The following section provides details about the implementation of the numerical solver for the boundary value problem given by the system of equations (4.18)-(4.20) that determines the saturated non-linear external kink mode amplitude η . Second and fourth order finite differences schemes were implemented.

C.2.1 Numerical scheme & Implementation

In the following calculations we assume a one-dimensional grid with $N + 1$ equally spaced grid points ρ_i with distance $h = \rho_{i+1} - \rho_i$. Expressions for finite differences are found via Taylor expansion of a function $f(\rho)$ around the grid points neighbouring a point ρ_i

$$\mathcal{T}f(\rho; \rho_i) = f(\rho_i) + f'(\rho_i)(\rho - \rho_i) + \frac{f''(\rho_i)}{2}(\rho - \rho_i)^2 + \dots \quad (\text{C.1})$$

Rearranging terms and dropping terms of higher order than two, yields a finite difference scheme of second order. For the inner derivatives we obtain central finite differences

$$f'(\rho_i) = \frac{f(\rho_{i+1}) - f(\rho_{i-1})}{2h} + \mathcal{O}(h^2), \quad (\text{C.2})$$

and

$$f''(\rho_i) = \frac{f(\rho_{i-1}) - 2f(\rho_i) + f(\rho_{i+1}))}{h^2} + \mathcal{O}(h^2). \quad (\text{C.3})$$

For the points on the boundary of the computational domain (first and last grid point) central finite differences are not applicable and replaced by one-sided formulas. A second order representation is again obtained by Taylor expansion of f around the neighbouring grid points (in only one direction) and reads

$$f'(\rho_i) = \frac{-3f(\rho_i) + 4f(\rho_{i+1}) - f(\rho_{i+2}))}{2h} + \mathcal{O}(h^2), \quad (\text{C.4})$$

$$f''(\rho_i) = \frac{2f(\rho_i) - 5f(\rho_{i+1}) + 4f(\rho_{i+2}) - f(\rho_{i+3}))}{h^2} + \mathcal{O}(h^2), \quad (\text{C.5})$$

for the right-handed differences (used at the left boundary $\rho_i = 0$), and

$$f'(\rho_i) = \frac{3f(\rho_i) - 4f(\rho_{i-1}) + f(\rho_{i-2}))}{2h} + \mathcal{O}(h^2), \quad (\text{C.6})$$

C.2. Solver for non-linearly saturated external kink amplitudes

$$f''(\rho_i) = \frac{2f(\rho_i) - 5f(\rho_{i-1}) + 4f(\rho_{i-2}) - f(\rho_{i-3})}{h^2} + \mathcal{O}(h^2), \quad (\text{C.7})$$

for the left-handed differences (used at the right boundary $\rho_i = 1$) respectively. Here, the error is of order h^2 . Similarly, higher order schemes can be derived by evaluating the Taylor series of f on more neighbouring grid points and keeping the associated higher order terms in the expansion. These schemes however lead to more matrix elements which requires more complex algorithms to solve the corresponding linear system of equations and hence increases the computational cost.

In the following, the superscript $j = (1, 2, 3)$ denotes the order of the solution. Subscript i means that a function is evaluated at the i -th grid point and prime denotes finite differences with respect to ρ . The radial grid is constituted by the points $0 \leq \rho_i \leq 1$, with $0 \leq i \leq N$. We write the discrete solutions as

$$\eta_i^1 = f_i^1 \hat{\eta}, \quad (\text{C.8a})$$

$$\eta_i^2 = f_i^2 n^2 \hat{\eta}^2 + g_i^2, \quad (\text{C.8b})$$

$$\eta_i^3 = g_i^3, \quad (\text{C.8c})$$

where f_i^j are the homogeneous and g_i^j the inhomogeneous parts. n^2 is the normalised amplitude of the second order solution at $\rho = 1$. The normalisation constant $\hat{\eta}$ is unknown at this stage. However, in the calculation of D_3 and thus in the calculations of η , this constant cancels out and can be set to an arbitrary value in the numerical solver (we use $\hat{\eta} = 1.0$).

Replacing the radial derivatives in the operator defined in Eq. (4.17) by finite differences of second order (Eqs. (C.2) and (C.3)), and rearranging terms, the system of differential equations (4.18)-(4.20) in discrete form reads

$$\begin{aligned} & \overbrace{\left\{ \frac{1}{h^2} - \left[\frac{3}{\rho_i} + \frac{2}{F_i} \frac{d}{d\rho} \Big|_{\rho_i} F(\rho) \right] \frac{1}{2h} \right\}}^{\equiv a_i} f_{i-1}^j + \overbrace{\left\{ \frac{1 - k^2 m^2}{\rho_i^2} - \frac{2}{h^2} \right\}}^{\equiv b_i} f_i^j \\ & + \overbrace{\left\{ \frac{1}{h^2} + \left[\frac{3}{\rho_i} + \frac{2}{F_i} \frac{d}{d\rho} \Big|_{\rho_i} F(\rho) \right] \frac{1}{2h} \right\}}^{\equiv c_i} f_{i+1}^j = d^j(\rho_i), \end{aligned} \quad (\text{C.9})$$

where $k = 1$ for $j = 1, 3$ and $k = 2$ for $j = 2$. For the multiple choices of current density profiles used in this work, the radial derivative of F in Eq. (C.9) can be calculated analytically as a function of ρ and thus is not replaced by a finite difference. The function $d^j(\rho_i)$ describes the inhomogeneous part. For the first order equation $d_i^1 = 0 \forall i$. For the second order equation with solution η_i^2 the r.h.s of Eq. (C.9) reads

$$\begin{aligned} d_i^2 = -\hat{\eta}^2 & \left\{ \frac{F'(\rho)|_{\rho_i}}{2F_i \rho_i^2} (3\rho_i^2 ((f_i^1)')^2 + m^2 (f_i^1)^2) \right. \\ & \left. - \frac{1}{2\rho_i^3} [(3m^2 - 1)(f_i^1)^2 + 2\rho_i f_i^1 (f_i^1)' + 5\rho_i^2 ((f_i^1)')^2] \right\}, \end{aligned} \quad (\text{C.10})$$

and for the third order equation

$$\begin{aligned}
 d_i^3 = -\hat{\eta}^3 & \left\{ (f_i^1)^3 \frac{1}{3\rho_i^4 F_i} [F_i(12m^2 - m^4 - 7) - 2\rho_i m^2 F_i'] \right. \\
 & + (f_i^1)' (f_i^1)^2 \frac{1}{4\rho_i^3 F_i} [F_i(2 - 16m^2) - 3\rho_i m^2 F_i'] \\
 & + ((f_i^1)')^2 f_i^1 \frac{1}{4\rho_i^2 F_i} [F_i(41 - 19m^2) + 12\rho_i F_i'] \\
 & + f_i^1 (\eta_i^2) \frac{1}{\rho_i^3 F_i} [F_i(1 - 3m^2) + 2\rho_i m^2 F_i'] \\
 & - f_i^1 (\eta_i^2)' \frac{1}{\rho_i^2} (1 - 3m^2) + ((f_i^1)')^3 \frac{1}{4\rho_i F_i} [18F_i + 15\rho_i F_i'] \\
 & \left. - (f_i^1)' (\eta_i^2)' \frac{1}{\rho_i F_i} [5F_i + 3\rho_i F_i'] - (f_i^1)' (\eta_i^2) \frac{1}{\rho_i^2} (1 - 6m^2) \right\}. \tag{C.11}
 \end{aligned}$$

Now, to obtain η_i^2 we need to calculate the constant n^2 in Eq. (C.8b):

$$n^2 = \frac{-\frac{1}{4} (A - 3((f_i^1)')^2 + 4(\hat{g}_i^2)' + 1) F_i^2 - B - 1}{(F(f_{2\rho} - 4m^2\beta_2 + 1) - 2) F_i}, \tag{C.12}$$

with $A = m^2(m^2\beta_1^2 + 8m^2\beta_1\beta_2 - 4\beta_2 - 2)$ and $B = (m^2(\beta_1 + 2\beta_2) - \frac{1}{2}) F_i$.

To obtain the saturated non-linear amplitude η , a total of five problems in the form of Eq. (C.9) need to be solved. First, the two homogeneous solutions f_i^1 and f_i^2 are calculated, where $d_i^{j=1,2} = 0$. In the next step, the particular solution g_i^2 is obtained and n^2 is calculated according to Eq. (C.12). Finally, the particular solution g_i^3 can be computed. Equation (C.9) can be conveniently written in matrix form as

$$\begin{pmatrix} b_1 & c_1 & 0 & & & & & 0 \\ a_2 & b_2 & c_2 & 0 & & & & 0 \\ 0 & a_3 & b_3 & c_3 & 0 & & \cdots & 0 \\ \vdots & & \ddots & \ddots & \ddots & & & \vdots \\ 0 & \cdots & 0 & a_i & b_i & c_i & \cdots & 0 \\ \vdots & & & 0 & \ddots & \ddots & \ddots & \vdots \\ 0 & \cdots & & 0 & a_{N-2} & b_{N-2} & c_{N-2} & \\ 0 & \cdots & & & 0 & a_{N-1} & b_{N-1} & \end{pmatrix} \cdot \begin{pmatrix} f_1^j \\ f_2^j \\ f_3^j \\ \vdots \\ f_i^j \\ \vdots \\ f_{N-2}^j \\ f_{N-1}^j \end{pmatrix} = \begin{pmatrix} d_1^j \\ d_2^j \\ d_3^j \\ \vdots \\ d_i^j \\ \vdots \\ d_{N-2}^j \\ d_{N-1}^j \end{pmatrix}, \tag{C.13}$$

with solution vector f_i^j , and the matrix coefficients a_i , b_i and c_i are defined in Eq. (C.9). The values f_0^j and f_N^j are determined from the boundary conditions Eq. (4.16):

$$\begin{aligned}
 f_0^1 = 0 \quad , \quad f_N^1 = 1, \\
 f_0^2 = 0 \quad , \quad f_N^2 = 1, \\
 g_0^2 = g_N^2 = 0 \quad , \quad g_0^3 = g_N^3 = 0.
 \end{aligned} \tag{C.14}$$

This system can in general be solved with any numerical implementation of Gaussian elimination, which is however computationally expensive. For the second order scheme

C.2. Solver for non-linearly saturated external kink amplitudes

employed here, the coefficient matrix in Eq. (C.13) is tridiagonal and a faster method of solution is the Thomas algorithm [142] consisting of two subsequent iterations. First, a forward iteration determines the coefficients

$$q_i = \begin{cases} \frac{c_1}{b_1} & ; i = 1 \\ \frac{c_i}{b_i - q_{i-1}a_i} & ; i = 2, 3, \dots, N-2 \end{cases}, \quad (\text{C.15})$$

and

$$p_i = \begin{cases} \frac{d_1}{b_1} & ; i = 1 \\ \frac{d_i - p_{i-1}a_i}{b_i - q_{i-1}a_i} & ; i = 2, 3, \dots, N-1 \end{cases}, \quad (\text{C.16})$$

followed by a backward iteration that provides the solution vectors f_i^j as

$$\begin{aligned} f_{N-1} &= p_{N-1}, \\ f_i &= p_i - q_i f_{i+1} \quad ; \quad i = N-2, N-3, \dots, 1. \end{aligned} \quad (\text{C.17})$$

This numerical scheme was implemented in MATLAB and in Python. A comparison showed that memory consumption and CPU time is considerably lower in the Python implementation.

The edge safety factor q_a is an input parameter to Eq. (C.9) and the boundary value problem is solved for numerous values of q_a in between the two marginal points. We recall that the upper marginal point is given by $q_a = m/n$, but the lower marginal point

$$q_a = \frac{m (f^1)' - m^2 \beta_1 - 1}{n (f^1)' - m^2 \beta_1 + 1}, \quad (\text{C.18})$$

depends on the solution to the first order boundary value problem. To find this point we start with an initial value for $(f^1)'$ in Eq. (C.18) and calculate f^1 at the corresponding value of q_a . The solution is then plugged back into Eq. (C.18) and the relative error between left and right hand side is determined. The value of $(f^1)'$ computed from the solution is then used as a new initial guess and the problem is solved again. This process is repeated until the initial guess for $(f^1)'$ and the resulting value from the solution are smaller than a predefined threshold.

In addition to the second order finite difference scheme, a fourth order scheme was implemented. For the fourth order finite difference scheme one obtains a pentadiagonal matrix and the Thomas algorithm is not applicable. LU factorisation is used instead to solve the linear system corresponding to the matrix. This increases the computational cost, while reducing the error to h^4 . The accuracy of the second order scheme is sufficiently good and was thus used for the results presented in this thesis. Nevertheless, for completion we provide the equations for the fourth order scheme. The inner derivatives are given by the central finite differences

$$f'(\rho_i) = \frac{f(\rho_{i-2}) - f(\rho_{i+2}) + 8f(\rho_{i+1}) - 8f(\rho_{i-1})}{12h^2} + \mathcal{O}(h^4), \quad (\text{C.19})$$

and

$$f''(\rho_i) = \frac{-f(\rho_{i-2}) + 16f(\rho_{i-1}) - 30f(\rho_i) + 16f(\rho_{i+1}) - f(\rho_{i+2})}{12h^2} + \mathcal{O}(h^2). \quad (\text{C.20})$$

Similar to the second order scheme, for the outer grid points we use non-central differences. They read

$$f'(\rho_i) = \frac{f(\rho_{i+3}) - 6f(\rho_{i+2}) + 18f(\rho_{i+1}) - 10f(\rho_i) - 3f(\rho_{i-1})}{12h^2} + \mathcal{O}(h^4), \quad (\text{C.21})$$

$$f''(\rho_i) = \frac{f(\rho_{i+4}) - 6f(\rho_{i+3}) - 14f(\rho_{i+2}) - 4f(\rho_{i+1}) - 15f(\rho_i) + 10f(\rho_{i-1})}{12h^2} + \mathcal{O}(h^4), \quad (\text{C.22})$$

for the two left hand sided grid-points, and

$$f'(\rho_i) = -\frac{f(\rho_{i-3}) - 6f(\rho_{i-2}) + 18f(\rho_{i-1}) - 10f(\rho_i) - 3f(\rho_{i+1})}{12h^2} + \mathcal{O}(h^4), \quad (\text{C.23})$$

$$f''(\rho_i) = \frac{f(\rho_{i-4}) - 6f(\rho_{i-3}) + 14f(\rho_{i-2}) - 4f(\rho_{i-1}) - 15f(\rho_i) + 10f(\rho_{i+1})}{12h^2} + \mathcal{O}(h^4), \quad (\text{C.24})$$

for the two right hand sided grid points respectively. The coefficient matrix that follows from this fourth order scheme is pentadiagonal.

For comparison with numerical results from VMEC, the current density profile can be directly read from the VMEC input file. Since the analytical model assumes a cylindrical plasma, the total current is

$$I(\rho) = 2 \sum_{i=0}^{20} ac[i] \frac{\rho^{2i+2}}{2i+2}, \quad (\text{C.25})$$

where ac is a list of polynomial coefficients. Again, the total current is normalised such that $I(1) = 0$. Instead of specifying a current density profile, we can also perform the non-linear stability calculation by providing a q profile. The normalised toroidal current is then

$$I(\rho) = \frac{q_a \rho^2}{q(\rho)}, \quad (\text{C.26})$$

and its radial derivative

$$I'(\rho) = q_a \frac{2\rho q(\rho) - \rho^2 q'(\rho)}{[q'(\rho)]^2}. \quad (\text{C.27})$$

C.2.2 Benchmark of the solver

For the case of a uniform current density profile $j(\rho) = \text{const.}$, the system of equations (4.18)-(4.20) can be solved analytically and compared to the result of the numerical solver for benchmarking. This is done at the lower marginal point. For simplicity $j(\rho) = 1$ is chosen. A comparison of the analytical calculation with the results of the numerical solver is shown in Table C.1 for $m = 2, n = 1, b = 1.5$ and different values of the radial step size. It can be seen that the results converge towards the analytical values as the grid becomes finer.

C.2. Solver for non-linearly saturated external kink amplitudes

	$h = 1/500$	$h = 1/1000$	$h = 1/6000$	analytical
f'_1	1.0	1.0	1.0	1.0
f'_2	2.99400	2.99700	2.99950	3.0
g'_2	-1.47763	-1.48878	-1.49813	-1.5
n_2	0.62324	0.62602	0.62835	0.62882
$n_{2\rho}$	0.38835	0.38740	0.38661	0.38645
$n_{3\rho}$	-0.62454	-0.61531	-0.60749	-0.60592
D_3	0.28413	0.28299	0.28205	0.28187

Table C.1 – Benchmark of the external kink solver. A comparison of numerical results with the analytical solution shows very good agreement.

In an additional test of the code with current density profile

$$j(\rho) = \begin{cases} (\nu + 1)(1 - \rho^2)^\nu, & \nu \geq 1 \\ \frac{1 - \nu\rho^2}{1 - \nu/2}, & \nu < 1 \end{cases}, \quad (\text{C.28})$$

the results of Fig. C.2 recover those obtained by Eriksson & Wahlberg [95].

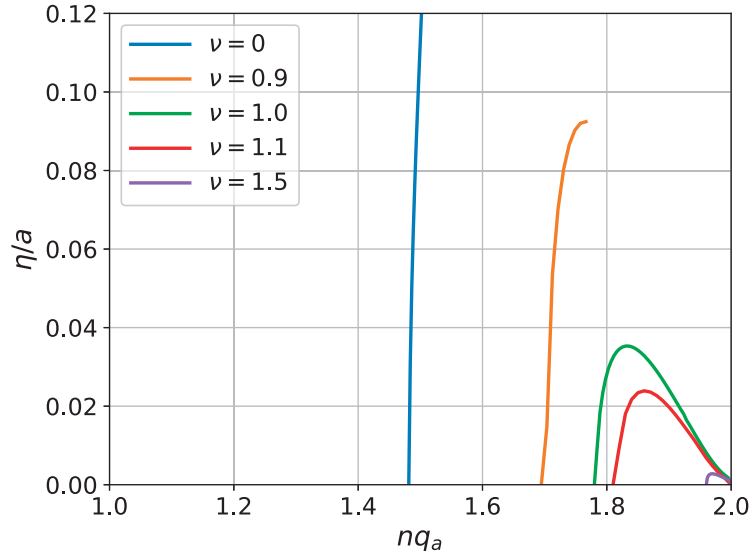


Figure C.2 – Non-linear external kink mode amplitude η as a function of nq_a for $b = 1.2$, $m = 2$, and taking into account magnetic flux conservation. The results shown here recover those of Fig. 4 of Ref. [95].

Bibliography

- [1] G. Miley, H. Towner, and N. Ivich, *Fusion cross sections and reactivities* (University of Illinois, Urbana, IL, 1974). (Cited on page 1.)
- [2] P. M. Bellan, *Fundamentals of Plasma Physics* (Cambridge University Press, 2006). (Cited on page 2.)
- [3] R. Abraham, J. E. Marsden, and T. Ratiu, *Manifolds, Tensor Analysis, and Applications* (Springer, New York, NY, New York, NY, 1988). (Cited on page 3.)
- [4] D. D. Schnack, editor, *Lectures in Magnetohydrodynamics*, , Lecture Notes in Physics, Berlin Springer Verlag Vol. 780, 2009. (Cited on page 4.)
- [5] F. Troyon, R. Gruber, H. Saurenmann, S. Semenzato, and S. Succi, *Plasma Physics and Controlled Fusion* **26**, 209 (1984). (Cited on page 4.)
- [6] L. Spitzer, *The Physics of Fluids* **1**, 253 (1958). (Cited on page 4.)
- [7] J. D. Lawson, *Proceedings of the Physical Society B* **70**, 6 (1957). (Cited on page 5.)
- [8] A. C. C. Sips, for the Steady State Operation, and the Transport Physics topical groups of the International Tokamak Physics Activity, *Plasma Physics and Controlled Fusion* **47**, A19 (2005). (Cited on page 6.)
- [9] C. Gormezano *et al.*, *Nuclear Fusion* **47**, S285 (2007). (Cited on pages 7 and 31.)
- [10] F. Wagner *et al.*, *Phys. Rev. Lett.* **49**, 1408 (1982). (Cited on pages 7 and 85.)
- [11] F. Wagner *et al.*, *Phys. Rev. Lett.* **53**, 1453 (1984). (Cited on page 7.)
- [12] H. Zohm, *Plasma Physics and Controlled Fusion* **38**, 105 (1996). (Cited on pages 7 and 85.)
- [13] T. E. Evans *et al.*, *Nature Physics* **2**, 419 (2006). (Cited on pages 7 and 19.)
- [14] R. Wenninger, H. Reimerdes, O. Sauter, and H. Zohm, *Nuclear Fusion* **53**, 113004 (2013). (Cited on pages 8, 27 and 105.)
- [15] P. H. Rutherford, *Physics of Fluids* **16**, 1903 (1973). (Cited on pages 8, 32 and 37.)
- [16] R. J. La Haye, *Physics of Plasmas* **13**, 055501 (2006). (Cited on pages 8 and 37.)
- [17] N. N. Gorelenkov, R. V. Budny, Z. Chang, M. V. Gorelenkova, and L. E. Zakharov, *Physics of Plasmas* **3**, 3379 (1996). (Cited on pages 8, 37 and 38.)
- [18] K. H. Burrell *et al.*, *Physics of Plasmas* **12** (2005). (Cited on pages 9, 86, 88, 89, 90, 92 and 103.)

-
- [19] D. Brunetti *et al.*, Helical equilibrium mhd flow effects on the stability properties of low-n ideal modes in weak shear tokamak configurations, submitted (2018). (Cited on page 10.)
- [20] D. Brunetti *et al.*, Excitation mechanism of low-n edge harmonic oscillations in elm-free high performance tokamak plasmas, submitted (2018). (Cited on pages 10 and 106.)
- [21] J. P. H. Goedbloed, J. P. Goedbloed, and S. Poedts, *Principles of Magnetohydrodynamics - With Applications to Laboratory and Astrophysical Plasmas* (Cambridge University Press, Cambridge, 2004). (Cited on pages 11 and 12.)
- [22] J. P. Freidberg, *Ideal MHD* (Cambridge University Press, 2014). (Cited on pages 12, 24, 26, 63, 65 and 116.)
- [23] L. Spitzer and R. Härm, *Phys. Rev.* **89**, 977 (1953). (Cited on page 13.)
- [24] A. G. Peeters, *Plasma Physics and Controlled Fusion* **42**, B231 (2000). (Cited on page 14.)
- [25] O. Sauter, C. Angioni, and Y. R. Lin-Liu, *Physics of Plasmas* **6**, 2834 (1999). (Cited on pages 15 and 52.)
- [26] O. Sauter, C. Angioni, and Y. R. Lin-Liu, *Physics of Plasmas* **9**, 5140 (2002). (Cited on pages 15 and 52.)
- [27] H. Grad and H. Rubin, Hydromagnetic Equilibria and Force-Free Fields, in *Proceedings of the 2nd U.N. International Conference on the Peaceful Uses of Atomic Energy*, pp. 190–197, 1958. (Cited on page 17.)
- [28] V. D. Shafranov, *Reviews of Plasma Physics* **2**, 103 (1966). (Cited on page 17.)
- [29] L. S. Solov'ev, *Sov. Phys. JETP* **26**, 400 (1968). (Cited on page 18.)
- [30] H. Lütjens, A. Bondeson, and O. Sauter, *Computer Physics Communications* **97**, 219 (1996). (Cited on pages 18, 38 and 53.)
- [31] O. Sauter and S. Medvedev, *Computer Physics Communications* **184**, 293 (2013). (Cited on page 19.)
- [32] D. Brunetti, J. Graves, W. Cooper, and D. Terranova, *Nuclear Fusion* **54**, 064017 (2014). (Cited on pages 19, 28, 63 and 64.)
- [33] M. D. Kruskal and R. M. Kulsrud, *The Physics of Fluids* **1**, 265 (1958). (Cited on page 19.)
- [34] S. P. Hirshman and J. C. Whitson, *The Physics of Fluids* **26**, 3553 (1983). (Cited on pages 19, 21, 64, 70 and 74.)
- [35] J. D. Hanson and S. P. Hirshman, *Physics of Plasmas* **9**, 4410 (2002). (Cited on pages 22 and 70.)

Bibliography

- [36] R. Dewar and S. Hudson, *Physica D: Nonlinear Phenomena* **112**, 275 (1998), Proceedings of the Workshop on Time-Reversal Symmetry in Dynamical Systems. (Cited on page 23.)
- [37] D. Biskamp, *Nonlinear Magnetohydrodynamics* (Cambridge University Press, 1993), Cambridge Books Online. (Cited on pages 26, 27 and 37.)
- [38] L. Degtyarev *et al.*, *Computer Physics Communications* **103**, 10 (1997). (Cited on pages 26 and 77.)
- [39] F. Liu *et al.*, *Nuclear Fusion* **55**, 113002 (2015). (Cited on pages 27, 86 and 105.)
- [40] Y. ping Pao, *The Physics of Fluids* **21**, 765 (1978). (Cited on pages 27 and 67.)
- [41] H. Lütjens and J.-F. Luciani, *Journal of Computational Physics* **227**, 6944 (2008). (Cited on pages 28, 48 and 49.)
- [42] H. Lütjens and J.-F. Luciani, *Journal of Computational Physics* **229**, 8130 (2010). (Cited on pages 28, 32, 48, 50, 52, 53 and 63.)
- [43] G. Huysmans and O. Czarny, *Nuclear Fusion* **47**, 659 (2007). (Cited on page 28.)
- [44] O. Czarny and G. Huysmans, *Journal of Computational Physics* **227**, 7423 (2008). (Cited on page 28.)
- [45] W. A. Cooper *et al.*, *Journal of Plasma Physics* **81**, 515810605 (2015). (Cited on pages 28 and 64.)
- [46] W. A. Cooper *et al.*, *Physics of Plasmas* **23**, 040701 (2016). (Cited on pages 28, 64 and 86.)
- [47] W. A. Cooper *et al.*, *Plasma Physics and Controlled Fusion* **58**, 064002 (2016). (Cited on pages 28, 64, 70, 71 and 86.)
- [48] A. Kleiner *et al.*, *Nuclear Fusion* **56**, 092007 (2016). (Cited on pages 31 and 96.)
- [49] A. Staebler *et al.*, *Nuclear Fusion* **45**, 617 (2005). (Cited on page 31.)
- [50] B. B. Kadomtsev, *Soviet Journal of Plasma Physics* **1**, 389 (1975). (Cited on page 32.)
- [51] F. Porcelli, D. Boucher, and M. N. Rosenbluth, *Plasma Physics and Controlled Fusion* **38**, 2163 (1996). (Cited on pages 32 and 34.)
- [52] J. Manickam, N. Pomphrey, and A. Todd, *Nuclear Fusion* **27**, 1461 (1987). (Cited on pages 32 and 96.)
- [53] L. A. Charlton, R. J. Hastie, and T. C. Hender, *Physics of Fluids B* **1**, 798 (1989). (Cited on pages 32, 39, 41 and 96.)
- [54] J. A. Wesson, *Plasma Physics and Controlled Fusion* **28**, 243 (1986). (Cited on pages 32 and 34.)

-
- [55] G. Canal *et al.*, Nuclear Fusion **53**, 113026 (2013). (Cited on pages 32, 33 and 34.)
- [56] D. Brunetti, J. P. Graves, W. A. Cooper, and C. Wahlberg, Plasma Physics and Controlled Fusion **56**, 075025 (2014). (Cited on pages 32, 40, 41, 45, 46, 86 and 96.)
- [57] J. P. Graves *et al.*, Nature Communications **3**, 624 (2012). (Cited on pages 32 and 33.)
- [58] J. Breslau *et al.*, Nuclear Fusion **51**, 063027 (2011). (Cited on page 32.)
- [59] F. Wang, G. Y. Fu, J. A. Breslau, and J. Y. Liu, Physics of Plasmas **20**, 102506 (2013). (Cited on page 32.)
- [60] F. Wang, G. Y. Fu, J. A. Breslau, K. Tritz, and J. Y. Liu, Physics of Plasmas **20**, 072506 (2013). (Cited on page 32.)
- [61] D. Brunetti *et al.*, Plasma Physics and Controlled Fusion **57**, 054002 (2015). (Cited on page 32.)
- [62] O. Sauter *et al.*, Phys. Rev. Lett. **88**, 105001 (2002). (Cited on page 33.)
- [63] J. Kamleitner, S. Coda, J. Decker, J. P. Graves, and the TCV team, Plasma Physics and Controlled Fusion **57**, 104009 (2015). (Cited on page 33.)
- [64] H. P. Furth, J. Killeen, and M. N. Rosenbluth, The Physics of Fluids **6**, 459 (1963). (Cited on pages 35 and 36.)
- [65] J. Wesson, *Tokamaks*, 3rd ed. (OUP Oxford, New York, London, 2004). (Cited on pages 35, 37 and 38.)
- [66] M. Nave *et al.*, Nuclear Fusion **43**, 179 (2003). (Cited on page 37.)
- [67] C. C. Hegna and J. D. Callen, Physics of Plasmas **1**, 2308 (1994). (Cited on page 38.)
- [68] R. B. White, D. A. Monticello, M. N. Rosenbluth, and B. V. Waddell, Physics of Fluids **20**, 800 (1977). (Cited on page 38.)
- [69] D. Escande and M. Ottaviani, Physics Letters A **323**, 278 (2004). (Cited on page 38.)
- [70] F. Militello and F. Porcelli, Physics of Plasmas **11**, L13 (2004). (Cited on page 38.)
- [71] A. I. Smolyakov, A. Poye, O. Agullo, S. Benkadda, and X. Garbet, Physics of Plasmas **20**, 062506 (2013). (Cited on page 38.)
- [72] O. Sauter *et al.*, Physics of Plasmas **4**, 1654 (1997). (Cited on pages 38 and 61.)
- [73] N. Bertelli, D. D. Lazzari, and E. Westerhof, Nuclear Fusion **51**, 103007 (2011). (Cited on page 38.)

Bibliography

- [74] A. H. Glasser, J. M. Greene, and J. L. Johnson, *Physics of Fluids* **18**, 875 (1975). (Cited on page 38.)
- [75] A. H. Glasser, J. M. Greene, and J. L. Johnson, *Physics of Fluids* **19**, 567 (1976). (Cited on page 38.)
- [76] H. R. Wilson, J. W. Connor, R. J. Hastie, and C. C. Hegna, *Physics of Plasmas* **3**, 248 (1996). (Cited on page 38.)
- [77] H. Lütjens, J.-F. Luciani, and X. Garbet, *Physics of Plasmas* **8**, 4267 (2001). (Cited on page 38.)
- [78] H. Lütjens and J.-F. Luciani, *Physics of Plasmas* **9**, 4837 (2002). (Cited on page 38.)
- [79] R. Fitzpatrick, *Nuclear Fusion* **33**, 1049 (1993). (Cited on page 38.)
- [80] L. Zakharov, *Nuclear Fusion* **18**, 335 (1978). (Cited on page 39.)
- [81] A. B. Mikhailovskii, *Instabilities in a Confined Plasma*, 1st ed. (CRC Press, Boca Raton, Fla, 1998). (Cited on pages 40 and 66.)
- [82] M. Abramowitz and I. Stegun, *Handbook of Mathematical Functions* (Dover Publications, New York, 1965). (Cited on page 46.)
- [83] F. L. Waelbroeck and R. D. Hazeltine, *Physics of Fluids* **31**, 1217 (1988). (Cited on page 46.)
- [84] S. I. Braginskii, *Reviews of Plasma Physics* **1**, 205 (1965). (Cited on page 48.)
- [85] O. Février *et al.*, *Nuclear Fusion* **58**, 096008 (2018). (Cited on page 49.)
- [86] D. Knoll and D. Keyes, *Journal of Computational Physics* **193**, 357 (2004). (Cited on page 50.)
- [87] M. Pernice and H. Walker, *SIAM Journal on Scientific Computing* **19**, 302 (1998). (Cited on page 51.)
- [88] S. Balay *et al.*, Argonne National Laboratory Report No. ANL-95/11 - Revision 3.9, 2018 (unpublished). (Cited on page 51.)
- [89] S. Balay, W. D. Gropp, L. C. McInnes, and B. F. Smith, Efficient management of parallelism in object oriented numerical software libraries, in *Modern Software Tools in Scientific Computing*, edited by E. Arge, A. M. Bruaset, and H. P. Langtangen, pp. 163–202, Birkhäuser Press, 1997. (Cited on page 51.)
- [90] A. Marx and H. Lütjens, *Computer Physics Communications* **212**, 90 (2017). (Cited on pages 51 and 63.)
- [91] A. Marx and H. Lütjens, *Plasma Physics and Controlled Fusion* **59**, 064009 (2017). (Cited on pages 51 and 108.)

-
- [92] A. Kleiner, J. Graves, W. Cooper, T. Nicolas, and C. Wahlberg, *Nuclear Fusion* **58**, 074001 (2018). (Cited on page 63.)
- [93] J. Wesson, *Nuclear Fusion* **18**, 87 (1978). (Cited on pages 63, 64, 65 and 71.)
- [94] H. G. Eriksson and C. Wahlberg, *Plasma Physics and Controlled Fusion* **36**, 1269 (1994). (Cited on pages 63 and 67.)
- [95] H. G. Eriksson and C. Wahlberg, *Plasma Physics and Controlled Fusion* **39**, 943 (1997). (Cited on pages 63, 64, 67, 68, 69, 71, 76, 87, 92 and 125.)
- [96] D. Pfefferlé *et al.*, *Nuclear Fusion* **54**, 064020 (2014). (Cited on page 64.)
- [97] M. Raghunathan *et al.*, *Plasma Physics and Controlled Fusion* **59**, 124002 (2017). (Cited on page 64.)
- [98] D. Pfefferlé, W. Cooper, J. Graves, and C. Misev, *Computer Physics Communications* **185**, 3127 (2014). (Cited on page 64.)
- [99] P. H. Rutherford, H. P. Furth, and M. N. Rosenbluth, Non-linear kink and tearing mode effects in Tokamaks (IAEA-CN-28/F-16), in *Plasma Physics and Controlled Nuclear Fusion Research, Volume II*, p. 553, 1971. (Cited on pages 67 and 92.)
- [100] Z. X. Jiang and C. Wahlberg, *Plasma Physics and Controlled Fusion* **35**, 551 (1993). (Cited on page 67.)
- [101] N. Nakajima, *Physics of Fluids B: Plasma Physics* **2**, 1170 (1990). (Cited on page 67.)
- [102] M. N. Rosenbluth, D. A. Monticello, H. R. Strauss, and R. B. White, *The Physics of Fluids* **19**, 1987 (1976). (Cited on page 67.)
- [103] C. Wahlberg, H. G. Eriksson, and Z. X. Jiang, *Physics of Plasmas* **4**, 2397 (1997). (Cited on page 68.)
- [104] S. Hirshman, W. van RIJ, and P. Merkel, *Computer Physics Communications* **43**, 143 (1986). (Cited on page 70.)
- [105] E. Strumberger, S. Günter, P. Merkel, E. Schwarz, and C. Tichmann, *Nuclear Fusion* **50**, 025008 (2010). (Cited on page 73.)
- [106] A. Kleiner *et al.*, Non-linear pressure & current driven edge harmonic oscillations modelled using 3d free-boundary equilibria, submitted (2018). (Cited on pages 85 and 103.)
- [107] J. Hughes *et al.*, *Nuclear Fusion* **53**, 043016 (2013). (Cited on page 85.)
- [108] P. B. Snyder *et al.*, *Physics of Plasmas* **9**, 2037 (2002). (Cited on page 85.)
- [109] J.-S. Lönnroth *et al.*, *Plasma Physics and Controlled Fusion* **46**, 1197 (2004). (Cited on page 85.)

Bibliography

- [110] W. Suttrop *et al.*, Nuclear Fusion **45**, 721 (2005). (Cited on pages 86 and 88.)
- [111] Y. Sakamoto *et al.*, Plasma Physics and Controlled Fusion **46**, A299 (2004). (Cited on pages 86 and 88.)
- [112] N. Oyama *et al.*, Nuclear Fusion **45**, 871 (2005). (Cited on page 86.)
- [113] J. S. Hu *et al.*, Phys. Rev. Lett. **114**, 055001 (2015). (Cited on page 86.)
- [114] E. R. Solano *et al.*, Phys. Rev. Lett. **104**, 185003 (2010). (Cited on page 86.)
- [115] M. Nave *et al.*, Nuclear Fusion **35**, 409 (1995). (Cited on pages 86 and 88.)
- [116] P. B. Snyder, R. J. Groebner, A. W. Leonard, T. H. Osborne, and H. R. Wilson, Physics of Plasmas **16** (2009). (Cited on page 86.)
- [117] P. Snyder *et al.*, Nuclear Fusion **47**, 961 (2007). (Cited on page 86.)
- [118] W. M. Solomon *et al.*, Phys. Rev. Lett. **113**, 135001 (2014). (Cited on page 86.)
- [119] L. Zheng, M. Kotschenreuther, and P. Valanju, Nuclear Fusion **53**, 063009 (2013). (Cited on pages 86, 96 and 98.)
- [120] D. Brunetti *et al.*, Nuclear Fusion **58**, 014002 (2018). (Cited on pages 86 and 87.)
- [121] D. Brunetti *et al.*, Journal of Plasma Physics **84**, 745840201 (2018). (Cited on pages 86, 87, 97, 98 and 100.)
- [122] ASDEX Upgrade Team, W. Suttrop *et al.*, Phys. Rev. Lett. **106**, 225004 (2011). (Cited on page 88.)
- [123] M. F. F. Nave *et al.*, Plasma Physics and Controlled Fusion **42**, A89 (2000). (Cited on page 88.)
- [124] T. H. Osborne *et al.*, Plasma Physics and Controlled Fusion **36**, A237 (1994). (Cited on page 88.)
- [125] G. Huysmans, T. Hender, and B. Alper, Nuclear Fusion **38**, 179 (1998). (Cited on page 88.)
- [126] D. Whyte *et al.*, Nuclear Fusion **50**, 105005 (2010). (Cited on page 88.)
- [127] K. H. Burrell *et al.*, Physics of Plasmas **8**, 2153 (2001). (Cited on pages 88 and 89.)
- [128] W. Suttrop *et al.*, Plasma Physics and Controlled Fusion **45**, 1399 (2003). (Cited on page 88.)
- [129] A. Garofalo *et al.*, Nuclear Fusion **51**, 083018 (2011). (Cited on page 88.)
- [130] T. Wilks *et al.*, Nuclear Fusion **58**, 112002 (2018). (Cited on page 88.)
- [131] A. M. Garofalo *et al.*, Physics of Plasmas **22**, 056116 (2015). (Cited on pages 89 and 91.)

- [132] J.-K. Park *et al.*, Nuclear Fusion **54**, 043013 (2014). (Cited on page 89.)
- [133] L. J. Zheng, M. T. Kotschenreuther, and P. Valanju, Physics of Plasmas **20**, 012501 (2013). (Cited on page 96.)
- [134] S. Y. Medvedev, A. A. Martynov, Y. R. Martin, O. Sauter, and L. Villard, Plasma Physics and Controlled Fusion **48**, 927 (2006). (Cited on page 98.)
- [135] G. Q. Dong *et al.*, Physics of Plasmas **24**, 112510 (2017). (Cited on page 102.)
- [136] X. Chen *et al.*, Nuclear Fusion **56**, 076011 (2016). (Cited on page 106.)
- [137] F. Liu *et al.*, Plasma Physics and Controlled Fusion **60**, 014039 (2018). (Cited on page 106.)
- [138] W. D. D'haeseleer, W. N. Hitchon, J. D. Callen, and J. L. Shohet, *Flux Coordinates and Magnetic Field Structure - A Guide to a Fundamental Tool of Plasma Theory* (Springer Science & Business Media, Berlin Heidelberg, 2012). (Cited on page 113.)
- [139] J. P. Goedbloed, R. Keppens, and S. Poedts, *Advanced magnetohydrodynamics : with applications to laboratory and astrophysical plasmas* (Cambridge University Press, Cambridge; New York, 2010). (Cited on page 114.)
- [140] J. P. Graves and C. Wahlberg, Plasma Physics and Controlled Fusion **59**, 054011 (2017). (Cited on page 117.)
- [141] R. D. Hazeltine, *Plasma Confinement* (Courier Corporation, New York, 2013). (Cited on page 117.)
- [142] P. Niyogi, *Introduction to Computational Fluid Dynamics* (Pearson Education India, Delhi, 2009). (Cited on page 123.)

Acknowledgements

The work on this thesis during the past 4 years was often demanding, but also rewarding. This thesis would not have been possible without the support of many people who contributed in multiple ways.

First, I want to thank my advisor Jonathan Graves for directing me throughout this scientific journey and for his support. Jon always had an open door whenever I had questions, and during our discussions gave me good ideas for my research. I am especially grateful to Jon for believing in me when others did not. I also like to thank Tony Cooper who offered me an interesting master's project and with that the possibility to discover the interesting world of fusion plasmas. I also thank him for sharing his experience with the VMEC code.

I would like to thank the colleagues I collaborated intensively with, namely Hinrich Lütjens, Timothée Nicolas and Olivier Février for answering all my questions regarding XTOR-2F and particularly for helping me with the code compilation. This also applies to Olivier Sauter, whose expertise with CHEASE saved me a lot of time and frustration. Further thanks go to Federico Halpern, Christopher Ham and Joaquim Loizu for useful and interesting discussions. I thank Christer Wahlberg and Hans Eriksson for taking the time to discuss and help me with their non-linear analytical external kink model. Special thanks go to Daniele Brunetti, whose analytical work on infernal modes motivated research I conducted during the past years. He did not only help me understand his analytical models, but we also had a lot of interesting discussions about plasma physics, but also about non-physical topics.

I also thank all the other colleagues from SPC and especially my fellow PhD students David, Madhu, Sam, Jérémy, Eduardo and André for the times we spent inside and outside of the office. Special thanks goes to my team mates from the CRPP/SPC football team. We even almost won a match in 2016!

Diese Doktorarbeit wäre auch nicht ohne die Unterstützung durch meine Familie möglich gewesen. Zuallererst danke ich meinen Eltern, die mich nicht nur während meines Bachelor- und Masterstudiums gefördert haben, sondern auch in den letzten vier Jahren und viel Verständnis für meine Abwesenheit hatten. Weiterhin danke ich meinem Großvater, der mein Interesse an der Naturwissenschaft maßgeblich geprägt hat. Das Gleiche gilt auch für meinen Cousin Frank, dem ich meine Begeisterung für Informatik und Programmierung verdanke.

I am most grateful for the loving support of my fiancée Patricia, who was always there for me in difficult times and understanding when I was not in a good mood. Finally, I also thank our cats Lee, Lola and Cowboy, who manage to cheer me up and entertain me during difficult times.

Andreas Kleiner

Address: EPFL SB SPC-TH, Station 13, 1015 Lausanne, Switzerland

Phone: +41 21 69 36536

Email: andreas.kleiner@epfl.ch

Place and date of birth: 97816 Lohr a. Main, Germany | 21.09.1987

Nationality: German

Profile

After exploring several fields in physics during my undergraduate studies, I started investigating macroscopic plasma instabilities in my master's project. As a PhD candidate, I am currently deepening my understanding of toroidal 3D equilibria and MHD instabilities while applying my experience as software developer in the numerical work.

Education

- 12/2014 – present **PhD candidate in plasma physics**
Swiss Plasma Center (SPC), Swiss Federal Institute of Technology (EPFL), Lausanne, Switzerland
Thesis title: Non-linear modelling of saturated internal and external MHD instabilities in tokamaks
Supervisor: Dr. Jonathan Graves
Description: The thesis investigates nonlinear stability of pressure and current driven MHD instabilities in tokamak plasmas as experienced in hybrid and advanced scenarios. Coupling of infernal modes with NTMs and external kink modes are the main focuses.
- 10/2012 – 10/2014 **Master of Science in physics**
Technische Universität Darmstadt, Darmstadt, Germany
 - Master's thesis carried out at CRPP (now SPC), EPFL
 - Thesis title:** Finite toroidal mode number ideal MHD instabilities in tokamak plasmas with externally applied magnetic perturbations
 - Supervisors:** Dr. W.A. Cooper, Dr. C.-V. Meister, Dr. J. Graves
 - Description:** This thesis studies finite n ballooning instabilities using the Wentzel-Kramers-Brillouin approximation in the MAST tokamak with externally applied resonant magnetic perturbations.
 - Erasmus semester at EPFL in spring term 2013
 - Fields of study include plasma physics, nuclear physics and space technologies
- 10/2009 – 09/2012 **Bachelor of Science in physics**
Technische Universität Darmstadt, Darmstadt, Germany
Bachelor's thesis: Comparisons of equations of state for core-collapse supernovae and neutron stars

Work Experience

- 02/2015 – 07/2018 **Teaching Assistant**
Swiss Federal Institute of Technology (EPFL), Lausanne, Switzerland
Tutoring of students in the courses general physics I & II in the spring and autumn terms.
- 02/2017 **Mobility Trip** to CPHT, Ecole Polytechnique, France.
XTOR-2F nonlinear extended MHD stability code with vacuum region for simulations of external MHD instabilities

- 02/2013 – 07/2013 **Teaching Assistant**
 EPFL, Lausanne, Switzerland
 Supporting a group of students in exercise sessions of the course general physics II (German), creating exercise sheets and a bonus test, teaching special theory of relativity and classical scattering
- 10/2012 – 02/2013 **Laboratory Supervisor**
 Technische Universität Darmstadt, Germany
 Supervision of first year physics students in laboratory sessions
- 07/2010 – 02/2013 **Research Assistant**
 Technische Universität Darmstadt, Germany
 Operating the S-DALINAC superconducting electron particle accelerator and associated facilities at the institute of nuclear physics at TU Darmstadt.
- 09/2006 – 08/2009 **Qualified IT Specialist in software development**
 multi-INTER-media GmbH, Lohr a. Main, Germany
 Professional training in software development focused on web applications.
 Achievements:
- Theoretical background of software development
 - Study and application of web technologies, e.g. HTML, CSS, ASP, Javascript
 - Image processing techniques and design of websites
 - Business and management skills

List of publications

First author

- A. Kleiner et al, *Non-linear pressure & current driven edge harmonic oscillations modelled using 3D free-boundary equilibria*, in preparation for PPCF
- A. Kleiner et al, *Free boundary 3D ideal MHD equilibrium calculations for non-linearly saturated current driven external kink modes in tokamaks*, Nucl. Fusion **58** 074001 (2018)
- A. Kleiner et al, *Neoclassical tearing mode seeding by coupling with infernal modes in low-shear tokamaks*, Nucl. Fusion **56** 092007 (2016)

Co-author

- W.A. Cooper et al, *Stellarator nonlinearly saturated periodicity-breaking ideal magnetohydrodynamic equilibrium states*, Nucl. Fusion **58** 124002 (2018)
- W.A. Cooper et al, *Saturated ideal kink/peeling formations described as three-dimensional magnetohydrodynamic tokamak equilibrium states*, Phys. Plasmas **23** 040701 (2016)
- W.A. Cooper et al, *Three-dimensional magnetohydrodynamic equilibrium of quiescent H-modes in tokamak systems*, Plasma Phys. Control. Fusion **58** 064002 (2016)

Conference contributions

- A. Kleiner et al., *Ideal saturated 3D external kink structures in quiescent H mode plasmas*, **oral presentation** at 643rd WEH Seminar Impact of 3D magnetic fields on hot plasmas, 22-24 May 2017, Bad Honnef, Germany
- A. Kleiner et al., *Free boundary 3D equilibrium calculations for non-linearly saturated current and pressure driven external kink modes*, contributed poster at Theory of Fusion Plasmas - Joint Varenna-Lausanne International Workshop, 27-31 August 2018, Varenna, Italy
- A. Kleiner et al., *Calculation of ideal saturated 3D external kink structures in quiescent H mode plasmas using nonlinear approaches*, contributed poster at 17th European Fusion Theory Conference, 9-12 October 2017, Athens, Greece
- A. Kleiner et al., *Ideal saturated 3D external kink structures in quiescent H mode plasmas*, contributed poster at 643rd WEH Seminar Impact of 3D magnetic fields on hot plasmas, 22-24 May 2017, Bad Honnef, Germany

- A. Kleiner et al., *Triggering of fast growing secondary resistive MHD modes during sawtooth cycles*, contributed poster at 597th WEH Seminar Stochasticity in Fusion Plasmas, 10–12 September 2015, Bad Honnef, Germany

Awards

- 2009 Kammersieger in the IHK Würzburg-Schweinfurt for best result in the exam for qualified IT specialists in software development
- 2009 Sponsorship award of the friends of Klara-Oppenheimer-Schule Würzburg for developing a website for a nonprofit organization from Würzburg, Germany

Memberships

- 2009 – present Member of the German physical society DPG (Deutsche Physikalische Gesellschaft)

Computer Skills

- Scientific software Mathematica, Matlab, L^AT_EX, Linux, MPI, OpenMP
- Programming languages Fortran, Python, C#, Java, Visual Basic, PHP, Javascript
- Other Microsoft Windows, SQL based databases, HTML, CSS, image processing

Languages

- German Mother tongue
- English Proficient
- French Basic
- Portuguese Basic

Interests

Sports (running, football, skiing, volleyball), photography, (classical) music, natural history

